

AFWAL-TR-82-4090

ADA129049

PHYSICAL-CHEMICAL PROPERTIES OF ARTICULATED RODLIKE POLYMERS

G. C. Berry
Y. Einaga
R. Furukawa
L. Marwaha
H. H. Tsai

Carnegie-Mellon University
4400 Fifth Avenue
Pittsburgh, PA 15213

August, 1982

Final Report for Period 1 March 1981 to 28 February 1982

Approved for Public Release, Distribution Unlimited

MATERIALS LABORATORY
AIR FORCE WRIGHT AERONAUTICAL LABORATORIES
AIR FORCE SYSTEMS COMMAND
WRIGHT-PATTERSON AIR FORCE BASE, OHIO 45433

BEST AVAILABLE COPY

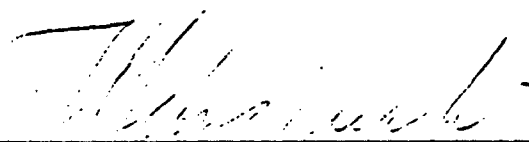
20040223067

NOTICE

When Government drawings, specifications, or other data are used for any purpose other than in connection with a definitely related Government procurement operation, the United States Government thereby incurs no responsibility nor any obligation whatsoever; and the fact that the Government may have formulated, furnished, or in any way supplied the said drawings, specifications, or other data, is not to be regarded by implication or otherwise as in any manner licensing the holder or any other person or corporation, or conveying any rights or permission to manufacture, use, or sell any patented invention that may in any way be related thereto.

This report has been reviewed by the Office of Public Affairs (ASD/PA) and is releasable to the National Technical Information Service (NTIS). At NTIS, it will be available to the general public, including foreign nations.

This technical report has been reviewed and is approved for publication.




Project Scientist



R.L. VAN DEUSEN
Chief, Polymer Branch

FOR THE COMMANDER



F. D. CHERRY, Chief
Nonmetallic Materials Division

"If your address has changed, if you wish to be removed from our mailing list, or if the addressee is no longer employed by your organization, please notify AFWAL/MLBP, W-PAFB, Ohio 45433 to help us maintain a current mailing list.

Copies of this report should not be returned unless return is required by security considerations, contractual obligations, or notice on a specific document.

UNCLASSIFIED

SECURITY CLASSIFICATION OF THIS PAGE (When Data Entered)

REPORT DOCUMENTATION PAGE		READ INSTRUCTIONS BEFORE COMPLETING FORM
1. REPORT NUMBER AFWAL-TR-82-4090	2. GOVT ACCESSION NO.	3. RECIPIENT'S CATALOG NUMBER
4. TITLE (and Subtitle) PHYSICAL-CHEMICAL PROPERTIES OF ARTICULATED RODLIKE POLYMERS	5. TYPE OF REPORT & PERIOD COVERED Final Report March 1981--February 1982	
	6. PERFORMING ORG. REPORT NUMBER	
7. AUTHOR(s) G. C. Berry L. Marwaha Y. Einaga H. H. Tsai R. Furukawa	8. CONTRACT OR GRANT NUMBER(s) F33615-81K-5043	
9. PERFORMING ORGANIZATION NAME AND ADDRESS Carnegie-Mellon University 5000 Forbes Avenue Pittsburgh, PA 15213	10. PROGRAM ELEMENT, PROJECT, TASK AREA & WORK UNIT NUMBERS 24190420	
11. CONTROLLING OFFICE NAME AND ADDRESS Materials Laboratory (AFWAL/MLBP) Air Force Wright Aeronautical Labs (AFSC) Wright-Patterson AFB, Ohio 45433	12. REPORT DATE August, 1982	
	13. NUMBER OF PAGES 164	
14. MONITORING AGENCY NAME & ADDRESS (if different from Controlling Office)	15. SECURITY CLASS. (of this report) UNCLASSIFIED	
	15a. DECLASSIFICATION/DOWNGRADING SCHEDULE N/A	
16. DISTRIBUTION STATEMENT (of this Report) Approved for Public Release, Distribution Unlimited		
17. DISTRIBUTION STATEMENT (of the abstract entered in Block 20, if different from Report)		
18. SUPPLEMENTARY NOTES		
19. KEY WORDS (Continue on reverse side if necessary and identify by block number)		
20. ABSTRACT (Continue on reverse side if necessary and identify by block number) Photon correlation and absolute intensity light scattering studies have been coupled with size exclusion chromatography, viscometry and spectroscopic studies to investigate several articulated polymers. The results show that the polymers investigated tend to form intermolecular aggregates in solution. The effect of these can be reduced in number by increased temperature, sonication and centrifugation, but not completely removed. Results on solutions so		

treated are presently being analyzed in terms of a quasi-two component mixture of large aggregates (few in number) and molecularly dissolved species. Phase equilibria studies show that articulated polymers can form nematogenic solutions with the tendency increased with decreasing content of non-rodlike comonomer, as expected. For reasons unknown in detail, SPBT copolymers more readily form nematogenic solutions than do SPBO copolymers--a possible explanation may rest with increased intermolecular aggregation with SPBO copolymers. The critical concentration c_c for stability of the nematic phase appears to be increased for rodlike polymers in polyphosphoric acid, PPA, as compared with methane sulfonic acid, MSA. This may reflect complex formation with PPA, effectively increasing the chain diameter. Mixtures of a nematogenic rodlike chain and an isotropic articulated chain exhibit depressed c_c , as expected. Nonetheless, physical separation of the phases appears to be very difficult with the system studied thus far. Rheological data including measurements of the creep, recovery and dynamic compliances on solutions of an articulated rodlike copolymer in MSA are interpreted in terms of interchain association that is susceptible to cleavage and reformation in flow. Data on solution of an articulated rodlike copolymer in PPA do not exhibit this behavior; the latter viscosity proportional to the cube of the polymer concentration. Rheological data are also reported for solutions of rodlike polymers and rodlike copolymers in PPA. The latter is found to exhibit very high viscosity in comparison with previously studied solutions, and long relaxation times for disorientation. Conversely, rheological data on solutions of mixtures of articulated rodlike copolymers and rodlike polymers were characterized by rapid disorientation on cessation of flow. A special ribbon forming apparatus has been used to process solutions of rodlike polymers, rodlike copolymers, and articulated rodlike copolymers into oriented ribbons. Orientational relaxation was too rapid with the articulated polymers to allow successful processing with the apparatus in hand, and the rodlike copolymers did not appear to give homogeneous solutions, with consequential degradation of the orientation achieved in flow.

FOREWORD

This report on the "Physical-Chemical Properties of Articulated Rodlike Polymers" was prepared in the Department of Chemistry, Carnegie-Mellon University, 4400 Fifth Avenue, Pittsburgh, Pennsylvania 15213, under Contract F33615-81K-5043 (Project No. 24190420). It was administered under the direction of the Materials Laboratory, Air Force Wright Aeronautical Laboratories, Wright-Patterson Air Force Base, Ohio, Dr. T. E. Helminiak.

The report covers work conducted from 1 March 1981 to 28 February 1982. It was submitted in May, 1982. Authors are G. C. Berry, Principal Investigator, Y. Einaga, R. Furukawa, H. H. Tsai, and L. Marwaha.

Best Available Copy

TABLE OF CONTENTS

I CHARACTERIZATION BY DILUTE SOLUTION STUDIES	1
1. INTRODUCTION	1
2. SIZE EXCLUSION CHROMATOGRAPHY	4
3. LIGHT SCATTERING	7
3.1 Preliminary Remarks	7
3.2 Theoretical Basis for Light Scattering Analysis	7
3.2.1 Photon Correlation Light Scattering	7
3.2.2 Integrated Intensity Light Scattering	11
3.3 Light Scattering Apparatus and Methods	13
3.3.1 Light Scattering Apparatus	13
3.3.2 Light Scattering Methods	17
3.4 Results and Discussion	22
3.4.1 Polystyrene Solutions	22
3.4.1.1 Solution Preparation	22
3.4.1.2 Photon Correlation Scattering	22
3.4.2 d-PBT Solutions	31
3.4.2.1 Solution Preparation	31
3.4.2.2 Photon Correlation Scattering	31
3.4.2.3 Integrated Intensity Scattering	33
3.4.2.4 Speculation on the Size of d-PBT Molecule and its Aggregates	34
3.4.2.5 Summary	35
3.4.3 Articulated Polymers	48
3.4.3.1 Solution Preparation	48
3.4.3.2 Light Scattering Results	48
3.4.3.3 Data Analysis	50
3.4.4 Copolymer of PBT and PBO	78
3.4.4.1 Solution Preparation	78
3.4.4.2 Light Scattering	78
4. VISCOMETRY	81
5. SUMMARY	84
II PHASE EQUILIBRIA OF SOLUTIONS OF ARTICULATED POLYMERS, RODLIKE POLYMERS AND THEIR MIXTURES	85
6. INTRODUCTION	85
7. EXPERIMENTAL METHODS	86
8. RESULTS AND DISCUSSION	87
8.1 Articulated Polymers	87
8.2 Rodlike Polymers	87
8.3 Mixtures of Articulated and Rodlike Polymers	91
9. SUMMARY	93
III RHEOLOGICAL STUDIES OF SOLUTIONS OF ARTICULATED POLYMERS, RODLIKE POLYMERS AND THEIR MIXTURE	94

10. INTRODUCTION	94
11. EXPERIMENTAL METHODS	100
12. RESULTS AND DISCUSSION	101
12.1 Articulated Polymers	101
12.1.1 Solutions in Methane Sulfonic Acid	101
12.1.2 Solutions in Polyphosphoric Acid	103
12.2 Rodlike Polymers	104
12.2.1 PBT in Polyphosphoric Acid	104
12.2.2 PBT in Methane Sulfonic Acid	104
12.2.3 P(BT-co-BO) in Polyphosphoric Acid	104
12.3 Mixtures of Articulated and Rodlike Polymers	106
13. SUMMARY	107
IV PROCESSING OF ARTICULATED POLYMERS	134
14. INTRODUCTION	134
15. RIBBON FORMATION APPARATUS	135
15.1 Ribbon Fabrication	135
15.2 SPBT Articulated Polymer	135
15.3 Fabrication of PBT/PBO Copolymers	135
16. SUMMARY	138
V APPENDIX	139
17. THE THIRD FACTORIAL MOMENT TO THE PHOTON COUNT DISTRIBUTION	139
18. COMPILATION OF RHEOLOGICAL TERMS, SYMBOLS AND RELATIONS	140
18.1 Basic Experiments and Material Properties	140
18.2 Linear Viscoelasticity	142
18.3 Time-Temperature Equivalence	145
REFERENCES	147

LIST OF FIGURES

- Figure 1: 19
Schematic diagram of light scattering apparatus showing the principal components discussed in the text.
- Figure 2: 20
The distribution $P(n, \gamma)$ determined for a polystyrene solution for several values of $\Delta\tau$. Numbers on each curve give $\log \Delta\tau/\tau_h$. The solid curves were constructed with Eqn. 2.7 using the experimental $n^{(2)}$ to compute $m^{-1} = n^{(2)} - 1$.
- Figure 3: 21
The coherence factor $f(A)$ determined for several values of the pinhole diameter D . The curve is a theoretical estimate, fitted to the data by use of an arbitrary proportionality between D^2 and the coherence area A .
- Figure 4: 25
 $\log[g^{(2)}(\tau)-1]$ versus $\tau \sin^2\theta/2$ for a polystyrene solution in t-butyl acetate at 50.2°C , $C = 5 \text{ mg/ml}$, $\theta = 60^\circ$.
- Figure 5: 26
 $\log[g^{(2)}(\tau)-1]$ versus $\tau \sin^2\theta/2$ for a polystyrene solution in t-butyl acetate at 50.2°C , $C = 5 \text{ mg/ml}$, $30 < \theta < 135^\circ$.
- Figure 6: 27
 $\log[n^{(2)}(\Delta\tau)-1]$, O , and $\log [g^{(2)}(\Delta\tau)-1]$, \odot , versus $\Delta\tau \sin^2\theta/2$ for solutions of polystyrene in t-butyl acetate at 50.6°C ; $C = 10 \text{ mg/ml}$, $30 < \theta < 135^\circ$ (pip up at 30° , rotating clockwise with increasing θ).
- Figure 7: 28
 $\langle \tau^{(h)} \rangle \sin^2\theta/2$ versus $^2\theta/2$ for polystyrene in t-butyl acetate at 50.6°C ; $C = 10 \text{ mg/ml}$; $J = N, \odot$; g, \odot ; K, O .
- Figure 8: 29
Relation between $n^{(3)}(\Delta\tau)$ and $n^{(2)}(\Delta\tau)$ for four optical arrangements. Dashed lines represent Eqn. 3.31 — solid lines represent asymptotic behavior.

- Figure 9: 30
 $\langle \tau^{(h)} \rangle, \sin^2 \theta / 2$ versus C for solutions of polystyrene in t-butyl acetate at three temperatures. Symbols as in Fig. 7.
- Figure 10: 36
 $\log[g^{(2)}(\tau)-1]$ versus $\tau \sin^2 \theta / 2$ for solutions of d-PBT in MSA at 30°C; $C = 0.65$ mg/ml, $\theta = 75^\circ$.
- Figure 11: 37
 $\log[n^{(2)}(\Delta\tau)-1]$, \circ , and $\log[g^{(2)}(\Delta\tau)-1]$, \square , versus $\Delta\tau \sin^2 \theta / 2$ for solutions of d-PBT in MSA at 30°C; $C = 0.65$ mg/ml, $45 < \theta < 135$, (pip clockwise from up to 45° with increasing θ).
- Figure 12: 38
 $\langle \tau^{(h)} \rangle, \sin^2 \theta / 2$ versus $\sin^2 \theta / 2$ for solutions of d-PBT in MSA at 30°C; $C = 0.65$ mg/ml. Symbols as in Fig. 7.
- Figure 13: 39
 $\log\{[g^{(2)}(\tau)-1]^{1/2} - (f(A))^{1/2} - \sum \exp - \tau / \tau^{(h)}\}$ versus τ for solutions of d-PBT in MSA at 30°C; $C = 0.65$ mg/ml; $\theta = 90^\circ$.
- Figure 14: 40
 (a) $\langle \tau^{(h)} \rangle, \sin^2 \theta / 2$, $\tau_1^{(h)} \sin^2 \theta / 2$ versus $\sin^2 \theta / 2$ for a solution of d-PBT in MSA at 30°C; $C = 0.65$ mg/ml. Symbols as in Fig. 7. Solid lines calculated with relations in Table 1 (self-beating mode) and values of $\tau_1^{(h)}$ and r_1 given in Figs. 14a and 14b, respectively. (b) r_1, \ominus , versus $\sin^2 \theta / 2$ for solutions of d-PBT in MSA at 30°C; $C = 0.65$ mg/ml.
- Figure 15: 41
 $\tau_1^{(h)} \sin^2 \theta / 2$ and $\tau_2^{(h)} \sin^2 \theta / 2$ versus C for solutions of d-PBT in MSA at 30°C.
- Figure 16: 42
 r_1 and r_2 versus $\sin^2 \theta / 2$ for solutions of d-PBT in MSA at 30°C; \circ, \circ, \circ and \circ for $C = 0.65, 0.87, 1.21$ and 1.93 mg/ml, respectively.
- Figure 17: 43
 Comparison of experimental $n^{(2)}\Delta(\tau)$ and $g^{(2)}(\tau)$ with values calculated using $\tau_1^{(h)}, \tau_2^{(h)}$ and r_1, r_2 given in Figs. 15 and 16.

Figure 18:	44
(Kc/R _{VV}) ^{1/2} versus sin ² θ/2 for solutions of d-PBT in MSA at 30°C (633 nm wavelength); C = 0.65, 0.87, 1.21, 1.93 mg/ml from top to bottom.	
Figure 19:	45
(Kc/R _{HV}) ^{1/2} versus sin ² θ/2 for solutions described in Fig. 18.	
Figure 20:	46
[Kc/R _{VV} ^(F)] ^{1/2} versus sin ² θ/2 for solutions described in Fig. 18. R _{VV} ^(F) calculated from R _{VV} as described in text.	
Figure 21:	47
[Kc/R _{VV} ^(S)] ^{1/2} versus sin ² θ/2 for solutions described in Fig. 18. R _{VV} ^(S) = R _{VV} - R _{VV} ^(F) .	
Figure 22:	54
λ _{max} vs % PBT for the series SPBT-352-38 (95%), SPBT-352-36 (90%), SPBT-388-7 (85%), SPBT-388-12 (80%) in MSA.	
Figure 23:	55
Emission spectra excited by 514 nm source. I/I _{std} conc (dl/g) vs λ(nm). ○ SPBT-388-12/MSA 0.788 g/L, ○ SPBT-352-38/MSA 0.506 g/L.	
Figure 24:	56
Absolute intensity light scattering data for filtered SPBO-352-39 in MSA at 633 nm, ○ 0.494 g/L, ○-0.383 g/L, ○ 0.204 g/L, -○ 0.106 g/L. a) filtered b) filtered and centrifuged	
Figure 25:	57
Photon correlation light scattering data for filtered (top) and filtered and centrifuged (bottom) of SPBO-352-39/MSA 0.106 g/L, ○ 45°, ○ 60°, ○-75°, ○ 90°, -○ 105°, ○ 120°, ○ 135°.	
Figure 26:	58
Photon correlation light scattering data for filtered (top) and filtered and centrifuged (bottom) of SPBO-352-39/MSA 0.494 g/L, ○ 45°, ○ 60°, ○-75°, ○ 90°, -○ 105°, ○ 120°, ○ 135°.	

Figure 27:

59

Absolute intensity light scattering data for filtered SPBT-352-38/MSA at 514 nm, O 0.506 g/L, O-0.374 g/L, Q 0.267 g/L, -O 0.108 g/L a) filtered b)filtered and centrifuged

Figure 28:

60

Photon correlation light scattering data for filtered (top) and filtered and centrifuged (bottom) of SPBT-352-38/MSA, 0.108 g/L, O 45°, O 60°, O-75°, Q 90°, -O 105°, O 120°, Q 135°.

Figure 29:

61

Photon correlation light scattering data for filtered (top) and filtered and centrifuged (bottom) of SPBT-352-38/MSA, 0.506 g/L, O 45°, O 60°, O-75°, Q 90°, -O 105°, O 120°, Q 135°.

Figure 30:

62

Absolute intensity light scattering data for SPBT-352-36 in MSA at 633 nm. O = 0.576 g/L, O-0.378 g/L, Q 0.201 g/L, -O 0.0998 g/L. a) filtered b)filtered and centrifuged

Figure 31:

63

Photon correlation light scattering for filtered (top) and filtered and centrifuged (bottom) of SPBT-352-36/MSA, 0.0998 g/L, O 45°, O 60°, O-75°, Q 90°, -O 105°, O 120°, Q 135°.

Figure 32:

64

Photon correlation light scattering data for filtered (top) and filtered and centrifuged (bottom) of SPBT-352-36/MSA 0.516 g/L, O 45°, O 60°, O-75°, Q 90°, -O 105°, O 120°, Q 135°.

Figure 33:

65

Absolute intensity light scattering data for filtered SPBT-388-7/MSA at 633 nm, O 0.558 g/L, O-0.378 g/L, Q 0.266 g/L, -O 0.114 g/L a) filtered b)filtered and centrifuged

Figure 34:

66

Photon correlation light scattering data for filtered (top) and filtered and centrifuged (bottom) of SPBT-388-7/MSA, 0.114 g/L, O 45°, O 60°, O-75°, Q 90°, -O 105°, O 120°, Q 135°.

Figure 35:

67

Photon correlation light scattering data for filtered (top) and filtered and centrifuged (bottom) of SPBT-388-7/MSA 0.558 g/L, O 45°, O 60°, O 75°, Q 90°, O 105°, O 120°, Q 135°.

Figure 36:

68

Absolute intensity light scattering for filtered SPBT-388-12/MSA at 574 nm, O 0.788 g/L, O-0.45513 g/L, Q 0.3295 g/L, -O 0.116 g/L. a) filtered b) filtered and centrifuged

Figure 37:

69

a) Relaxation times, multiplied by $\sin^2 \tau/2$, for a solution of SPBT-352-38/MSA (0.108 g/L) as a function of $\sin^2 \theta/2$, O $\tau_{h1} \sin^2 \theta/2$, Q $\tau_{h2} \sin^2 \theta/2$, $\oplus \langle \tau_h \rangle \sin^2 \theta/2$, $\ominus \langle \tau_h \rangle_N \sin^2 \theta/2$, uncentrifuged sample. b) The weight factors r_i , corresponding to data in part (a).

Figure 38:

70

a) Relaxation times multiplied by $\sin^2 \theta/2$ for a solution of SPEO-352-39 (0.106 g/L) as a function of $\sin^2 \theta/2$, O $\tau_{h1} \sin^2 \theta/2$, Q $\tau_{h2} \sin^2 \theta/2$, $\oplus \langle \tau_h \rangle_K \sin^2 \theta/2$, $\ominus \langle \tau_h \rangle_N \sin^2 \theta/2$, uncentrifuged sample. b) After centrifugation.

Figure 39:

71

The weight factor r_i corresponding to data in Fig. 38: O, \bullet r_1 ; Q, \circ r_2 ; open for uncentrifuged and filled for sample after centrifugation.

Figure 40:

72

Relaxation times for $\tau_{h1} \sin^2 \theta/2$ as a function of concentration for uncentrifuged solutions of SPBT-352-38/MSA.

Figure 41:

73

Relaxation times $\tau_{h1} \sin^2 \theta/2$ and $\tau_{h2} \sin^2 \theta/2$ as a function of concentration for centrifuged solutions of SPBO-352-39/MSA.

Figure 42:

74

Absolute light scattering, $c/R_{90}(\theta)$ as a function of $\sin^2 \theta/2$ for several concentrations of SPBT-352-38/MSA at 514 nm, -O 0.108 g/L, Q 0.267 g/L, O-0.375 g/L and O 0.503 g/L. a) uncentrifuged and b) centrifuged.

Figure 43:

75

Values of constant $K c/R_{v_v}(\theta)$ for SPBT-352-38/MSA from Fig. 42 as a function of concentration, \circ uncentrifuged, \bullet after centrifuged.

Figure 44:

76

Absolute intensity light scattering, $c/R_{v_v}(\theta)$ as a function of $\sin^2\theta/2$ for several concentrations for SPBO-352-39/MSA at 633 nm, \circ 0.106 g/L, \circ 0.204 g/L, \circ 0.383 g/L, \circ 0.494 g/L a) uncentrifuged and b) centrifuged.

Figure 45:

77

Values of $Kc/R_{v_v}(\theta)$ for SPBO-352-39 from Fig. 44 as a function of concentration: \circ uncentrifuged, \bullet centrifuged.

Figure 46:

79

Absolute intensity light scattering for P(BO-co-BT) (75/25) 4952-S in PPA diluted in MSA at 633 nm, \circ 0.529 g/L, \circ 0.327 g/L, \circ 0.268 g/L, \circ 0.138 g/L.

Figure 47:

80

Absolute intensity light scattering for P(BO-co-BT) (90/10) 4592/13 in PPA diluted in MSA at 633 nm, \circ 0.491, \circ 0.388 g/L, \circ 0.145 g/L.

Figure 48:

83

Intrinsic viscosity data for SPBT-352-36, \circ η_{sp}/c , \circ $\ln\eta/c$, \bullet $[\eta]$; a) solution in MSA and b) solution in MSA + 1 N K_2SO_4 salt.

Figure 49:

108

Steady state viscosity η_{sp} for solutions of articulated PBT copolymers in MSA: \circ , 388-12 at 0.0674 g/g, 30°C (isotropic); \circ , 352-38 at 0.0747 g/g, 28°C (nematic); and \circ , 352-36 at 0.0740 g/g, 24°C (nematic).

Figure 50:

109

Steady state viscosity η_{sp} and recoverable compliance R_{σ} for articulated copolymer 388-12 in MSA (0.0674 g/g). \circ at 30°C and Δ at 51.4°C.

Figure 51:

110

Creep compliance $J_{\sigma}(t)$ and recoverable compliance function $R_{\sigma}(S, \theta)$ for articulated copolymer 388-12 in

MSA (0.0674 g/g); the creep duration S may be seen on the figure (e.g. $S \sim 7,000$ s). \otimes for creep and \circ for recovery. Figure a for 30°C stresses in Pa, \circ , 0.36, $\dot{\circ}$, 1.4, $\ddot{\circ}$, 6.6; Figure b for 51.9°C , stresses are \circ , 0.36, $\dot{\circ}$, 1.4, $\ddot{\circ}$, 6.3.

Figure 52:

111

Dynamic creep compliance $|J_\sigma^*(\omega)|$, a, and storage compliance $J'_\sigma(\omega)$, b, for articulated copolymer 388-12 in MSA (0.0674 g/g), for several temperatures: 5°C , $\dot{\circ}$, 40°C , $\ddot{\circ}$, 80°C \circ .

Figure 53:

112

Dynamic creep compliance $|J_\sigma^*(\omega)|$, a, and storage compliance $J'_\sigma(\omega)$, b, for articulated copolymer 352-38 in MSA (0.0747 g/g) for two temperatures: \circ , 40°C , $\dot{\circ}$, 80°C .

Figure 54:

113

Dynamic creep compliance $|J_\sigma^*(\omega)|$, a, and storage compliance $J'_\sigma(\omega)$, b, for articulated copolymer 352-34 in MSA (0.0716 g/g) for two temperatures: \circ , 40°C , $\dot{\circ}$, 80°C .

Figure 55:

114

Dynamic compliance $|J_\sigma^*(\omega)|$ for articulated copolymer 388-39 in PPA at 25°C for several polymer concentrations (g/g): Δ , PPA; \circ , 0.0012; $\dot{\circ}$, 0.0067; $\ddot{\circ}$, 0.0161; \circ , 0.0375; $\dot{\circ}$, 0.0557.

Figure 56:

115

Dynamic compliance $|J_\sigma^*(\omega)|$ for articulated copolymer 388-39 in PPA at 40°C for several polymer concentrations (g/g): Δ , PPA; \circ , 0.0012; $\dot{\circ}$, 0.0067; $\ddot{\circ}$, 0.0161; \circ , 0.0375; $\dot{\circ}$, 0.0557.

Figure 57:

116

Dynamic viscosity $|\eta_\sigma^*(\omega)|$ for the solution identified in Fig. 55 caption. \circ is the excess dynamic viscosity $|\bar{\eta}_\sigma^*(\omega)| = |\eta_\delta^*(\omega)| - |\eta_\sigma^*(\omega)|_{\text{SOLVENT}}$ for concentration at 0.0012.

Figure 58:

117

Dynamic viscosity $|\eta_\sigma^*(\omega)|$ for the solution identified in Fig. 56 caption. \circ is the same as in Fig. 57 caption.

Figure 59:

118

Reduced plot of $|\bar{\eta}_\sigma^*(\omega)| / |\bar{\eta}_\sigma^*(0)|$ versus ωa for the data given in Fig. 58 (40°C). Values of $|\bar{\eta}_\sigma^*(0)|$ used are given in Fig. 60 for solutions with concentrations (g/g): 0.0012 ($a=1$), -O; 0.0067 ($a = 20$), O; 0.0161 ($a_c = 100$), O, and 0.0375 ($a_c = 500$), O.

Figure 60:

119

Excess dynamic viscosity $|\bar{\eta}_\sigma^*(0)|$ as a function of concentration for solutions of articulated copolymer 388-39 in PPA (40°C).

Figure 61:

120

Steady state viscosity η_K and recoverable compliance R_K for a PBT polymer in PPA at 40°C; 0.092 g/g for several experiments: -O, O, O-. Data from rheometric experiments O, Δ.

Figure 62:

121

Dynamic compliance $|J_\sigma^*(\omega)|$, a, and storage compliance $J'_\sigma(\omega)$, b, for rodlike polymer PBT-53 in MSA (0.0343 g/g), for several temperatures: O, 5°C; -O, 40°C; Q, 80°C.

Figure 63:

122

Dynamic viscosity $|\eta_\sigma^*(\omega)|$ for rodlike polymer PBT-53 in MSA (0.0343 g/g) for several temperatures: O, 5°C; -O, 40°C; Q, 80°C.

Figure 64:

123

Steady state viscosity η_K and recoverable compliance R_K for a rodlike PBO-PBT copolymer (0.75 mole fraction PBT), 0.057 g/g in PPA, at 26.6°C. Data from creep experiment Δ.

Figure 65:

124

Creep compliance $J_\sigma(t)$ and recoverable compliance function $R_\sigma(S, t)$ for the solution described in the caption to Fig. 64; the creep duration S may be obtained by inspection of the creep data. Stresses used were 130 Pa, O; 248 Pa, -O; and 405 Pa, O-. The dashed line is $|J_\sigma^*(\omega)|$ versus $(a\omega)^{-1}$ for a deformation with peak-to-peak amplitude 0.01; a is 0.88 at 10°C; -0.80 at 40°C; -1.77 at 80°C; and -1.96 at 100°C.

Figure 66:

125

Dynamic compliance $|J_g^*(\omega)|$, a, and storage compliance $J_g'(\omega)$, b, for the rodlike copolymer solution described in the caption to Fig. 64. Data are at -8°C , \circ ; 10°C , \circ ; 27°C , \circ ; 40°C , \circ ; 80°C , \circ ; and 100°C , \circ . In Figure b, -8°C , \circ , 10°C , \circ .

Figure 67:

126

Steady state viscosity η_K versus (Δ) or dynamic viscosity $|\eta_g^*(\omega)|$ b versus $a\omega$ (O) for solutions of the rodlike copolymer described in Fig. 64. Data on η_K at 27°C ; data on $|\eta_g^*(\omega)|$ b at 10°C ($a_1 = 7.60$), \circ ; 27°C ($a_1 = 1.0$), \circ ; 40°C ($a_1 = 0.16$), \circ ; 80°C ($a_1 = 0.02$), \circ ; and 100°C ($a_1 = 0.011$), \circ .

Figure 68:

127

The relaxation function $G_K(\infty, t)/\eta_K$ versus t/τ_K at 27°C for solutions of the rodlike copolymer described in Fig. 64, for K equal to $5.02 \times 10^{-3}\text{s}^{-1}$, \circ ($\tau_K = 2.74 \times 10^4\text{s}$), $25.1 \times 10^{-3}\text{s}^{-1}$, \circ ($\tau_K = 0.76 \times 10^4\text{s}$).

Figure 69:

128

Steady state viscosity η_K and recoverable compliance R_K for a mixture of rodlike PBT-53 (0.0105 g/g) and the articulated copolymer 352-34 (0.0395 g/g) in MSA at several temperatures: 29.5 and 52°C , nematic, and 70°C , biphasic.

Figure 70:

129

Creep compliance $J_g(t)$ and recoverable compliance $R_g(S, t)$ for the mixture described in the caption to Fig. 69. The creep duration S may be obtained by inspection of the figure. Stresses used were part a, at (29°C) 0.38 Pa, \circ ; 1.37 Pa, \circ ; 6.33 Pa, \circ ; 19.6 Pa, \circ ; 48.2 Pa, \circ ; part b, (at 52°) 0.42 Pa, \circ ; 1.46 Pa, \circ ; 6.57 Pa, \circ .

Figure 71:

130

The relaxation function $G_K(\infty, t)/\eta_K$ versus t/K for the mixture described in the caption to Fig. 69 at 29°C , a, and 52°C , b. In part a, K is 0.00502s^{-1} ($\tau_K = 56\text{s}$), \circ ; 0.0305s^{-1} ($\tau_K = 13.25\text{s}$), \circ ; and 0.0752s^{-1} ($\tau_K = 6.25\text{s}$), \circ . In part b, K is 0.0075s^{-1} ($\tau_K = 38.4\text{s}$), \circ ; 0.030s^{-1} ($\tau_K = 13.65\text{s}$), \circ ; 0.0752s^{-1} ($\tau_K = 7.1\text{s}$), \circ ; and 0.3s^{-1} ($\tau_K = 2.1\text{s}$), \circ .

Figure 72:

131

Dynamic compliance $|J^*(\omega)|$, a, and storage compliance $J'(\omega)$, b, for the mixture described in the caption to Fig. 69. Data are at 5°C, ○; 40°C, -○ (both nematic); and 80°C, ○ (isotropic). The lines with no points give $J(t)$ versus t^{-1} for the same mixture at 52°C, —, and 29°C, —.

Figure 73:

132

Dynamic compliance $|J^*(\omega)|$, a, and storage compliance $J'(\omega)$, b, for a mixture of the rodlike PBT-53, 0.0118 g/g, and the articulated copolymer 352-4, 0.0341 g/g, in MSA. Data are at 8.5°C, ○; 40°C, -○ (both nematic); and 80°C, ○ (isotropic).

Figure 74:

133

Dynamic compliance $|J^*(\omega)|$, a, and storage compliance $J'(\omega)$, b, for a mixture of the rodlike PBT-53, 0.0397 g/g, and the articulated copolymer 352-4, 0.0132 g/g, in MSA. Data are at 40°C, ○ (nematic); 63°C, -○ (biphasic); and 80°C, ○ (isotropic).

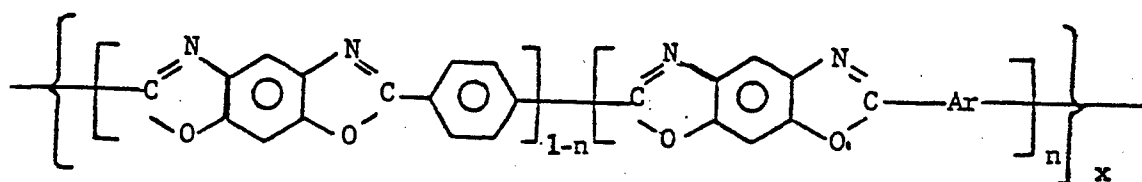
LIST OF TABLES

Table 1:	ARTICULATED COPOLYMERS USED IN THIS STUDY	3
Table 2:	APPARENT M_w/M_n FOR ARTICULATED COPOLYMERS	6
Table 3:	DEFINITION OF AVERAGE COHERENCE TIMES	12
Table 4:	EXPERIMENTS ON DILUTE SOLUTIONS OF ARTICULATED COPOLYMERS IN METHANE SULFONIC ACID ^(a)	53
Table 5:	OBSERVATION ON THE TIME FOR RELAXATION OF STRAIN INDUCED BIREFRINGENCE FOR SOLUTIONS OF SPBT 388/39 ^(a)	88
Table 6:	PHASE EQUILIBRIA DATA FOR SOLUTIONS IN METHANE SULFONIC ACID	89
Table 7:	OBSERVATION ON PHASE EQUILIBRIA AND THE TIME FOR RELAXATION OF STRAIN-INDUCED BIREFRINGENCE FOR SOLUTIONS OF PBT-53	90
Table 8:	SOLUTIONS OF ARTICULATED POLYMERS AND THEIR MIXTURE WITH RODLIKE POLYMERS INVESTIGATED	92
Table 9:	RHEOLOGICAL STUDIES ON ARTICULATED SPBT COPOLYMERS ^(a)	97
Table 10:	RHEOLOGICAL STUDIES ON RODLIKE POLYMERS ^(a)	98
Table 11:	RHEOLOGICAL STUDIES ON MIXTURES OF RODLIKE AND ARTICULATED POLYMERS ^(a)	99
Table 12:	SUMMARY OF PROCESSING EXPERIMENTS	137

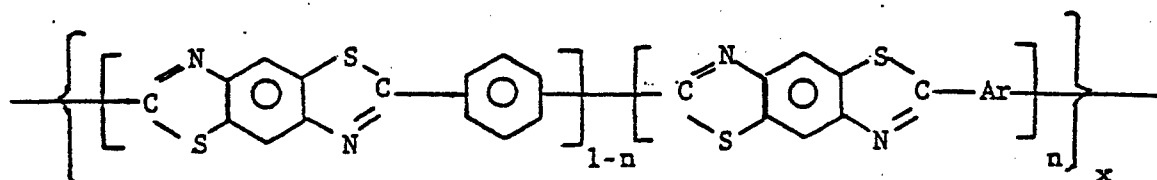
I CHARACTERIZATION BY DILUTE SOLUTION STUDIES

1. INTRODUCTION

Investigations of copolymers based on PBT or PBO have included photon correlation and integrated intensity light scattering, viscometry, and size exclusion chromatography for molecular characterization, phase equilibria by polarized microscopy, rheological studies by creep, recovery and dynamic mechanical measurements, and fabrication of ribbons using the CMU ribbon fabrication apparatus. These copolymers, termed articulated polymers have the stoichiometric structures.

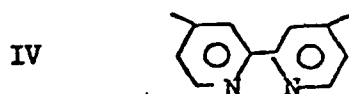
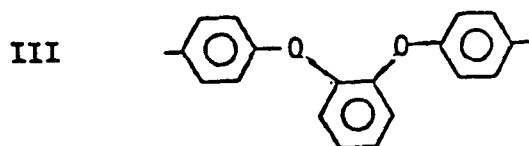
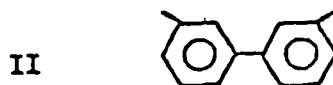
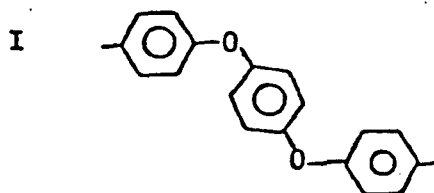


SPBO



SPBT

with (assumed random placement of the -AR- units. Comonomers used for the polymers studied have -Ar- given by



The polymers studied are listed in Table 1 along with the stoichiometric values of n . In the following sections we will present data on these polymers. In addition, data on mixtures of some of these polymers with PBT will also be considered, and some preliminary results on copolymers of PBT and PBO will be discussed (this will be referred to as P(BO-co-BT)).

Table 1: ARTICULATED COPOLYMERS USED IN THIS STUDY

Polymer	n (Fraction-Ar-)	-Ar-	$\{\eta\}_{\text{INHR}}$ (dl/g)
Copolymers Based on PBO			
SPBO 292/70	0.05	I	6.0
SPBO 352/4	0.10	I	7.1
SPBO 37/2	0.25	I	1.9
SPBO 292/71	0.05	II	6.9
SPBO 292/80	0.10	II	5.2
SPBO 292/96	0.05	III	6.7
SPBO 292/88	0.10	III	5.4
SPBO 352/39	0.05	IV	4.1

Copolymers Based on PBT			
SPBT 352/34	0.10	II	4.6
SPBT 352/38	0.05	IV	8.0
SPBT 388/39	0.05	IV	
SPBT 352/36	0.10	IV	6.0
SPBT 388/38	0.10	IV	
SPBT 388/7	0.15	IV	
SPBT 388/72	0.20	IV	
SPBT 388/12	0.20	IV	

2. SIZE EXCLUSION CHROMATOGRAPHY

Size exclusion chromatography (SEC) has been carried out on solutions in methane sulfonic acid (MSA) using a chromatograph described elsewhere. In this instrument the absorbance A of the effluent is monitored as a function of the elution volume V_e . A correlation between V_e and $[\eta]M$ previously determined for the column is used to convert V_e to $[\eta]M$ for each fraction. Since A for a given fraction divided by the sum of the A for all fractions is equal to the weight fraction w , these data give $[\eta]M$ as a function w . Thus, it is possible to compute from the experimental data the quantity

$$S_{\delta}^{(s)} = \sum (M[\eta])^{s/1+\alpha_A} A w_i \quad (2.1)$$

for any choice of s , where α_A is a parameter chosen to be as close as possible to the expected value α of $\partial \ln[\eta] / \partial \ln M$ for the polymer under study, so that $\delta = (\alpha - \alpha_A) / (1 + \alpha_A)$ is small. Then, the apparent ratio $(M_w/M_n)_{APP}$ of the weight to number average molecular weights is given by

$$(M_w/M_n)_{APP} = A_{\delta}^{(1)} A_{\delta}^{(-1)} \quad (2.2)$$

The deviation of $(M_w/M_n)_{APP}$ from the correct value of M_w/M_n can be evaluated with an assumed molecular weight distribution. For example, if a Schulz-Zimm distribution is used, then

$$(M_w/M_n)_{APP} = (M_w/M_n) \Gamma(1+h+\delta) \Gamma(h-\delta) / \Gamma(1+h) \Gamma(h) \quad (2.3)$$

where $(M_w/M_n) - 1 = h^{-1}$ and Γ is the Gamma function. Thus, with $h=1$ and $\delta=0.1$, the apparent estimate is in error by 17%.

Values of $(M_w/M_n)_{APP}$ calculated with $\alpha_A=1$ are listed in Table 2; other reasonable values of α_A would not change $(M_w/M_n)_{APP}$ very much. These results indicate that some of

the chains have M_w/M_n near 2, as might be expected for a step-growth polymer with a (partially) flexible backbone. In other cases, M_w/M_n seems to be much larger than this estimate.

Values of $(M[\eta])_{AVG}$, calculated with Eqn. 2.1 with $s=1$ and $\delta_A=0$ (e.g., $S_{\delta-\alpha}^{(1)}$) are also listed in Table 2. With reliable estimates of $[\eta]$, these could be converted to an SEC-averaged molecular weight $M_{SEC} = (M[\eta])_{AVG}/[\eta]$.

Table 2: APPARENT M_w/M_n FOR ARTICULATED COPOLYMERS

Polymer	-Ar-	n (Fraction) -Ar-	$(M_w/M_n)_{APP}^{(a)}$	$(M[\eta])_{AVG}$ (mL/mol)
SPBO 352/ 4	I •	0.10	2.1	340×10^5
SPBO 352/37			2.9	320
SPBO 352/39			4.9	1,110
SPBO 352/70			2.7	700
SPBO 352/71			3.0	1,820
SPBO 352/96			2.2	
SPBO 352/38	II	0.10	4.2	7,680

(a) Calculated as described in text with $\alpha_A=1$

3. LIGHT SCATTERING

3.1 Preliminary Remarks

In the following, integrated intensity and photon correlation light scattering measurements will be described for several articulated polymers. In addition, studies on some polystyrene solutions and solutions of a deuterated PBT, d-PBT, will be described. The latter serve as convenient models for the parallel studies on the articulated polymers, providing a means to evaluate the methods used to analyze data on the latter. The theoretical basis for the analysis is given in section 3.2, the apparatus is described in section 3.3. The studies on polystyrene, d-PBT and the articulated polymers are given in subsequent sections, concluding with preliminary results on P(BO-co-BT) samples.

3.2 Theoretical Basis for Light Scattering Analysis

3.2.1 Photon Correlation Light Scattering

Photon correlation light scattering is frequently used to study the bivariate photon count distribution $P(n,m)$ through the normalized autocorrelation $g^{(2)}(\tau)$ of the photon count distribution: 1-5

$$g^{(2)}(k\Delta\tau) = \frac{\sum_{n_0, n_\tau}^{\infty} n_0 n_\tau P(n_0, n_\tau, 0)}{\langle n \rangle^2} \quad (3.1)$$

where n_0 and n_τ are the number of photons in sampling intervals of duration $\Delta\tau$, separated by interval $\tau = k\Delta\tau$, and $\langle n \rangle$ is the average number of photons in $\Delta\tau$. Interpretation of 3.1 provides information on the coherence time $\tau^{(2)}$ for the relaxation of fluctuations of the polarizability of scattering elements, and its relation to molecular properties of the scattering system. Study of the photon count distribution $P(n)$ offers an alternative method to determine $\tau^{(2)}$ through analysis of the normalized factorial moments defined by:

$$n^{(s)}(\Delta\tau) = \sum_{n=0}^{\infty} n(n-1)\dots(n-s+1) P(n) / \langle n \rangle^s \quad (3.2)$$

for the s -th moment. Although the theoretical treatment for $n^{(s)}(\Delta\tau)$ advanced earlier, and in some respects more richly, than that for $g^{(2)}(\tau, \Delta\tau)$ use of $n^{(2)}(\Delta\tau)$ to study $\tau^{(2)}$ is unusual.^{1,6-8} Here, we will report studies in which $\tau^{(h)}$ is studied by measurements of both $g^{(2)}(\tau, \Delta\tau)$ and $n^{(2)}(\Delta\tau)$. Of course, for a simple system (e.g., monodisperse, non-interacting scatterers with only molecular translation to contribute to $\tau^{(h)}$ estimates of $\tau^{(h)}$ based on $g^{(2)}(\tau, \Delta\tau)$ and $n^{(2)}(\Delta\tau)$ should be identical. For more realistic systems, with polydispersed scatterers, etc., average values $\langle \tau^{(h)} \rangle$ will differ among experimental methods, so that comparisons among average values becomes useful.

For identical, non-interacting solutes, the experimental quantities $g^{(2)}(\tau, \Delta\tau)$ and $n^{(2)}(\Delta\tau)$ are related to $\tau^{(h)}$ by expressions^{1,8,9}

$$g^{(2)}(\tau, \Delta\tau) - 1 = f(A)q(2\gamma) |g^{(1)}(\tau, \Delta\tau)|^2 \quad (3.3)$$

$$n^{(2)}(\Delta\tau) - 1 = f(A)h(2\gamma) \quad (3.4)$$

where $\gamma = \Delta\tau/\tau_h$, $f(A)$ is a coherence factor, fixed by the detector optics, and

$$q(2\gamma) = \left(\frac{\sinh \gamma}{\gamma} \right)^2 \quad (3.5)$$

$$h(\gamma) = \frac{2}{\gamma} - \frac{2}{\gamma^2} (1 - \exp - \gamma) \quad (3.6)$$

In deriving these relations, it is assumed that the electric field correlation function $g^{(1)}(\tau, \Delta\tau)$ is represented by

$$|g^{(1)}(\tau, \Delta\tau)| = \exp(-\gamma\tau/\Delta\tau) \quad (3.7)$$

For solute with radius of gyration R_G small enough that $R_G h < 1$, the diffusion coefficient $D = (\tau^{(h)} h^2)^{-1}$ is expected to be independent of the amplitude of the scattering vector $h = (4\pi \bar{n} / \lambda_0) \sin \theta / 2$, with \bar{n} the refractive index, λ_0 the wavelength of the incident light in vacuum, and θ the scattering angle.

We will consider three methods to estimate τ_h from $g^{(2)}(\tau, \Delta\tau)$ and $n^{(2)}(\Delta\tau)$ given by Eqn. 3-7. The first, the well-known method of cumulants,¹⁰ gives τ_h from the first cumulant:

$$K_1 = -\frac{1}{2} \lim_{\tau \rightarrow 0} \frac{\partial \ln[g^{(2)}(\tau) - 1]}{\partial \tau} \quad (3.8)$$

with $\tau_h = 1/K_1$. The second, also based on $g^{(2)}(\tau, \Delta\tau)$ utilizes only $g^{(2)}(\Delta\tau, \Delta\tau)$, and so offers potential advantage, in computational time. A bilogarithmic plot of $g^{(2)}(\Delta\tau, \Delta\tau)^{-1}$ versus $\Delta\tau$ will exhibit two asymptotic regions: $g^{(2)}(\Delta\tau, \Delta\tau)^{-1} = f(A)$ for small $\Delta\tau$, and $\ln[g^{(2)}(\Delta\tau, \Delta\tau)^{-1}] \propto \ln(\tau_h / \Delta\tau)^2$ for large $\Delta\tau$. These asymptotic relations cross for $\Delta\tau = \Delta\tau_G$ with $2\Delta\tau_G = \tau_h$, permitting an estimate for τ_h if $g^{(2)}(\Delta\tau, \Delta\tau)$ is determined as a function of $\Delta\tau$. The third estimate for τ_h is based on $n^{(2)}(\Delta\tau)$ and Eqns. 3.4 and 3.6. A bilogarithmic plot of $n^{(2)}(\Delta\tau)^{-1}$ versus $\Delta\tau$ will also have two asymptotic regions: $n^{(2)}(\Delta\tau)^{-1} = f(A)$ for small $\Delta\tau$, and $\ln[n^{(2)}(\Delta\tau)^{-1}] \propto \ln(\tau_h / \Delta\tau)$ for large $\Delta\tau$. These cross for $\Delta\tau = \Delta\tau_N$, with $\Delta\tau_N = \tau_h$.

Whereas for simple systems, one expects to find $K_1^{-1} = \Delta\tau_N = 2\Delta\tau_G$ this behavior may not obtain if the scatterers are polydisperse, or exhibit other complications. In such cases, it is useful to represent the electric field correlation as a sum over components giving rise to the total scattering. The components are characterized by their coherence time $\tau_i^{(h)}$ and the fraction r_i contributed to the total light scattered by the solute. Thus

$$|g^{(1)}(\tau, \Delta\tau)| = \sum_i r_i \exp(-\gamma_i \tau / \Delta\tau) \quad (3.9)$$

with $\gamma_i = \Delta\tau / \tau_{h,i}$. The sum runs over all solute components, with $r = \sum r_i$ being the fraction of the total intensity resulting from the solution; $1-r$ is the fraction from other sources, e.g., a coherent reference beam. With Eqn. 3.3,

$$g^{(2)}(\tau, \Delta\tau) - 1 = f(A) \left[\sum_i \sum_j r_i r_j q(\gamma_i + \gamma_j) \exp[-(\gamma_i + \gamma_j)\tau / \Delta\tau] \right. \\ \left. + 2(1-r) \sum_i r_i q(\gamma_i) \exp[-\gamma_i \tau / \Delta\tau] \right] \quad (3.10)$$

and

$$\Delta\tau K_1 = \frac{1}{2r(2-r)} \left[\sum_i \sum_j r_i r_j (\gamma_i + \gamma_j) + 2(1-r) \sum_i r_i \gamma_i \right] \quad (3.11)$$

Equation 3.11 permits evaluation of an averaged coherence times as given in Table 1. If τ is put equal to $\Delta\tau$ in Eqn. 3.11, the result gives

$$\Delta\tau_G = \Delta\tau \left\{ \frac{1}{r(2-r)} \left[\sum_i \sum_j r_i r_j (\gamma_i + \gamma_j)^2 + 2(1-r) \sum_i r_i \gamma_i^2 \right] \right\}^{1/2} \quad (3.12)$$

permitting evaluation of a second average coherence time defined by $\langle \tau_h \rangle_G$ as given in Table 1.

Finally, the s -th factorial moment, given by⁷

$$n^{(s)}(\Delta\tau) = (s-1)! r^s \int_0^{\Delta\tau} W^{(s)}(t, t) dt \\ + s!(1-r)r^{s-1} \frac{1}{\Delta\tau} \int_0^{\Delta\tau} \int_0^{\Delta\tau} e^{i\omega(t_1, t_2)} W^{(s-1)}(t_1, t_2) dt_1 dt_2 \quad (3.13)$$

$$W^{(1)}(t_1, t_2) = g^{(1)}(t_1 - t_2) \quad (3.14)$$

$$W^{(s)}(t_1, t_2) = \int_0^{\Delta\tau} g^{(1)}(t_1 - t) W^{(s-1)}(t, t_2) dt; \quad s \geq 2 \quad (3.15)$$

provides the means to determine another average coherence time. Thus for $s = 2$ Eqns. 3.2 and 3.4-3.13 give

$$n^{(2)}(\Delta\tau) - 1 = f(A) \left[2 \sum_i \sum_j r_i r_j h(\gamma_i + \gamma_j) + 2(1-r) \sum_i r_i h(\gamma_i) \right] \quad (3.16)$$

for the second factorial moment so that evaluation of $\Delta\tau_N$ results in

$$\Delta\tau_N = \Delta\tau \frac{2}{r(2-r)} \left[\sum_i \sum_j r_i r_j (\gamma_i + \gamma_j)^{-1} + 2(1-r) \sum_i r_i \gamma_i^{-1} \right] \quad (3.17)$$

The average coherence times given by these results are listed in Table 3. Self-beating method (sometimes referred to as homodyning) directly gives the intensity fluctuation of the scattering light by photon counting on electrical filtering, whereas the reference beam method utilizes mixing of scattering light with reference light of the same frequency (homodyne) or different frequency (heterodyne)⁸.

3.2.2 Integrated Intensity Light Scattering

Absolute, or integrated intensity light scattering measurements yield the Rayleigh ratios $R_{V_V}(h)$ and $R_{H_V}(h)$ for the vertically and horizontally polarized components, respectively of the scattering with vertically polarized incident light. For dilute solutions, these are related to the molecular weight M , second virial coefficient A_2 , root mean square radius of gyration R_G and molecular anisotropy δ and polymer concentration c by the expressions

$$\frac{Kc}{R_{V_V}(0)} = \left[\frac{Kc}{R_{V_V}(0)} \right]^0 \left\{ 1 + A_2 M \left(1 + \frac{4}{5} \delta^2 \right)^{-1} c + \dots \right\}^2$$

$$\left(\frac{R_{V_V}(h)}{KcM} \right)^0 = \left(1 + \frac{4}{5} \delta^2 \right) - \frac{1}{3} \left[1 - \frac{4}{5} f_1 \delta + \frac{4}{7} (f_2 \delta)^2 \right] u + \dots$$

Table 3: DEFINITION OF AVERAGE COHERENCE TIMES

Average Coherence Time	Self-Beating Method		Reference-Beam Method	
	Experimental Quantities	Definition	Experimental Quantities	Definition
$\langle \tau^{(h)} \rangle_K$	$1/K_1$	$2\Delta\tau \left[\sum_i \sum_j r_i r_j (\gamma_i + \gamma_j) \right]^{-1}$	$1/2 K_1$	$\Delta\tau r \left(\sum_i r_i \gamma_i \right)^{-1}$
$\langle \tau^{(h)} \rangle_N$	$\Delta\tau_N$	$2\Delta\tau \sum_i \sum_j r_i r_j (\gamma_i + \gamma_j)^{-1}$	$(1/2) \Delta\tau_N$	$\Delta\tau r \sum_i r_i \gamma_i^{-1}$
$\langle \tau^{(h)} \rangle_G$	$2\Delta\tau_G$	$2\Delta\tau \left[\sum_i \sum_j r_i r_j (\gamma_i + \gamma_j)^{-2} \right]^{1/2}$	$\Delta\tau_G$	$\Delta\tau r^{-1/2} \left(\sum_i r_i \gamma_i^{-2} \right)^{1/2}$

$$\gamma_i = \Delta\tau / \tau^{(h)}$$

$$\frac{Kc}{R_{Hv}(h)} = \left(\frac{Kc}{R_{Hv}(0)} \right)^0 + O(c^2)$$

$$\left(\frac{R_{Hv}(h)}{KcM} \right)^0 = \frac{3}{5} \delta^2 - \frac{9}{35} (f_3 \delta)^2 u + \dots$$

where $u = R_G^2 h^2$, superscript 0 denotes quantities extrapolated to infinite dilution, and the f_i are parameters that may, for practical purposes, be set to unity.

3.3 Light Scattering Apparatus and Methods

3.3.1 Light Scattering Apparatus

The light scattering apparatus is shown schematically in Fig. 1. It is equipped with Birnboim Digital Correlation used as a data acquisition and processing system, DAPS, by Science Research Systems of Troy (Model DAS 6). Other components include argon-ion laser with etalon (Lexel Model 85), a He-Ne laser (Spectra-Physics Model 120), a photomultiplier with an S-2 photocathode (ITT, FW-130-RF) photomultiplier, housing (Products for Research, Inc.) and a discriminator amplifier (SSR Instruments Co.) Optical components allow for beam alignment, rotation of the incident beam (one-half wave plate), beam spreading for total intensity measurements, transfer of an auxiliary light beam to the photomultiplier with an optical fiber (Oriel Corp., Model 7167), definition of the scattering volume by slits S_H and S_V , collimation of the accepted rays by pinhole P, selection of the wavelength of the light impinging on the photomultiplier (by use of interference filters for fixed or variable band pass, e.g., Oriel Corp., Model 7155, or fixed band rejection, to eliminate light with wavelength of the incident beam); and an analyzer to select the polarization of the scattered beam.

In the mode used here, the DAPS, which is based on a Texas Instruments 980B computer, acquires pulses in each of 4,736 intervals of length $\Delta\tau$, with a deadtime of 25 ns included in each interval; the number of pulses per interval can be large as 2^{15} . The full auto-correlation function $G^{(2)}$ is computed over the primary data base of 2^{12} intervals to give a correlation with up to 512 points spaced at intervals of $\Delta\tau$. Usually, a 16 point correlation was used in this work. The first point of a correlation can be shifted up to 128. After each acquisition cycle, the unnormalized correlation $G^{(2)}(k\Delta\tau)$ and the mean-count rate are calculated as

$$G^{(2)}(k\Delta\tau) = \frac{1}{T} \sum_i^T n_i n_{i+k} \quad (3.18)$$

$$\langle n \rangle = \left\langle \frac{1}{T} \sum_{i=1}^T n_i \right\rangle \quad (3.19)$$

where $T = 2^{12}$ and $k = 0, 1, 2, \dots$. The acquisition and calculation cycle is repeated M times, and averaged in the form

$$G^{(2)}(k\Delta\tau) = \frac{1}{M} \sum_{j=1}^M G_j^{(2)}(k\Delta\tau) \quad (3.20)$$

$$\langle n \rangle^2 = \frac{1}{M} \sum_{j=1}^M \langle n \rangle_j^2 \quad (3.21)$$

and the unnormalized factorial moments are calculated over the data base of TM intervals as

$$N^{(s)} = \frac{1}{TM} \sum_{i=1}^{TM} \{n(n-1)\dots(n-s+1)\}_i \quad (3.22)$$

$$\langle n \rangle = N^{(1)} \quad (3.23)$$

The distribution $P(n, \gamma)$ of photon pulses per interval is also computed over the data base of TM intervals. If $P(n, \gamma)$ is the same for each of the M data sets, then $\langle \langle n \rangle^2 \rangle$ and $(N^{(1)})^2$ are

equal. If the $\bar{P}(n, \gamma)$ differ (e.g., because of scattering 'dust' in a few of the M sets), then $\langle\langle n \rangle^2\rangle \geq (N^{(1)})^2$.

Further data processing includes calculations of $g^{(2)}(\tau)$ and $n^{(s)}$. For the former $\langle\langle n \rangle^2\rangle$ is used to give

$$g^{(2)}(k\Delta\tau) = G^{(2)}(k\Delta\tau) / \langle\langle n \rangle^2\rangle ; k > 0 \quad (3.24)$$

$$g^{(2)}(0) = \frac{G^{(2)}(0) - \langle n \rangle}{\langle\langle n \rangle^2\rangle} \quad (3.25)$$

It may be remarked that the use of $\langle\langle n \rangle^2\rangle$ rather than $(N^{(1)})^2$ or $G_M^{(2)}(\infty)$ to normalize $G^{(2)}(\tau)$ is not trivial for realistic data, owing to the effects of noise and drift, etc. Values of $g^{(2)}(\tau)$ calculated with Eqn. 3.24 exhibit the expected property that $g^{(2)}(\infty)$ tends to unity, even under conditions for which $\langle\langle n \rangle^2\rangle > (N^{(1)})^2$. An estimate for K_1 is calculated by least-squares fit of $\ln(g^{(2)}(\tau)-1)$ versus τ , using correlation points for k from 1 to 7. with the algorithm in use in the DAPS, the time $\Delta\tau$ per correlation point required to compute $G^{(2)}(\Delta\tau)$ is fixed (80 ms) for $\langle n \rangle$ larger than 2, but decreases with increasing $\langle n \rangle$ for smaller $\langle n \rangle$. Consequently, the efficiency $(1+C\Delta t/2^{12}\Delta\tau)^{-1}$ varies with $\Delta\tau$, Δn and the number of correlation points C , but generally ranges from about 0.2 to nearly unity, with values being about 0.8 or greater for typical experiments.

The normalized factorial moments are calculated as

$$n^{(s)} = N^{(s)} / (N^{(1)})^s$$

Rigorous expressions for the photon distribution function $P(n, \Delta\tau)$ have only been obtained for the limiting cases at $\Delta\tau = 0$ and at $\Delta\tau = \infty$, where equations have been derived for both self-beating and reference-beam methods.^{8,11} However, usually, $P(n; \Delta\tau)$ for self-beating measurements at arbitrary sampling interval is closely given by the approximate two parameter function.¹²

$$P(n, \Delta\tau) = \frac{\Gamma(n+m)}{n! \Gamma(m)} \left(1 + \frac{\langle n \rangle}{m}\right)^{-m} \left(1 + \frac{m}{\langle n \rangle}\right)^{-n} \quad (3.26)$$

$$m = [n^{(2)}(\Delta\tau) - 1]^{-1} \quad (3.27)$$

so that

$$n^{(s)} = \frac{\Gamma(m+s)}{\Gamma(s)m^s} \quad (3.28)$$

Examples of comparison of Eqn. (3.26) with experimental $P(n, \Delta\tau)$ are given in Fig. 2 for several values of $\Delta\tau/\tau_h$. Distortion of $P(n, \Delta\tau)$ by excessive scattering during a few of the sampling intervals can result in values of $n^{(s)}$ ($s \geq 3$) far larger than the estimate given by Eqn. 3.28 with m calculated from $n^{(2)}$, providing a test for the internal consistency of the data. Another test is provided by comparison $g^{(2)}(0)$ with $n^{(1)}$. These should be equal, but may differ if $P(n, \Delta\tau)$ varies substantially among the M data sets.

Other sources of experimental errors should also be taken into account. The experimental $P(n, \Delta\tau)$ is truncated by the digital nature of experiments at photon number n_m such that $TM\langle n \rangle P(n_m; \Delta\tau) < 1$. The experimental estimator $\hat{n}^{(s)}$ to $n^{(s)}$ is given by

$$\hat{n}^{(s)} = n^{(s)} \left[1 - \left(\frac{\langle n \rangle}{m + \langle n \rangle} \right)^n m^{-s+1} \left(n_{m,j}^{-s+j} \sum_{j=0}^{m+s-1} \left(\frac{m}{m + \langle n \rangle} \right) \right) \right] \quad (3.29)$$

using the approximate photon distribution function Eqn. 3.26 (with integer m). The photon number n_m is determined by

$$\frac{TM\langle n \rangle n_m}{(1 + \langle n \rangle)^{1 + n_m}} \leq 1 \quad (3.30)$$

for small $\Delta\tau$, which is the only case for which the correction is important. Thus, the correction terms in Eqn. (3.29) depend on $\langle n \rangle$ and M . They can be made sufficiently small for $n^{(2)}$ by setting the optimum conditions of data acquisition: e.g., large M or small $\langle n \rangle$.

When the average photon count rate $\langle n \rangle$ is small, contribution of dark counts from the photomultiplier to $n^{(2)}(\Delta\tau)$ and $g^{(2)}(\tau)$ becomes significant. The experimental estimators are given by

$$\hat{n}^{(2)}(\Delta\tau)-1 = [n^{(2)}(\Delta\tau)-1](1-\delta)^2 + [n_d^{(2)}(\Delta\tau)-1]\delta^2 \quad (3.31)$$

$$\hat{g}^{(2)}(\tau)-1 = [g^{(2)}(\tau)-1](1-\delta)^2 + [g_d^{(2)}(\tau)-1]\delta^2 \quad (3.32)$$

where $n_d^{(2)}$ and $g_d^{(2)}$ are the second factorial moment and correlation functions for dark counts, and δ is the fraction of dark counts in the total counts registered. Usually, $n_d^{(2)}-1$ and $g_d^{(2)}-1$ are not very large in the range of time scale corresponding to macromolecular diffusion. The correction terms in Eqns. 3.31 and 3.32, therefore, only increase the experimental values of $\hat{n}^{(2)}$ and $\hat{g}^{(2)}$ to larger values, but do not affect evaluation of $\langle \tau^{(h)} \rangle_N$ or $\langle \tau^{(h)} \rangle_G$. On the other hand, distortions by dead time of photomultiplier or computer become large at high counting rate of photons. A correction for this effect is already given in the literature.¹³

The function $f(A)$ is fixed by the detector optics. With the optical system used in this study, $f(A)$ is principally determined by the pinhole P and is less dependent on slits S_H and S_V . Pinholes from 100 to 1000 μm diameter are used. Typical data for $f(A)$ as a function of the pinhole diameter are given in Fig. 3, along with a theoretical estimate for $f(A)$.¹³

3.3.2 Light Scattering Methods

In this study, all data were taken in the self-beating mode and in V_V mode (vertically polarized incident and vertically polarized scattering lights) at 514 nm. As discussed above, estimations for $g^{(2)}(\tau, \Delta\tau)$, $g^{(2)}(\Delta\tau, \Delta\tau)$, and $n^{(2)}(\Delta\tau)$ ($s = 1-5$) are calculated for each data set as a function of scattering angle θ , usually over the range 30–135 deg. In most cases, the number of M of post-autocorrelation averages was adjusted so that the total number of photon counts $TM\langle n \rangle$ was about 10^6 .

The DAPS provides for automatic scan through θ and Δr ranges to facilitate these measurements. The light scattering cells are immersed in a fluid with refractive index close to that of the scattered fluid. The immersion fluid is held in a cylindrical cell with flat entrance and exit windows (Brice-Phoenix, cylindrical light scattering cell) using teflon rings at the top and bottom of the light scattering cell to position it. The cylindrical cell is held in a concentric cylinder thermostat, with incident and scattered rays passing through small (6 mm dia.) ports.

Absolute intensity light scattering (elastic scattering) was also measured on solutions of d-PBT both in Hv and Vv modes with $\lambda_0 = 633$ nm. Calibration methods, corrections for absorption and fluorescence, scattering volume, etc. have been described previously.¹⁴ In these experiments, the scattering from a solution of polystyrene in butanone served as a secondary standard. In addition, the scattering from the polystyrene solution was used to align the analyzer in the Hv mode (by adjustment to give minimum scattering at 90° scattering angle).

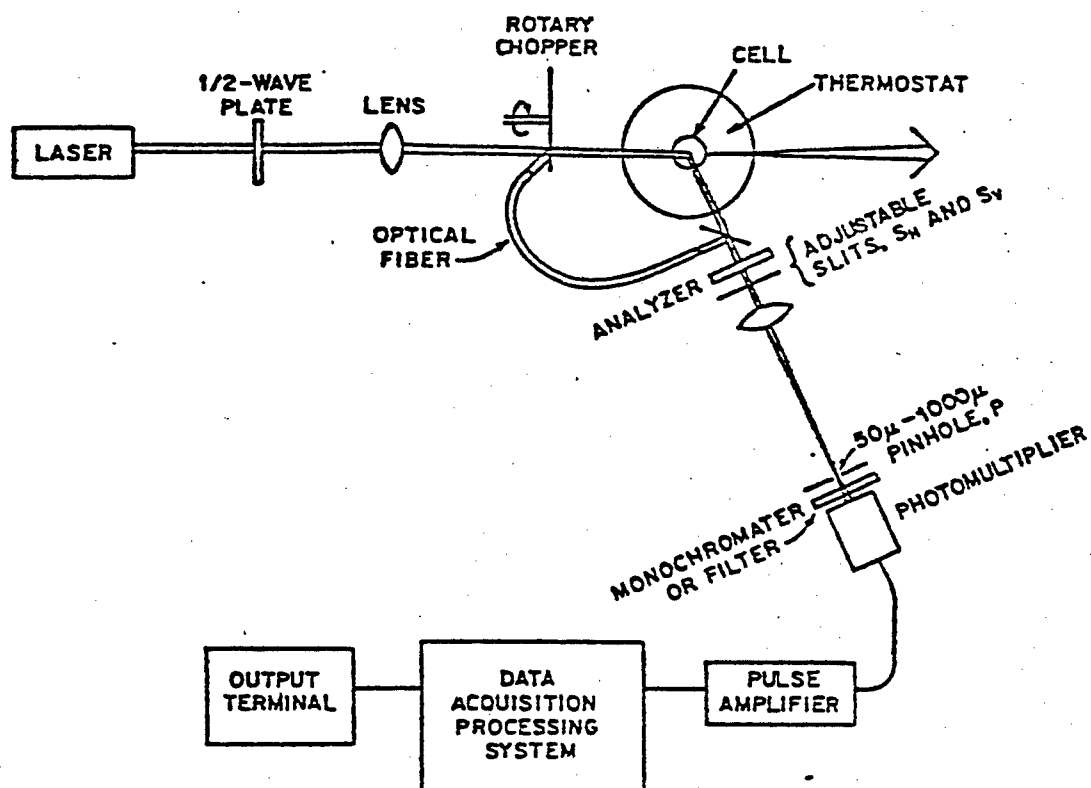


Figure 1:

Schematic diagram of light scattering apparatus showing the principal components discussed in the text.

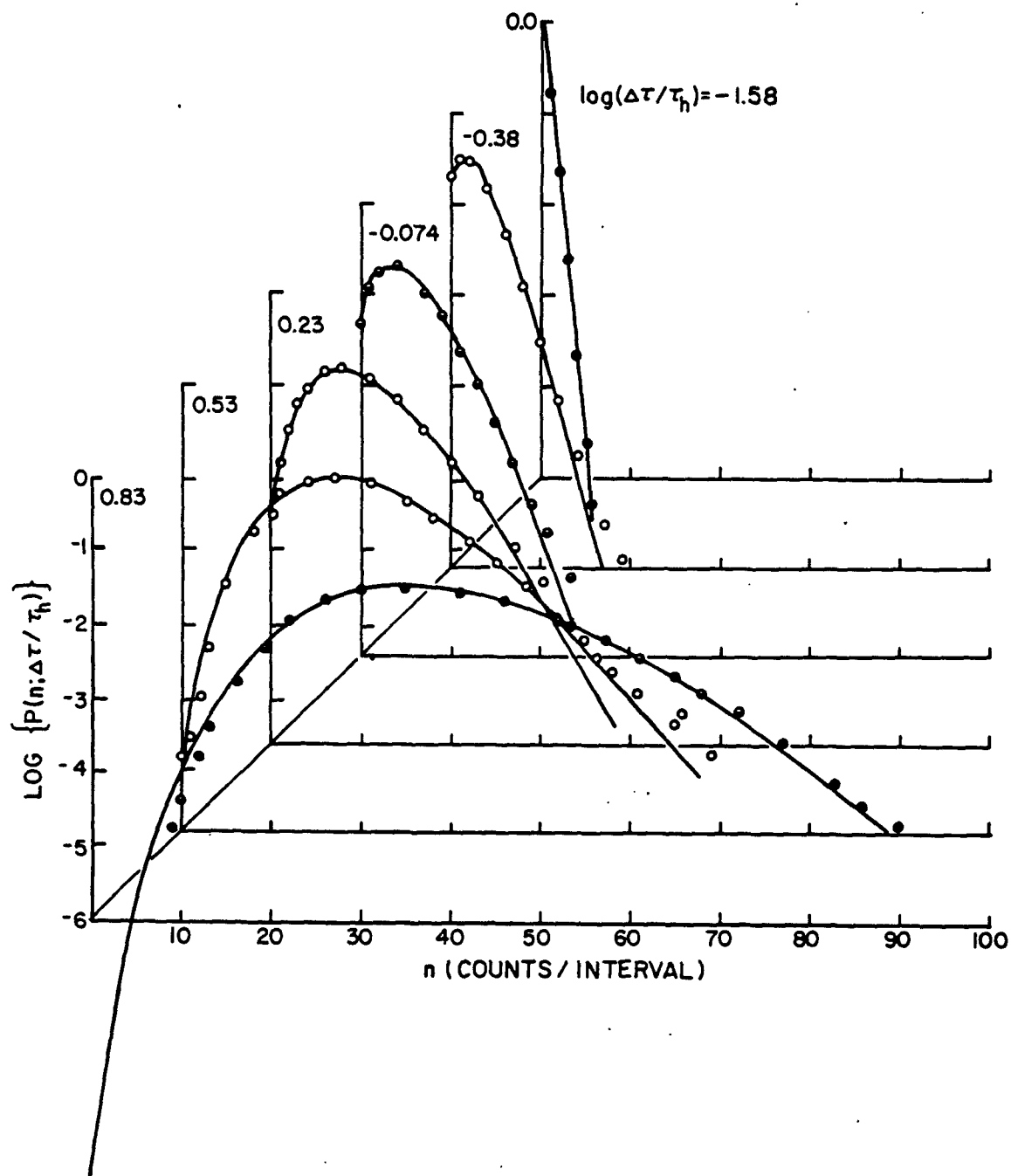


Figure 2:

The distribution $P(n, \gamma)$ determined for a polystyrene solution for several values of $\Delta\tau$. Numbers on each curve give $\log \Delta\tau/\tau_h$. The solid curves were constructed with Eqn. 2.7 using the experimental $n^{(2)}$ to compute $m^{-1} = n^{(2)} - 1$.

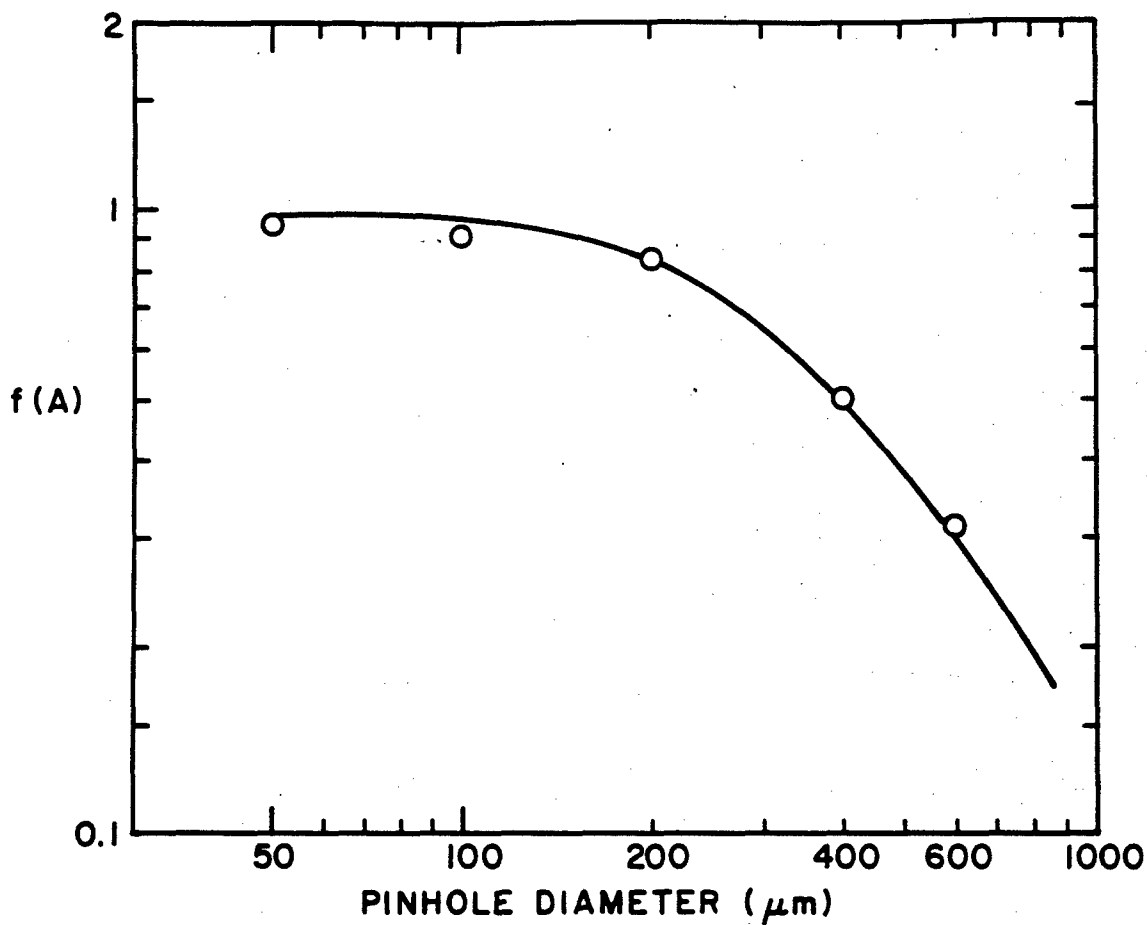


Figure 3:

The coherence factor $f(A)$ determined for several values of the pinhole diameter D . The curve is a theoretical estimate, fitted to the data by use of an arbitrary proportionality between D^2 and the coherence area A .

3.4 Results and Discussion

3.4.1 Polystyrene Solutions

3.4.1.1 Solution Preparation

One of the polymer samples studied is an anionic polystyrene supplied from Pressure Chemicals Co. The weight-average molecular weight M_w and the ratio of M_w to the number-average molecular weight M_w/M_n of this sample are 4.0×10^5 and 1.06, respectively, according to the supplier's note. The polystyrene sample was dissolved in tert-butyl acetate which was distilled prior to use. The solutions were filtered into the light scattering cells, sealed under vacuum, and then centrifuged for 24 hours before light-scattering measurements while suspended by flotation in the centrifuge tubes in a swinging-bucket rotor.

3.4.1.2 Photon Correlation Scattering

A semilogarithmic plot of the autocorrelation function $g^{(2)}(\tau)-1$ against $\tau \sin^2(\theta/2)$ is given in Fig. 4 for a solution with $c = 5$ mg/ml. The delay time τ was changed in increments of the sampling interval $\tau = k\Delta\tau$ where $\Delta\tau = \Delta\tau^\circ 2^\alpha$, with $\Delta\tau^\circ = 50^\circ$ ns and $1 \leq \alpha \leq 24$. Correlation was taken over 16 points ($k = 0-15$) for four different values of $\Delta\tau$ ($\alpha = 7-10$) at 60° . It is seen that data points for different $\Delta\tau$ can be fitted with a single straight line. The slope of this straight line gives $3.04 \times 10^4 \sin^2(\theta/2)$ as a first cumulant and an average coherence time with $\langle \tau^{(h)} \rangle_K \sin^2 \theta / 2 = 32.9 \mu s$.

Correlation functions was also obtained at 7 different scattering angles between 30 and 135° for a solution with $C = 10$ mg/ml at $50^\circ C$. In this measurement, sampling interval $\Delta\tau$ was fixed at $6.4 \mu sec$ ($\alpha = 7$). Data points at each scattering angle follow a straight line when they are semilogarithmically plotted against $\tau \sin^2(\theta/2)$ as in Fig. 5. The slope of the straight line, i.e., the first cumulant, depends only slight on scattering angle, so that $K \sin^2(\theta/2)$ is determined as $2.64 \times 10^4 \text{ sec}^{-1}$ independently of scattering angle.

In Fig. 6, $n^{(2)}(\Delta\tau)-1$ and $g^{(2)}(\Delta\tau)-1$ are plotted bi-logarithmically against $\Delta\tau \sin^2(\theta/2)$. Single composite curves are obtained from data taken at different angles both for $n^{(2)}(\Delta\tau)$ and $g^{(2)}(\Delta\tau)-1$. They can be approximated by the theoretical curves corresponding to single exponential in time domain (single Lorentzian in frequency domain) (Eqns. (4) and (6) for $n^{(2)}(\Delta\tau)-1$). It may be concluded that the molecular weight distribution of the polystyrene sample is narrow. From Fig. 6 $\Delta\tau_N \sin^2 \theta / 2$ and $\Delta\tau_G \sin^2 \theta / 2$ are graphically evaluated as 40 and $20 \mu s$, respectively.

Angular dependence of three average relaxation times $\langle \tau^{(h)} \rangle_K$, $\langle \tau^{(h)} \rangle_N$, and $\langle \tau^{(h)} \rangle_G$ is shown in Fig. 7. Values of $\langle \tau^{(h)} \rangle_N$ and $\langle \tau^{(h)} \rangle_G$ are quite close to each other, though the former is slightly larger than the latter. Both $\langle \tau^{(h)} \rangle_N$ and $\langle \tau^{(h)} \rangle_G$ are larger than $\langle \tau^{(h)} \rangle_K$. The ratios $\langle \tau^{(h)} \rangle_N / \langle \tau^{(h)} \rangle_K$ and $\langle \tau^{(h)} \rangle_G / \langle \tau^{(h)} \rangle_K$ are 1.07 and 1.06, respectively. These ratios give characteristic indices of the width of relaxation spectra and then that of molecular size distribution. Thus, the molecular weight heterogeneity can be sensitively detected by either $\langle \tau^{(h)} \rangle_N / \langle \tau^{(h)} \rangle_K$ or $\langle \tau^{(h)} \rangle_G / \langle \tau^{(h)} \rangle_K$, even though correlation functions $g^{(2)}(\tau)$, $n^{(2)}(\Delta\tau)$, and $g^{(2)}(\Delta\tau)$ are closely approximated by a single exponential equation or its equivalents as illustrated in Figs. 4, 5, and 6.

The relation between $n^{(2)}(\Delta\tau)-1$ and $n^{(3)}(\Delta\tau)-1$ shown in Fig. 8 includes various data sets taken under different detector optics. Each data set follows a theoretical curve represented by

$$\frac{n^{(3)}(\Delta\tau)-1}{3n^{(2)}(\Delta\tau)-1} - 1 = \frac{g(A)}{f(A)} \frac{2[\gamma-1 + (\gamma+1)e^{\gamma}]}{2\gamma^2-1 + e^{-2\gamma}} \quad (3.33)$$

Equation 3.33 is derived from the equation given in Appendix and Eqn. 3.10 by taking single term and putting $r = 1$. All data sets merge to a straight line with slope unit as small as $n^{(2)}(\Delta\tau)-1$ or at large $\Delta\tau$. From shift factors $g(A)/f(A)$ along the ordinate and $f(A)$ along the abscissa chosen to fit Eqn. 3.33 to the data, the relation between $g(A)$ and $f(A)$ is obtained as

$$g(A) \sim \frac{4}{3} f(A)^2$$

There is no theoretical estimate for a $g(A)$.

The concentration dependence of average relaxation times $\langle \tau^{(h)} \rangle_K$, $\langle \tau^{(h)} \rangle_N$, and $\langle \tau^{(h)} \rangle_G$ at three temperatures 19.6, 50.6 and 89.8°C is shown in Fig. 9. The zero-concentration values of the average relaxation time are easily evaluation from the intercept of the straight line fitted to the data points for each temperature. Zero-concentration diffusion coefficients D_0 are calculated as

T/°C	19.6	50.6	89.8
D ₀ x 10 ⁷ /cm ² sec ⁻¹	2.80	3.66	6.36
R _H /nm	10.4	13.1	12.9

using the relation

$$D_0 = \lim_{C \rightarrow 0} [\langle \tau^{(h)} \rangle h^2]^{-1}$$

$$R_H = kT/6\pi\eta_s D_0$$

where $\lambda_0 = 514$ nm and η_s is the solvent viscosity; here \bar{n} and its temperature dependence was obtained from the literature and η_s was determined to be 0.740, 0.495 and 0.323 (cp), respectively, at 19.6, 50.6 and 89.8°C by capillary viscometry.

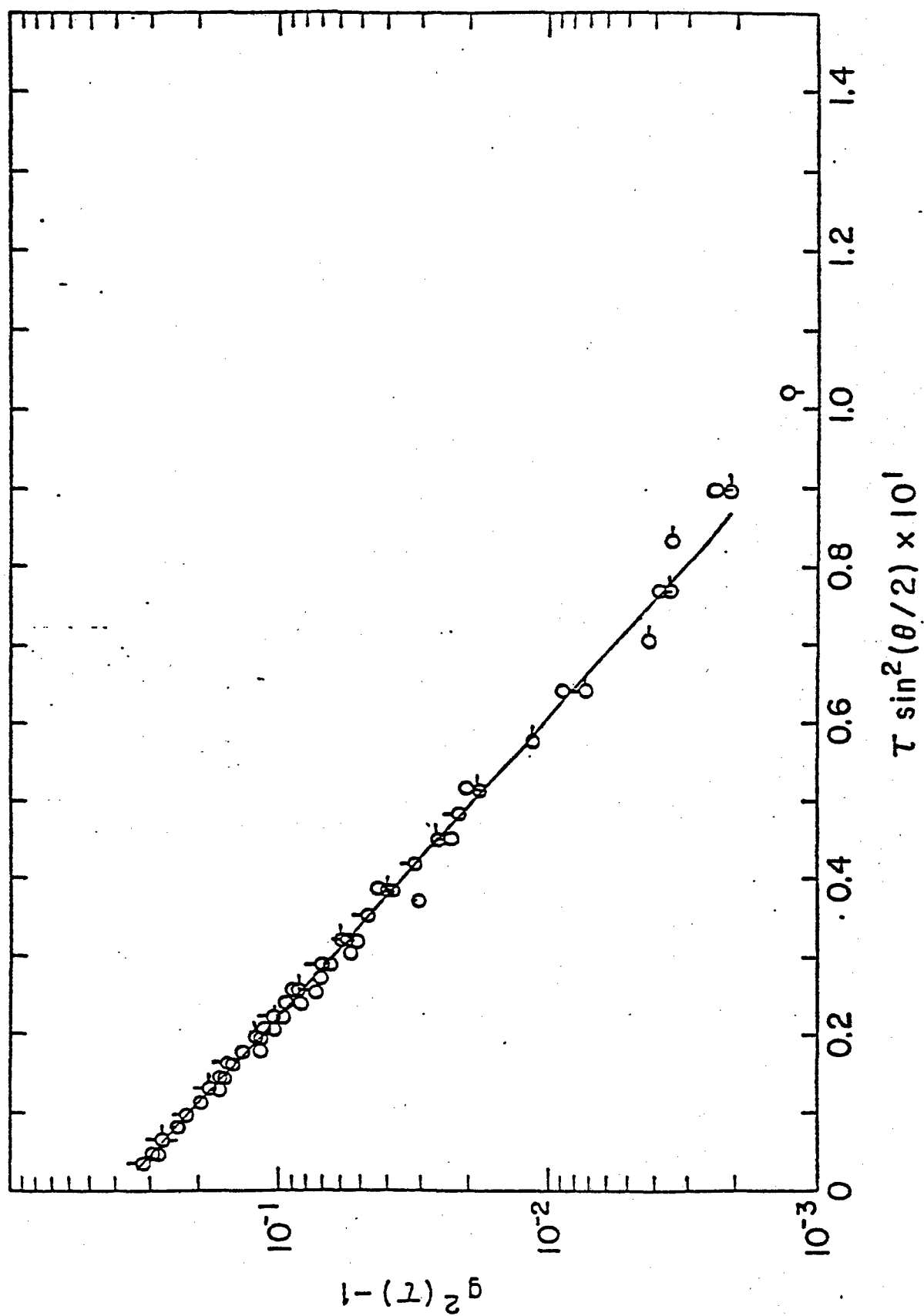


Figure 4:

$\log[g^{(2)}(\tau)-1]$ versus $\tau \cdot \sin^2 \theta/2$ for a polystyrene solution in t-butyl acetate at 50.2°C, $C = 5$ mg/ml, $\theta = 60^\circ$.

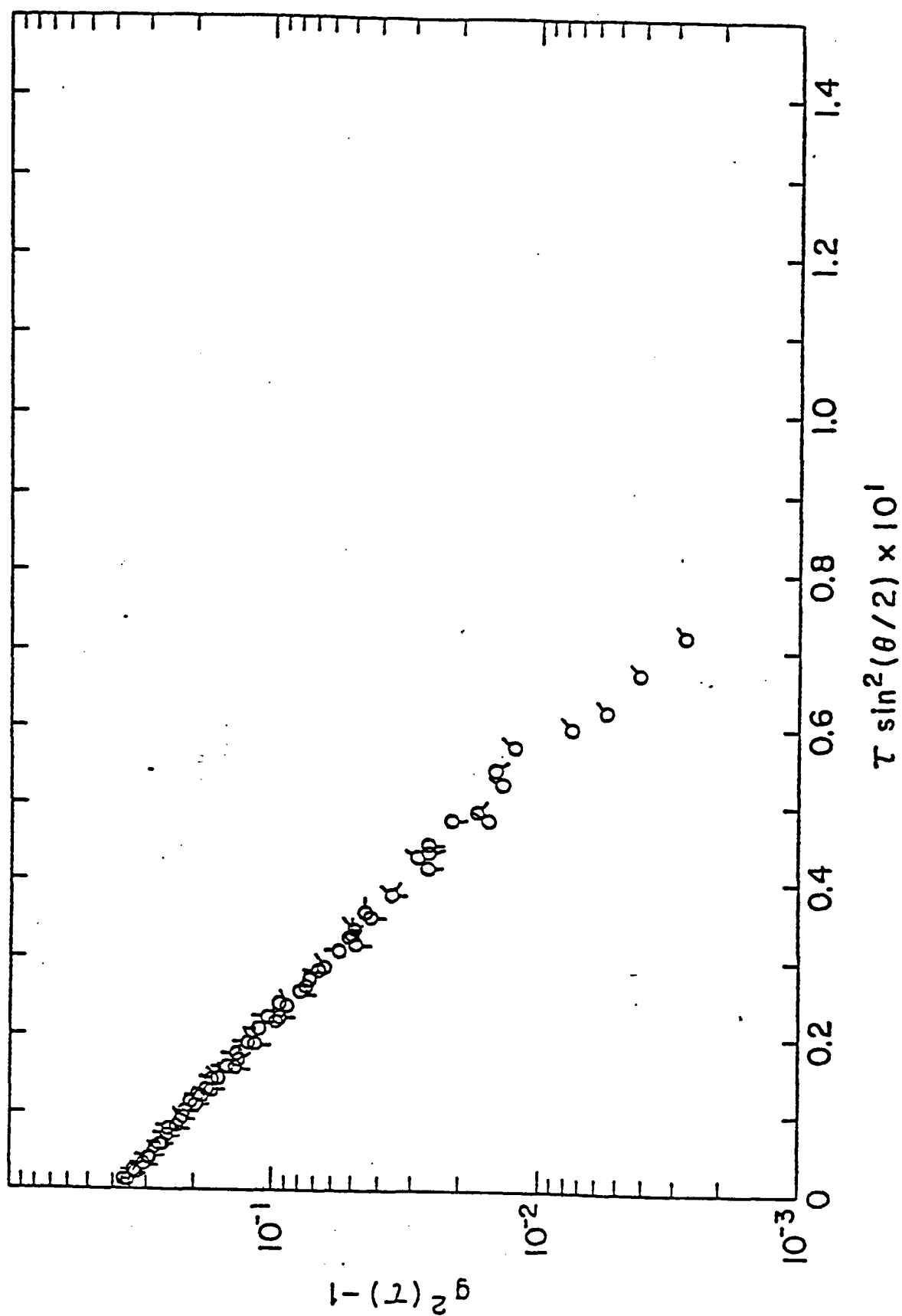


Figure 5:

$\log[g^{(2)}(r)-1]$ versus $\tau \sin^2 \theta/2$ for a polystyrene solution in t-butyl acetate at 50.2°C , $C = 5 \text{ mg/ml}$, $30 < \theta < 135^\circ$.

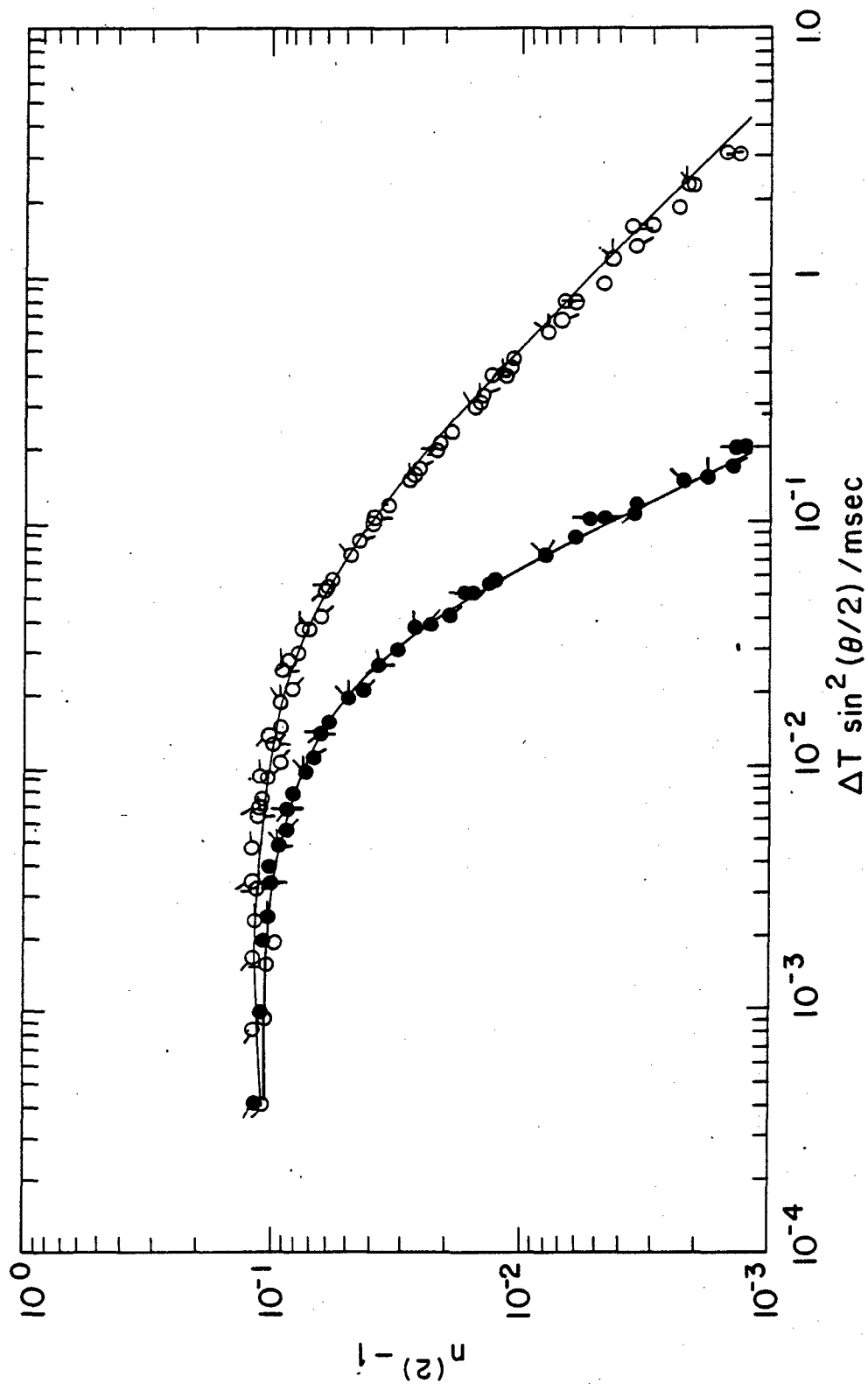


Figure 6:

$\log \ln^2(\Delta\tau)-1$, O, and $\log [\ln^2(\Delta\tau)-1]$, ●, versus $\Delta\tau \sin^2\theta/2$ for solutions of polystyrene in t-butyl acetate at 50.6°C; $C = 10$ mg/ml, $30 < \theta < 135^\circ$ (pip up at 30, rotating clockwise with increasing θ).

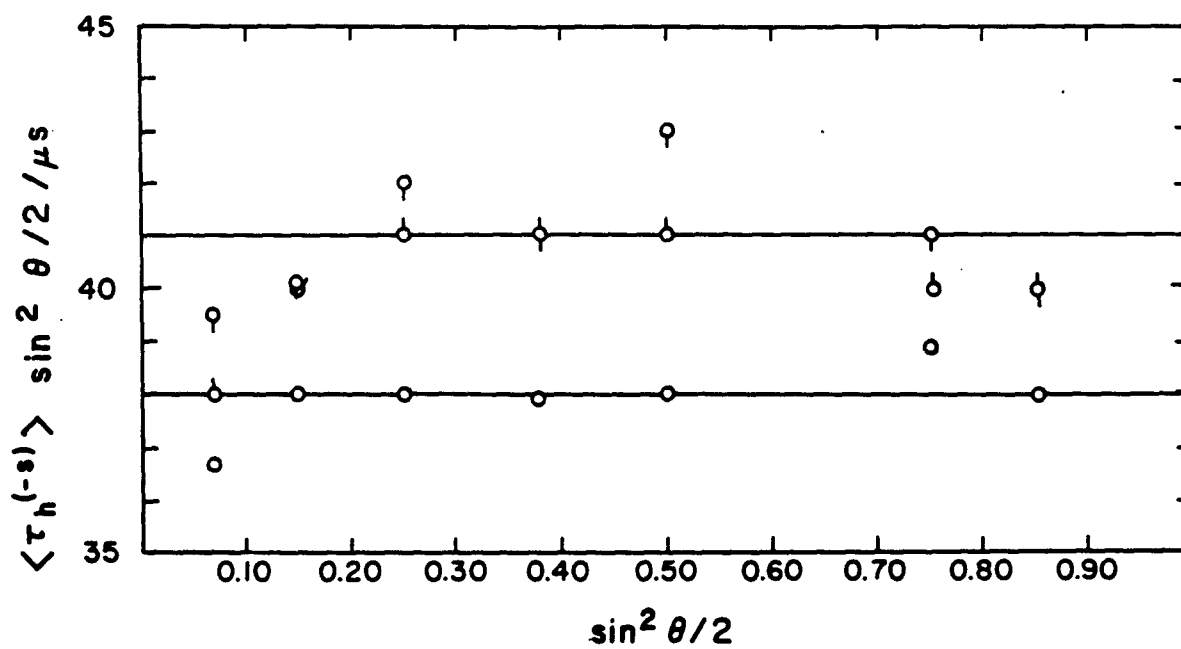


Figure 7:

$\langle \tau_h^{(n)} \rangle \sin^2 \theta / 2$ versus $\sin^2 \theta / 2$ for polystyrene in t-butyl acetate at 50.6°C; C = 10 mg/ml; J = N, \circ ; g, \circ ; K, \circ .

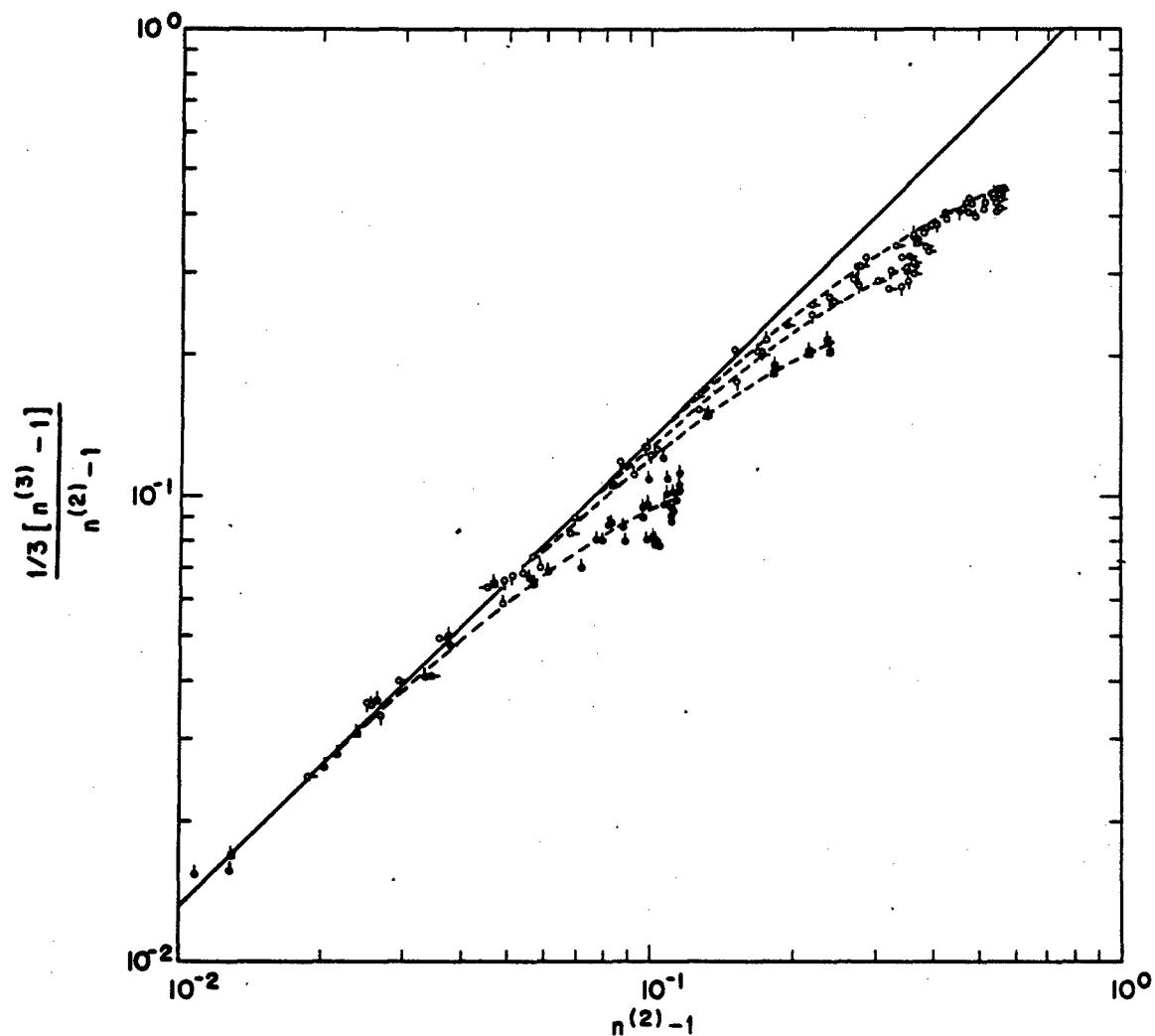


Figure 8:

Relation between $n^{(3)}(\Delta\tau)$ and $n^{(2)}(\Delta\tau)$ for four optical arrangements. Dashed lines represent Eqn. 3.31 — solid lines represent asymptotic behavior.

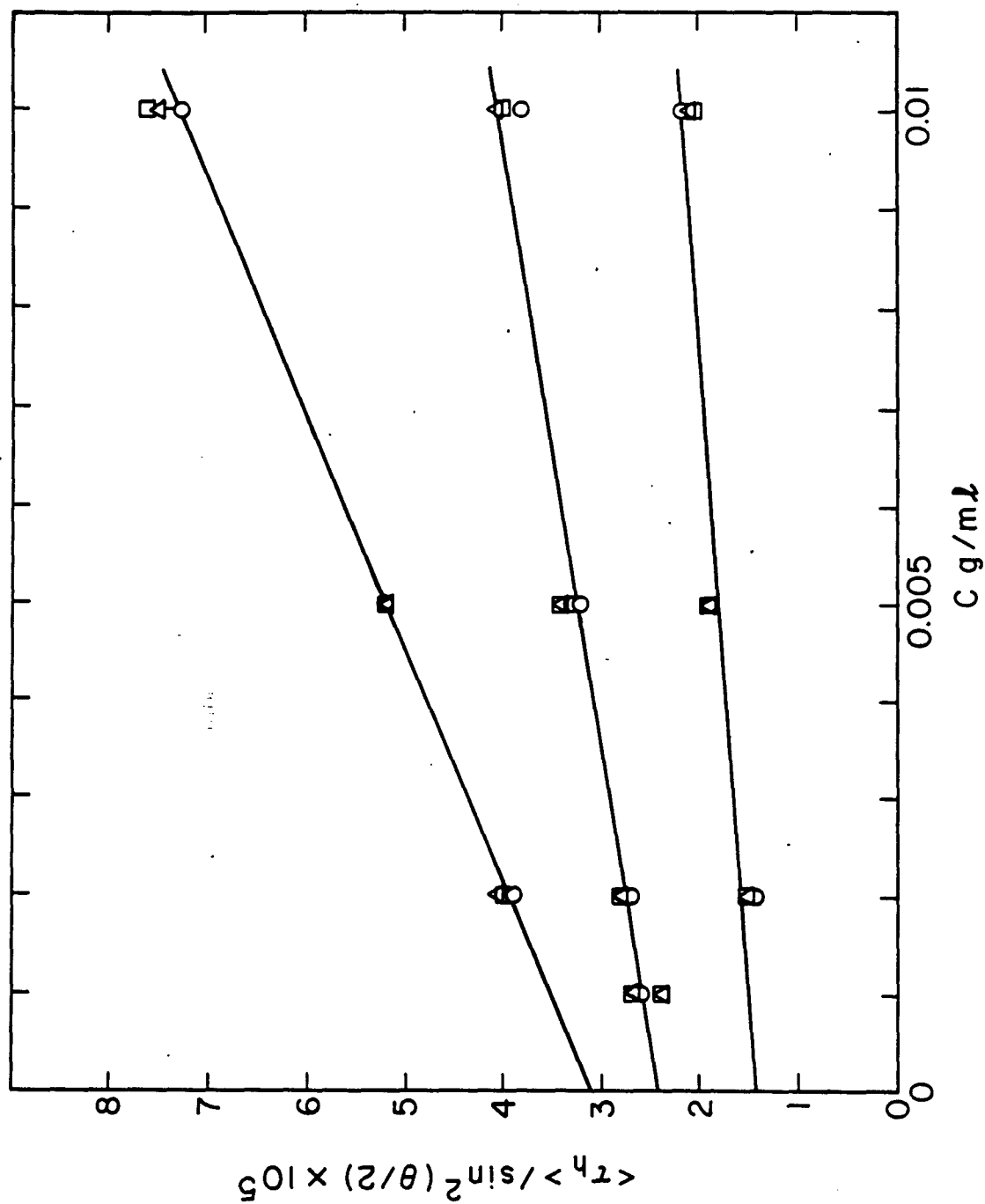


Figure 9:

$\langle \tau^{(h)} \rangle \sin^2 \theta / 2$ versus C for solutions of polystyrene in t-butyl acetate at three temperatures. Symbols as in Fig. 7.

3.4.2 d-PBT Solutions

3.4.2.1 Solution Preparation

Solutions of a rodlike macroion were prepared by dissolution in methanesulfonic acid (MSA) of deuterized poly (1,4-phenylene-2,6-benzobisthiazole) (d-PBT), which was supplied by Dr. J. R. Wolfe, SRI International. Solutions were prepared in a glove box with air circulated over drierite. The solvent MSA was distilled under vacuum. The solutions were filtered several times with teflon millipore filter into the light scattering cells in a glove box filled with dry nitrogen. Cells were sealed with flame under vacuum and then centrifuged for 24 hours before measurements.

3.4.2.2 Photon Correlation Scattering

Examples of correlation functions $g^{(2)}(\tau)$, $n^{(2)}(\Delta\tau)$, and $g^{(2)}(\Delta\tau)$ are given in Figs. 10 and 11. In contrast to the data for polystyrene solutions, the plot of $\ln g^{(2)}(\tau)$ vs τ given in Fig. 10 is not linear. Curvature becomes more severe as the scattering angle θ increases. It is, however, not difficult to evaluate the initial slope or the first cumulant. The data sets of $n^{(2)}(\Delta\tau)-1$ and $g^{(2)}(\Delta\tau)-1$ versus $h^2\Delta\tau$ are not independent of the scattering angle; the curves shift to shorter $\Delta\tau$ region with increasing scattering angle. These results indicate that the system d-PBT/MSA has a broad distribution of molecular (or particle) size, or modes of relaxations other than translational diffusion as a whole molecule.

In Fig. 12, the average relaxation times $\langle\tau^{(h)}\rangle_K \sin^h\theta/2$, $\langle\tau^{(h)}\rangle_N \sin^2\theta/2$ and $\langle\tau^{(h)}\rangle_G \sin^2\theta/2$ for a solution with $C = 6.5$ mg/ml are plotted against $\sin^2(\theta/2)$. Data points of each average-relaxation time give a curve convex downward and are not proportional to $\sin^2(\theta/2)$. Values of $\langle\tau^{(h)}\rangle_N$ are slightly smaller than those of $\langle\tau^{(h)}\rangle_G$, and much larger than $\langle\tau^{(h)}\rangle_K$ values. The ratio $\langle\tau^{(h)}\rangle_N/\langle\tau^{(h)}\rangle_K$ is about 2.0, which indicates that distribution of molecular size is quite broad, if the distribution of relaxation time detected is due to the heterogeneity of molecular size.

For the self-beating mode ($r=1$), Eqn. 3.10, can be put in the form

$$[g^{(2)}(\tau)-1]^{1/2} = [f(A)]^{1/2} \sum_i \tau_i \exp -\gamma_i \tau/\Delta\tau \quad (3.34)$$

for γ_i small enough that $q(\gamma)$ may be put equal to unity (as is usual with studies of $g^{(2)}(\tau)$). Equation 3.34 is reminiscent of relations encountered in other applications in which the

measured quantity represents a weighted sum of exponential contributions (e.g., stress relaxation, small-angle X-ray scattering, absorption spectroscopy, total intensity light scattering, etc.). In this case, the relation between r_i and the concentration c_i and molecular weight M_i of the components with coherence time $\tau_i^{(h)}$ is complex, but need not be known to attempt assessment of a resolution of $g^{(2)}(\tau)$ into representative components. If the $\tau_i^{(h)}$ are sufficiently widely spaced then $[g^{(2)}(\tau)-1]^{1/2}$ may be decomposed into a sum of exponentials by simple graphical methods. Thus, as may be seen in Fig. 10 $\ln [g^{(2)}(\tau)-1]$ versus τ is a linear function (within experimental error) for large τ , permitting assessment of the longest coherence time $\tau_1^{(h)}$ and the weight r_1 . Subsequent analysis of $\ln\{[g^{(2)}(\tau)-1]^{1/2}-f^{1/2}r_1\exp-\tau/\tau_1^{(h)}\}$ versus τ permits evaluation of $\tau_2^{(h)}$ and r_2 , etc., until the residual between $[g^{(2)}(\tau)-1]^{1/2}$ and $f^{1/2}\sum r_i\exp-\tau/\tau_i^{(h)}$ at small τ is within experimental error—this method is exactly that of "Procedure X" used to represent stress relaxation data.¹⁶ This procedure provides a method to represent the component contributions to $g^{(2)}(\tau)$ with minimal computational effort, and will usually provide a reasonable representation within the limits of the data. The graphical method is not suitable to represent components with closely spaced $\tau_i^{(h)}$ in a meaningful way (e.g., to accurately represent the molecular weight distribution of a polymer). The uniqueness of the representation is strongly dependent on the behavior of large τ and the accuracy to which $\tau_i^{(h)}$ and r_i may be obtained.

Application of successive approximations to $g^{(2)}(\tau)$ is illustrated in Fig. 13 with data that are fitted by two terms with coherence times differing by about ten-fold. All of the data for d-PBT could be fitted by Eqn. 3.34 with two components. Typical results are shown in Fig. 14, for one concentration, and the dependence of the coherence times $\tau_1^{(h)}$ and $\tau_2^{(h)}$ and the weight factors r_1 and $r_2 = 1-r_1$ on concentrations is given in Figs. 15 and 16, respectively. As seen in Fig. 14, $h^2\tau^{(h)}$ and $h^2\tau_2^{(h)}$ are independent of h , as expected, even though the average coherence times $h^2\langle\tau^{(h)}\rangle_K$, etc., depend markedly on h . The curves given in Fig. 14 for the angular dependence of the average coherence times calculated with the relations in Table 1, are in good agreement with the observed data. Similarly, as may be seen in Figs. 17 and 18, the functions $n^{(2)}(\Delta\tau)$ and $g^{(2)}(\Delta\tau)$ calculated with Eqns. 3.13 and 3.16, respectively, are in reasonable agreement with experiment.

The significance of the two components found by the preceding analysis will be considered in the following, after the results for the total intensity light scattering are presented.

3.4.2.3 Integrated Intensity Scattering

Reciprocal scattering intensities for Vv and Hv modes are plotted against $\sin^2(\theta/2)$ in a form of square plot in Figs. 19 and 20. Values of $(Kc/R_{Vv})^{1/2}$ for each solution indicate significant deviation at small scattering angles (ca. 30% at 30°) from the straight line fitted with data at higher angles, while those of $(Kc/R_{Hv})^{1/2}$ deviate from constant value at high angles to less extent ca. 12% at 0°). Thus, the scattering from large particle (presumed to be aggregates of d-PBT molecules) contribute to Vv scattering intensity more severely than to Hv intensity. This means that most of the aggregated particles are optically isotropic. Hv scattering is, therefore, mainly attributed to non-associated molecules and Vv scattering includes components from both single molecules and aggregates. The fast and slow modes found above correspond to these two species. Based on this conjecture, the Vv scattering data in Fig. 19 may be separated into two components, corresponding to the fast and the slow modes, using r_1 and r_2 in Fig. 16. Values of $[Kc/R_{Vv}^{(F)}]^{1/2}$ and $[Kc/R_{Vv}^{(s)}]^{1/2}$ thus obtained are plotted against $\sin^2(\theta/2)$ in Fig. 20 and 21, respectively. Here $R_{Vv}^{(F)}$ and $R_{Vv}^{(s)}$ indicate the fast and slow components, respectively. Then, the data for R_{Vv} and R_{Hv} were used in the usual analysis with the expressions¹⁷

$$(Kc/R_{Vv}^{(F)})^{1/2} = \left(\frac{Kc}{R_{Vv}^{(F)}} \right)_0^{1/2} \left[1 + \frac{A_2 M_w}{(1 + 4/5 \delta^2)} c + \dots \right] \quad (3.35)$$

$$(R_{Vv}^{(F)}/Kc)_0 = M_w(1+4/5 \delta^2) - 1/3 M_w [1-4/5 f_1 \delta + 4/7 (f_2 \delta)^2] R_G^2 h^2 + \dots \quad (3.36)$$

$$(Kc/R_{Hv}) = (Kc/R_{Hv})_0 + (0c^2) \quad (3.37)$$

$$(R_{Hv}/Kc)_0 = 3/5 \delta^2 M_w - 9/35 M_w (f_2 \delta)^2 R_G^2 h^2 + \dots \quad (3.38)$$

on the assumption that both R_{Hv} and $R_{Vv}^{(F)}$ result from unassociated d-PBT molecules. Here, A_2 is the second virial coefficient, R_G is the root-mean-square radius of gyration, δ is the

molecular optical anisotropy, and the factors f_1, f_2, f_3 , which are functions of L/ρ are unity for rodlike chains. The results give δ equal to 0.53, using the intercept of the horizontal line for each solution in Figs. 20 and 21 with Eqns. (3.35) and (3.37). The value is close to that estimated previously¹⁸ for PBT. The weight-average molecular weight M_w obtained is 4600, if the original concentration can be used as the concentration for unassociated molecules.

In contrast with $R_{vv}^{(F)}$, $R_{vv}^{(S)}$ is very dependent on the scattering angle, indicating a large size for the aggregates. The slopes of the straight lines in Fig. 22 give the apparent radius of gyration of the aggregates in each solution, which increases with increasing original concentration. The apparent radius of gyration obtained for each solution is extrapolated 0 zero concentration to give about 600 Angstroms, if we can assume that the concentration of the aggregates is proportional to the original polymer concentration.

3.4.2.4 Speculation on the Size of d-PBT Molecule and its Aggregates

The average contour length L of the rodlike chain may be estimated from diffusion constant by use of the relation¹⁹

$$L = [3.77 R_H / d^{0.2}]^{5/4} \quad (3.39)$$

where d is the diameter of the rod (η_s of MSA is 9.0 cp at 30°C). Use of R_H for the fast components (which is assigned as unassociated d-PBT molecules) gives 30 nm as the rod length of the d-PBT sample studied. This value can be compared to the $L_w = 21$ nm calculated from M_w , with $M_L = M/L = 220$ dalton/nm. These values of the rod length is consistent with the fact that the angular dependence of $R_{Hv}^{(F)}$ and $R_{vv}^{(F)}$ is negligible, as shown in Figs. 19 and 20.

There is no available information about the shape of the aggregated particles. If we assume an ellipsoid for the aggregates, diffusion constant D and radius of gyration R_G are represented as:²⁰

$$D = \frac{kT}{6\pi\eta_s a} \cdot \frac{\ln P[1+(1-P^{-2})^{1/2}]}{P(1-P^{-2})^{1/2}} \quad (3.40)$$

where a is the radius of the minor axis and P is the ratio of the major axis to the minor. Using the values of D_1^0 and R_G obtained for slow components, a and P are estimated as 5 and 25 nm, respectively.

3.4.2.5 Summary

Three average coherence times, $\langle \tau^{(h)} \rangle_K$, $\langle \tau^{(h)} \rangle_N$, and $\langle \tau^{(h)} \rangle_G$ have been determined by use of the photon correlation function $g^{(2)}(\tau, \Delta\tau)$ and the photon count distribution function $P(n, \Delta\tau)$. Application to polystyrene solutions for a polymer with a narrow molecular weight distribution show that comparison of the average coherence times provides a means to detect distribution of coherence times and/or molecular distribution. The ratios $\langle \tau^{(h)} \rangle_N / \langle \tau^{(h)} \rangle_K$ and $\langle \tau^{(h)} \rangle_G / \langle \tau^{(h)} \rangle_K$ give characteristic indices of the size distribution of solvents. The size heterogeneity index $\langle \tau^{(h)} \rangle_G / \langle \tau^{(h)} \rangle_K$ by measurements can be obtained by use of only the correlation function $g^{(2)}(\tau)$, even when photon distribution function $P(n)$ is not available.

Correlation data for d-PBT solutions did not follow a single exponential decay curve, showing contribution from components with widely different coherence times. Thus, for d-PBT solutions, the correlation function was decomposed into two representative components by a simple graphical method to obtain two average coherence times, differing by about ten-fold ($D_0^{(S)} = 7.20 \times 10^{-9}$ cm² sec for slow component). These two components were attributed to a single d-PBT molecule and its aggregates (since PBT molecules have a strong tendency to aggregate, even in acid solution).¹⁹

Absolute scattering intensity in the Vv mode was also resolved into two components corresponding to decomposition of the correlation function. Values of $D_0^{(F)}$, $D_0^{(S)}$, M_w and R_G thus obtained, allowed estimate of the size of the d-PBT molecule and its aggregates.

The method used here to analyze the photon correlation function is quite simple in comparison with least-square fitting to $g^{(2)}(\tau)$ with a specific form of correlation function, or a histogram method recently proposed.²¹ It is a useful tool to elucidate the effects of polydispersity of solutes, especially for self-associated systems as heterocyclic polymers, polysaccharides, or biomacromolecules in solution.

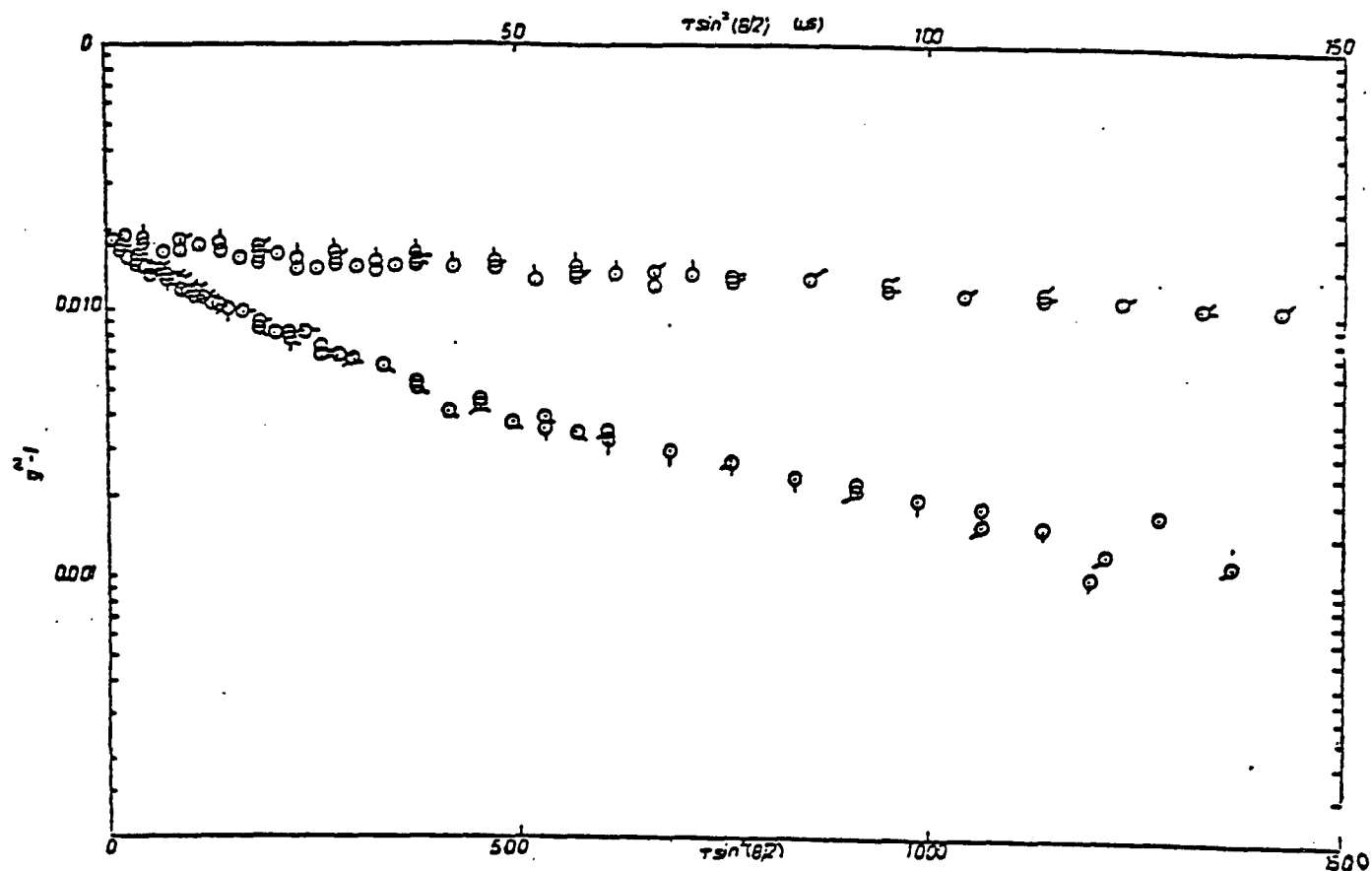


Figure 10:

$\log[g^{(2)}(\tau)-1]$ versus $\tau \sin^2\theta/2$ for solutions of d-PBT in MSA at 30°C; $C = 0.65$ mg/ml, $\theta = 75^\circ$.

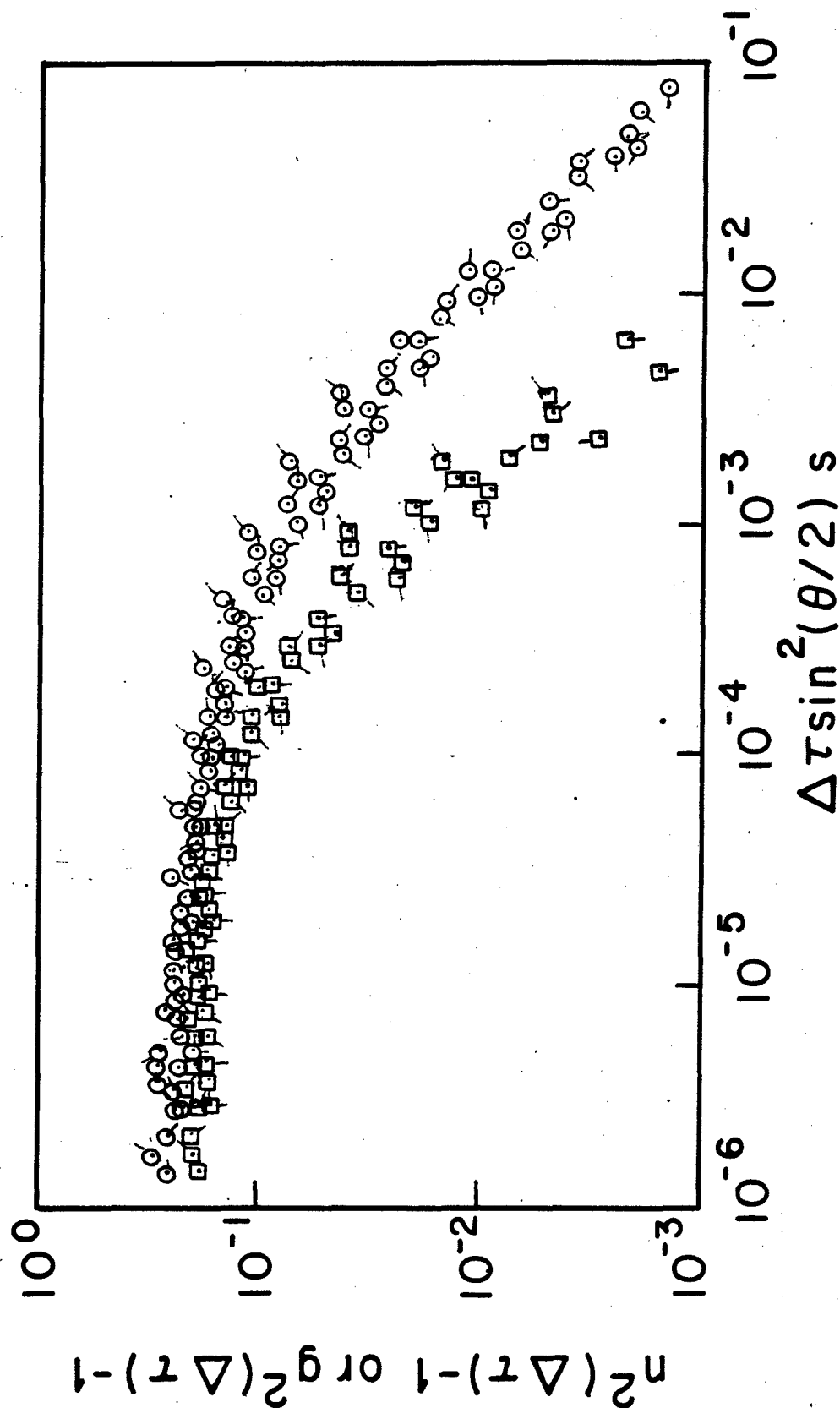


Figure 11:

$\log[n^2(\Delta\tau)-1]$, \circ , and $\log[g^2(\Delta\tau)-1]$, \square , versus $\Delta\tau \sin^2\theta/2$ for solutions of d-PBT in MSA at 30°C ; $C = 0.65 \text{ mg/ml}$, $45 < \theta < 135$, (pip clockwise from up to 45° with increasing θ).

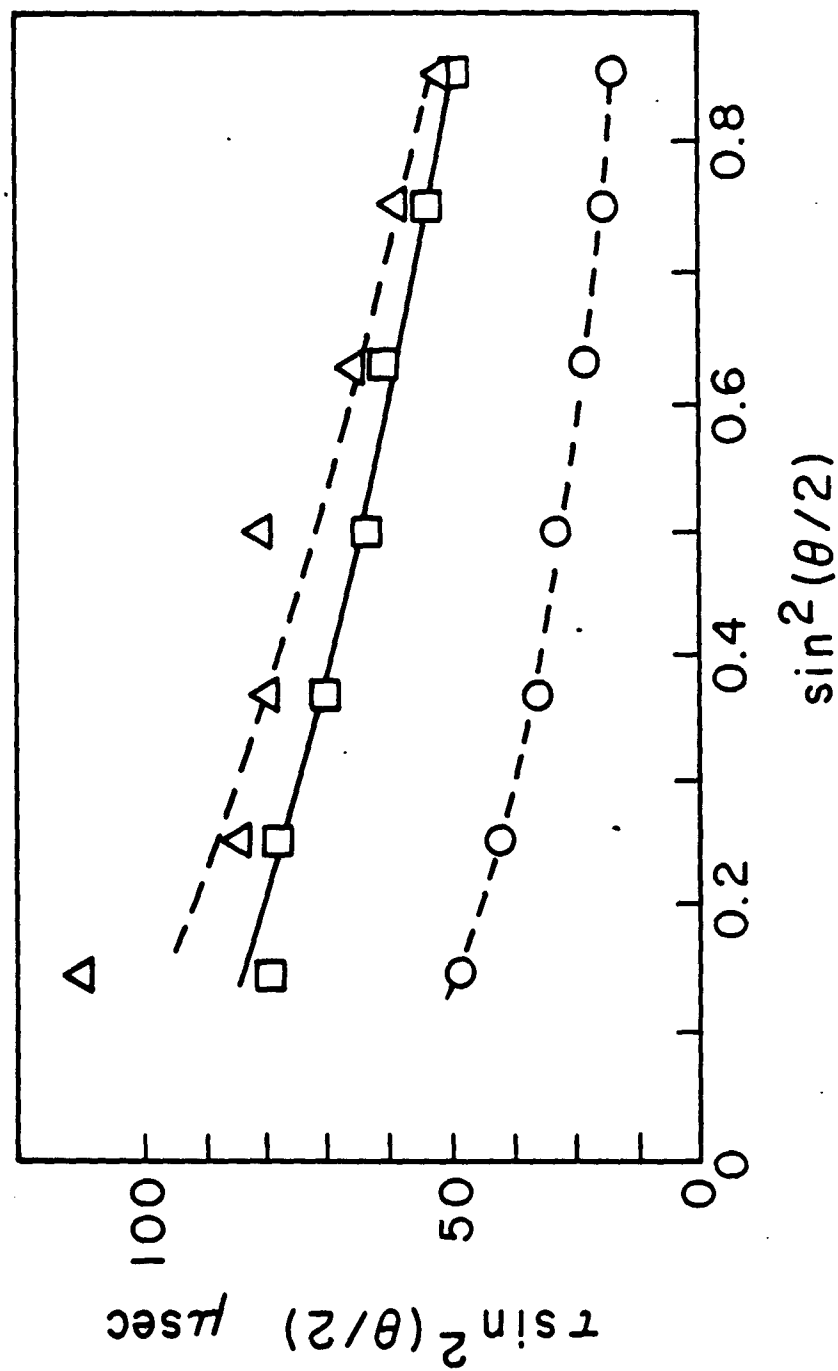


Figure 12:

$\langle \tau^{(b)} \rangle$ versus $\sin^2 \theta/2$ for solutions of d-PBT in MSA at 30°C; C = 0.65 mg/ml. Symbols as in Fig. 7.

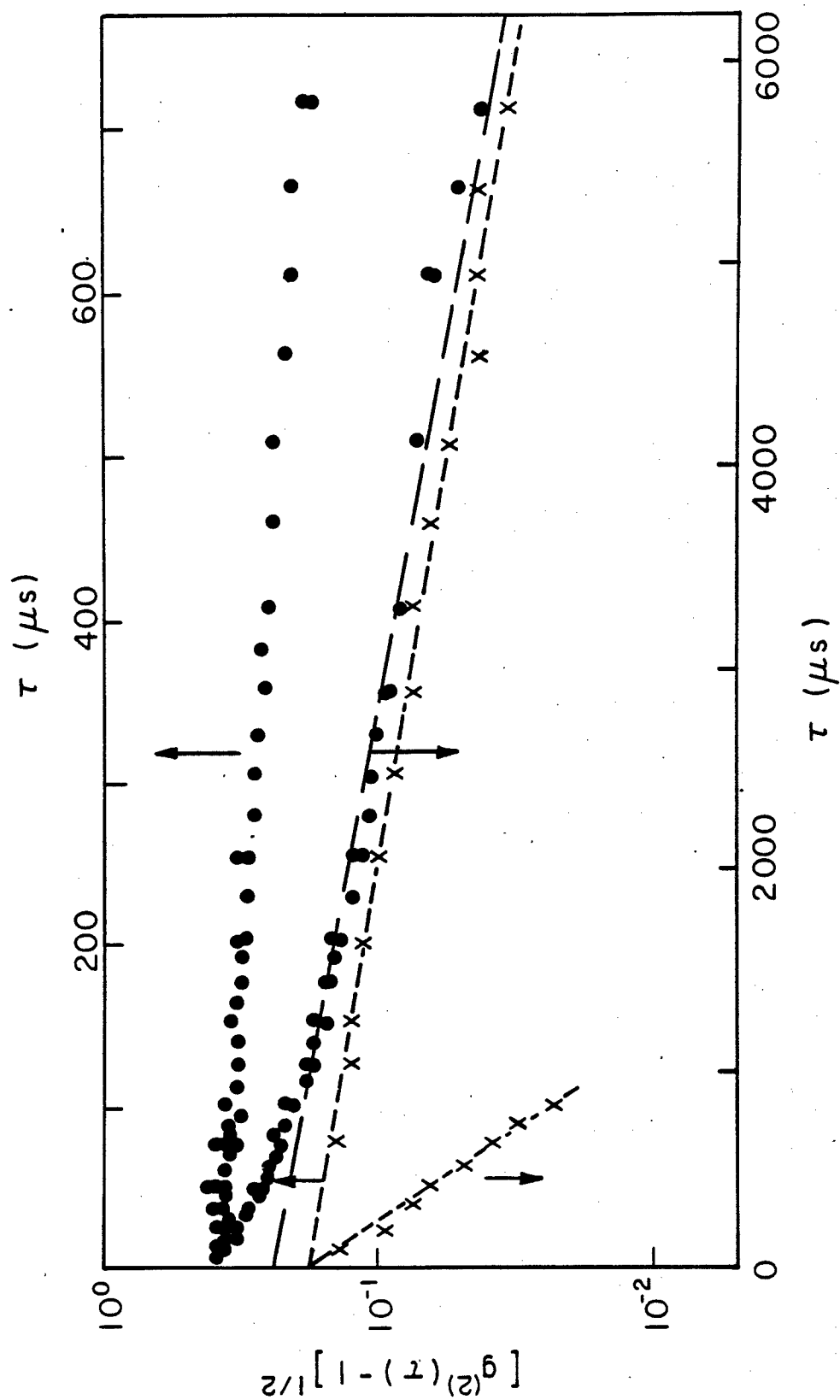


Figure 13:

$\log\{[g^{(2)}(\tau)-1]^{1/2} - (\langle I(\Lambda) \rangle)^{1/2} - \sum_i \tau_i^{(n)}\}$ versus τ for solutions of d-PBT in MSA at 30°C; $C = 0.65$ mg/ml; $\theta = 90^\circ$.

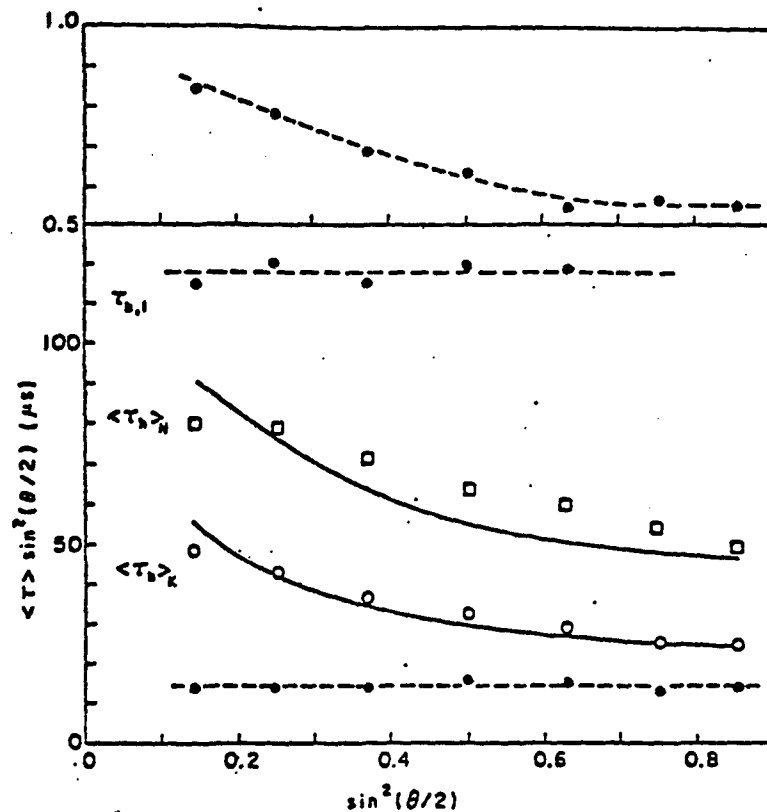


Figure 14:

(a)

$\langle \tau^{(b)} \rangle, \sin^2 \theta/2, \tau_1^{(b)} \sin^2 \theta/2$ versus $\sin^2 \theta/2$ for a solution of d-PBT in MSA at 30°C ; $C = 0.65 \text{ mg/ml}$. Symbols as in Fig. 7. Solid lines calculated with relations in Table 1 (self-beating mode) and values of $\tau_1^{(b)}$ and r_1 given in Figs. 14a and 14b, respectively. (b) $r_1, O,$ versus $\sin^2 \theta/2$ for solutions of d-PBT in MSA at 30°C ; $C = 0.65 \text{ mg/ml}$.

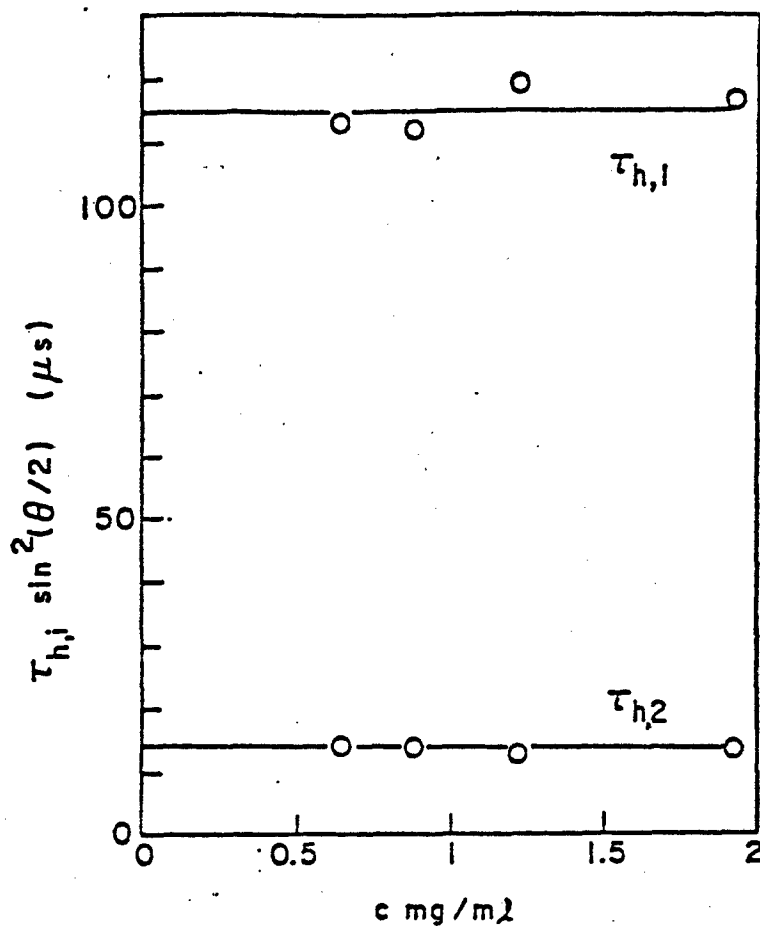


Figure 15:

$\tau_1^{(h)} \sin^2 \theta / 2$ and $\tau_2^{(h)} \sin^2 \theta / 2$ versus C for solutions of d-PBT in MSA at 30°C.

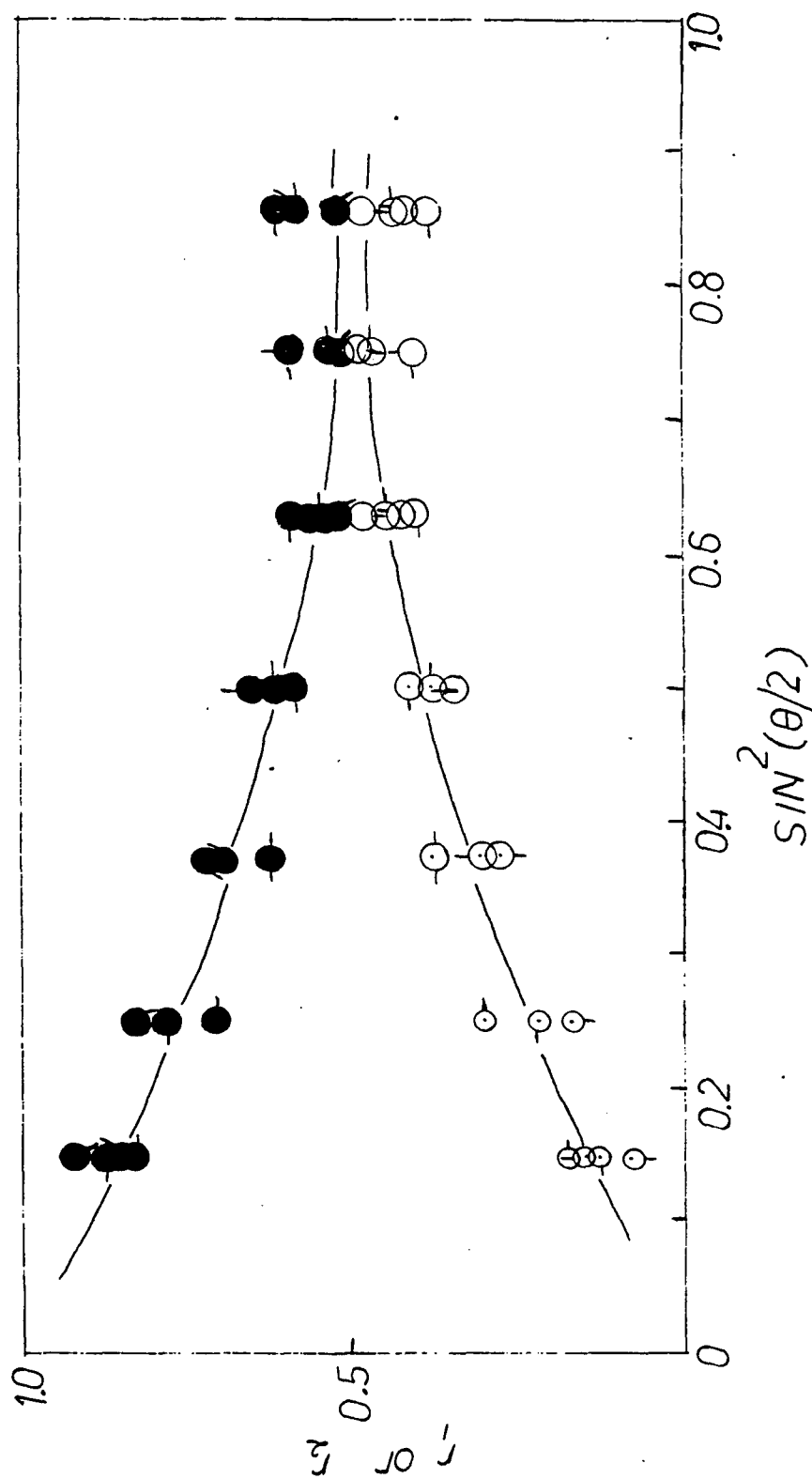


Figure 16:

I_1 and I_2 versus $\sin^2\theta/2$ for solutions of d-PBT in MSA at 30°C; ●, ○; C and -O for C = 0.65, 0.87, 1.21 and 1.93 mg/ml, respectively.

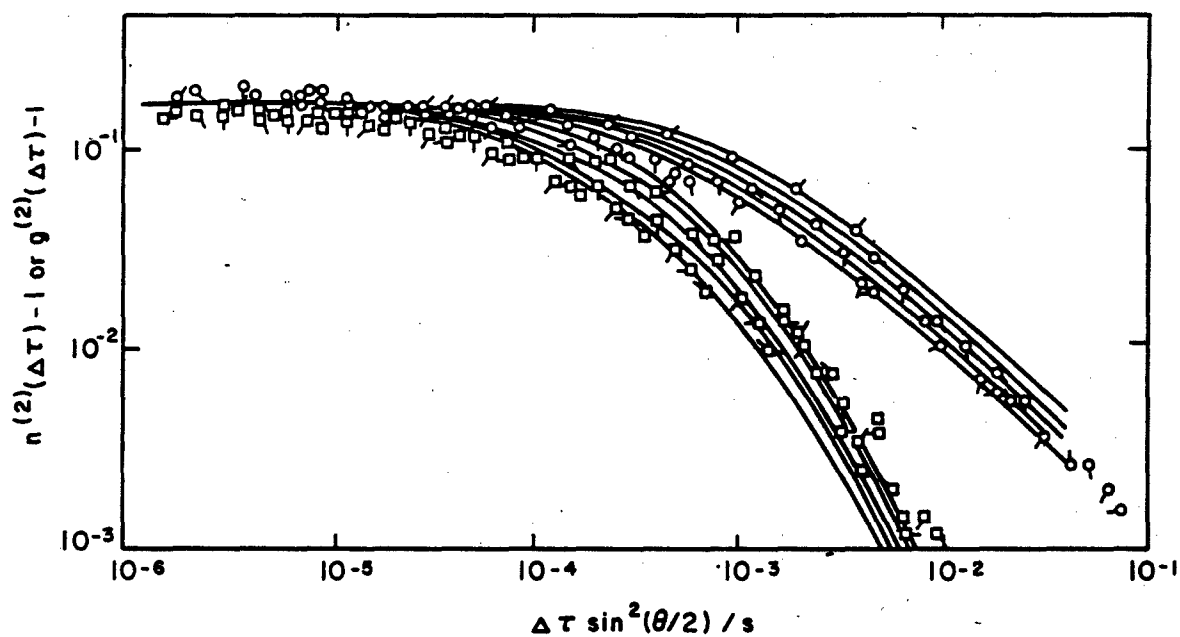


Figure 17:

Comparison of experimental $n^{(2)}(\Delta\tau)$ and $g^{(2)}(\tau)$ with values calculated using $\tau_1^{(h)}, \tau_2^{(h)}$ and r_1, r_2 given in Figs. 15 and 16.

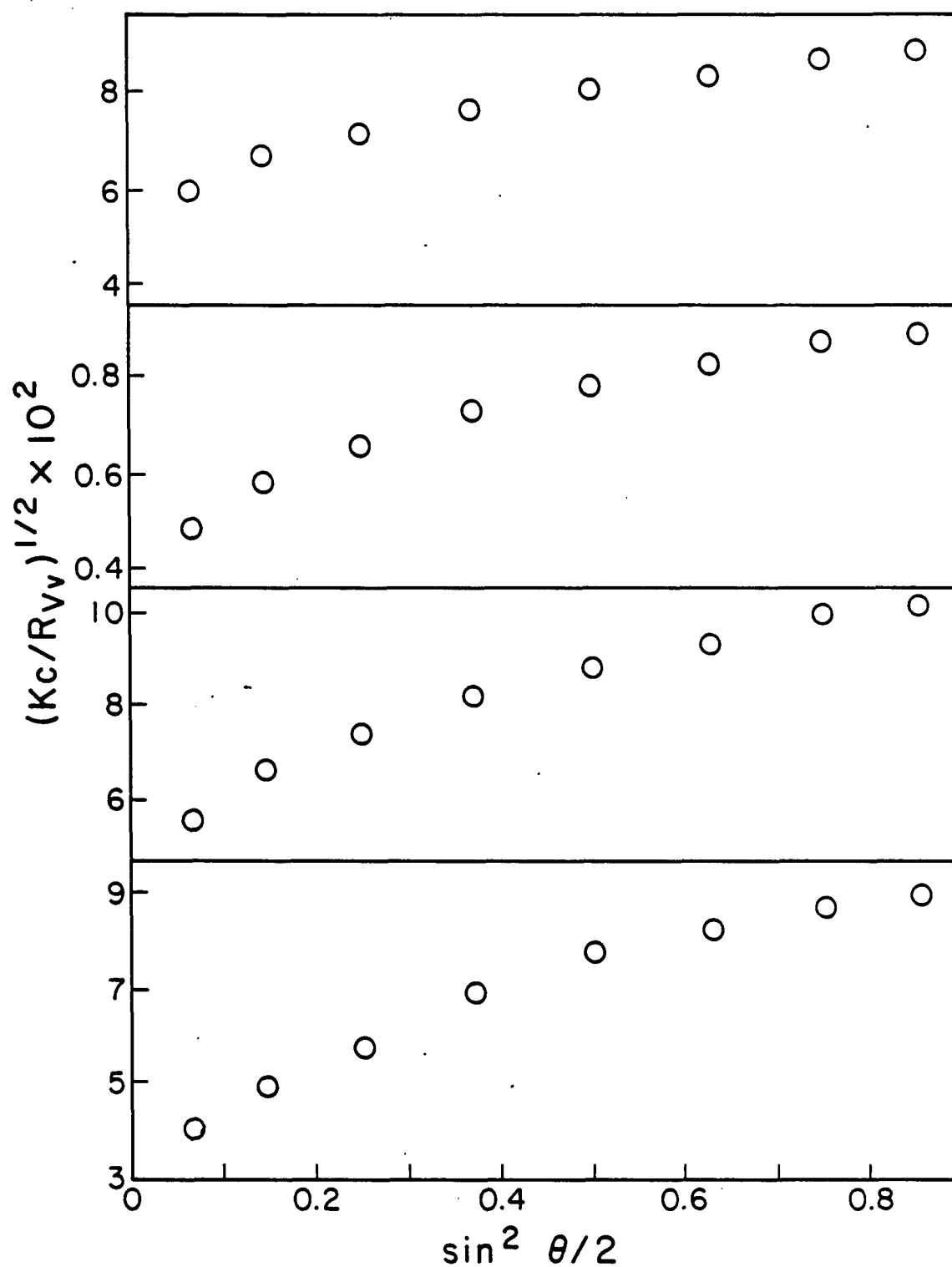


Figure 18:

$(Kc/R_{vv})^{1/2}$ versus $\sin^2 \theta/2$ for solutions of d-PBT in MSA at 30°C (633 nm wavelength); $C = 0.65, 0.87, 1.21, 1.93$ mg/ml from top to bottom.

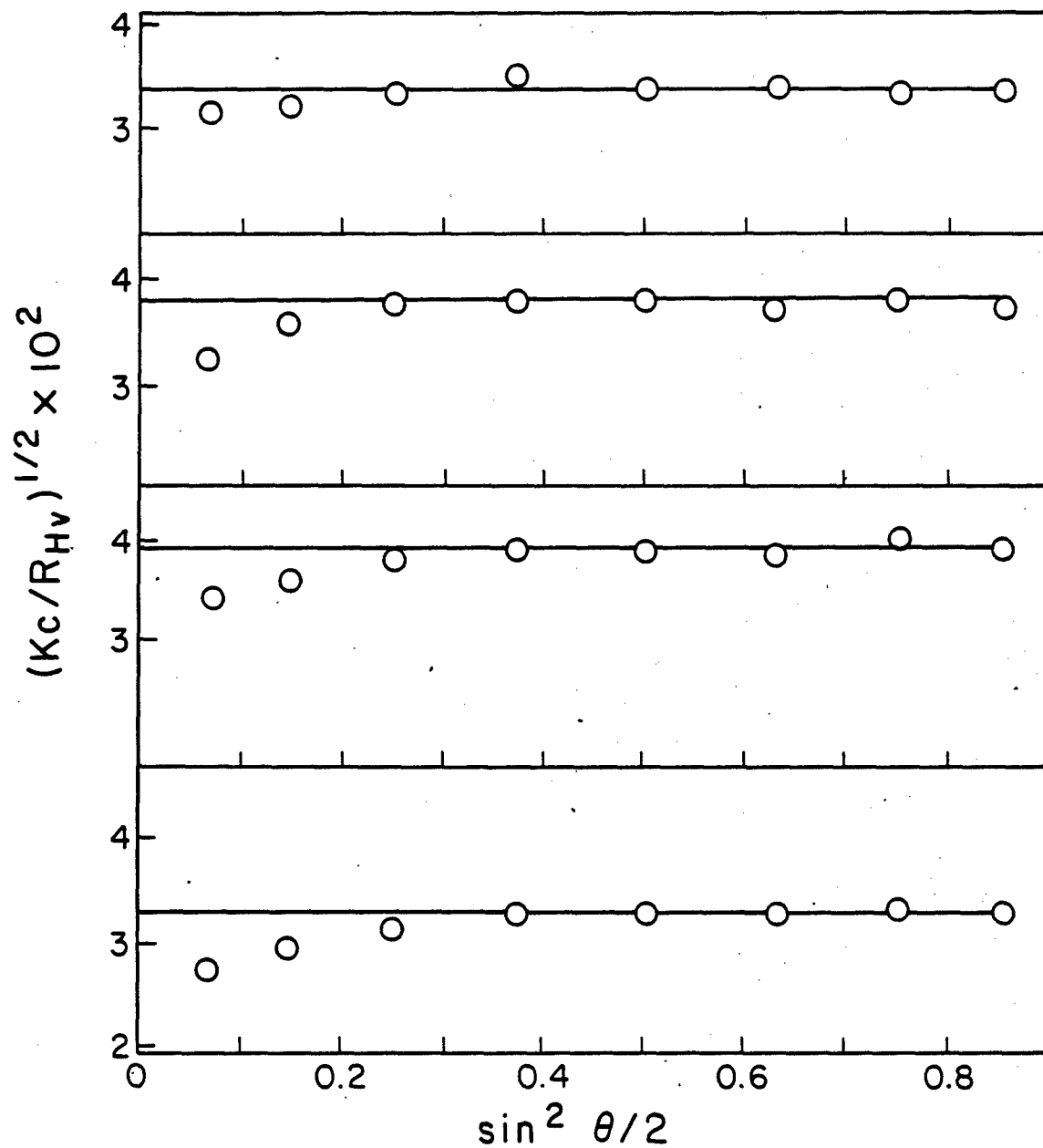


Figure 19:

$(Kc/R_{Hv})^{1/2}$ versus $\sin^2 \theta/2$ for solutions described in Fig. 18.

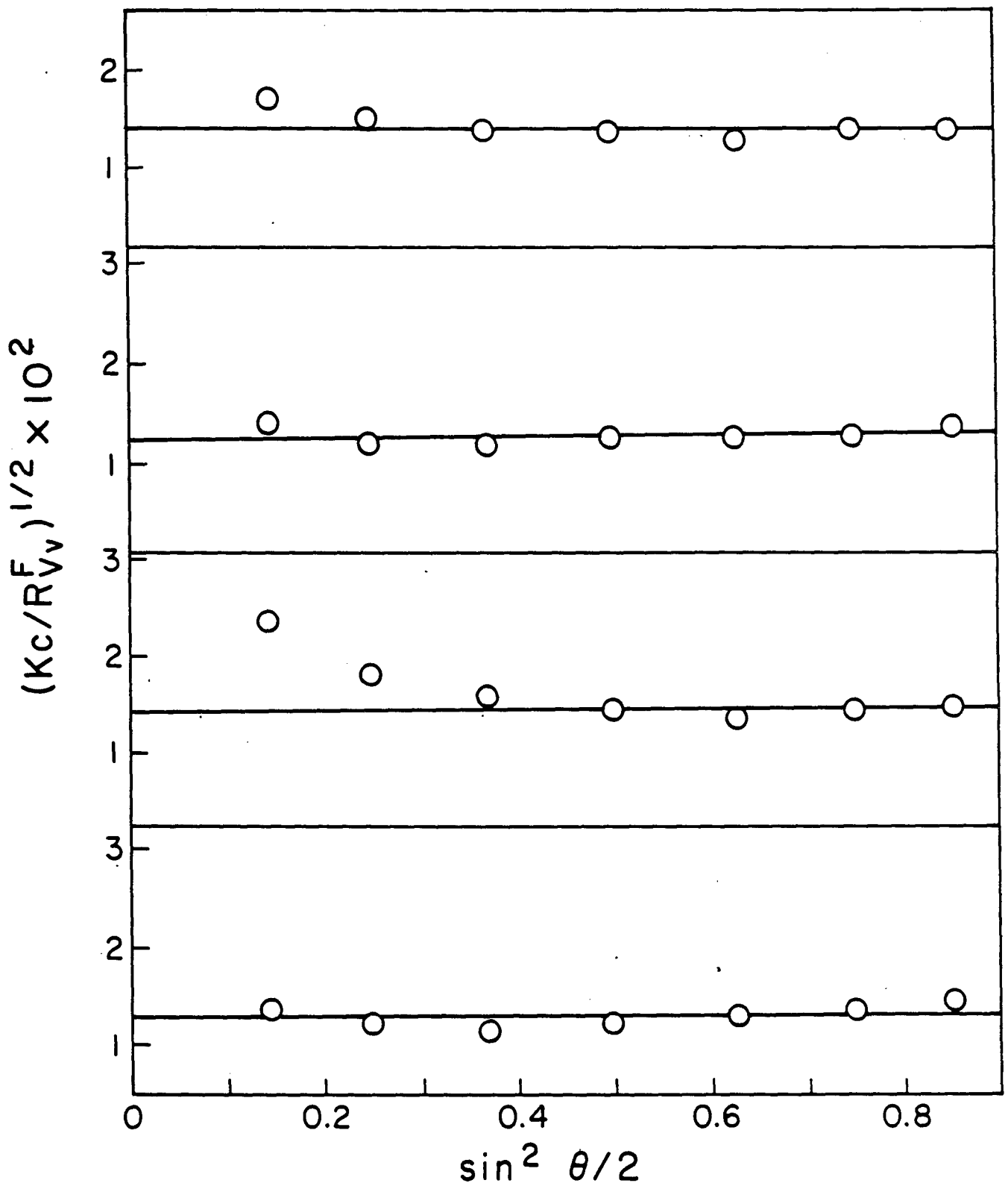


Figure 20:

$[Kc/R_{vv}^F]^{1/2}$ versus $\sin^2 \theta/2$ for solutions described in Fig. 18. R_{vv}^F calculated from R_{vv} as described in text.

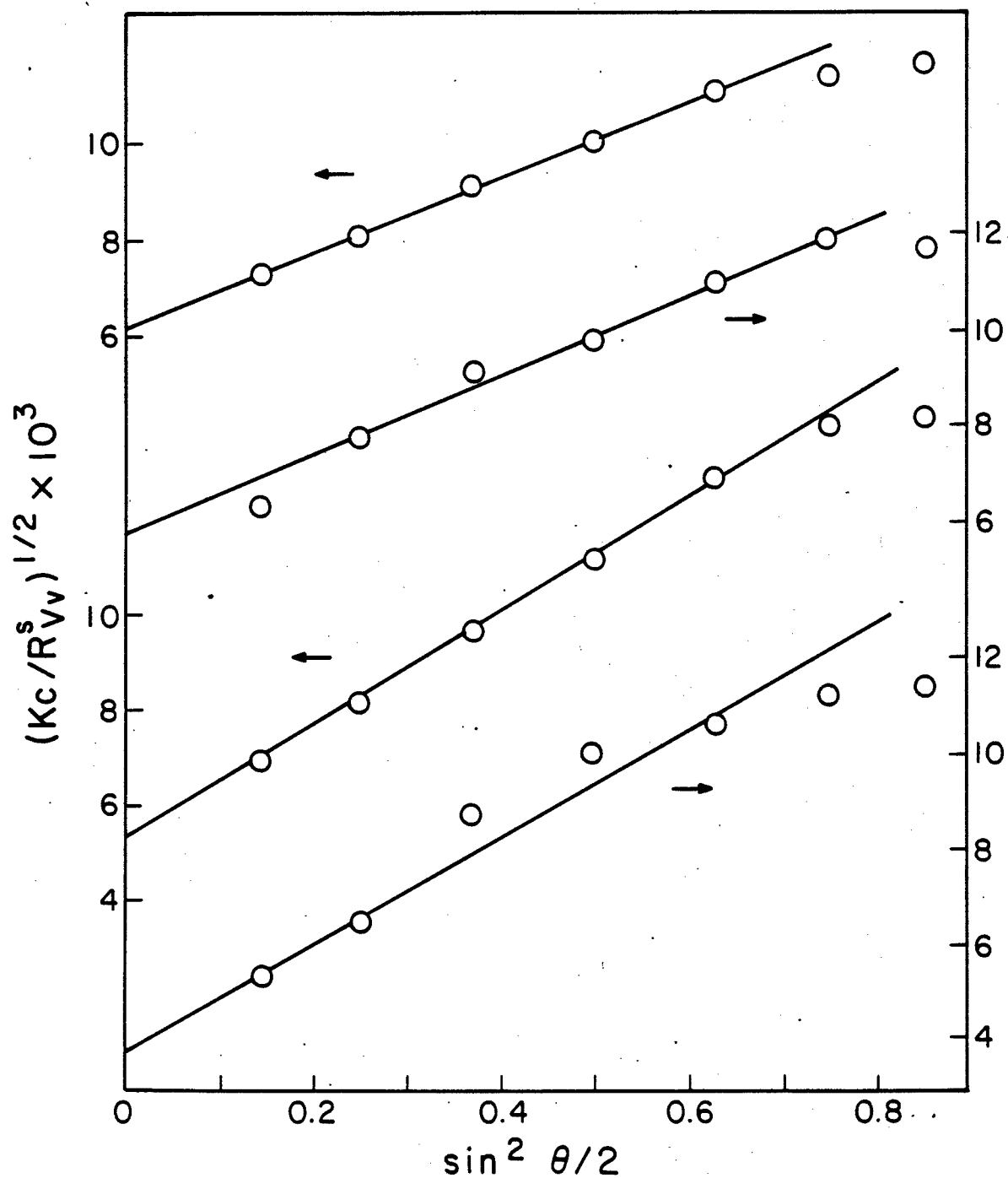


Figure 21:

$[Kc/R_{vv}^{(s)}]^{1/2}$ versus $\sin^2 \theta/2$ for solutions described in Fig. 18. $R_{vv}^{(s)} = R_{vv} - R_{vv}^{(f)}$.

3.4.3 Articulated Polymers

3.4.3.1 Solution Preparation

Stock solutions were prepared by dissolving dried polymer in methanesulfonic acid which had been distilled previously and stored under nitrogen. Unless otherwise noted, the following procedures were used to prepare solutions for study. The solution was centrifuged to remove any large moities; stock solutions were sonicated prior to centrifugation. The clarified solutions were diluted, filtered through filter under nitrogen into light scattering cells which were flame sealed under vacuum after being degassed. Light scattering cells were precleaned by repeated rinsing with filtered acetone, and dried before use. Solutions were examined before and after centrifugation.

3.4.3.2 Light Scattering Results

Integrated intensity light scattering data were obtained with 633 nm wavelength light. Emission spectra were measured with 633 nm incident light to evaluate the fluorescence contribution at 633 nm in comparison with the Hv and Vv scattering. Spectra were obtained using a interference filter with a variable wavelength transmission along its length. as a monochromater. These data were augmented by determination of fluorescence at 650 nm using an interference filter with band-width comparable to the interference filter used to isolate the 633 nm scattering, or an interference filter that alternates light at 633 nm, but has high transmission at other wavelengths (a "band-reject filter"). Similar data were obtained with 514 nm incident light using the monochromater, a 546 nm band-pass filter or a 514 nm band-reject filter.

Photon correlation data were collected as described in previous reports (Vv scattering, with 514 nm light) to give the autocorrelation function

$$g^{(2)}(\tau) = \frac{\langle n(0)n(\tau) \rangle}{\langle n \rangle^2}$$

as a function of the correlation time τ and scattering angle θ , and the second factorial moment.

$$n^{(2)} = \frac{\langle n(n-1) \rangle}{\langle n \rangle^2}$$

as a function of the sampling interval $\Delta\tau$ and θ .

The range of the completed work is given in Table 4. Results are in various stages of completion; in some cases data are fully collected and analyzed, but in other cases analysis is incomplete or more data are to be collected. Spectroscopic data given in Figure 22 show that the maximum extinction coefficient ϵ and the wavelength λ_M for this value both vary with the copolymer composition for the SPBT copolymers with the type IV comonomer (see Section 1). This result is quite welcome since it verifies that the type IV comonomer is incorporated with the sample used--of course, other data do not show that the type IV comonomer is in the chain backbone, as opposed to being in separate chains, but such severe segregation would be unexpected.

Fluorescence spectra are shown in Figure 23. The fluorescence is far more intense for excitation at 514 nm in comparison with 633 nm, but fluorescence is observed even with excitation at 633 nm. The fluorescence prohibits the use of 514 nm wavelength light for Hv total intensity experiments, and make it necessary to correct the Hv total intensity for fluorescence when 633 nm light is used; owing to the larger intensity, the Vv total intensity is not much affected with 633 nm incident light if a 633 nm band pass filter is used in the scattered beam.

Illustrations of results on several articulated polymers are given in Figures 24 to 36. The large upward curvature in the Vv total intensity at small angles illustrated in Figures 30 and 33 indicate the filtered solutions of SPBT-352/36 and 388/7 in MSA contain fractions of large aggregates. Similar behavior was reported for SPBT-352/38 in the previous report. The data in Figure 36 show a smaller effect of aggregation for filtered solutions SPBT-388/12, with the effect further diminished for the centrifuged sample. Those data will be analyzed in detail in a later report when the data for centrifuged samples are available for all of the solutions.

The effects of aggregation noted above for samples SPBT-352/36 and 388/7 are also manifested in the photon correlations data for the autocorrelations function $g^{(2)}(\tau)$ and the second factorial moment $n^{(2)}$. For example, centrifugation tends to result in data with $g^{(2)}(\tau)$ a function only of $\tau \sin^2 \theta / 2$ and $n^{(2)}$ a function only of $\Delta \tau \sin^2 \theta / 2$, whereas with filtered samples this dependence is not obeyed, reflecting a severely polydispersed material. We presume that the polydispersity arises from aggregate structure, see below. In a future report these data will be analyzed in terms of Eqns. 3.10-3.16 to obtain estimates of the size and fraction of the aggregate and the (nearly) molecularly dissolved species.

3.4.3.3 Data Analysis

At this time, data analysis is complete only for two of the polymers studied: SPBT 352/38 and SPBO 352/39. The data on these two polymers exhibited similar behavior in that $g^{(2)}(\tau)-1$ was neither a simple exponential function of $\tau \sin^2 \theta / 2$, nor the same function at all θ , see Figs. 25-26 and 28-29, and $n^{(2)}(\Delta \tau)-1$ was not a single-value function of $\Delta \tau \sin^2 \theta / 2$, see Figs. 25-26 and 28-29. After centrifugation, the data for $g^{(2)}(\tau)-1$ are shifted to smaller $\tau \sin^2 \theta / 2$, as shown in Fig. 28, and $\langle \tau^{(h)} \rangle_N$ is decreased, as shown in Fig. 38.

The coherence factor $f(A)$ was observed to be abnormally small for SPBO 352/39. This suggests the presence of aggregates possessing a time constant so long that it appears to be stationary for the duration of the experiment, e.g., this postulate represents a complication in the data analysis. The digital data processing requires an estimate of the unnormalized correlation function $G^{(2)}(\tau)$ at large τ to compute $g^{(2)}(\tau)$:

$$g^{(2)}(\tau) = \frac{G^{(2)}(\tau) - G^{(2)}(\infty)}{G^{(2)}(\infty)} \quad (3.41)$$

The mean-square count rate $\langle n \rangle^2$ is usually an acceptable measure of $G^{(2)}(\infty)$. However, if a (nearly) stationary source is present, then $\langle n \rangle^2$ will be too large, and consequently $g^{(2)}(\tau)$ calculated with $G^{(2)}(\infty) \sim \langle n \rangle^2$ will be too small. Experimentally, this will appear as an unexpectedly small value of $f(A)$. Since all methods of data analysis are based on a normalized correlation function, this problem is non-trivial. The presence of this long time component is ignored in the present preliminary analysis.

Following the methods described in detail in Section 3.4.2.2 Eqn. 3.34 can be used to extract information on the components in $g^{(2)}(\tau)$. In this case, the relation between r_i and the concentration c_i and molecular weight M_i of the components with coherence time $\tau_{h,i}$ is complex, but need not be known to attempt assessment of a resolution of $g^{(2)}(\tau)$ into representative components. If the $\tau_{h,i}$ are sufficiently widely spaced then $[g^{(2)}(\tau)-1]^{1/2}$ may be decomposed into a sum of exponentials by simple graphical methods or computer-aided analysis. Thus, $\ln[g^{(2)}(\tau)-1]$ versus τ is a linear function (within experimental error) for large τ , permitting assessment of the longest coherence time $\tau_{h,1}$ and the weight r_1 . Subsequent analysis of $\ln\{[g^{(2)}(\tau)-1]^{1/2} - f^{1/2} r_1 \exp - \tau / \tau_{h,1}\}$ versus τ permits evaluation of $\tau_{h,2}$ and r_2 , etc., until the residual between $[g^{(2)}(\tau)-1]^{1/2}$ and $f^{1/2} \sum_i r_i \exp - \tau / \tau_{h,i}$ at small τ is within experimental error—this method is exactly that of "Procedure X" used to represent stress relaxation data. This procedure provides a method to represent the component contributions to

$g^{(2)}(\tau)$ with minimal computational effort, and will usually provide a reasonable representation within the limits of the data. The graphical method is not suitable to represent components with closely spaced $\tau_{h,i}$ in a meaningful way (e.g., to accurately represent the molecular weight distribution of a polymer). The uniqueness of the representation is strongly dependent on the behavior of the large τ and the accuracy to which $\tau_{h,i}$ and r_i may be obtained.

Values of $\langle \tau_h \rangle_K$, $\langle \tau_h \rangle_N$, $\tau_{h,1}$ and $\tau_{h,2}$, all multiplied by $\sin^2 \theta / 2$ are given in Figs. 40 and 41 for one of the four concentrations studied for each system—data for other concentrations were similar. Corresponding values of r_1 , r_2 are given in Figs. 37 and 39. For the uncentrifuged samples of SPBO 39, both $\langle \tau_h \rangle_K \sin^2 \theta / 2$ and $\langle \tau_h \rangle_N \sin^2 \theta / 2$ increased markedly with decreasing θ , whereas $\tau_{h,1} \sin^2 \theta / 2$ and $\tau_{h,2} \sin^2 \theta / 2$ were sensibly constant (see Fig. 7). The latter behavior indicates that the pseudo-binary component distribution used to treat the data provides a reasonable representation, at least for the solution for which the data are given in Fig. 38. In fact, the pseudo-binary approximation was satisfactory approximation for the SPBT 38 solutions and all of the centrifuged SPBO 39 solutions, but was not adequate for some of the uncentrifuged SPBO 39 solutions. For the latter, it may be necessary to introduce a third component, with a very long relaxation time.

As seen by comparison of Fig. 38, after filtration the variation of $\langle \tau_h \rangle_K \sin^2 \theta / 2$ and $\langle \tau_h \rangle_N \sin^2 \theta / 2$ with θ is lessened, and the disparity between $\tau_{h,2}$ and $\tau_{h,1}$ is decreased—the latter is due to a marked decrease in $\tau_{h,1}$, since $\tau_{h,2}$ (the smaller time constant) is decreased relatively less after centrifugation. Unexpectedly, the relative fraction r_1 of light scattered due to the component with time constant $\tau_{h,1}$ is increased after centrifugation. These results reveal that the pseudo-binary distribution used to represent uncentrifuged SPBO 39 solutions is too simple, e.g., centrifugation apparently preferentially removed some extremely large aggregate components, but also removed species over a wide range of $\tau_{h,i}$, leaving a new distribution which we here again treat in simplified form as pseudo-binary.

The dependence of $\tau_{h,1} \sin^2 \theta / 2$ and $\tau_{h,2} \sin^2 \theta / 2$ on concentration is shown in Figs. 40 and 41 for the uncentrifuged solutions of SPBT 38 and the centrifuged SPBO 39 solutions, respectively. For both polymers, $\tau_{h,2} \sin^2 \theta / 2$ is relatively independent of c , which is typical behavior. The significance of the variation of $\tau_{h,1} \sin^2 \theta / 2$ with c is less clear—with SPBO 39 solutions, the peculiar dependence may suggest appreciable change in the aggregate structure with c .

Since the Hv scattering was small or zero, see below, the Vv scattering data was analyzed with expression for an isotropic solute. Based on the chemical structure, the

articulated polymers are expected to have rodlike segments separated by rotatable units. The molecular anisotropy should result in Hv scattering appropriate to the rodlike segments. Consequently, the Hv scattering is expected to be small, corresponding to the chain length of the rodlike sequences. The relations for the Vv scattering are

$$\left[\frac{KcM}{R_{Vv}(\theta)} \right]^0 = 1 + \frac{1}{3} R_G^2 h^2 + \dots + O(R_G^2 h^2)^2 \quad (3.42)$$

$$\left[\frac{KcM}{R_{Vv}(0)} \right] = 1 + 2 A_2 Mc + O(c^2) \quad (3.43)$$

with A_2 the second virial coefficient and R_G the root-mean square radius of gyration.

With solutions of both polymers, centrifugation tended to result in reduced scattering at small θ , and sometimes increased the extrapolated $Kc/R_{Vv}(0)$ as well, e.g., Figs. 12-15. With both polymers, the extrapolated value $(Kc/R_{Vv}(0))^0$ is far too small to be attributed to true molecular scattering (e.g., the data give $M_w \sim 10^6$). After all the data are collected, an analysis similar to that described in the previous quarterly report will be attempted to permit assessment of M_w for the completely dissolved polymer and M_w for the aggregate structure.

The Hv scattering for SPBT 38 was negligible, but an apparent Hv scattering was observed for SPBO 39. Since the intensity observed was very small and, comparable to the fluorescence intensity interpolated from the fluorescence spectrum. Consequently, at this time, the apparent Hv scattering has not been utilized.

Table 4: EXPERIMENTS ON DILUTE SOLUTIONS OF ARTICULATED COPOLYMERS IN METHANE SULFONIC ACID^(a)

Sample	-Ar-	$n^{(b)}$ (Fraction-Ar-)	η_{sp}	R_{Vv}	R_{Hv}	R^{Fl}	$g^{(2)}$	$n^{(2)}$
SPBT 352/38	IV	0.05	0	4F	4F	4F	4F	4F
				4C	4C	4C	4C	4C
SPBT 352/36	IV	0.10	8F	4F	4F	4F	4F	4F
			8F	1C	1C	1C	4C	4C
SPBT 388/7	IV	0.15	0	4F	4F	4F	4F	4F
				2C	2C	2C	4C	4C
SPBT 388/12	IV	0.20	0	4F	4F	4F	0	0
				4C	4C	4C	0	0
SPBO 352-39	IV	0.05	0	4F	4F	4F	4F	4F
				4C	4C	4C	4C	4C
SPBO 352/4	I	0.10	7F	4F	4F	4F	4F	4F
				4C	4C	4C	4C	4C
SPBO 292/96	III	0.05	5F	4F	4F	4F	4F	4F
				4C	4C	4C	4C	4C

(a) Numbers tabulated give the number of concentrations examined; suffix F and C indicate sample filtered and sample filtered and centrifuged, respectively.

(b) See text.

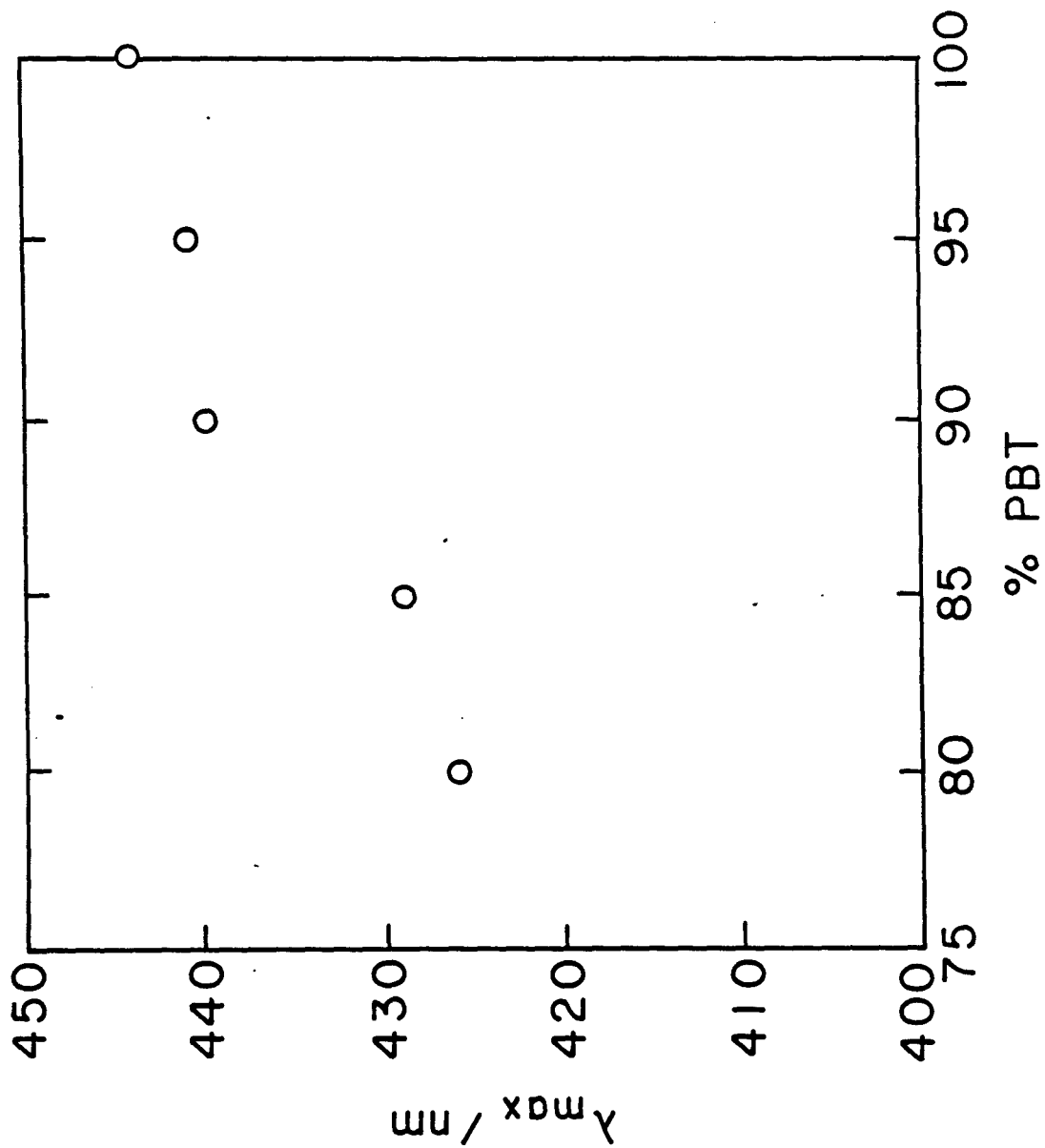


Figure 22:

λ_{max} vs % PBT for the series SPBT-35-38 (95%), SPBT-352-36 (90%), SPBT-388-7 (85%), SPBT-388 (80%) in MSA.

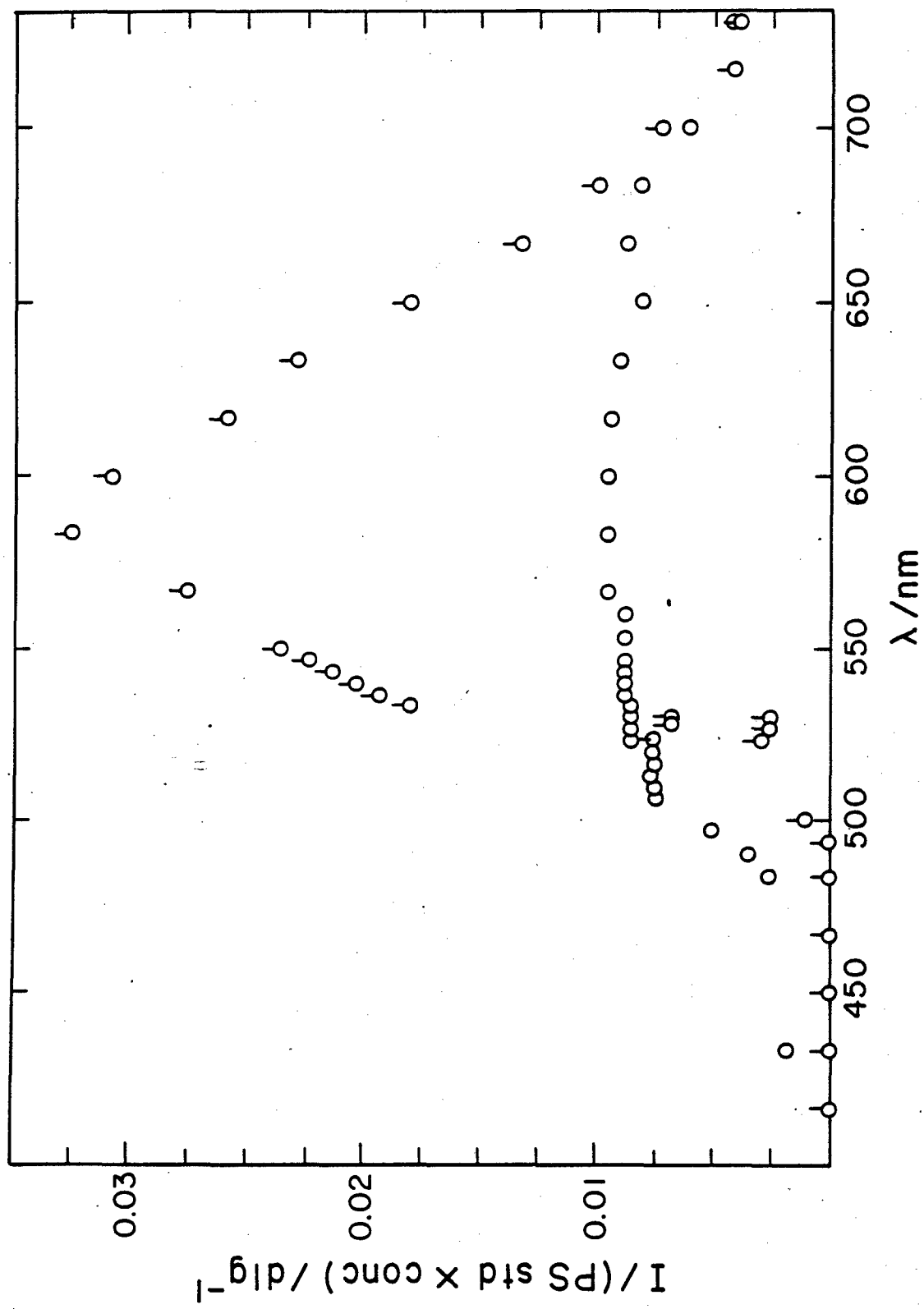


Figure 23:

Emission spectra excited by 514 nm source. I/I_{std} conc (dl/g) vs λ (nm). \odot SPBT-388-12/MSA 0.788 g/L, O SPBT-352-38/MSA 0.506 g/L.

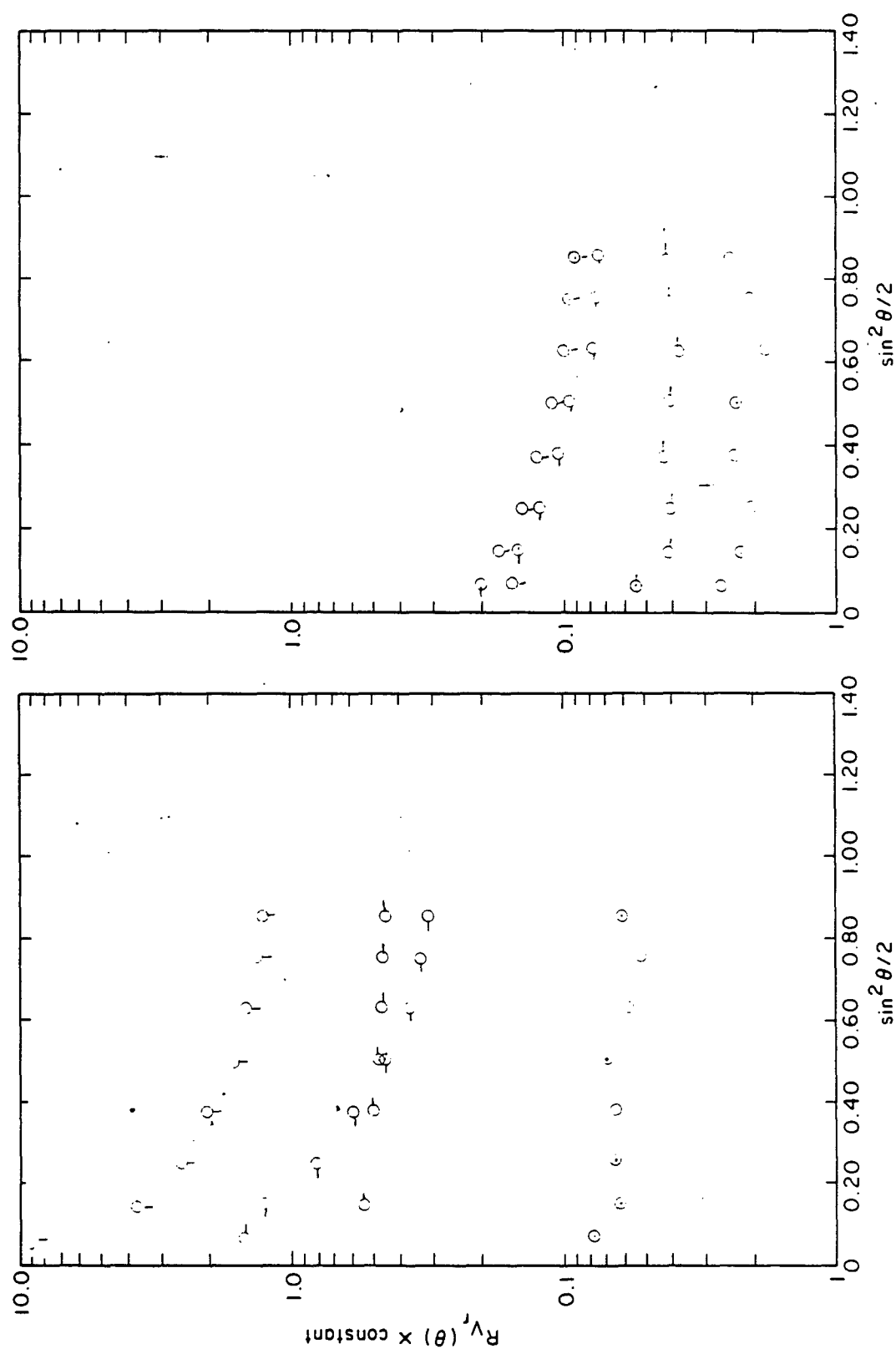


Figure 24:

Absolute intensity light scattering data for filtered SPBO-352-39 in MSA at 633 nm. \circ 0.494 g/L, \circ 0.363 g/L, \circ 0.204 g/L, \circ 0.106 g/L. a) filtered b) filtered and centrifuged

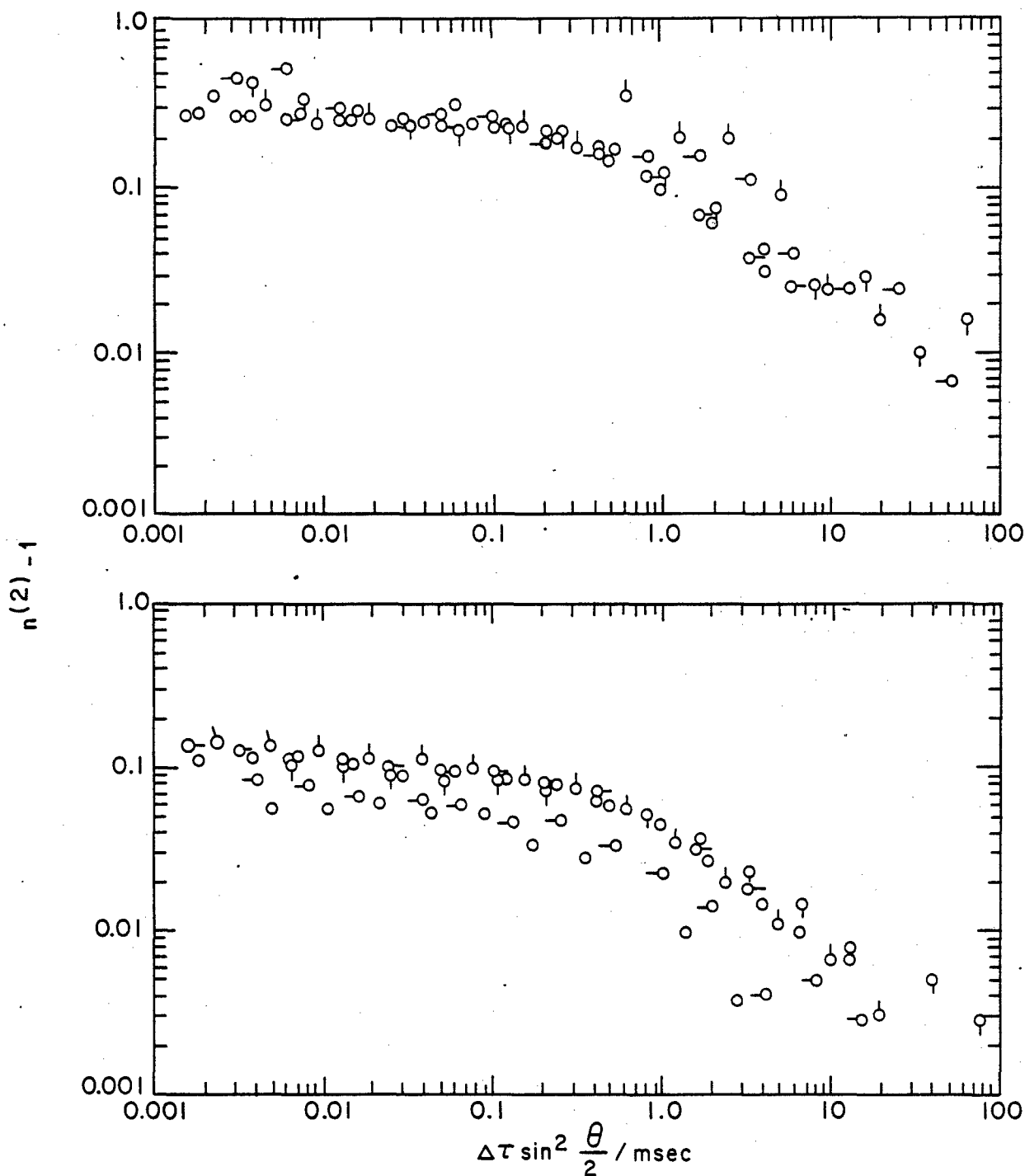


Figure 25:

Photon correlation light scattering data for filtered (top) and filtered and centrifuged (bottom) of SPBO-352-39/MSA 0.106 g/L. \circ 45°, \circ 60°, \circ 75°, \circ 90°, \circ 105°, \circ 120°, \circ 135°.

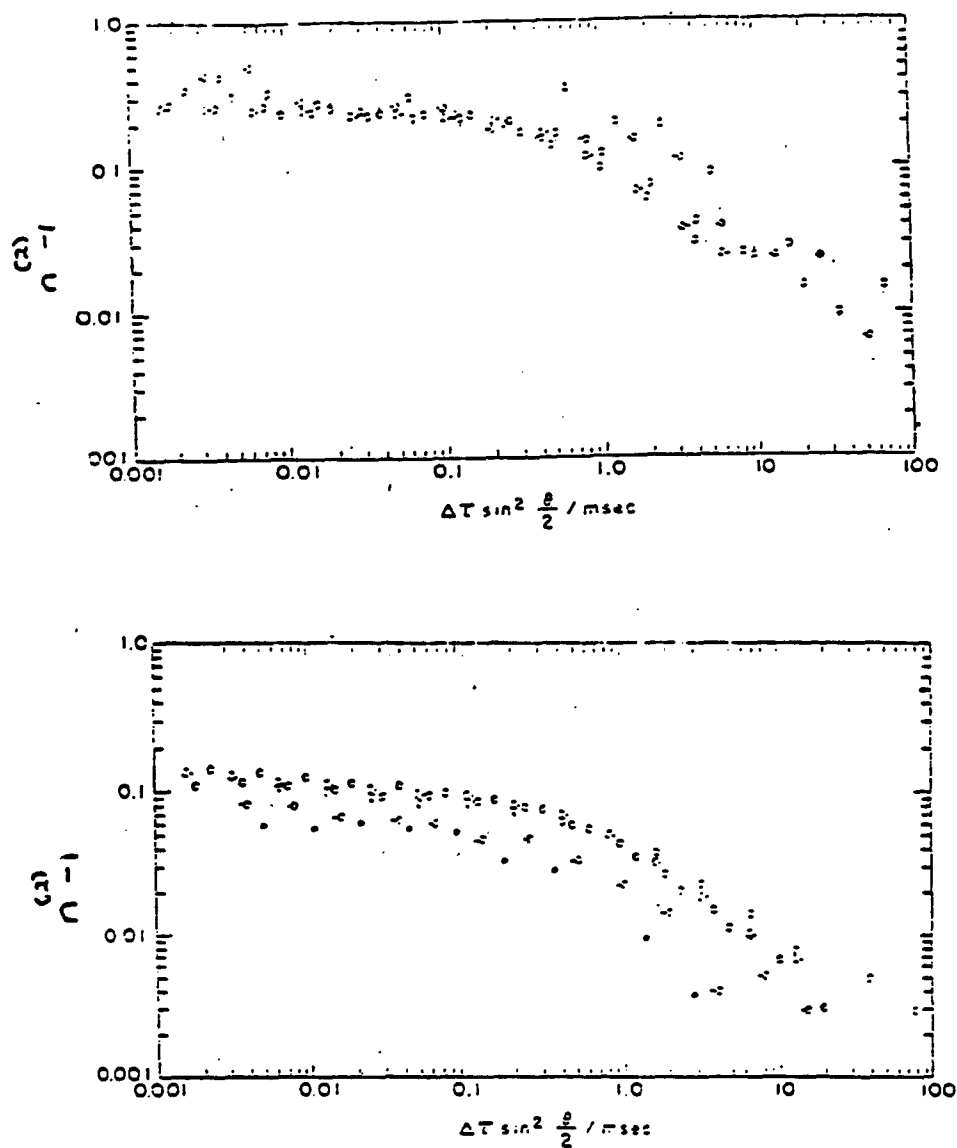


Figure 26:

Photon correlation light scattering data for filtered (top) and filtered and centrifuged (bottom) of SPBO-352-39/MSA 0.494 g/L, \circ 45°, \circ 60°, \circ 75°, \circ 90°, \circ 105°, \circ 120°, \circ 135°.

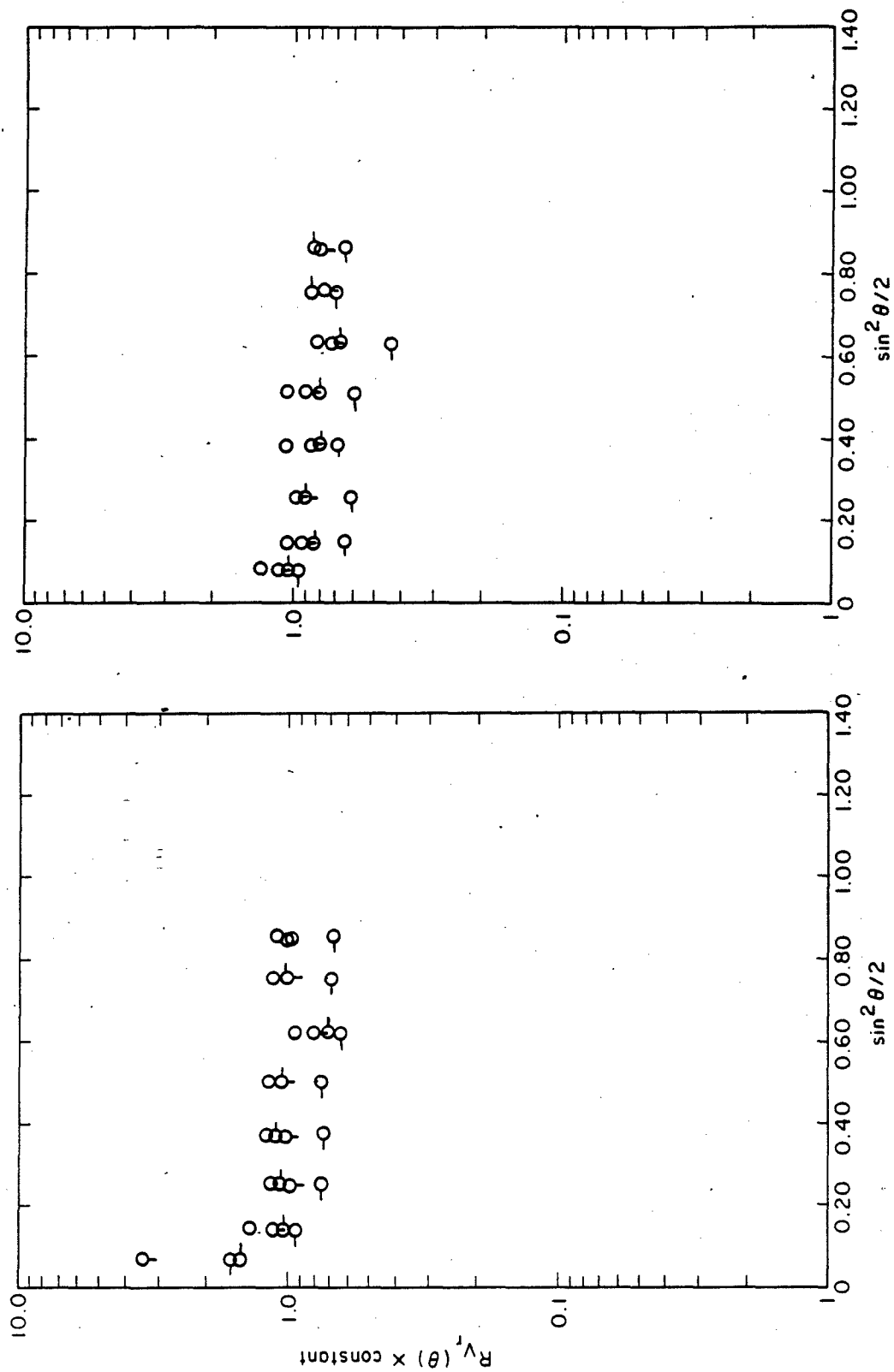


Figure 27:

Absolute intensity light scattering data for filtered SPBT-352-38/MSA at 514 nm, O 0.506 g/L, O• 0.374 g/L, O 0.267 g/L, O• 0.105 g/L. a) filtered b) filtered and centrifuged

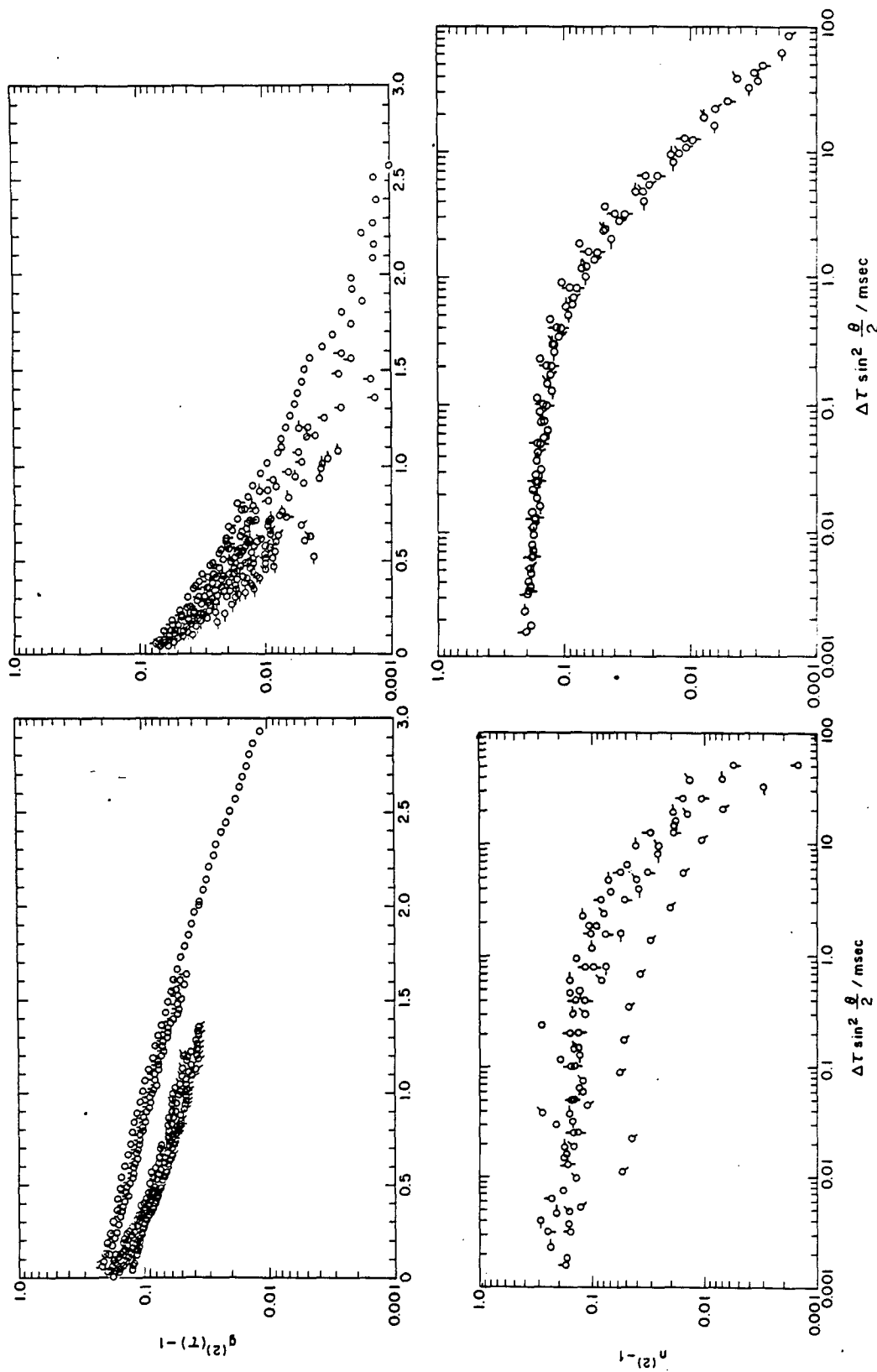


Figure 28:

Photon correlation light scattering data for filtered (top) and centrifuged (bottom) of SPBT-352-38/MSA . 0.108 g/L. \circ 45°, \circ 60°, \circ 75°, \circ 90°, \circ 105°, \circ 120°, \circ 135°.

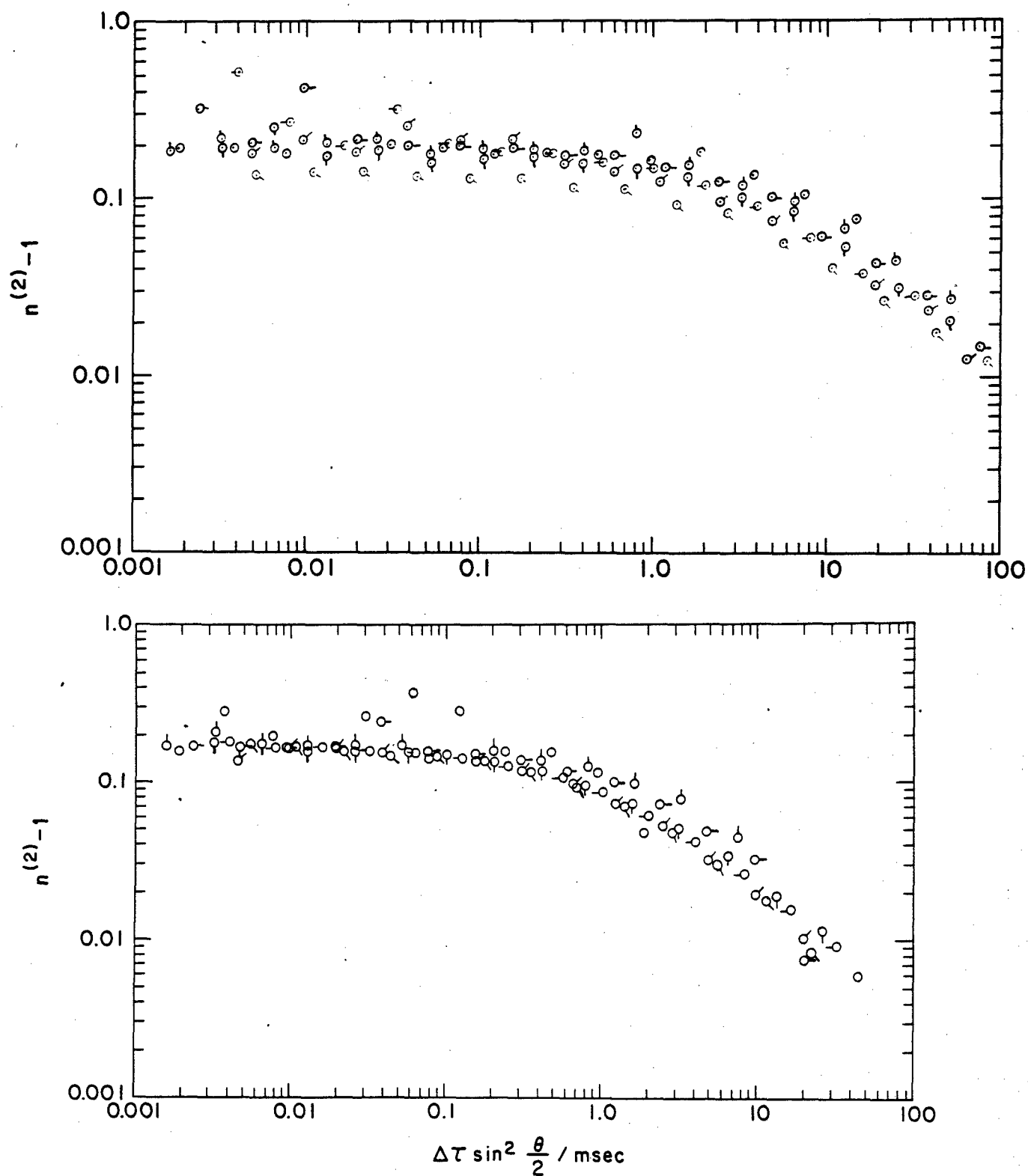


Figure 29:

Photon correlation light scattering data for filtered (top) and filtered and centrifuged (bottom) of SPBT-352-38/MSA, 0.506 g/L, \circ 45°, \circ 60°, \circ 75°, \circ 90°, \circ 105°, \circ 120°, \circ 135°.

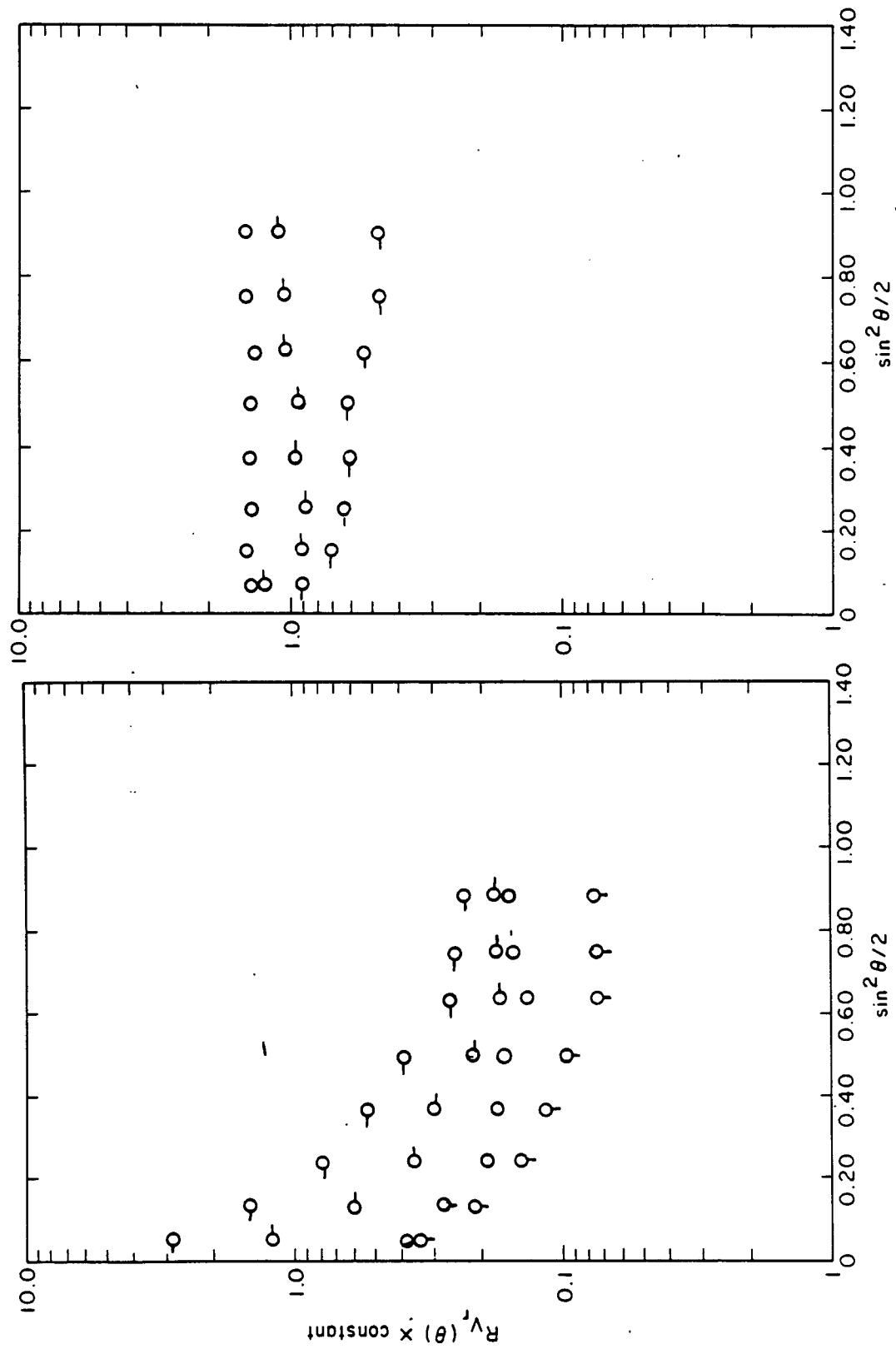


Figure 30:

Absolute intensity light scattering data for SPET-352-36 in MSA at 633 nm. O
 * = 0.576 g/L, O-0.378 g/L, Q 0.201 g/L, -O 0.0998 g/L. a) filtered b) filtered
 and centrifuged

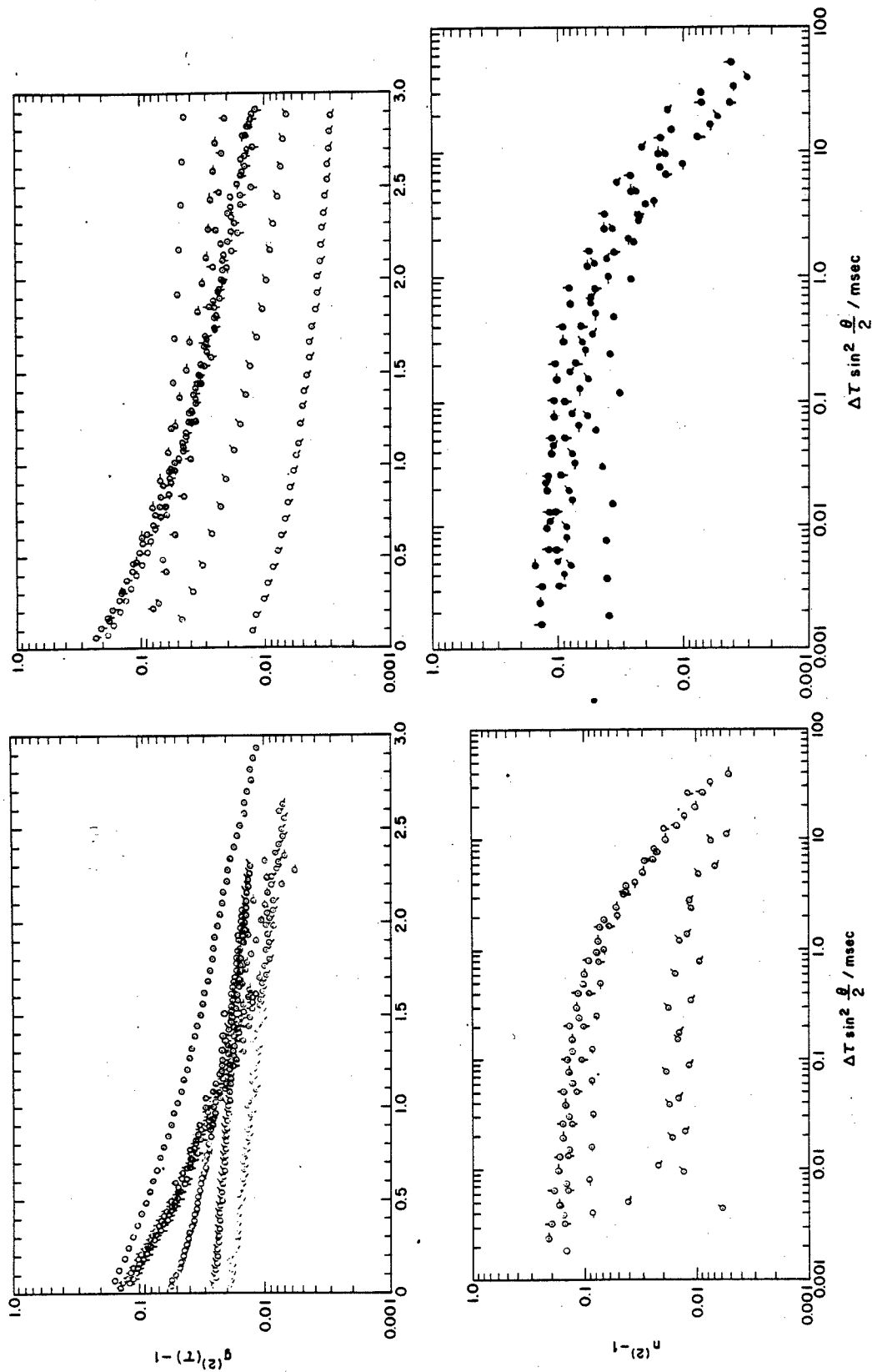


Figure 31:

Photon correlation light scattering for filtered (top) and centrifuged (bottom) of SPBT-352-36/MSA, 0.0998 g/L, O 45° , □ 60° , O 90° , □ 105° , O 120° , O 135° .

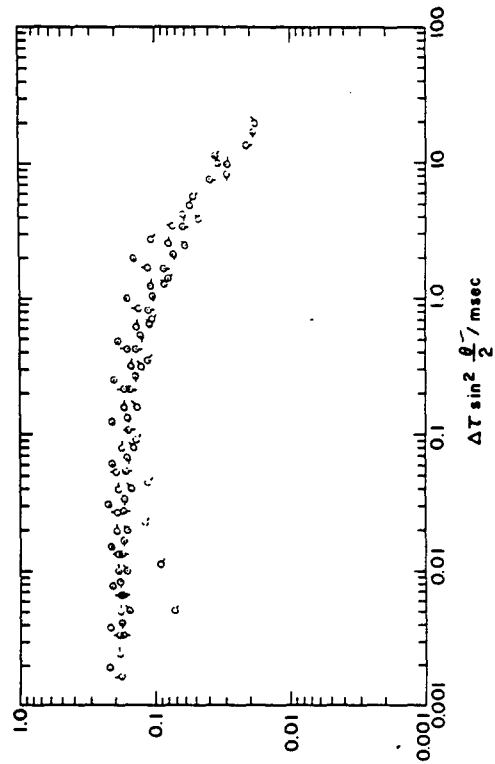
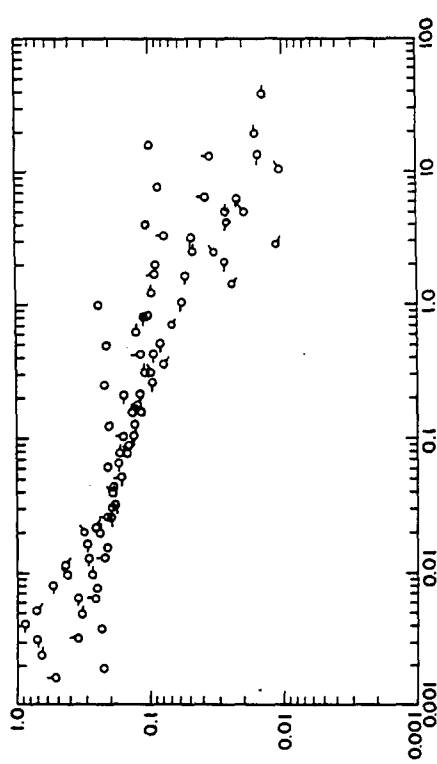
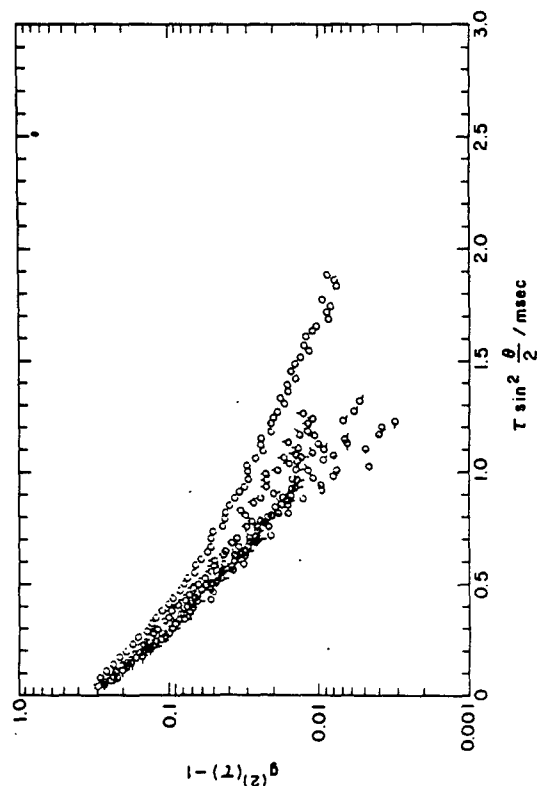
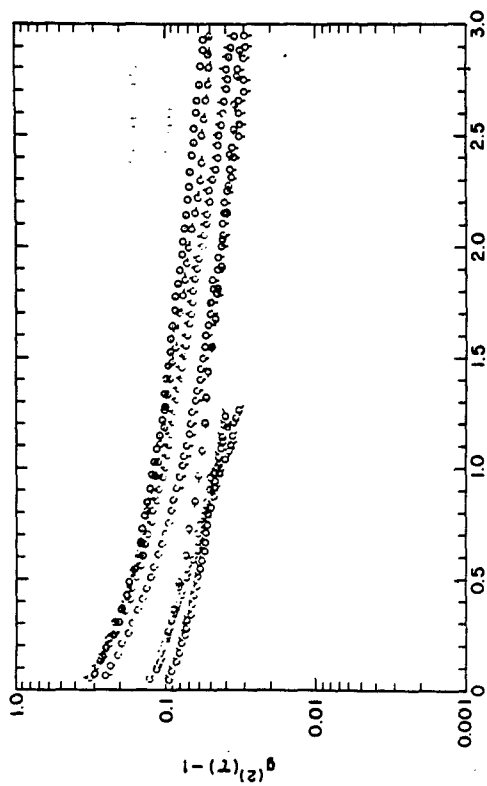


Figure 32:

Photon correlation light scattering data for filtered (top) and filtered and centrifuged (bottom) of SPBT-352-36/MSA 0.516 g/L, O 45°, O 60°, O 75°, Q 90°, O 105°, O 120°, Q 135°.

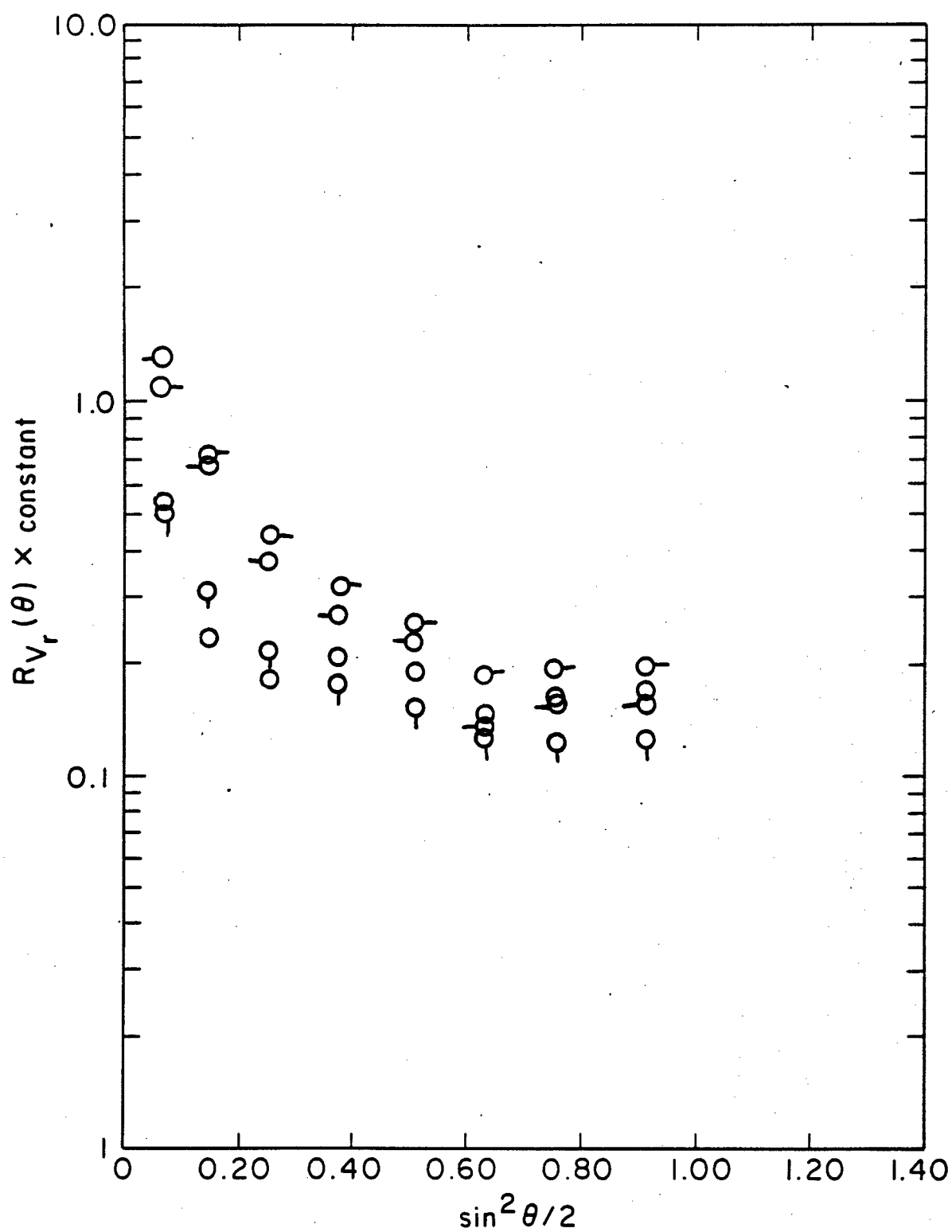


Figure 33:

Absolute intensity light scattering data for filtered SPBT-388-7/MSA at 633 nm. O 0.558 $^\circ$ /L, □ 0.378 $^\circ$ /L, △ 0.266 $^\circ$ /L. -O 0.114 $^\circ$ /L.

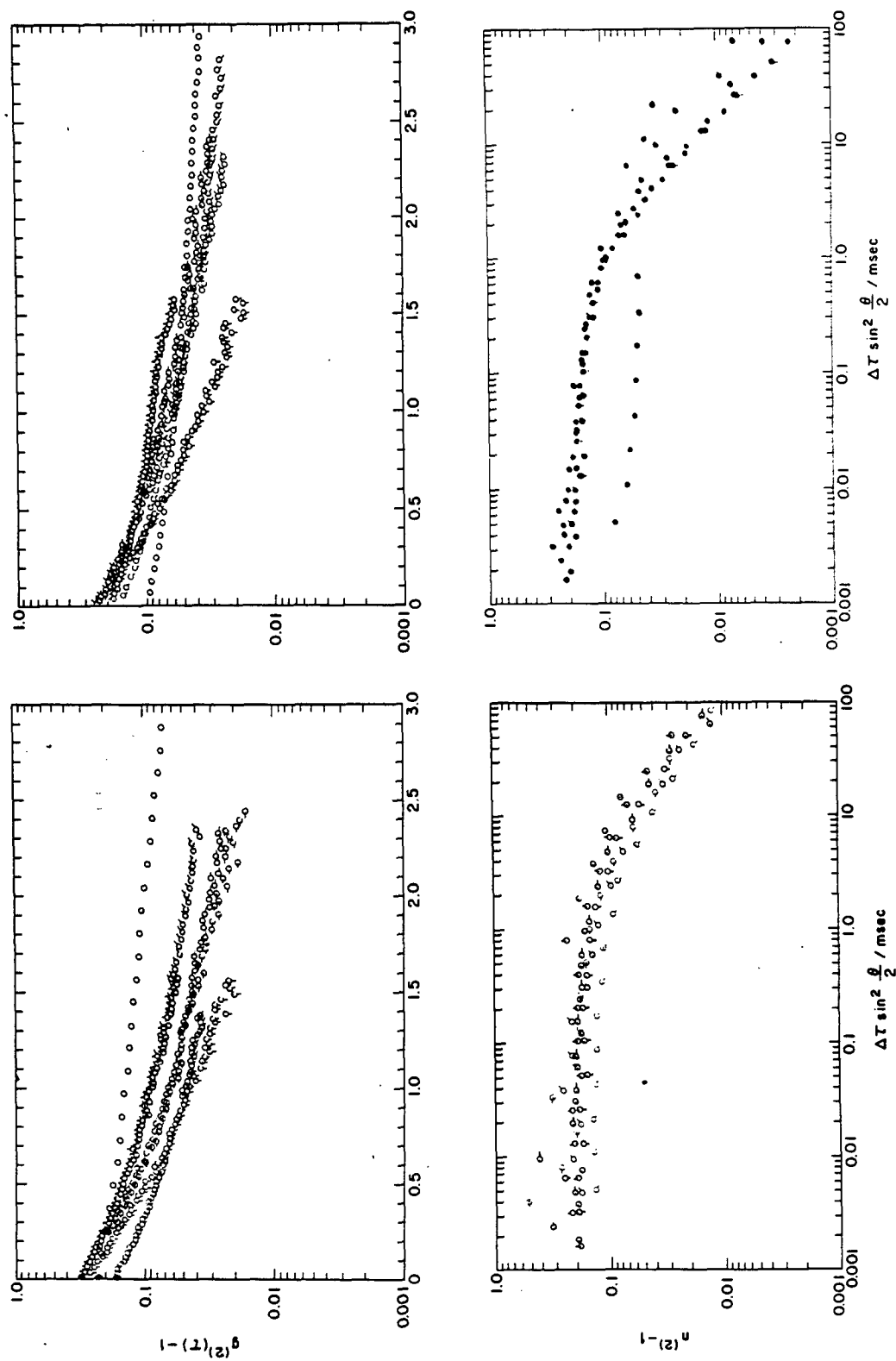


Figure 34:

Photon correlation light scattering data for filtered (top) and filtered and centrifuged (bottom) of SPBT-388-7/MSA, 0.114 g/L, \circ 45° , \circ 60° , \circ 75° , \circ 90° , \circ 105° , \circ 120° , \circ 135° .

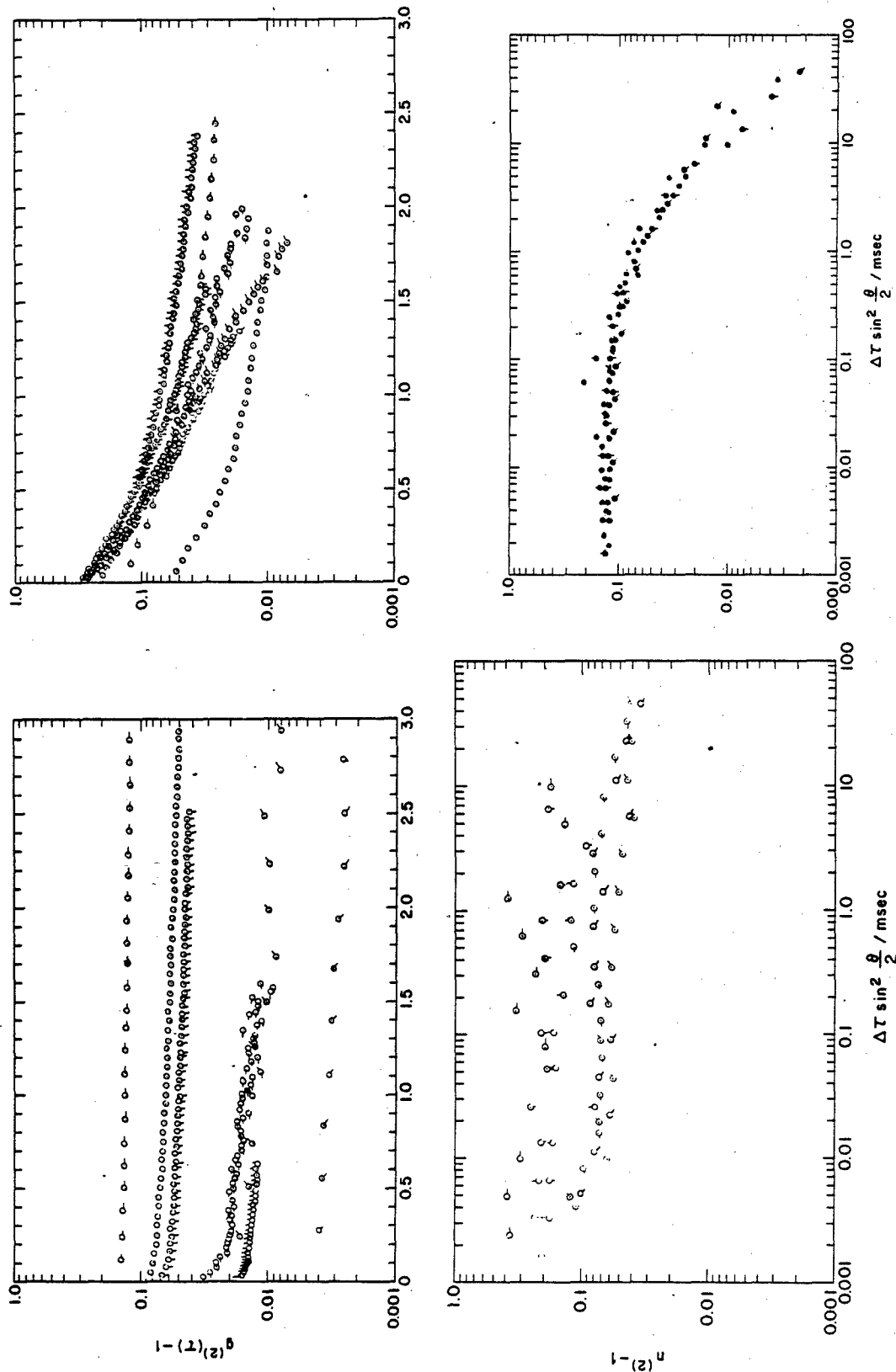


Figure 35:

Photon correlation light scattering data for filtered (top) and filtered and centrifuged (bottom) of SPBT-388-7/MSA 0.558 g/L, \circ 45° , \odot 60° , \otimes 75° , \oplus 90° , \odot 105° , \otimes 120° , \oplus 135° .

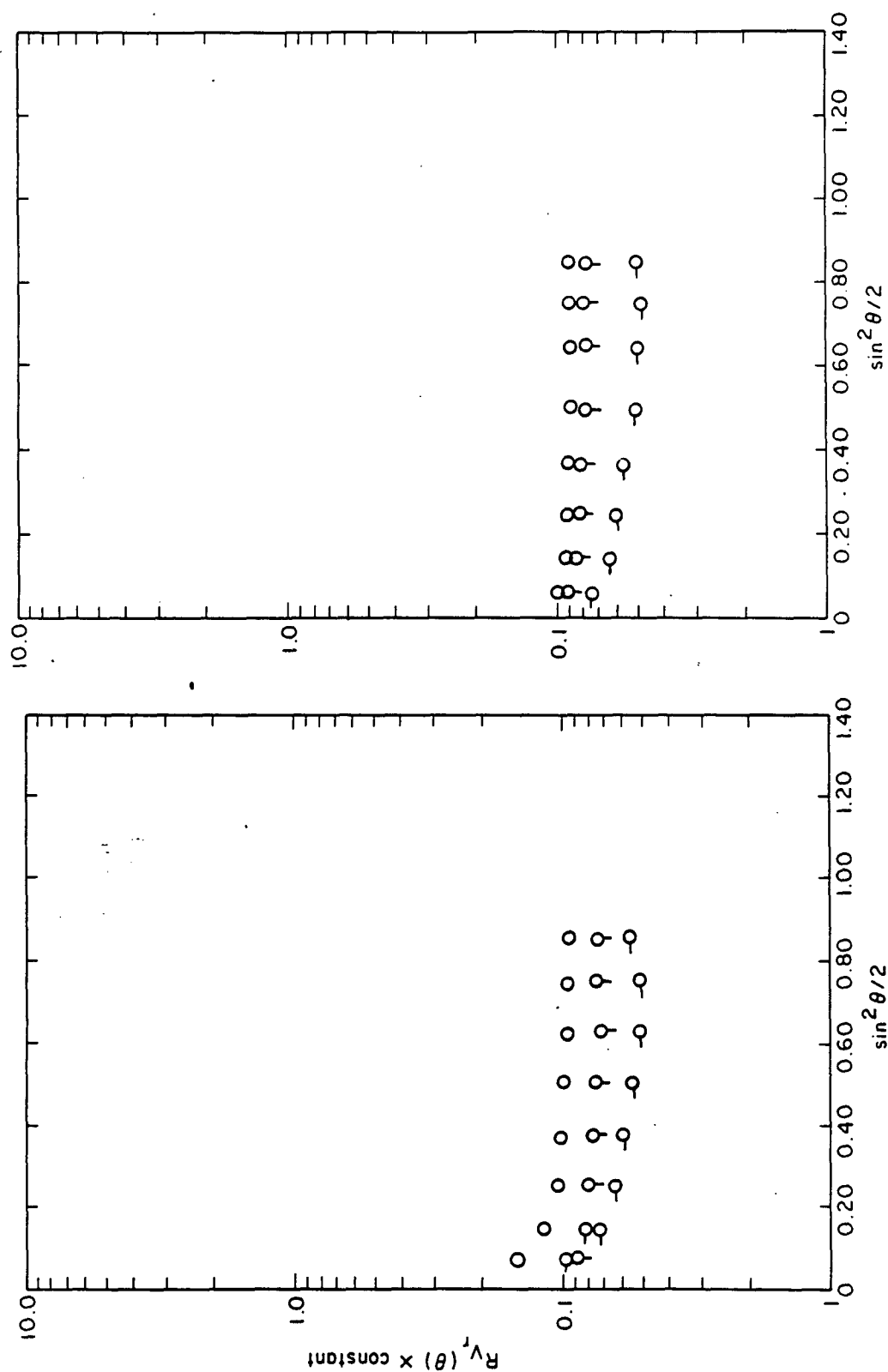


Figure 36:

Absolute intensity light scattering for filtered SPBT-355-12/MSA at 574 nm, O
 0.785 g/L, □ 0.45513 g/L, □ 0.3295 g/L, O 0.116 g/L. a) filtered b) filtered
 and centrifuged

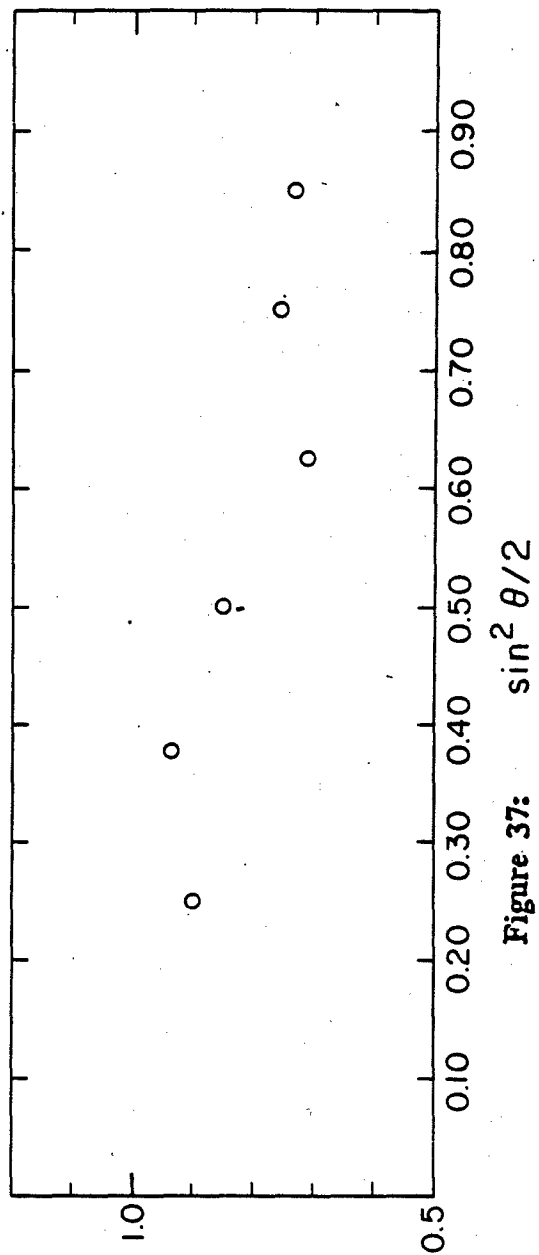
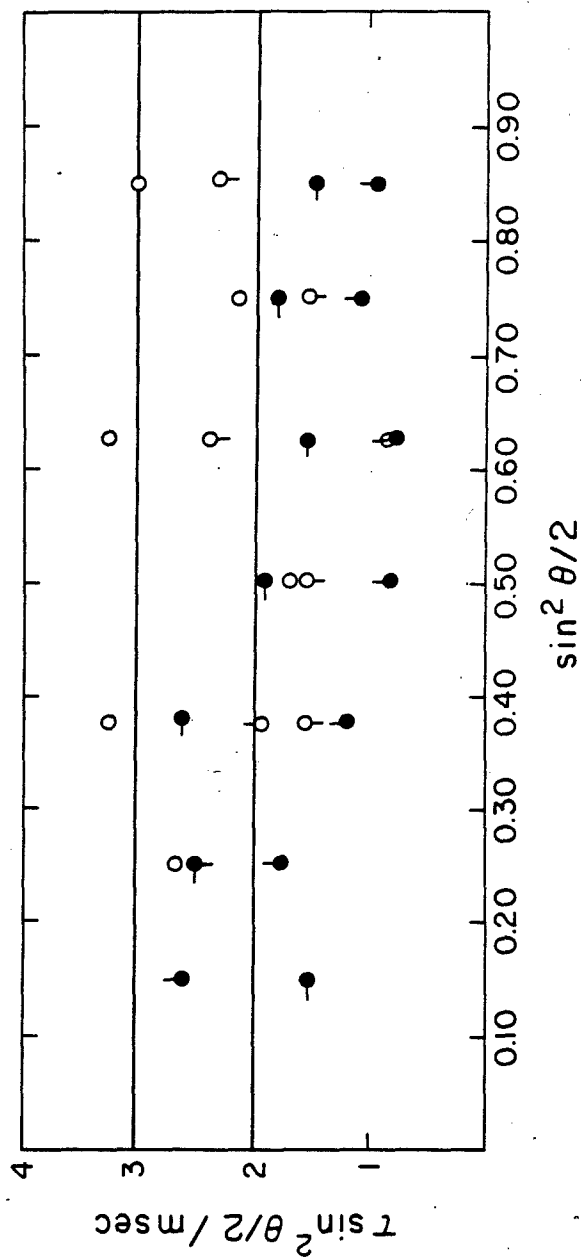


Figure 37: $\sin^2 \theta / 2$

a) Relaxation times, multiplied by $\sin^2 \theta / 2$, for a solution of SPBT-352-38/MSA (0.108 g/L) as a function of $\sin^2 \theta / 2$. \circ $\tau_1 \sin^2 \theta / 2$, $\circ \cdot$ $\tau_2 \sin^2 \theta / 2$, \bullet $\tau_3 \sin^2 \theta / 2$. b) The weight factors r_i , corresponding to data in part (a).

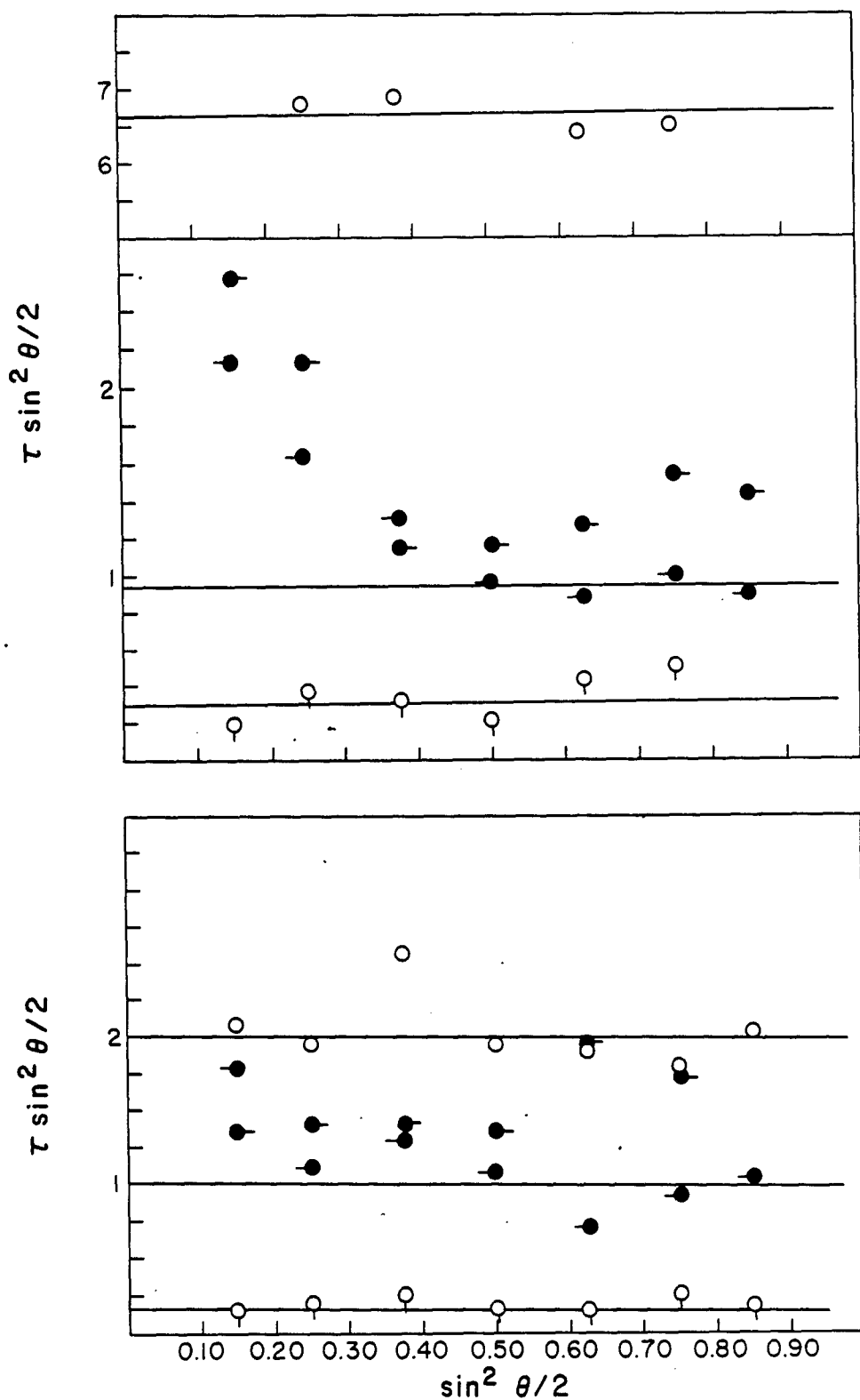


Figure 38:

a) Relaxation times multiplied by $\sin^2 \theta / 2$ for a solution of SPBO-352-39 (0.106 g/L) as a function of $\sin^2 \theta / 2$, $\circ \tau_{\text{H}} \sin^2 \theta / 2$, $\square \tau_{\text{K}} \sin^2 \theta / 2$, $\bullet \langle \tau_{\text{H}} \rangle_{\text{K}} \sin^2 \theta / 2$, uncentrifuged sample. b) After centrifugation.

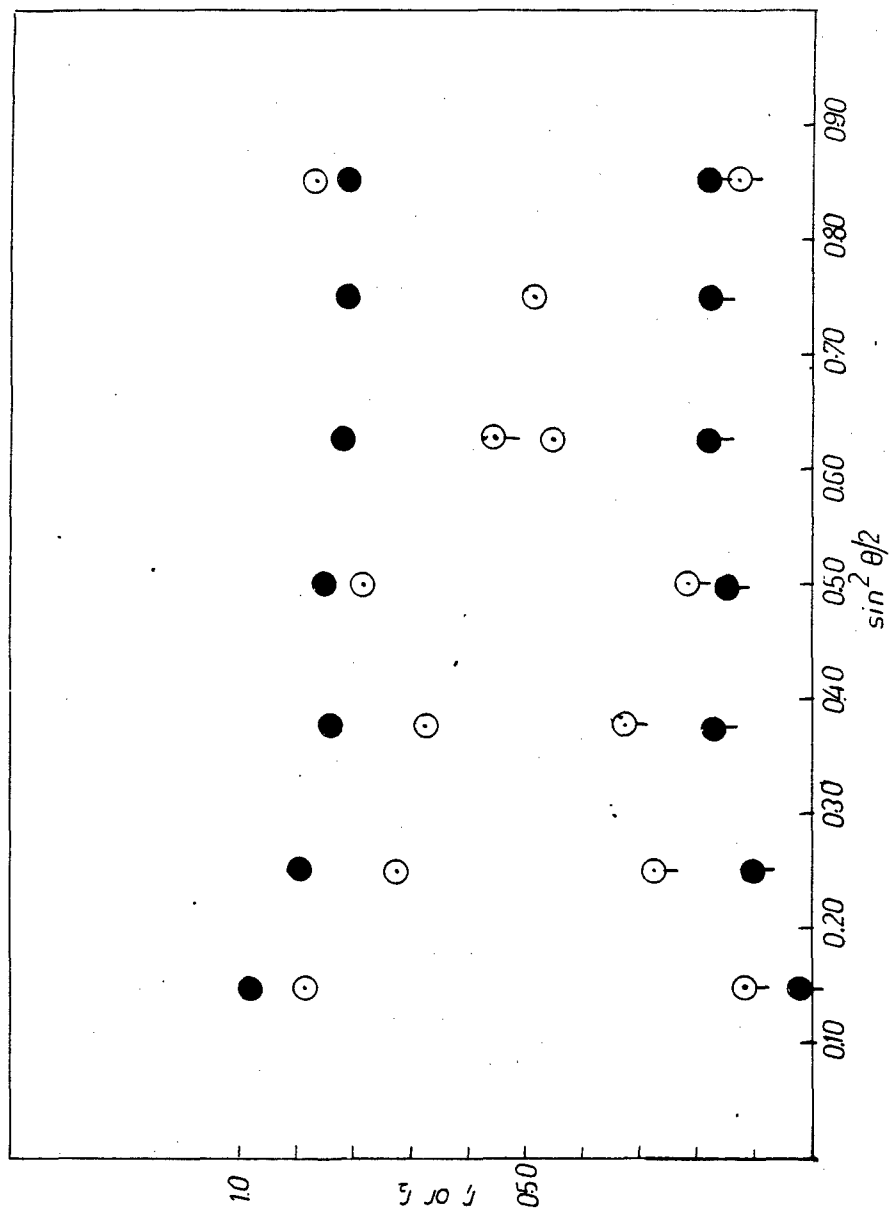


Figure 39:

The weight factor r_i corresponding to data in Fig. 38: O, r_i ; \bullet , r_i ; open for uncentrifuged and filled for sample after centrifugation.

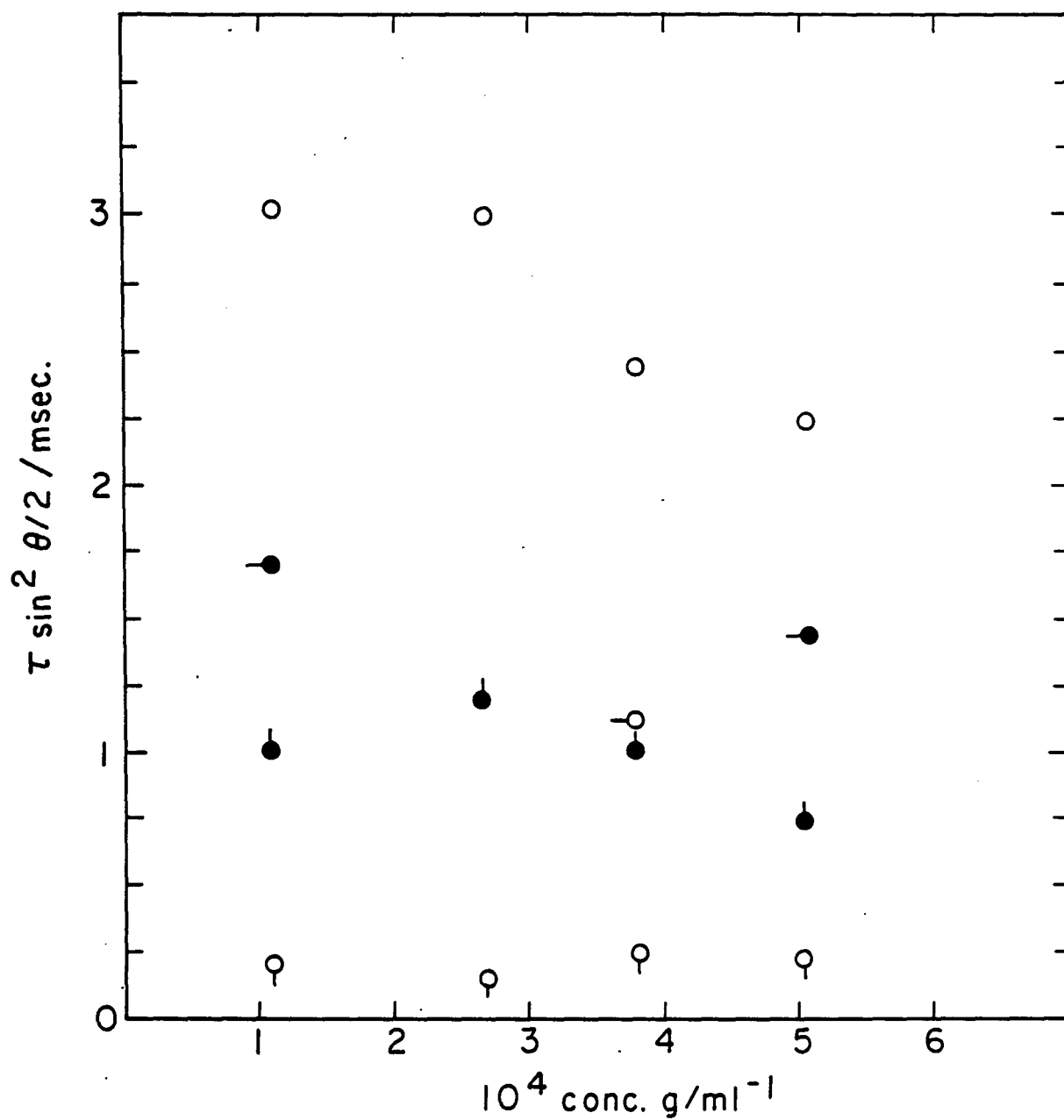


Figure 40:

Relaxation times for $\tau \sin^2 \theta / 2$ as a function of concentration for uncentrifuged solutions of SPBT-352-38/MSA.

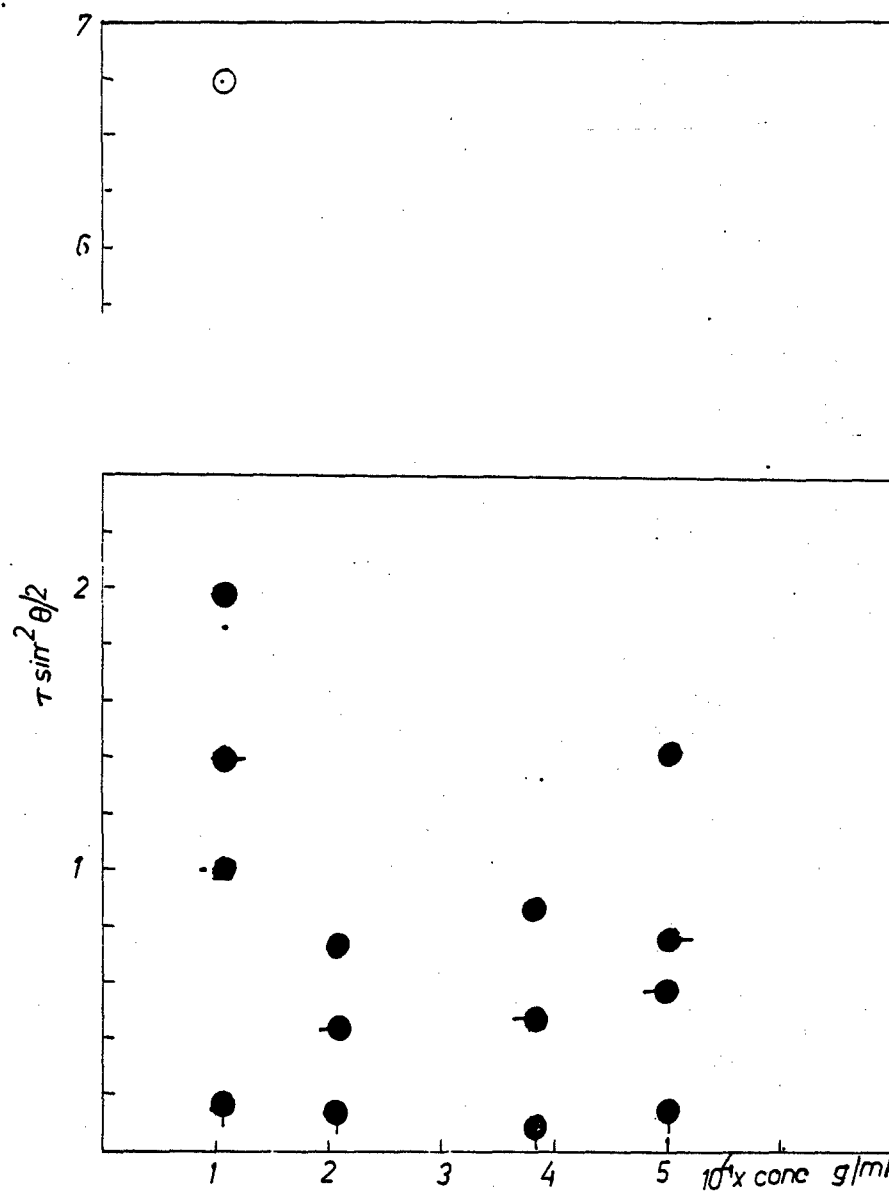


Figure 41:

Relaxation times $\tau_{b1} \sin^2 \theta / 2$ and $\tau_{b2} \sin^2 \theta / 2$ as a function of concentration for centrifuged solutions of SPBO-352-39/MSA.

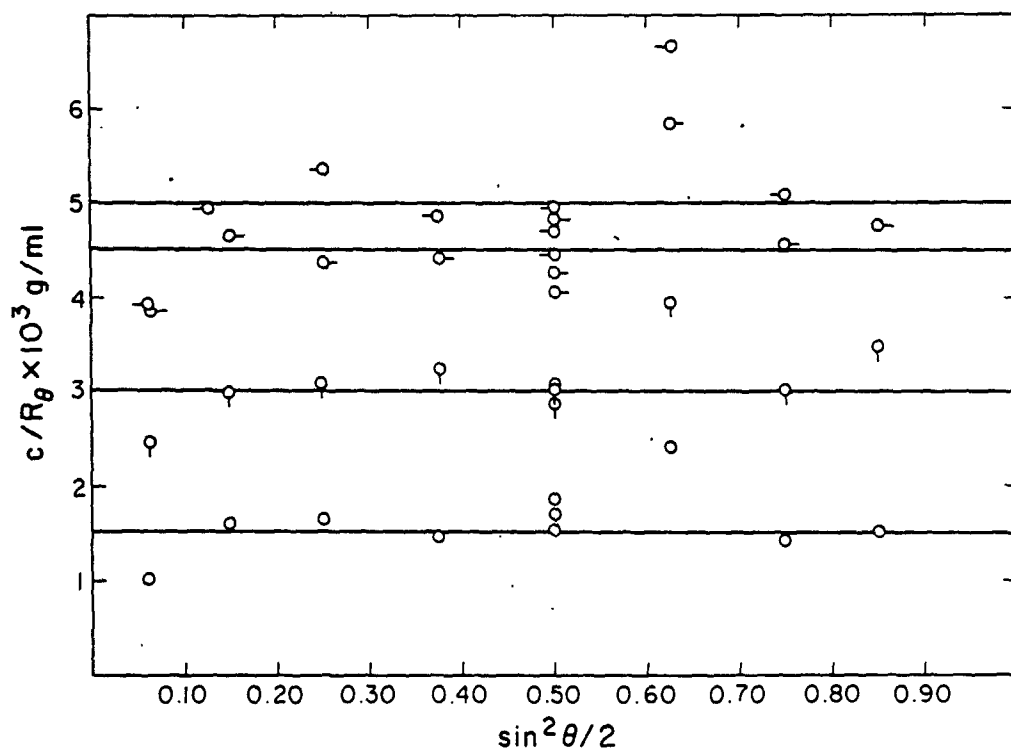
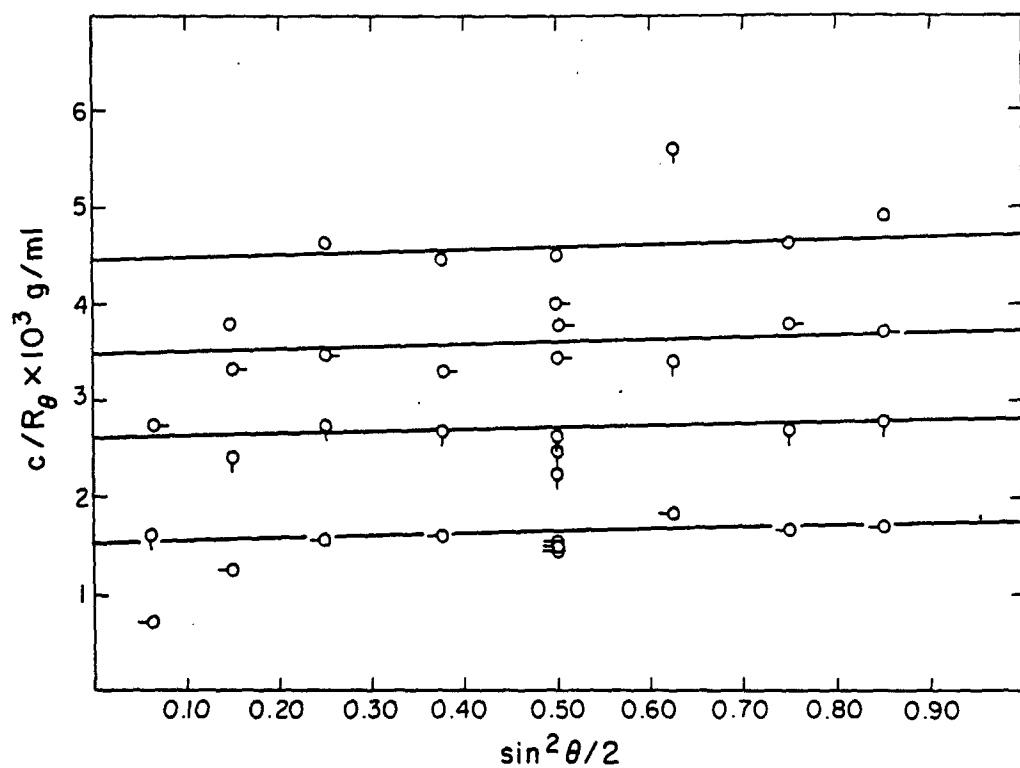


Figure 42:

Absolute light scattering, $c/R_\theta(\theta)$ as a function of $\sin^2 \theta/2$ for several concentrations of SPBT-352-38/MSA at 514 nm, \circ 0.108 g/L, \circ 0.267 g/L, \circ 0.375 g/L and \circ 0.503 g/L a) uncentrifuged and b) centrifuged.

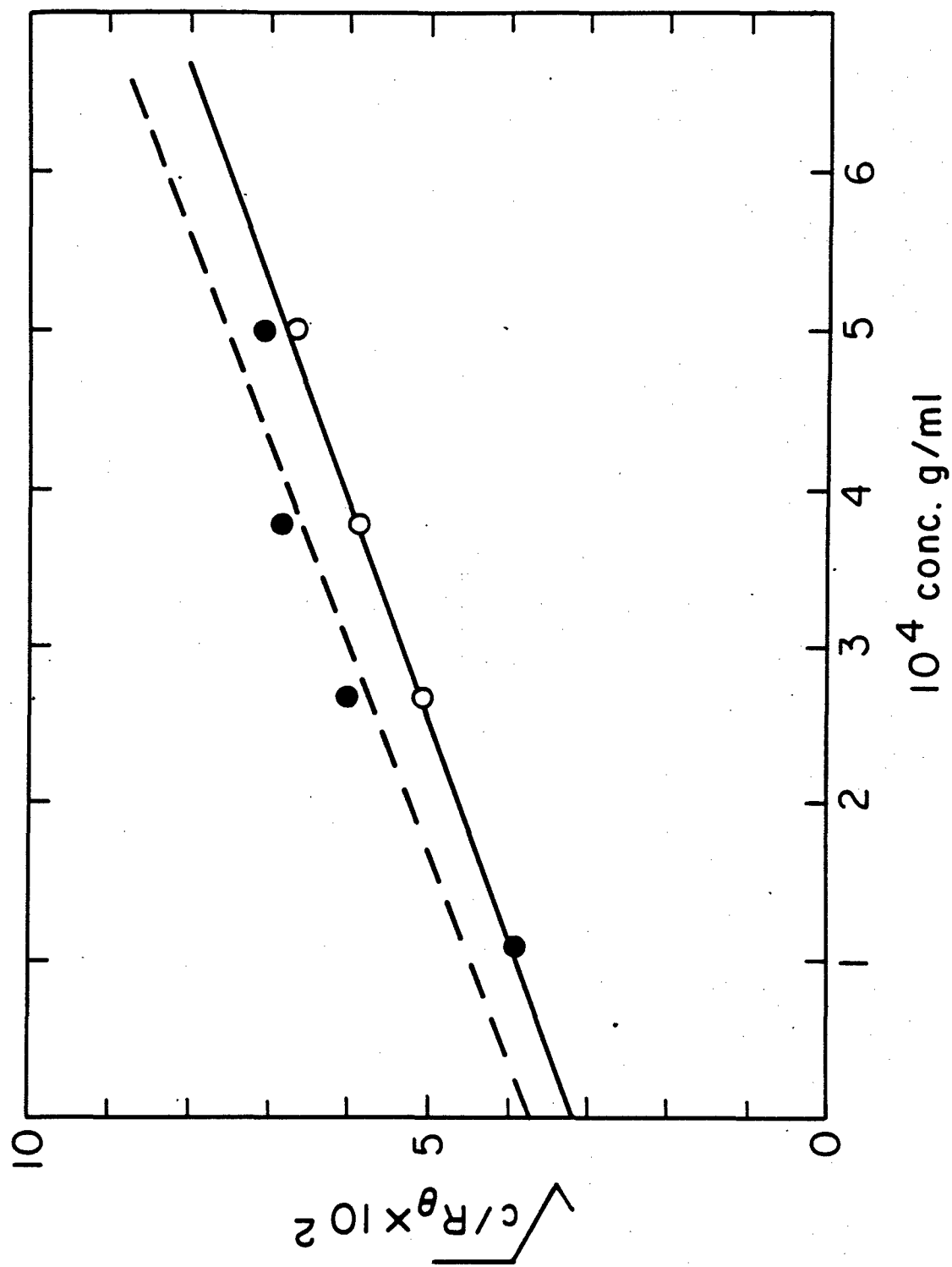


Figure 43:

Values of constant $K \times c/R_\theta(\theta)$ for SPBT-352-38/MSA from Fig. 42 as a function of concentration, O uncentrifuged, • after centrifuged.

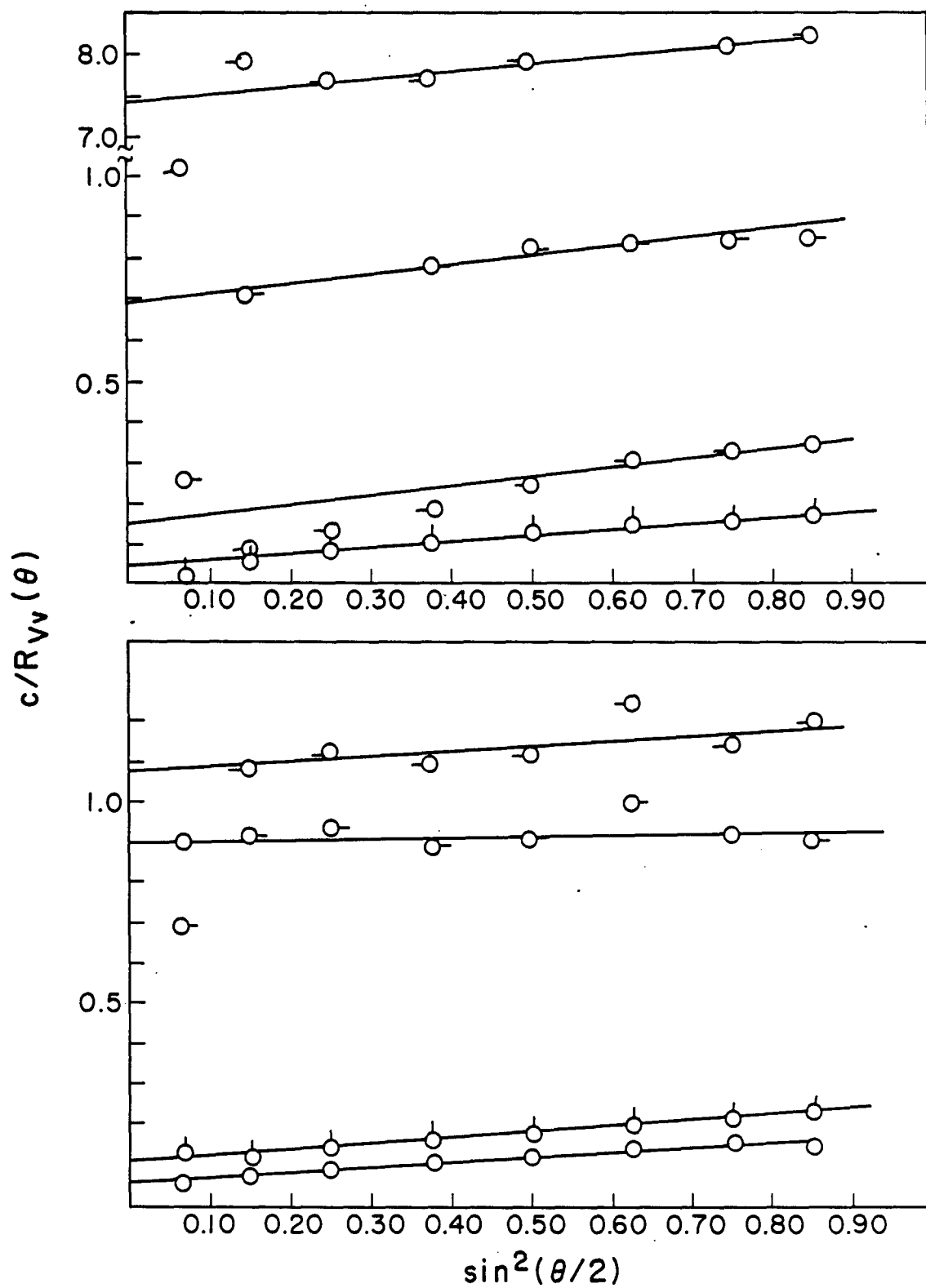


Figure 44:

Absolute intensity light scattering, $c/R_{vv}(\theta)$ as a function of $\sin^2\theta/2$ for several concentrations for SPBO-352-39/MSA at 633 nm. O 0.106 g/L, O 0.204 g/L, O 0.383 g/L, O 0.494 g/L. a) uncentrifuged and b) centrifuged.

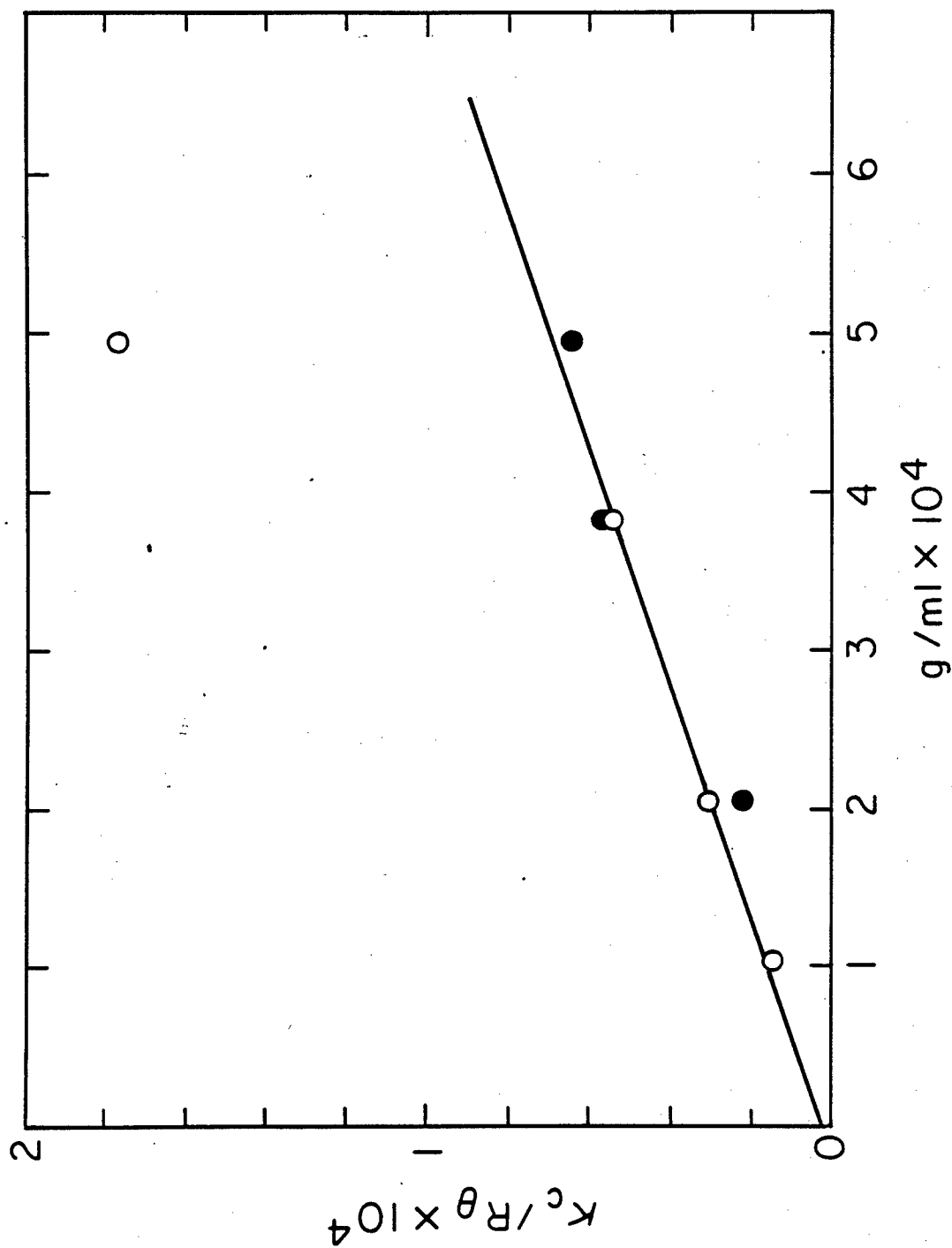


Figure 45:

Values of $K_c/R_\theta(\theta)$ for SPBO-352-39 from Fig. 44 as a function of concentration: \circ uncentrifuged, \bullet centrifuged.

3.4.4 Copolymer of PBT and PBO

3.4.4.1 Solution Preparation

Copolymers of PBO and PBT were supplied by Dr. J. Wolfe as solutions (ca. 7 weight percent polymer) in polyphosphoric acid, PPA. These were diluted with methane sulfonic acid to prepare solutions of an appropriate concentration for light scattering. Direct dilution was used in contrast to precipitation and eventual recovery of dried polymer for subsequent dissolution in an attempt to reduce interchain association. The copolymers studied were P(BO-co-BT) 4952-5 and 4952-13, with 75 and 25 mole percent PBO, respectively.

3.4.4.2 Light Scattering

Results for integrated intensity scattering on filtered solution are given in Figs. 46 and 47. The marked increase in intensity at small scattering angle reveals the presence of a fraction of some large component. At this stage, we presume it to be an intermolecular aggregate. Photon correlation data are being collected.

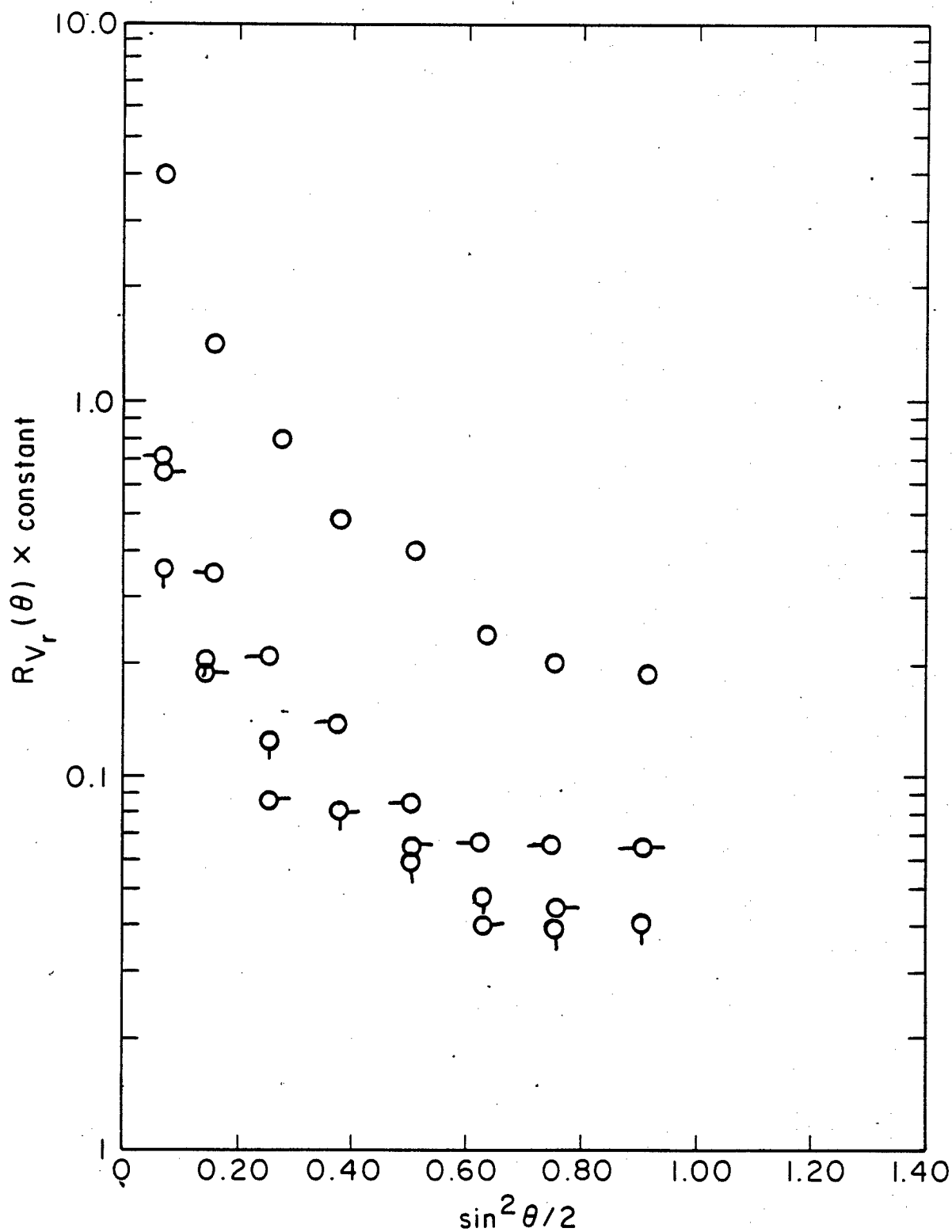


Figure 46:

Absolute intensity light scattering for P(BO-co-BT) (75/25) 4952-S in PPA diluted in MSA at 633 nm, O 0.529 g/L, O 0.327 g/L, Q 0.268 g/L, -O 0.138 g/L

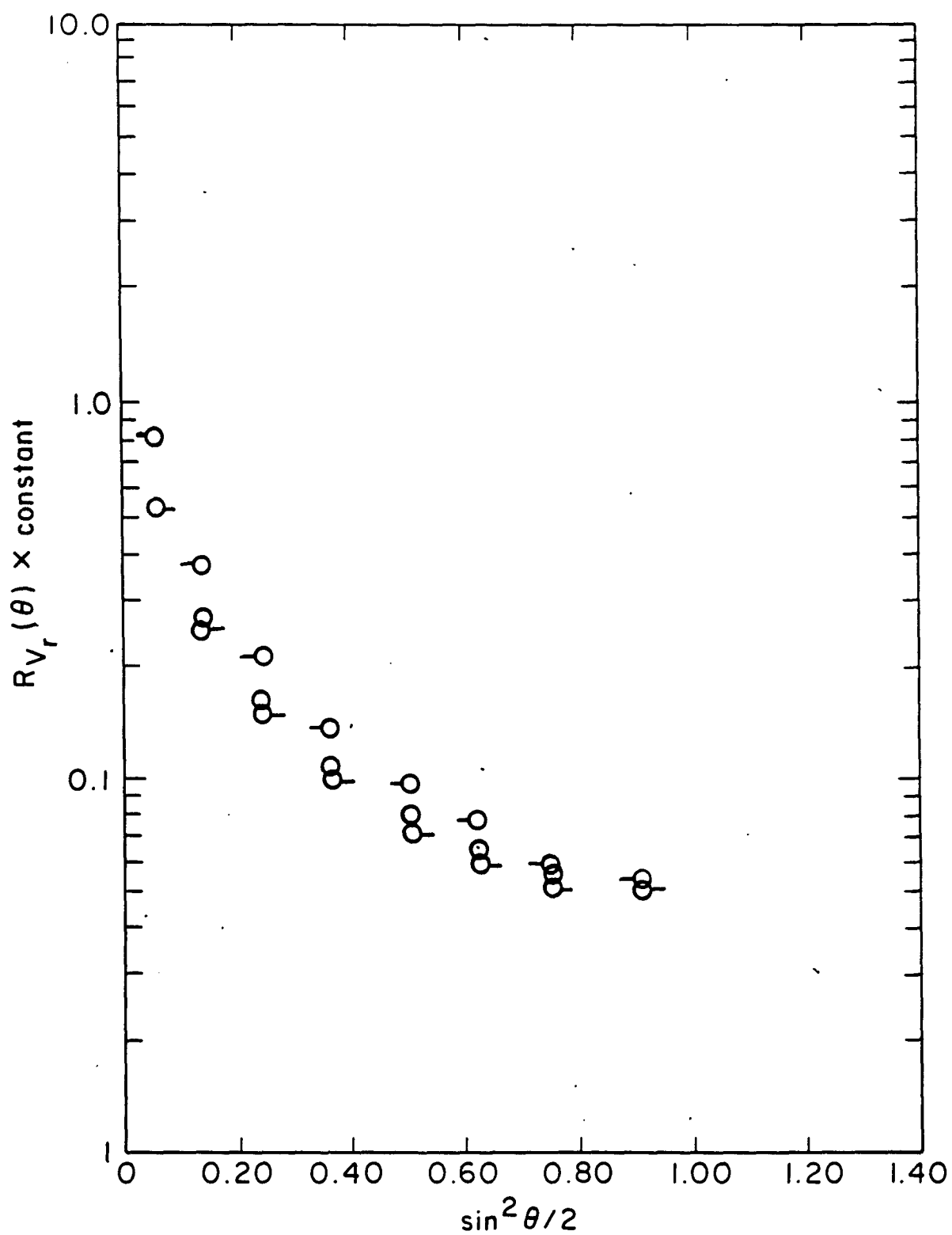


Figure 47:

Absolute intensity light scattering for P(BO-co-ET) (90/10) 4592/13 in PPA diluted in MSA at 633 nm, \circ 0.491, \odot 0.388 g/L, $\text{---}\circ$ 0.145 g/L.

4. VISCOMETRY

With solutions of rodlike polymers it was found that the reduced specific viscosity η_{sp}/c was extremely dependent on the ionic strength (μ). For example, in solvents like MSA, the usual relations

$$\eta_{sp} = c[\eta] + k'(c[\eta])^2 + \dots \quad (4.1)$$

$$\ln \eta_{rel} = c[\eta] - (\frac{1}{2} - k')(c[\eta])^2 + \dots \quad (4.2)$$

$$c[\eta]_c \equiv [2(\eta_{sp} - \ln \eta_{rel})]^{1/2} = c[\eta] - (1/3 - k')(c[\eta])^2 + \dots \quad (4.3)$$

were observed (with $\eta_{rel} = \eta_{sp} + 1$), but in CSA, η_{sp}/c increased very rapidly with increasing c until $c[\eta] \sim 0.05$, thereafter decreasing such that $[\eta]_c^{-1}$ was about linear in $c^{-1/2}$. For $c[\eta] \sim 0.05$, the mean separation of molecular centers is about equal to L , such that with further increase in c , the domains swept out by a molecule must overlap on the average. Thus, the observed behavior was attributed to the effects of electrostatic interactions among the rodlike chains, this effect becoming 'saturated' when the domains swept out by the rodlike chains reach a condition of overlap.

With solutions in MSA of articulated polymers with -Ar- type III ($n = 0.05$ and 0.10) and type II ($n = 0.10$), Eqns. 3.44 and 3.45 were found to fit the data satisfactorily. However, with solutions of two polymers, with -Ar- type I and type IV ($n = 0.10$ for both), η_{sp}/c was found to decrease rapidly, with $[\eta]_c^{-1}$ about linear in $c^{1/2}$. Of the latter polymers, the chain with type IV -Ar- units (SPBT 352/36 form nematogenic solution at higher concentration (see Part II). With addition of 1N potassium methyl sulfonate, this behavior is modified such that η_{sp}/c is markedly reduced, and about independent of c (e.g., $k' \sim 0$), see Fig. 48.

Based on this behavior, $[\eta]$ is estimated to be about 200 mL g^{-1} , so that $c = 2.5 \times 10^{-4} \text{ g mL}^{-1}$ for $c[\eta] = 0.05$ -- data were not taken to this low concentration.

Based on the effect of added electrolyte, the unusual behavior observed for the dependence of η_{sp}/c on c for solutions of SPBT 352/36 (and probably SPBO 352/4) in MSA is

attributed to electrostatic interactions. It is not known why these effects are observed with MSA, which has a reasonably high ionic strength, or why they are not completely suppressed (e.g., so that $k' \sim 1/3$) with 1N added electrolyte. With the rodlike polymers, the effect was attributed to intermolecular interactions. With the articulated polymers, it is probable that these are also important, perhaps dominant, but possible intramolecular contributions (e.g., conformational changes) may also be present.

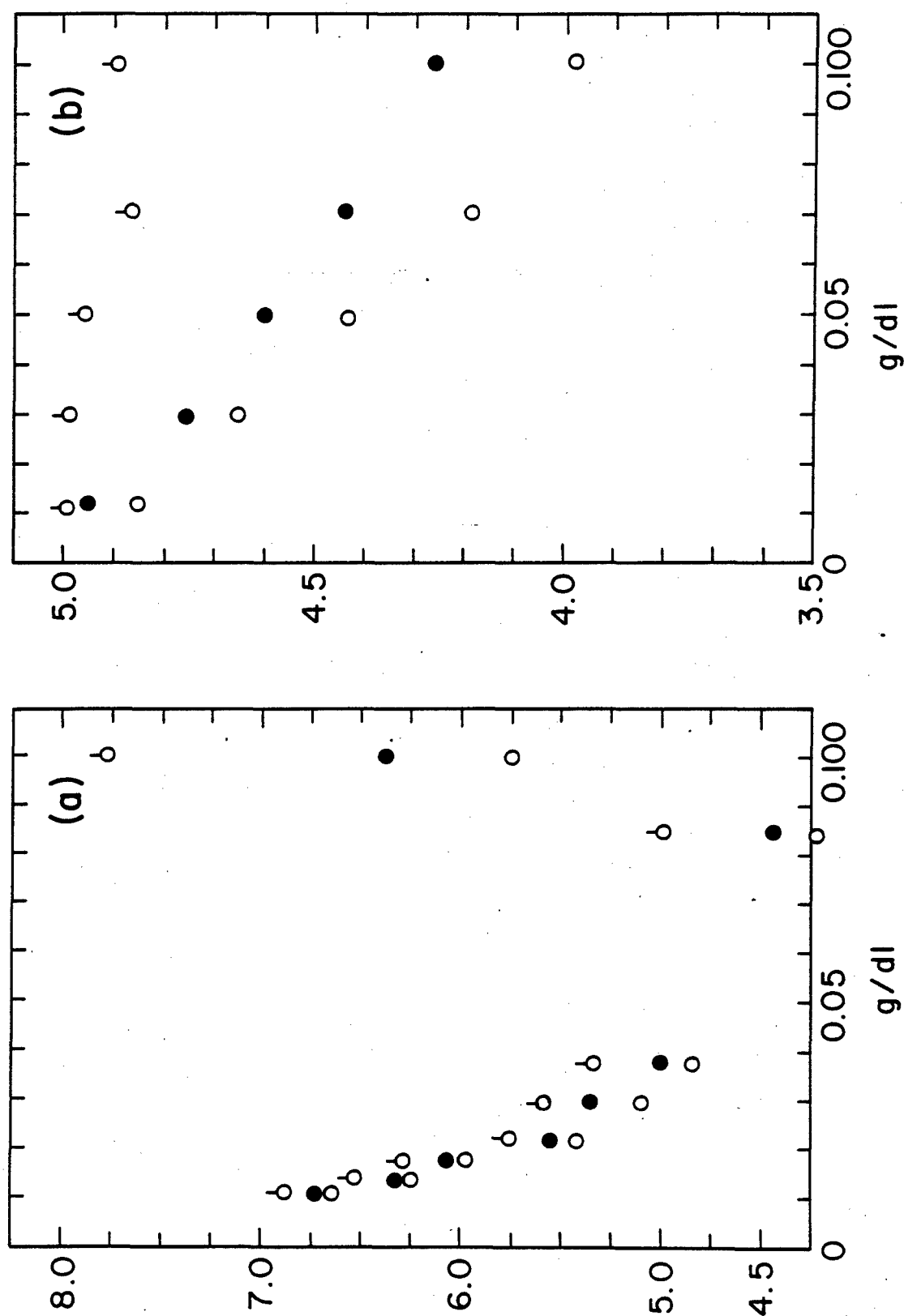


Figure 48:

Intrinsic viscosity data for SPBT-352-36, ○ η_{sp}/c , ○ $\ln \eta/c$, ● $[\eta]$; a) solution in MSA and b) solution in MSA + 1N K₂SO₃ salt

5. SUMMARY

Photon correlation and absolute intensity light scattering studies have been coupled with size exclusion chromatography, viscometry and spectroscopic studies to investigate several articulated polymers. The results show that the polymers investigated tend to form intermolecular aggregates in solution. The effect of these can be reduced in number by increased temperature, sonication and centrifugation, but not completely removed. Results on solutions so treated are presently being analyzed in terms of a quasi-two component mixture of large aggregates (few in number) and molecularly dissolved species.

II PHASE EQUILIBRIA OF SOLUTIONS OF ARTICULATED POLYMERS, RODLIKE POLYMERS AND THEIR MIXTURES

6. INTRODUCTION

The articulated polymers are expected to exhibit a nematic phase transition if the rodlike sequences are long enough.²³ In addition, it is expected that addition of the articulated polymers to solutions of (homologous) rodlike chains should suppress the concentration c_c of the rodlike chains required to attain a thermodynamically stable nematic phase. Theoretical estimates of these effects have been made²⁴ using a lattice model similar to that²⁵ used to study c_c for rodlike chains alone. One may be concerned that the intermolecular association discussed in Part I may interfere with attainment of thermodynamic equilibrium, see below.

7. EXPERIMENTAL METHODS

Solutions were sealed in a glass cell between parallel plates separated by 0.4 mm--this cell has been described in previous reports.¹⁹ The sealed cell was placed on a heated microscope stage and monitored visually between crossed-polars as the temperature was changed (ca. 1/Kh⁻¹). The temperatures for the first appearance of nematic solution and the last traces of isotropic material on increasing the temperature were noted.

To study the time τ_{BR} for relaxation of shear induced birefringence, the solution was placed between a microscope slide and cover slip. The solution was partially sealed against contamination by moisture by teflon tape placed along the periphery. Birefringence was induced by translating the microscope slide (by about 1-2 mm). The time τ_{BR} for relaxation was noted.

In some cases with PPA solutions, the cell described above was used owing to the high viscosity of these solutions. In these cases, contamination by water was not a problem owing to the temperature used.

8. RESULTS AND DISCUSSION

8.1 Articulated Polymers

Data on phase equilibrium for solutions of SPBT 388/39 over a range of concentrations in both methane sulfonic acid (MSA) and polyphosphoric acid (PPA) are given in Table 5. Also included are estimates of the time required for strain-induced birefringence to relax—these data were collected using polarized light microscopy. Additional data on SPBT polymers in MSA are given in Table 6, along with data for SPBO polymers in MSA reported previously. The data in Table 5 show that strain-induced birefringence was observed with all solutions of SPBT 388/39, and that these were isotropic at rest for solutions with less than about 5 weight percent polymer. As expected, the relaxation time for solutions in PPA is several orders of magnitude longer than that in MSA, reflecting the larger viscosity of the PPA solvent. We were unable to prepare homogeneous solutions of SPBT 388/39 in PPA at compositions similar to those which result in nematic fluids with MSA solutions. The reasons for this are not known to us.

The generally better success in achieving nematic solutions with SPBT polymers in comparison with SPBO polymers may be attributed to greater extent of intermolecular aggregation with the latter. For example, this may be one reason why a nematic solution was obtained with SPBO 352/18 in chlorosulfonic acid (CSA), but not in MSA—the electrostatic interaction being longer ranged in CSA than in MSA.

Nematic solutions were prepared with PBT-53 in MSA, PPA and CSA, with c_c being smallest in MSA (e.g., 0.043 g/ml in MSA in comparison with $c_c \sim 0.07$ g/ml in PPA). The difference in c_c between solutions in MSA and PPA may relate to suspected complex formation of oligomeric PPA to the PBT, thereby increasing the effective chain diameter d (i.e., $c_c \propto d/L$). As expected, τ_{BR} is exceedingly long for solutions in PPA, owing to the high viscosity of the solvent.

8.2 Rodlike Polymers

Data on phase equilibria and birefringence relaxation are given in Table 7 for the rodlike PBT-53 in 100% sulfuric acid (HSA), methane sulfonic acid (MSA), chlorosulfonic acid (CSA) and polyphosphoric acid (PPA). Of special interest with this polymer is the heterogeneous nature of mixtures in sulfuric acid at temperatures below 50–100°C (depending on the polymer concentration). They appear to be solid-like in consistency, and ill-suited for

Table 5: OBSERVATION ON THE TIME FOR RELAXATION OF STRAIN INDUCED
BIREFRINGENCE FOR SOLUTIONS OF SPBT 388/39^(a)

Weight Fraction Polymer	Phase	τ_{BR} (25°C) ^(b)
<u>Solutions in Methane Sulfonic Acid</u>		
0.0012	---	---
0.0067	---	---
0.0099	T > 10°C; Isotropic ^(c)	< 5s
0.0161	---	---
0.0325	T > 10°C; Isotropic ^(c)	5-20s
0.0375	---	---
0.0441	T > 14°C; Isotropic ^(c)	5-20s
0.0559	---	---
0.0757	T > 119; Isotropic T < 107; Nematic	
0.0872	T < 158; Nematic ^(d)	
<u>Solutions in Polyphosphoric Acid</u>		
0.0012	T > 25°C; Isotropic ^(e)	< 1s
0.0067	T > 25°C; Isotropic ^(e)	40s
0.0099	---	---
0.0161	T > 25°C; Isotropic ^(c)	100-700s
0.0325	---	---
0.0375 ^(e)	T > 25°C; Isotropic ^(c)	2-3 days
0.0441	---	---
0.0559 ^(e)	T > 25°C; Isotropic	> 10 days
0.0757 ^(e)	Sample not homogeneous	

^(a) $\eta = 0.05$, -Ar- = IV, see Part I.

^(b) Time for relaxation of strain-induced birefringence orientation at 25°C.

^(c) Lowest temperature used; MSA will crystallize at lower temperatures.

^(d) Highest temperature used.

^(e) Solution in PPA studied between glass plates partially sealed, see text.

Table 6: PHASE EQUILIBRIA DATA FOR SOLUTIONS IN METHANE SULFONIC ACID

Sample	n Fraction -Ar-	-Ar-	η_{inh} (dl/g)	100W ₂	Isotropic for T > -10°C	Easily Developed Flow Birefringence	Nematic at 25°C	Biphas Temp Range
PBO POLYMERS								
31	1	I	1.72	8.4	✓			
37-2	0.25	I	1.94	7.9	✓			
45-1	0.25	I	1.99	8.3	✓			
352-4	0.10	I	7.08	8.0	✓			
292-70	0.05	I	6.04	7.4	✓	✓		
292-59	0.05	I	3.57	8.8			v	48.5-53
352-54	0.05	I	8.58	8.6		No Homogeneous Solution		
352-54	0.05	I	8.58	5.0	v	v		
292-80	0.10	II	5.24	7.8	✓			
292-86	0.05	II	6.81	9.7		No Homogeneous Solution		
292-71	0.05	II	6.92	7.3	✓	✓		
292-88	0.10	III	5.44	7.9	✓			
292-96	0.05	III	6.74	7.0	✓	✓		
352-58	0.10	III	5.04	7.4	✓	✓		
352-39	0.05	IV	4.07	7.6	v	v		
352-39	0.05	IV	4.07	6.4(CSA)			v	
PBT POLYMERS								
352-18	0.10	I	12.02	7.4		No Homogeneous Solution		
352-18	0.10	I	12.02	4.7	v	v		
352-34	0.10	II	4.60	7.2	v	v		
352-28	0.05	II	6.43	7.1			v	75.5-92.
388-12	0.20	IV	4.97	6.7	v	v		
388-7	0.15	IV	5.68	7.2	v	v		
352-36	0.10	IV	6.04	7.4			v	77-92
352-38	0.05	IV	8.01	7.5			v	78-99.5

Table 7: OBSERVATION ON PHASE EQUILIBRIA AND THE TIME FOR RELAXATION OF STRAIN-INDUCED BIREFRINGENCE FOR SOLUTIONS OF PBT-53

Weight Fraction Polymer	Solutions in Polyphosphoric Acid		Solutions in Methane Sulfonic Acid		Solutions in Chlorosulfonic Acid	
	Solutions in Sulfuric Acid	Phase	Phase	Time for Relaxation of Strain-Induced Birefringence	Phase	T_{IR}
0.0011	$T < 53^\circ$; Heterogeneous $T > 53^\circ$; Isotropic	$T > 25$; Isotropic (b)	$T > -10^\circ\text{C}$; Isotropic	$< 1s$		
0.0099	$T < 53^\circ$; Heterogeneous $T > 53^\circ$; Isotropic					
0.0033		$T > 25$; Isotropic (b)		3-10s		
0.0096	$T < 65^\circ$; Heterogeneous $T > 65^\circ$; Isotropic					$T > -10$; Isotropic $< 1s$
0.0175						
0.0270		$T > 25$; Isotropic (b,d)	$T > -10$; Isotropic	10 hr		
0.0292			$T > 15^\circ$; Isotropic (b) $T < 5^\circ$; Nematic (a)			$T > 20$; Isotropic
0.0306			$T > 27^\circ$; Isotropic $T < 20^\circ$; Nematic			
0.0340 (d)		$T > 25$; Isotropic (b,d)	$T > 31$; Isotropic $T < 43$; Nematic	days		
0.0370			$T > 71$; Isotropic $T < 65$; Nematic			
0.0430 (d)		$T > 38$; Isotropic (d) $T < 47$; Nematic	$T > 86$; Isotropic $T < 80$; Nematic			
0.0460 (d)	$T < 100^\circ$; Heterogeneous $T > 100^\circ$; Isotropic	$T > 101$; Isotropic (b,d) $T < 90$; Nematic (c)				$T > 126^\circ$; Isotropic $T < 103^\circ$; Nematic
0.0471						
0.0376						
0.0602	$T < 110^\circ$; Heterogeneous $T > 110^\circ$; Isotropic					
0.0662		$T < 130$; Nematic (d)				
0.0920						
0.0936						
0.1036						

(a) Time for relaxation of strain-induced birefringence at 25°C.

(b) Lowest temperature used.

(c) Highest temperature used.

(d) Solution in PPA studied between glass plates partially sealed, see text.

direct processing to produce oriented forms. Perhaps the low temperature solid-like form could prove useful to quench orientation induced at higher temperature, but it should be noted that with the solutions studied, PBT-53 is isotropic in HSA at concentration and temperature for which solutions of PBT-53 in MSA, PPA and CSA are nematic. It seems likely that extensive interchain association obtains in HSA solutions, even at elevated temperatures. If so, these solutions would be ill-suited for processing into well oriented forms.

8.3 Mixtures of Articulated and Rodlike Polymers

Data for phase equilibria observed for solutions of two articulated polymers mixed with PBT-53 are given in Table 8. In both cases the articulated polymers are isotropic over the concentration range studied. In two of the cases, the rodlike polymer is isotropic at the concentration used to prepare the mixture. The expected decrease in c_c relative to c_c for the nematogenic rodlike polymer is observed--the effect is similar with PBT-53 mixed with either a SPBO or SPBT polymer. Moreover, marked increase of the weight fraction of PBT-53 does not appear to drastically alter the temperature range for the phase transition.

Efforts to effect physical separation of the phases by centrifugation were only marginally successful. Although this would have been analytically useful, the slowness of demixing of the phases might be useful in eventual fabrication processes.

Table 8: SOLUTIONS OF ARTICULATED POLYMERS AND THEIR MIXTURE WITH RODLIKE POLYMERS INVESTIGATED

(Solvent: Methane Sulfonic Acid)					
Polymer	n Fraction -Ar-	-Ar- (a)	Weight Fraction Articulated Polymer	Weight Fraction Rodlike Polymer (b)	Comment (c)
SPBT 352-34	0.10	II	0.0716	0	Isotropic, $T > 5^{\circ}\text{C}$
SPBT 352-34	0.10	II	0.0395	0.0105	Biphasic, $61-71^{\circ}\text{C}$
SPBO 352-4	0.10	I	0.0807	0	Isotropic, $T > 5^{\circ}\text{C}$
SPBO 352-4 (d)	0.10	I	0.0341	0.0118	Biphasic, $64-65^{\circ}\text{C}$
SPBO 352-4 (d)	0.10	I	0.0132	0.0397	Biphasic, $58-68^{\circ}\text{C}$

(a) See text

(b) PBT-53 used as the rodlike polymer; the biphasic range is about $18-25^{\circ}\text{C}$ for $w_2 = 0.034$ with this polymer.

(c) Entry "biphasic, T_1-T_2 " indicates isotropic for $T > T_2$, fully nematic for $T < T_1$, and coexisting phases for $T_1 < T < T_2$.

(d) Solution of SPBO 352-4 in methane sulfonic acid are isotropic over the range of concentrations for which homogeneous mixtures may be prepared.

9. SUMMARY

Phase equilibria studies show that articulated polymers can form nematogenic solutions, with the tendency increased with decreasing content of nonrodlike comonomer, as expected. For reasons unknown in detail, SPBT copolymers more readily form nematogenic solutions than do SPBO copolymers—a possible explanation may rest with increased intermolecular aggregation with SPBO copolymers. The critical concentration c_c for stability of the nematic phase appears to be increased for rodlike polymers in PPA as compared with MSA. This may reflect complex formation with PPA, effectively increasing the chain diameter. Mixtures of a nematogenic rodlike chain and an isotropic articulated chain exhibit depressed c_c , as expected. Nonetheless, physical separation of the phases appears to be very difficult with the system studied thus far.

III RHEOLOGICAL STUDIES OF SOLUTIONS OF ARTICULATED POLYMERS, RODLIKE POLYMERS AND THEIR MIXTURE

10. INTRODUCTION

Rheological properties explored in this study include the creep compliance $J_\sigma(t)$ as a function of the shear stress σ , the recoverable compliance function $R_\sigma(S,t)$, equal to the recoverable strain $\gamma_\sigma^{(R)}(S,t)$ at time t after creep of duration S at stress σ , the dynamic compliance $J'_\sigma(\omega)$ and $J''_\sigma(\omega)$ determined with a sinusoidal shear stress $\sigma_0 \exp(i\omega t)$, and the shear viscosity function $\eta_\kappa(t)$ equal to the stress $\sigma(t)$ at time t following imposition of a steady rate of shear κ . A compilation of rheological terms, symbols and relations is given in the Appendix to properly define these and other terms to be used throughout this discussion.

The range of rheological experiments on articulated SPBT copolymers, rodlike polymers, and their mixtures completed thus far is given in Tables 9 to 11. These studies are intended to provide information on rheological behavior as influenced by molecular structure (articulated or rodlike), solution morphology (isotropic, nematic or biphasic), solute concentration, etc.

For small σ , many polymers can be described by linear viscoelastic properties, such that, for example, the compliances become independent of σ , and equal to limiting values denoted here by $J_0(t)$, $R_0(S,t)$, $J'_0(\omega)$, $J''_0(\omega)$, etc., with well established relations among the parameters. This is discussed in more detail in the Appendix, for a linear viscoelastic fluid $J'_0(\omega)$ and $J''_0(\omega)$ are related to the linear recoverable compliance $R_0(t)$ and the viscosity η_0 through the expressions:

$$J'_0(\omega) = R_0 - \omega \int_0^\infty [R_0 - R_0(t)] \sin(\omega t) dt \quad (10.1)$$

$$J''_0(\omega) = (\omega \eta_0)^{-1} + \omega \int_0^\infty [R_0(t)] \cos(\omega t) dt \quad (10.2)$$

where the creep compliance $J_0(t)$ is given by

$$J_0(t) = R_0(t) + t/\eta_0 \quad (10.3)$$

and R_0 is the limiting value of $R_0(t)$ for large t (often R_0 is denoted J_e^0). To a useful approximation,

$$J_0(t) \sim |J_0^*(\omega = t^{-1})| \quad (10.4)$$

where

$$|J_0^*(\omega)|^2 = J_0'^2(\omega) + J_0''^2(\omega) \quad (10.5)$$

These relations provide a basis for the analysis to be given here for data at small σ .

As is well-known, $R_0(t)$ can frequently be represented in terms of a distribution $L(\tau_d)$ of retardation times τ_d :

$$R_0(t) = J_e + \int_{-\infty}^{\infty} L(\tau_d)[1 - \exp(-t/\tau_d)] d \ln \tau_d \quad (10.6)$$

For the materials and temperature range of interest here, J_e may be neglected for most purposes. In the latter case, it is useful to recast Eqn. 10.3 in the form

$$J_0(t) = R_0[\psi(t) + t/\tau_c] \quad (10.7)$$

where $\psi(t) \equiv R_0(t)/R_0$ and $\tau_c = R_0\eta_0$. Then if the temperature dependence of τ_c and all the

τ_d are identical, Eqn. (10.7) represents a form of the "time-temperature" equivalence principle. According to this principle, the function $b(T) J(t, T)$ is a universal function of t/a_T for a given material at all temperatures, with

$$a_T = \tau_c(T)/\tau_c(T_0) \quad (10.8)$$

$$b_T = R_0(T_0)/R_0(T) \quad (10.9)$$

where T_0 is an arbitrarily chosen reference temperature (if $T > T_0$, then for most materials, $a_T < 1$; usually, b_T is nearly unity). Similarly, $b_T J'_0(\omega, T)$ and $b_T J''_0(\omega, T)$ are expected to be universal functions of $a_T \omega$ for a given material, with the same a_T and b_T used with $J_0(t)$. This time-temperature equivalence may not be realized with complex, multiphase materials such as those under study here, see below.

The components $\eta'_0(\omega)$ and $\eta''_0(\omega)$ of the dynamic viscosity $\eta^*(\omega)$ may be defined in terms of $J'_0(\omega)$ and $J''_0(\omega)$.

$$\eta'_0(\omega) = \frac{J''_0(\omega)}{\omega |J^*_0(\omega)|^2} = \frac{[\omega J''_0(\omega)]^{-1}}{1 + (\tan^2 \delta)^{-1}} \quad (10.10)$$

$$\eta''_0(\omega) = \frac{J'_0(\omega)}{\omega |J^*_0(\omega)|^2} = \frac{[\omega J'_0(\omega)]^{-1}}{1 + \tan^2 \delta} \quad (10.11)$$

so that for $\omega \ll \tau_c^{-1}$, $\eta' \sim \eta_0$; here $\tan \delta = J''_0/J'_0$. If the time-temperature equivalence principle applies, then $\eta'_0(\omega, T)(b_T a_T)^{-1}$, etc., are expected to be universal functions of $a_T \omega$ for all temperatures for a given material.

Table 9: RHEOLOGICAL STUDIES ON ARTICULATED SPBT COPOLYMERS^(a)

Polymer	n Fraction -Ar-	-Ar-	Weight Fraction Polymer	J'_G, J''_G	J_G	R_K	η_K
<u>Solutions in Methane Sulfonic Acid</u>							
352-34	0.10	II	0.0716	40,80	---	---	---
352-38	0.05	IV	0.0747	40,80	---	---	25,53,71
388-39	0.05	IV	0.0099	25,40	---	---	---
			0.0325	25,40	---	---	---
			0.0441	25,40	---	40	40
			0.0757	25,40	40	28,40	28,40
			0.0872	25,40	---	---	---
352-36	0.10	IV	0.0740	---	---	---	24
388-38 ^(b)	0.10	IV	0.0100	---	---	---	---
			0.0312	---	---	---	---
			0.0511	---	---	---	---
			0.0745	---	---	---	---
			0.0877	---	---	---	---
388-7	0.15	IV	0.0721	10,40,80	---	---	---
388-72	0.20	IV	0.0671	40,80	30,52	---	30,52
<u>Solutions in Polyphosphoric Acid</u>							
388-39	0.05	IV	0.0012	25,40	---	---	---
			0.0067	25,40	---	---	---
			0.0161	25,40	---	---	---
			0.0375	25,40	---	---	---
			0.0559	25,40	---	---	---

(a) Entries under J'_G , etc. give the temperature ($^{\circ}\text{C}$) of measurements.

(b) Solutions recently prepared, with studies underway.

Table 10: RHEOLOGICAL STUDIES ON RODLIKE POLYMERS^(a)

Polymer	Weight Fraction Polymer	J'_σ	J''_σ	J_σ	R_κ	η_κ	G_κ
<u>Solutions in Methane Sulfonic Acid</u>							
PBT-53	0.0343	40,80	40,80	—	—	—	—
<u>Solutions in Polyphosphoric Acid</u>							
PBT	0.092	—	—	—	40	40	—
P(BO-co-BT)	0.057	-8-100	10-100		27	27	27

(a) Entries under J'_σ , etc., give the temperature ($^{\circ}\text{C}$) of measurement

Table 11: RHEOLOGICAL STUDIES ON MIXTURES OF RODLIKE AND ARTICULATED POLYMERS^(a)

Rodlike polymer	Weight Fraction	Articulated Copolymer	n		Weight Fraction	J'_σ	J_σ	R_χ	η_χ	G_χ
			-Ar-	Fraction -Ar-						
PBT-53	0.0105	SPBT 352/34	II	0.10	0.0395	5,40,80	29,52	29,50,70	29,50,70	29,52
PBT-53	0.0118	SPBO 352/4	I	0.10	0.0341	8,40,80	--	--	--	--
PBT-53	0.0397	SPBO 352/4	I	0.10	0.0132	40,63,80	--	--	--	--

(a) Entries under J'_σ , etc., give the temperature ($^{\circ}\text{C}$) of measurements.

11. EXPERIMENTAL METHODS

Polymers were received either as dry powders or as solution in polyphosphoric acid (PPA). The PPA solutions were either used as received or were diluted, either with PPA or methane sulfonic acid (MSA). Dry polymers were dissolved in appropriate solvents. The same mixing apparatus and procedures were used whether making a dilution or effecting dissolutions of a dry polymer. The initial component (e.g., dry polymer or PPA solution) was transferred in a dry bag into a weighed, dry tube containing a magnetic mixing bar—polymers were predried under vacuum. After weighing, the tube plus initial contents is returned to the dry bag and an appropriate amount of solvent is added; the tube is then reweighed. For mixing, the tube was placed in an oil bath between the poles of a permanent magnet. The tube was slowly rotated and translated up and down along its rotation axis to effect mixing. The temperature was in the range 25 to 50°C for MSA solutions, or 80–100°C for PPA solutions, depending on the viscosity.

With MSA solutions, part of the solution was transferred to a syringe in a dry bag, for later installation in the rheometer. With PPA solutions, the solution was placed in a teflon mold in a dry bag, evacuated, and pressed into a pellet for latter installation in the rheometer.

One of two rheometers was used for the study. Creep and recovery experiments were carried out with a custom CMU Wire Suspension Rheometer—this rheometer and its use are described in detail elsewhere.²⁶ Dynamic compliances were determined with a Mechanical Spectrometer (Rheometrics, Inc.), equipped with a Birnboim Digital Correlator (Science Research Systems of Troy). Plate and (truncated) cone geometries were used in all cases. With the Wire-Suspension Rheometer stresses in the range 0.1 to 10^5 Pa could be employed, in comparison with 1 to about 10^6 Pa with the Mechanical Spectrometer. Both instruments are fitted to operate over the temperature range -10 to 200°C.

12. RESULTS AND DISCUSSION

12.1 Articulated Polymers

12.1.1 Solutions in Methane Sulfonic Acid

The steady state viscosity η_κ calculated as $\eta_\kappa = (\partial J_\sigma(t)/\partial t)^{-1}$ during steady flow is given as a function of the shear rate $\kappa = \sigma/\eta_\kappa$ in Fig. 49-50 for solution of three articulated polymers in MSA; one of the solutions is isotropic, whereas the other two are nematic at the temperature of the creep measurement. The data on the isotropic solution of SPBT 388/12 also include R_κ at three values of κ and the creep and recovery data are shown in Fig. 50. For most isotropic polymers, η_κ and R_κ can be represented by the relations^{27,28}

$$\eta_\kappa = \eta_0 Q(\tau_c \kappa)$$

$$R_\kappa = R_0 P(\tau_c \kappa)$$

where $\tau_c = \eta_0 R_0$ and the functions Q and P are independent of temperature and, for a given solute, the polymer concentration, with both P and Q being unity for small $\tau_c \kappa$. Usually,²⁷ Q is essentially unity for $\tau_c \kappa < 1$. The data in Fig. 50 show that $R_0 > 0.5 \text{ Pa}^{-1}$, and suggest that η_0 may be about $1.5 \times 10^3 \text{ Pa}\cdot\text{s}$ at 30°C , so that $\tau_c > 750 \text{ sec}$ at 30°C . Thus Q would be expected to decrease with increasing κ for κ greater than about 0.0013 s^{-1} , whereas in fact, a small drop in η_κ is seen for $\kappa \sim 2 \times 10^{-5} \text{ s}^{-1}$, with η_κ about independent of κ over the extended range 4×10^{-4} to 0.1 s^{-1} . Additional unexpected features are observed in the data in Fig. 51 for $J_\sigma(t)$, which is seen to be proportional to t (within experimental error) over the range 1 to 10^4 s spanned by the data. Moreover, for small σ , $J_\sigma(t) \sim R_\sigma(\infty, \theta)$ for θ , ca 30 s. Data for $|J_\sigma^*(\omega)|_{\omega \rightarrow 1}$ shown in Fig. 52 obtained for σ_0 in the range 4 to 20 Pa do not exhibit the same behavior; rather, $-\partial \ln |J_\sigma^*(\omega)| / \partial \ln \omega$ is much less than unity over much of the range studied. Moreover, $|J_\sigma^*(\omega)|_{\omega \rightarrow 1}$ at 80°C , is less than $J_\sigma(t)$ at 50°C for $t > 2 \text{ s}$. For many materials, $J_0(t) \sim |J_0^*(\omega)|_{\omega \rightarrow 1}$, so that

$$|J_0^*(\omega)|_{\omega \rightarrow 1} \sim R_0(t) + t/\eta_0$$

No generalities are available for the relation between $J_\sigma(t)$ and $|J_\sigma^*(\omega)|_{\omega_{1-1}}$. It is interesting to note that the data for $|J_\sigma^*(\omega)|_{\omega_{1-1}}$ obtained with $\sigma_0 \sim 4$ to 20 Pa exhibit an inflection with $|J_\sigma^*(\omega)|_{\omega_{1-1}}$ about equal to $R_\sigma(\infty, \infty)$ obtained with $\sigma = 6.3$ Pa.

The results in Figs. 50 and 51 show that for the solutions of SPBT 388/12 in MSA:

1. the rate of creep $\partial J_\sigma(t)/\partial t$ was essentially constant ($\eta_\kappa = 9,000$) for σ over the range 0.2 to 90 Pa, and
2. the recoverable strain $\gamma_\kappa^R = \sigma R_\kappa$ increased from 0.17 to 0.37 (at 30°C) as σ increased from 0.36 to 6.6 Pa,
3. $J_\sigma(t) \sim R_\sigma(\infty, t)$ for small σ and short t .

These attributes suggest that the kinetics of the cleavage and reformations of intermolecular aggregates may be responsible for part of the rheological behavior. In work on poly(ethylene tetrasulfide) networks (see review in reference 29), it was found that the shear stress relaxation modulus $G_\gamma(t)$ could be fitted by a single exponential

$$G_\gamma(t) \sim G_\gamma(0)\exp(-t/\tau_{CH}) \quad (12.1)$$

over a range of γ down to small γ ; i.e., the response appeared to be linear so that $G_\gamma(t) \sim G_0(t)$ in the range studied. Here $\tau_{CH} = k\bar{m}$, where \bar{m} is the average number of tetrasulfide links between crosslinks, and k is the rate constant for an interchange reaction among the tetrasulfide links. If the response is linear, then $J_0(t)$ may be calculated from Eqn. 12.1 using the relation

$$\int_0^t J_0(t-s)G_0(s)ds = t \quad (12.2)$$

to give the result

$$J_0(t) = R_0(1+t/\tau_{CH}) \quad (12.3)$$

with $R_0^{-1} = G_0(0)$; the viscosity η_0 is $\tau_{CH} R_0^{-1}$. Using the relations given in the Appendix, for this model,

$$|J_0^*(\omega)| = R_0(1+(\omega\tau)^{-2})^{1/2} \quad (12.4)$$

Thus, with Eqn. 12.1 for $G_0(t)$, no time dependence is expected for the recoverable compliance; $R_0(t) = R_0$. The data obtained for SPBT 388/12 deviate from this in that a) the recovery is time-dependent, and b) $R_0(\infty, \infty)$ depends on σ . For $\sigma = 0.36$ Pa, the data give $\tau_K = R_K \eta_K = 400$ s; this is comparable to τ_{CH} deduced for poly(ethylene tetrasulfide) networks at the lower end of network stability (i.e., $\bar{m} \sim 10$ and high T or $\bar{m} \sim 2$ and low T).

The possible importance of intermolecular association in solution of SPBT 388/12 is in accord with the dilute solution data reported in Part I, which revealed substantial aggregation of the polymer, even at very low concentrations. It may be that with this polymer, in more concentrated solutions a tenuous network is obtained with weakly bound loci of association acting as crosslinks; for the quiescent fluid, these may undergo slow interchange. When the aggregated 'solution' is deformed, some of the loci will be destroyed, leading to flow. Conversely, new loci may be reformed. If the latter process is fast, then perhaps the rate of deformation $\partial J_\sigma(t)/\partial t$ could be independent of t and σ , as observed. Conformational distortions stored in the aggregate structure could then be recovered following removal of the stress; the data suggest that the range of these distortions is limited since $\gamma_\sigma^{(R)}$ does not vary widely with σ . This model will be considered in more detail in future work.

12.1.2 Solutions in Polyphosphoric Acid

Data on $|J_\sigma^*(\omega)|$ for several concentrations of SPBT 388/39 in PPA are given in Figs. 55 and 56. As discussed in section II-3.1, these solutions were all found to be isotropic. Values of $|\eta_\sigma^*(\omega)| = (\omega |J_\sigma^*(\omega)|)^{-1}$ are given in Figs. 57-58 as $|\bar{\eta}_\sigma^*(\omega)| = |\eta_\sigma^*(\omega)| - |\eta_\sigma^*(\omega)|_{\text{SOLVENT}}$; a plot of $|\bar{\eta}_\sigma^*(\omega)| / |\bar{\eta}_\sigma^*(0)|$ versus $a_c \omega$ shown in Fig. 59 was used to obtain the estimates of $|\eta_\sigma^*(0)| - |\eta_\sigma^*(0)|_{\text{SOL}}$ are given as a function of w_2 in Fig. 60. Since $\sigma_0 \sim 100$ Pa for the data at small ω , it is not certain that all of the $\eta_\sigma^*(0)$ are accurate estimates of $\eta_0^*(0)$, as would be desirable—it is possible that the value of $|J_\sigma^*(\omega)|$, and hence $|\eta_\sigma^*(\omega)|$ are not in the linear viscoelastic range for the solution with $w_2 = 0.0557$. Attempts to acquire data at lower σ_0 will be included in future work.

For the $w_2 < 0.01$ (e.g., only two points), $|\bar{\eta}_\sigma^*(0)| \sim (\eta_s/20)w_2^3$ exhibiting the proportionality with w_2^3 expected for $|\bar{\eta}_0^*(0)|$ with moderately concentrated solutions of rodlike chains with concentrations well below that for transition to the nematic state. Here, $\eta_s = |\bar{\eta}_0^*(0)|$ for the solvent. For larger w_2 , $|\bar{\eta}_\sigma^*(0)| < (\eta_s/20)w_2^3$, perhaps reflecting deviation of $|\bar{\eta}_\sigma^*(0)|$ from $\bar{\eta}_0^*(0)$, as mentioned above. Alternatively, this deviation may reflect deviation from a rodlike conformation for the articulated polymer, which includes 0.05 mole fraction comonomer IV.

12.2 Rodlike Polymers

12.2.1 PBT in Polyphosphoric Acid

The viscosity η_κ calculated from $\partial J_\sigma(t)/\partial t$ at long t (e.g., $t \gg \tau_c$) is given in Fig. 61 for a solution of a PBT in PPA with $w_2 = 0.092$ (Celanese 2895-32); the solution is nematic. Values of R_κ obtained over the same range are given in Fig. 61. The estimates $\eta_0 = 7 \times 10^4$ Pa's and $R_0 = 0.2 \text{ P}_a^{-1}$ give $\tau_c = 1.4 \times 10^4$ s, so that appreciable deviation of η_κ from η_0 is expected for $\kappa > 7 \times 10^{-5} \text{ s}^{-1}$, as is observed. Thus, with this fluid, appreciable orientation would be expected for shear rates as low as 1 s^{-1} .

12.2.2 PBT in Methane Sulfonic Acid

Data for $|J_\sigma^*(\omega)|$, $J'_\sigma(\omega)$ and $|\eta_\sigma^*(\omega)|$ are given in Figs. 62 and 63 for solutions of PBT-53 in MSA over a temperature range for which the fluid is isotropic (80°), nematic (5°) and near the phase transition temperature (40°), see Table 7. The results for $|\eta_\sigma^*(\omega)|$ similar to data for η_κ in that $|\eta_\sigma^*(0)|$ decreases with decreasing T as the fluid transforms from the isotropic to the nematic state. With the estimates $R_0 \sim 0.032 \text{ Pa}^{-1}$, and $|\eta_\sigma^*(0)| \sim 1,400 \text{ Pa's}$, the time constant τ_c is found to be 44 s at 40°C , in accord with the range ω for which $|\eta_\sigma^*(\omega)|$ begins to deviate from $|\eta_\sigma^*(0)|$.

12.2.3 P(BT-co-BO) in Polyphosphoric Acid

Data for $J_\sigma(t)$, $R_\sigma(S,t)$, $|J_\sigma^*(\omega)|$, $|\eta_\sigma^*(\omega)|$, η_κ , R_κ and the relaxation function $G_\kappa(\infty,t)$ are given in Figs. 64 to 68 for a solution of a P(BT-co-BO), 0.75 mole fraction PBT, in PPA, $w_2 = 0.057$; the solution is nematic. The data on $J_\sigma(t)$ and $R_\sigma(S,t)$ given in Fig. 65 (with $S \sim 10^5$ s, or about equal to $\eta_\kappa R_\kappa$) show that η_κ is very large at low κ , e.g., $4 \times 10^7 \text{ Pa's}$ at 27°C for $\kappa = 3 \times 10^{-6} \text{ s}^{-1}$. From inspection of Fig. 64, it is doubtful that a

limiting value η_0 of η_κ was reached; an estimate of $\tau_c > \tau_\kappa = \eta_\kappa R_\kappa = 2 \times 10^5$ at the lowest κ studied shows that η_0 might be reached for κ close to the lowest values studied e.g., $\eta_0 \sim 10^8$ Pa·sec.

Data $|\eta_\sigma^*(\omega)| = |\omega J_\sigma^*(\omega)|^{-1}$ given in Fig. 67 shows that the data reduce reasonably over a wide temperature interval, with $\partial \log b_T / \partial T^{-1} = 3,630/K$, in comparison with $\partial \log \eta_0 / \partial T^{-1} = 2,930/K$ for PPA. In the range of overlap, $|\eta_\sigma^*(\omega)|_{\omega=\kappa}$ appears to be about 50% larger than η_κ —the range of ω was not low enough to permit an estimate for $|\eta_0^*(0)|$. With the temperature dependence given by $\partial \log b_T / \partial T^{-1}$, and the estimate for η_0 at 27°C given above, one might expect η_0 to drop to about 4×10^5 Pa·sec at 100°C. This would still be too high for satisfactory use with the CMU Ribbon Forming Apparatus, see below.

The results for $J_\sigma(t)$ and $R_\sigma(S,t)$ exhibit the general features seen with other materials. Since $R_\sigma(S,t)$ is independent of σ for $t < 60,000$ sec, one can surmise that in this range the data approximate $R_0(\infty,t)$ reasonably well. These data overlap well with $|J_\sigma^*(\omega)|_{\omega \rightarrow 1}$ for the range 0.5 to 10 sec for data on the former obtained with $\gamma_0 = 0.01$. By contrast, $|J_\sigma^*(\omega)|_{\omega \rightarrow 1}$ obtained with $\gamma_0 = 0.5$ are far larger; the response in the latter case also has Fourier components at 3ω , not discussed here.

The relaxation function $G_\kappa(\infty,t)$ is given in Fig. 68 as $G_\kappa(\infty,t)$ versus t/τ_κ , with $\tau_\kappa = \eta_\kappa R_\kappa$. This presentation is used by way of comparison with the presentation $G_0(\infty,t)/\eta_0$ versus t/τ_c that should be used with linear viscoelastic materials to obtain a reduced plot expected to be independent of temperature (and concentration as well for some materials). It should be recognized that since τ_κ decreases with increasing κ , for the data shown $G_\kappa(\infty,t)$ actually decreases more rapidly after flow at large κ than after flow at small κ —this is normal behavior. With reference to Fig. 65, it may be seen that $R_\sigma(\infty,t)$ does not reach R_κ until recovery times of order $4\tau_\kappa$. Consequently, it is not unexpected that $G_\kappa(\infty,t)$ has not dropped to zero for $t \sim \tau_\kappa$. (If $G_\kappa(\infty,t)$ was represented by a single relaxation time τ , then $G_\kappa(\infty,t)$ would be e^{-1} for $t = \tau$.)

Taken together, the rheological data on the P(BT-co-BO) polymer in PPA solution indicate liquid behavior, albeit with a high viscosity and long time constant (at 27°C). None of the data require one to consider the existence of a network structure (e.g., as was necessary with the data discussed in section 3.1 of this part).

12.3 Mixtures of Articulated and Rodlike Polymers

Data on η_κ , R_κ , $J_\sigma(t)$, $R_\sigma(t)$ and $G_\kappa(\infty, t)$ for one of the mixtures in solution in MSA discussed in section 3.3 of Part II, and data on $|J_\sigma^*(\omega)|$ and $J_\sigma'(\omega)$ for three of the mixtures are given in Figs. 69 to 74; in each case PBT-53 is the rodlike polymer, and the solutions are nematic at temperatures below about 60°C (see Table 8). The reduced relaxation modulus $G_\kappa(\infty, t)/\eta_\kappa$ are given in Fig. 71. The latter are plotted as a function of t/τ_κ , so that the curves are expected to converge on $G_0(\infty, t)/\eta_0$ versus t/τ_c as κ decreases. Since τ_κ decreases with increasing κ in the range studied, this means of plotting has the effect of reversing the order in which the curves would appear if plotted as $G_\kappa(\infty, t)/\eta_\kappa$ vs t ; e.g., the relaxation is actually faster after steady flow at large κ than for steady flow at very small κ . On the other hand, the curves can be expected to be independent of temperature in the format given, providing the material undergoes no phase transition, etc., as a function of temperature. The data in Fig. 71 show that the relaxation is considerably faster at 52 than at 29°C for fixed κ (and similar τ_κ). The difference may be related to changed morphology in the mixed system.

The data in Fig. 72 show that $|J_\sigma^*(\omega)|$ at 40 and 80°C and $J_\sigma(t)$ at 52°C appear to be similar in the range 0.01 to 0.1 Pa⁻¹, though it appears that η will be larger at 40 than at 52°C—the temperature range for the isotropic to nematic phase transition is 71(I) to 61(N)°C for this mixture. According to the data for this mixture, rather high shear rates will be required to achieve good orientation and orientation will relax rather quickly after cessation of flow.

Data on $|J_\sigma^*(\omega)|$ and $J_\sigma'(\omega)$ are given for two additional mixtures in Figs. 73 and 74. In both cases, the dynamic compliance data show a monotone change with temperature—it is also evident that the range covered by the data are too narrow to permit assessment of parameters such as $|J_\sigma^*(\omega)|$ or $J_\sigma'(0)$.

13. SUMMARY

Rheological data including measurements of the creep, recovery, and dynamic compliances on solutions of an articulated rodlike copolymer in MSA are interpreted in terms of interchain association that is susceptible to cleavage and reformation in flow. Data on solution of an articulated rodlike copolymer in PPA do not exhibit this behavior; the latter give a viscosity proportional to the cube of the polymer concentration. Rheological data are also reported for solutions of rodlike polymers and rodlike copolymers in PPA. The latter is found to exhibit very high viscosity in comparison with previously studied solutions, and long relaxation times for disorientation. Conversely, rheological data on solutions of mixtures of articulated rodlike copolymers and rodlike polymers were characterized by rapid disorientation on cessation of flow.

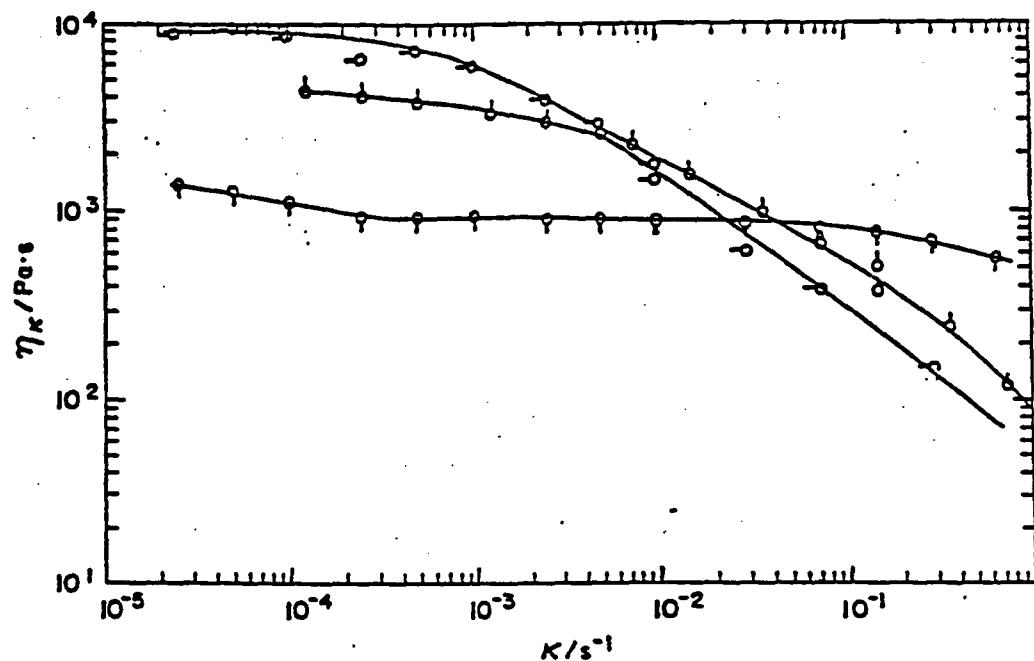


Figure 49:

Steady state viscosity η_K for solutions of articulated PBT copolymers in MSA: O, 388-12 at 0.0674 g/g, 30°C (isotropic); —O, 352-38 at 0.0747 g/g, 28°C (nematic); and ⊖, 352-36 at 0.0740 g/g, 24°C (nematic).

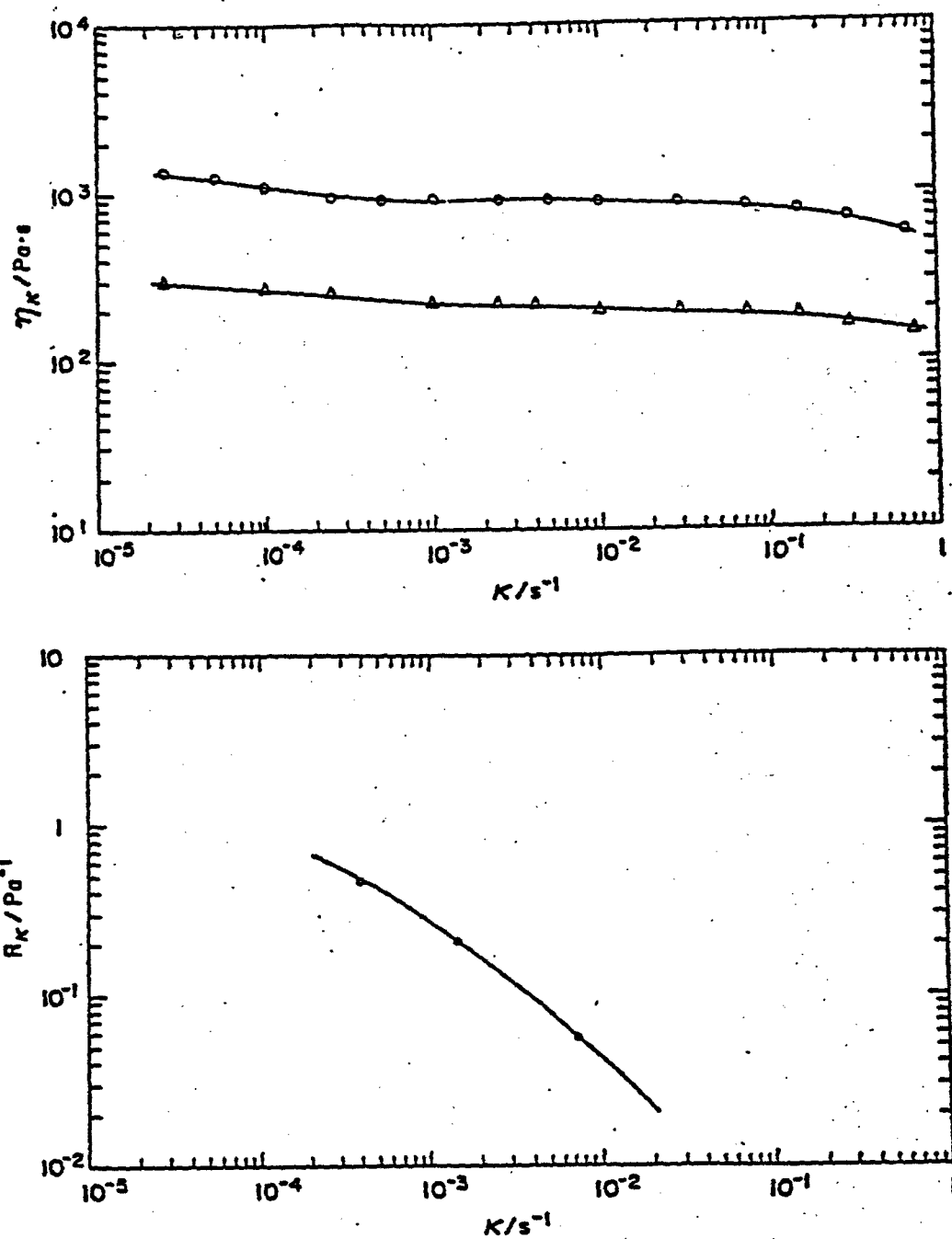
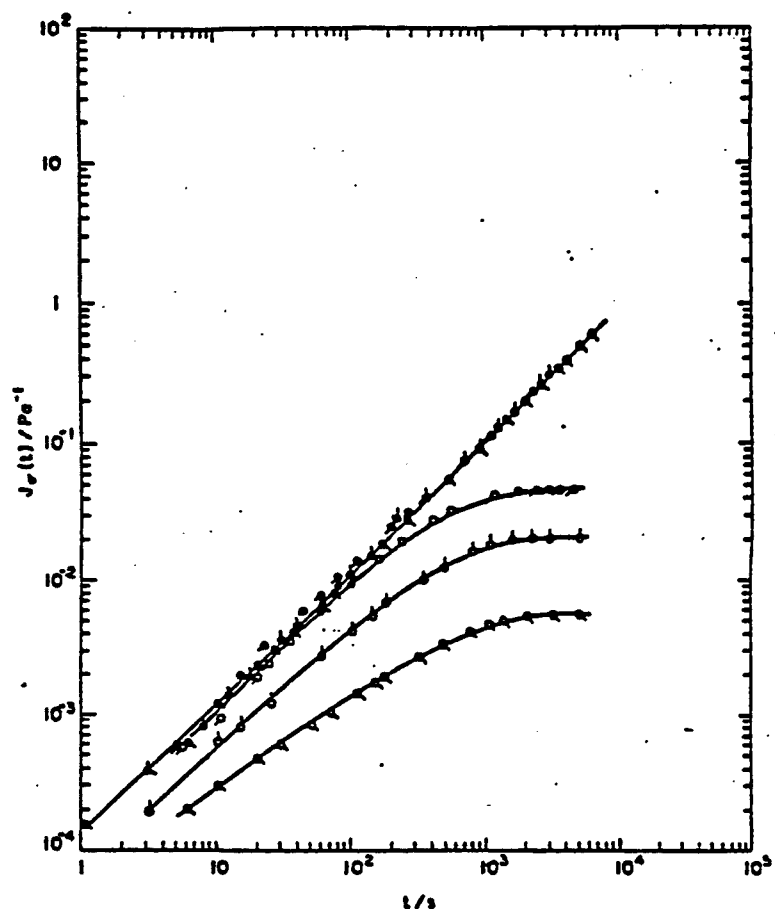


Figure 50:

Steady state viscosity η_K and recoverable compliance R_K for articulated copolymer 388-12 in MSA (0.0674 g/g). O at 30°C and Δ at 51.4°C .

(a)



(b)

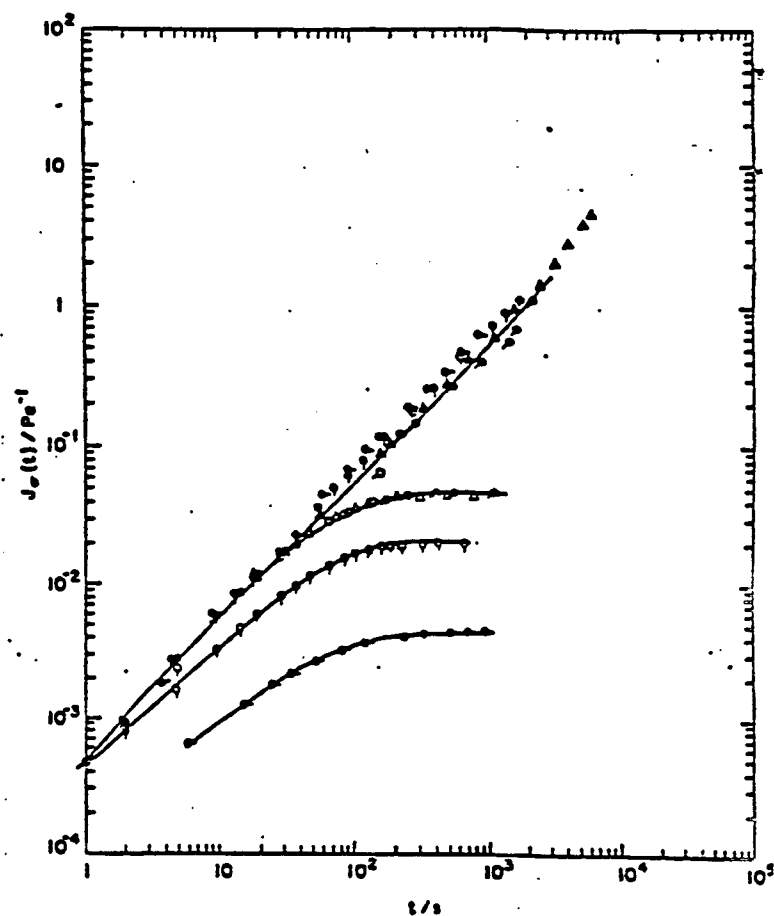


Figure 51:

Creep compliance $J_e(t)$ and recoverable compliance function $R_e(S, \theta)$ for articulated copolymer 388-12 in MSA (0.0674 g/g); the creep duration S may be seen on the figure (e.g. $S \sim 7,000$ s). \otimes for creep and \circ for recovery. Figure a for 30°C , stresses in Pa: \circ , 0.36, \circ , 1.4, \triangle , 6.6; Figure b for 51.9°C , stresses are \circ , 0.36, \circ , 1.4, \triangle , 6.3.

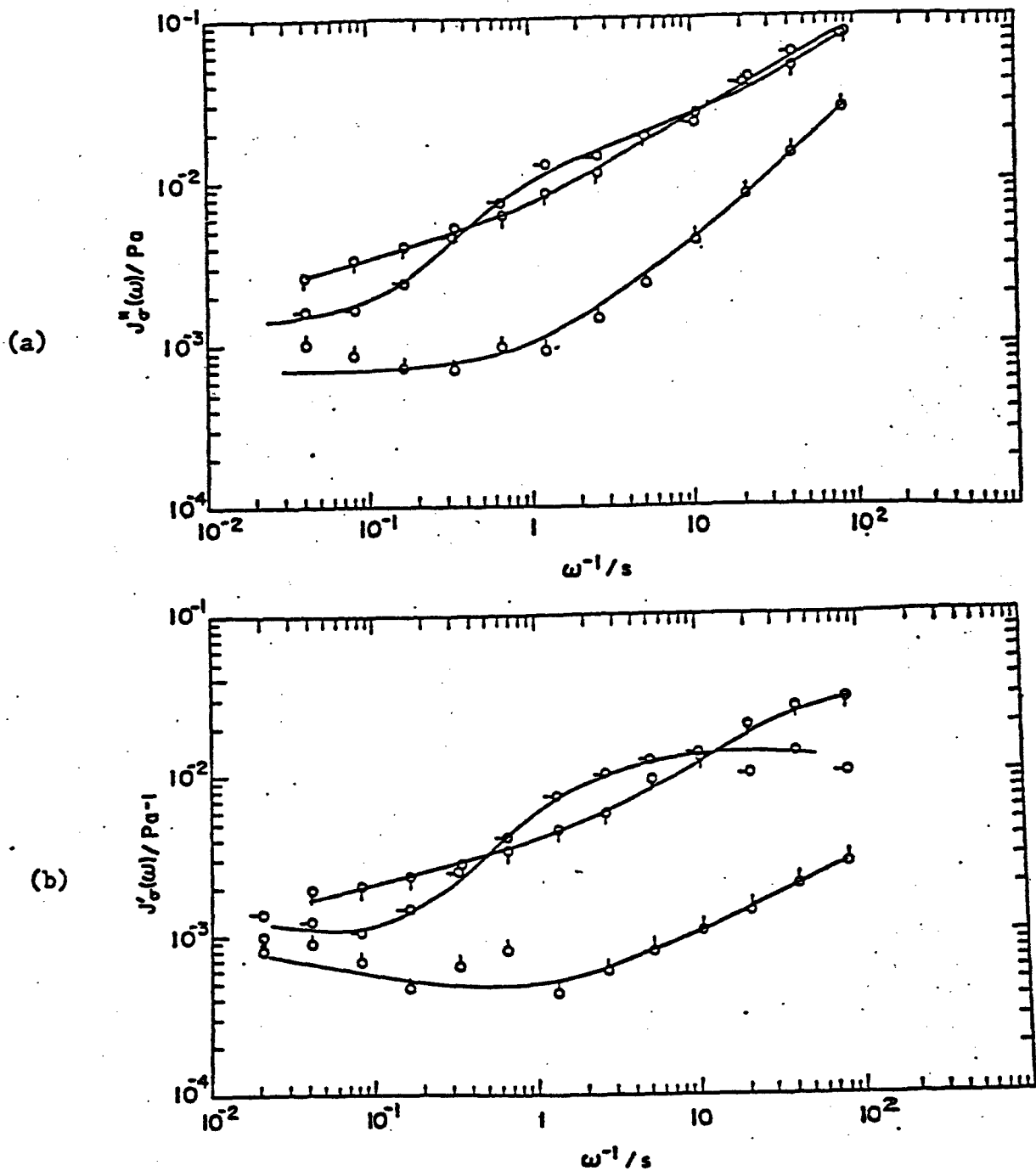
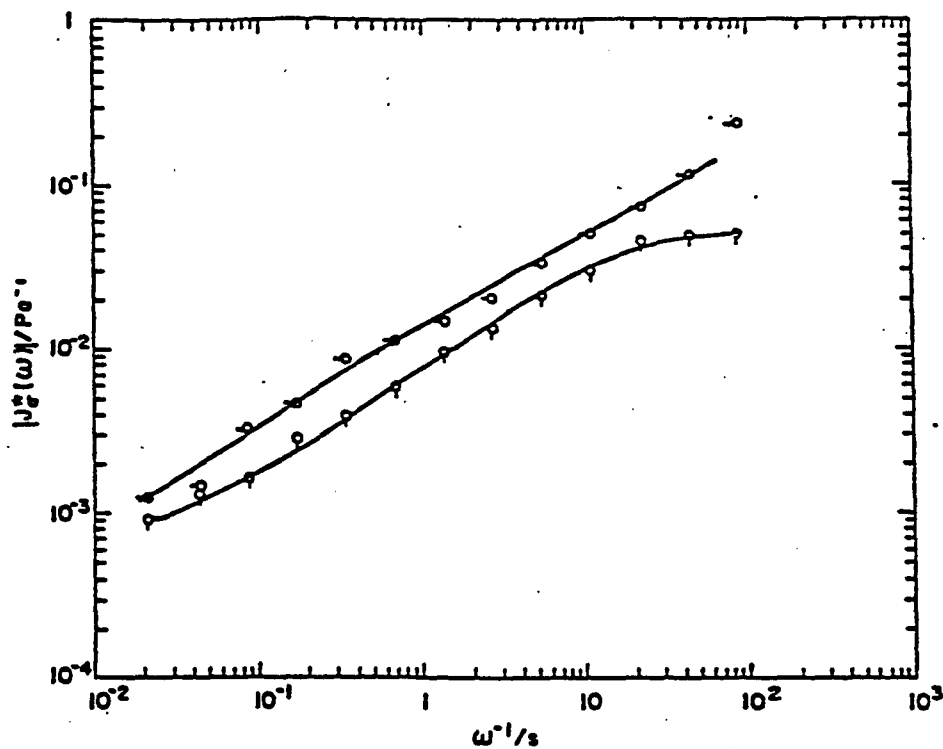


Figure 52:

Dynamic creep compliance $|J_c^*(\omega)|$, a, and storage compliance $J_c'(\omega)$, b, for articulated copolymer 388-12 in MSA (0.0674 g/g), for several temperatures: \circ 5°C, \square 40°C, \triangle 80°C.

(a)



(b)

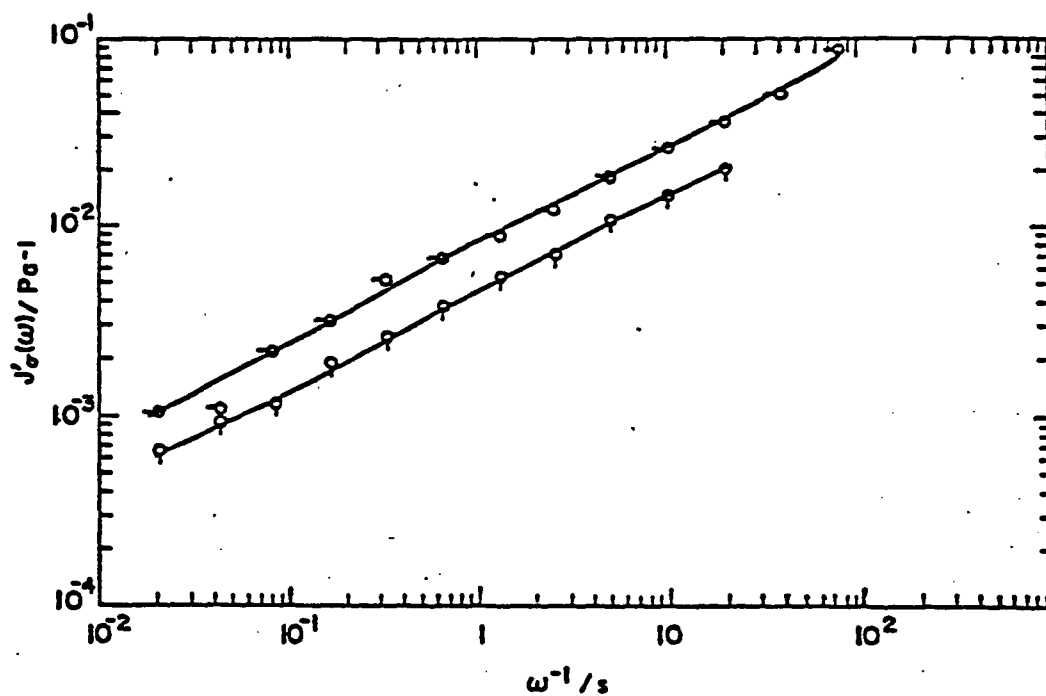


Figure 53:

Dynamic creep compliance $|J_c^*(\omega)|$, a, and storage compliance $J_c'(\omega)$, b, for articulated copolymer 352-38 in MSA (0.0747 g/g) for two temperatures: O, 40°C, Q, 80°C.

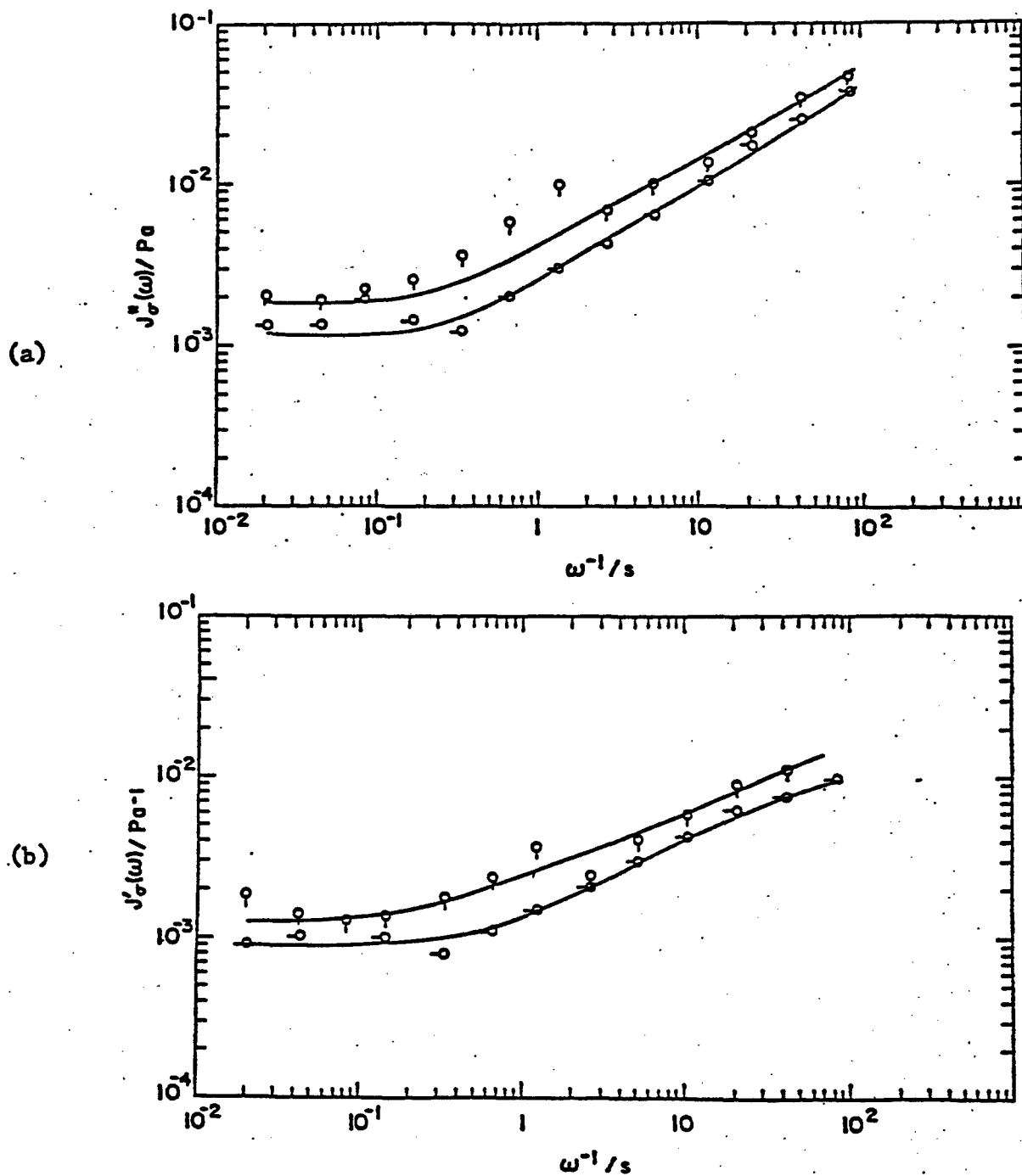


Figure 54:

Dynamic creep compliance $|J_c^*(\omega)|$, a, and storage compliance $J_c'(\omega)$, b, for articulated copolymer 352-34 in MSA (0.0716 g/g) for two temperatures: -O-, 40°C, -Q-, 80°C.

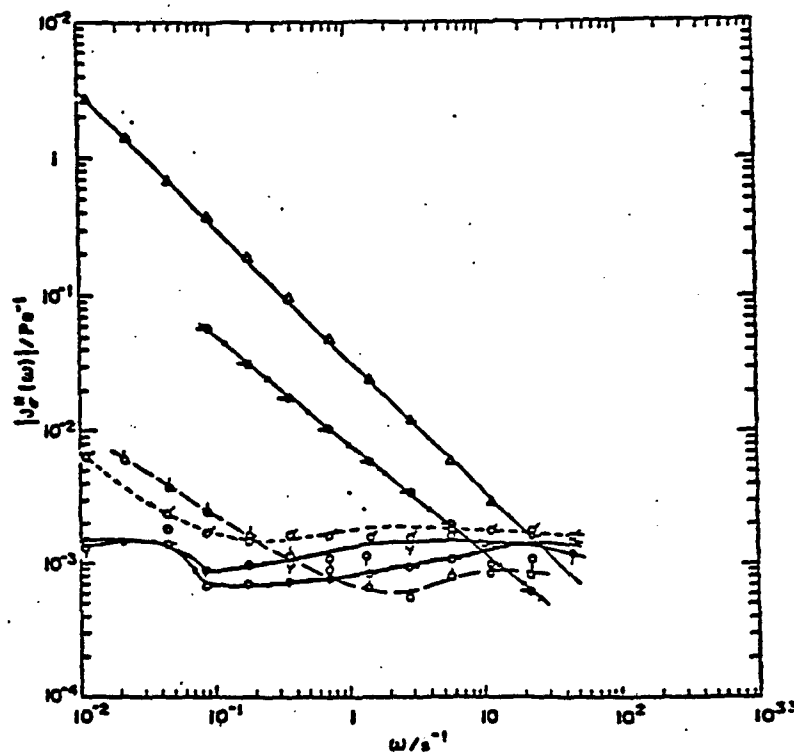


Figure 55:

Dynamic compliance $|J_{\sigma}^*(\omega)|$ for articulated copolymer 388-39 in PPA at 25°C for several polymer concentrations (g/g): Δ , PPA; \circ , 0.0012; \circ , 0.0067; \circ , 0.0161; $\bar{\circ}$, 0.0375; $\bar{\circ}$, 0.0557.

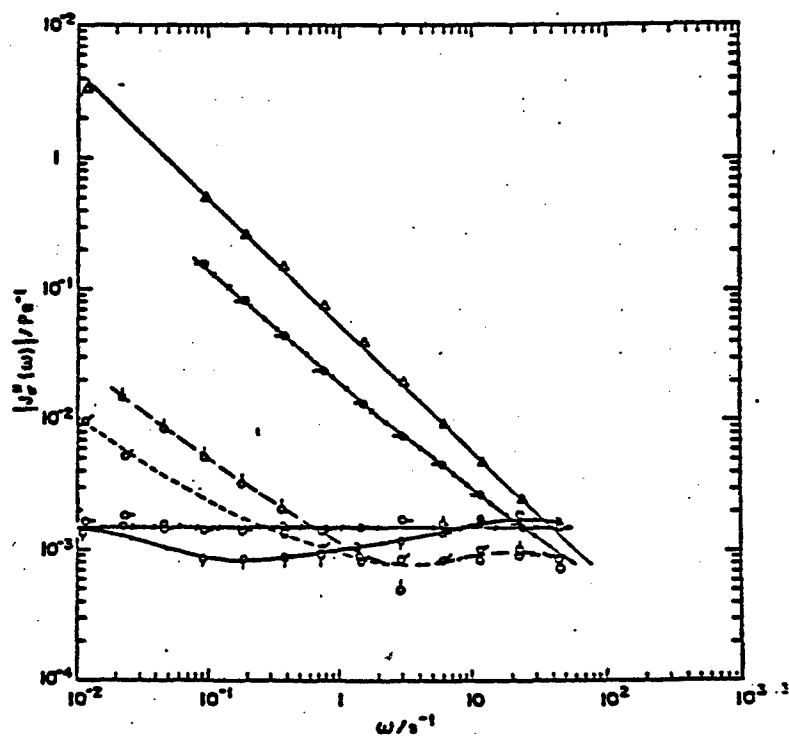


Figure 56:

Dynamic compliance $|J_{\sigma}^*(\omega)|$ for articulated copolymer 388-39 in PPA at 40°C for several polymer concentrations (g/g): Δ , PPA; \circ , 0.0012; \odot , 0.0067; \otimes , 0.0161; \oplus , 0.0375; \square , 0.0557.

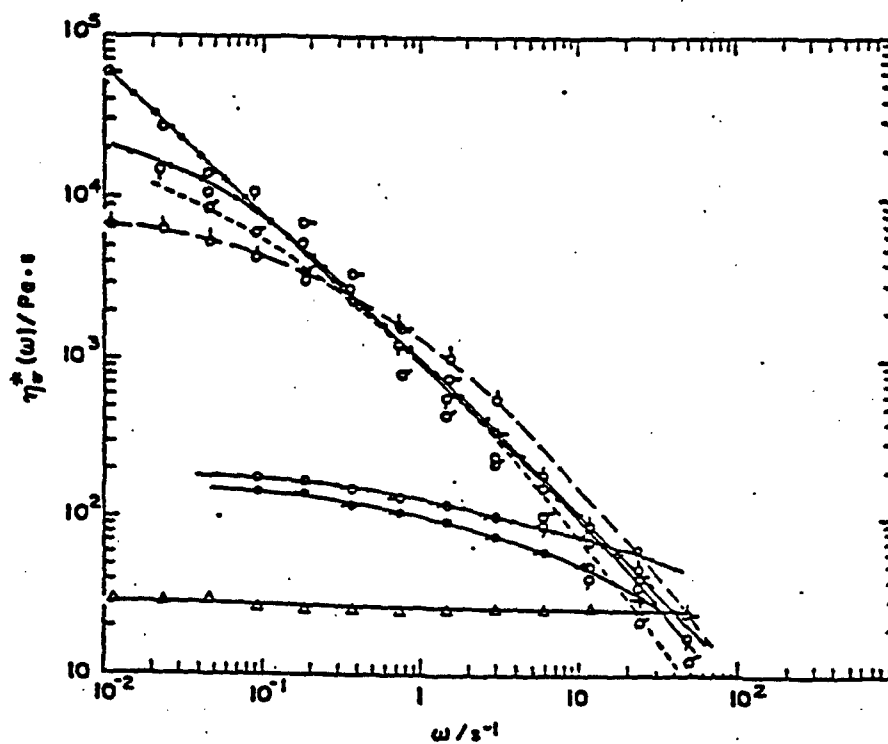


Figure 57:

Dynamic viscosity $|\eta^*(\omega)|$ for the solution identified in Fig. 55 caption. \circ is the excess dynamic viscosity $|\bar{\eta}^*(\omega)| = |\eta^*(\omega)| - |\eta^*(\omega)|_{\text{SOLVENT}}$ for concentration at 0.0012.

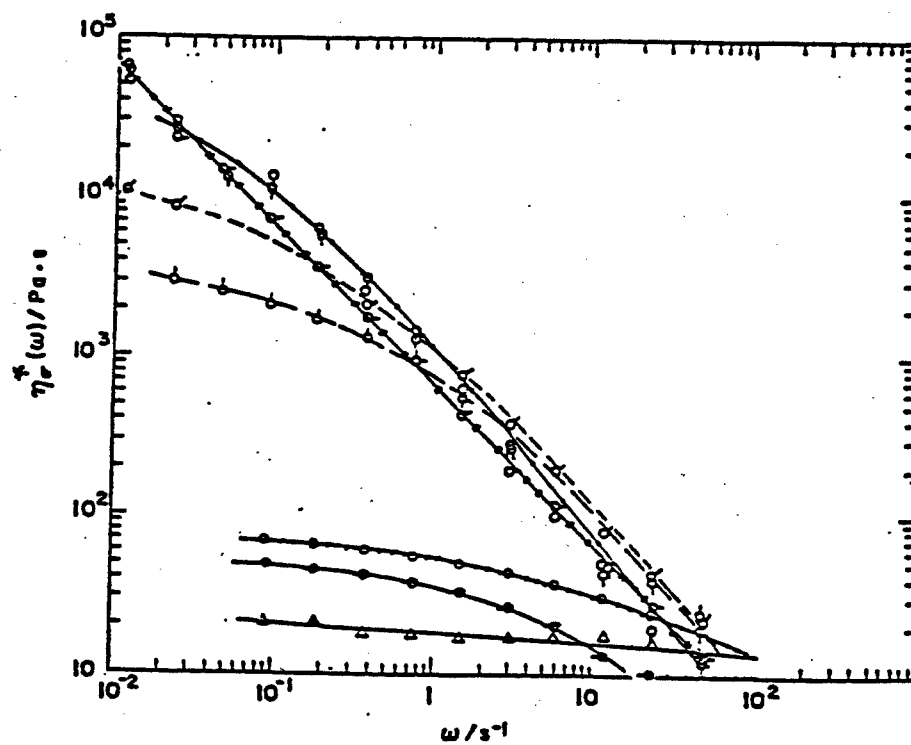


Figure 58:

Dynamic viscosity $|\eta_{\sigma}^*(\omega)|$ for the solution identified in Fig. 56 caption. \bullet is the same as in Fig. 57 caption.

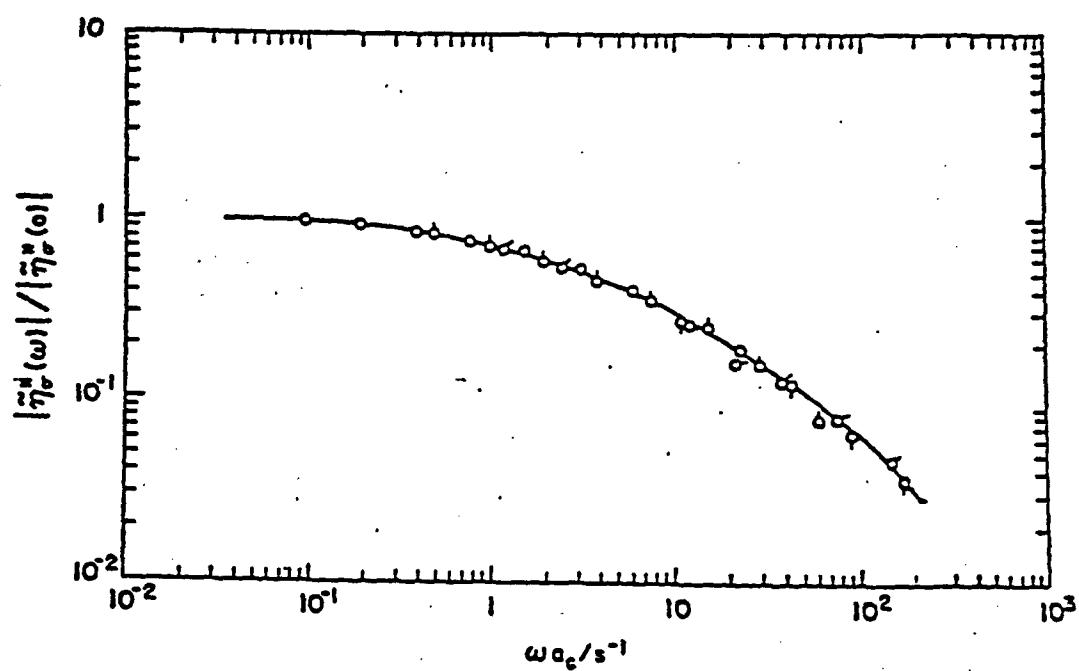


Figure 59:

Reduced plot of $|\bar{\eta}_{\sigma}^*(\omega)| / |\bar{\eta}_{\sigma}^*(0)|$ versus ωa_c for the data given in Fig. 58 (40°C). Values of $|\bar{\eta}_{\sigma}^*(0)|$ used are given in Fig. 60 for solutions with concentrations (g/g): 0.0012 ($a_c=1$), \bullet ; 0.0067 ($a_c = 20$), \circ ; 0.0161 ($a_c = 100$), \circ ; and 0.0375 ($a_c = 500$), \circ .

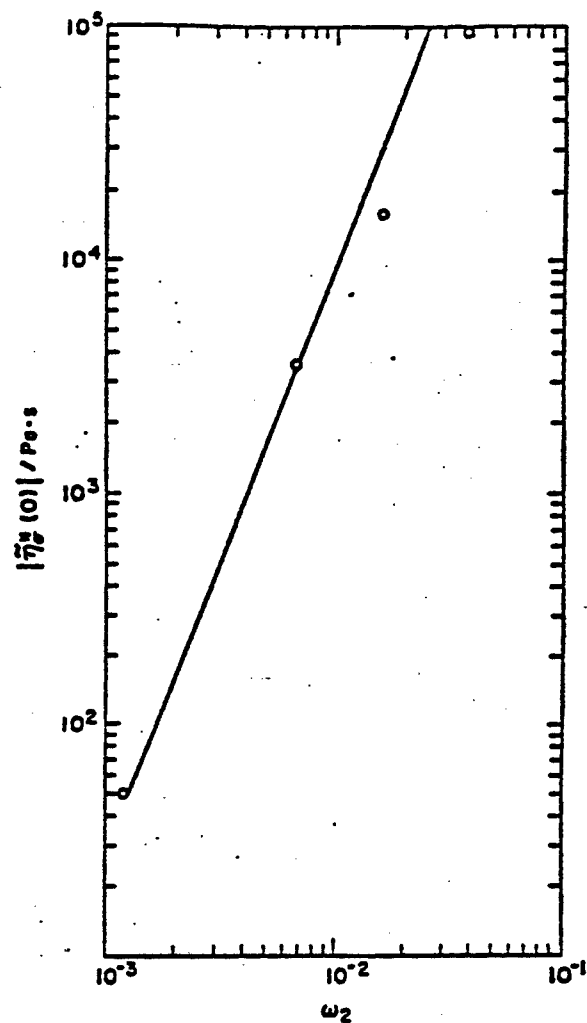


Figure 60:

Excess dynamic viscosity $|\tilde{\eta}_{\sigma}^*(0)|$ as a function of concentration for solutions of articulated copolymer 388-39 in PPA (40°C).

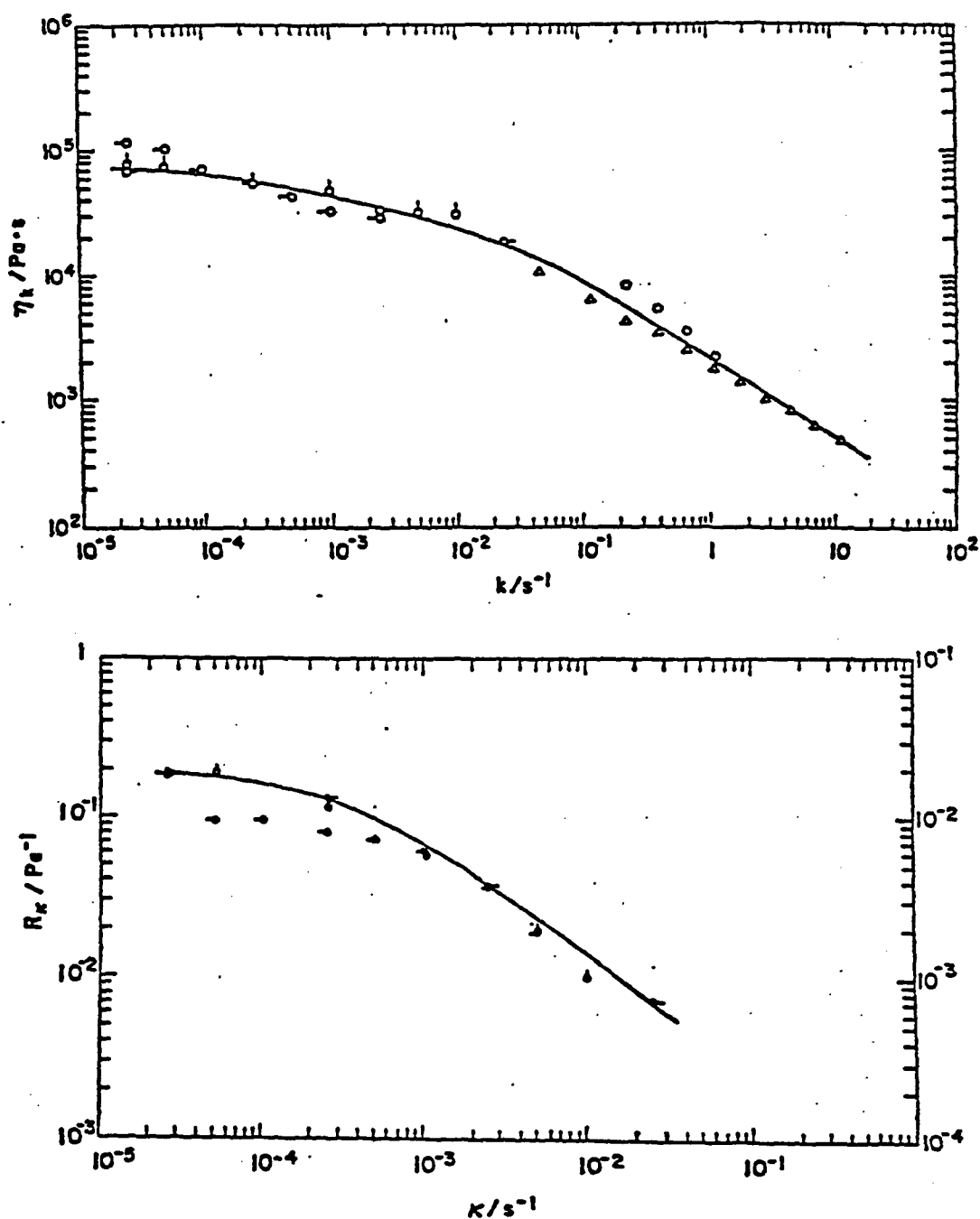


Figure 61:

Steady state viscosity η_K and recoverable compliance R_K for a PBT polymer in PPA at 40°C ; 0.092 g/g for several experiments: \circ , \triangle , \square . Data from rheometric experiments \circ, \triangle .

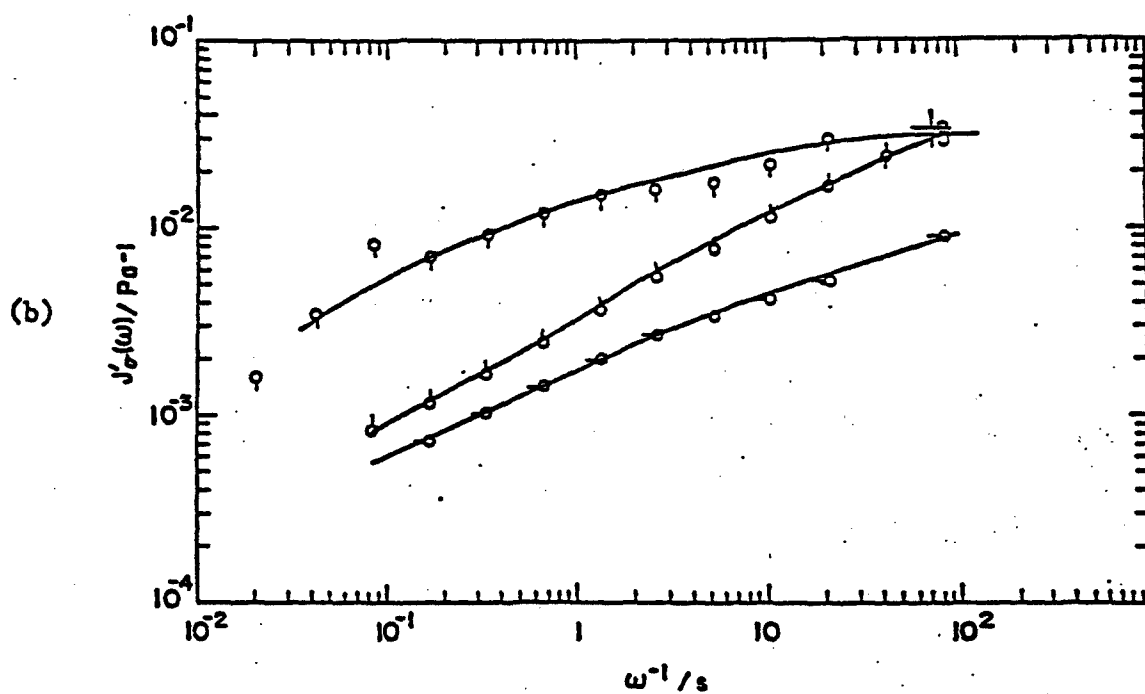
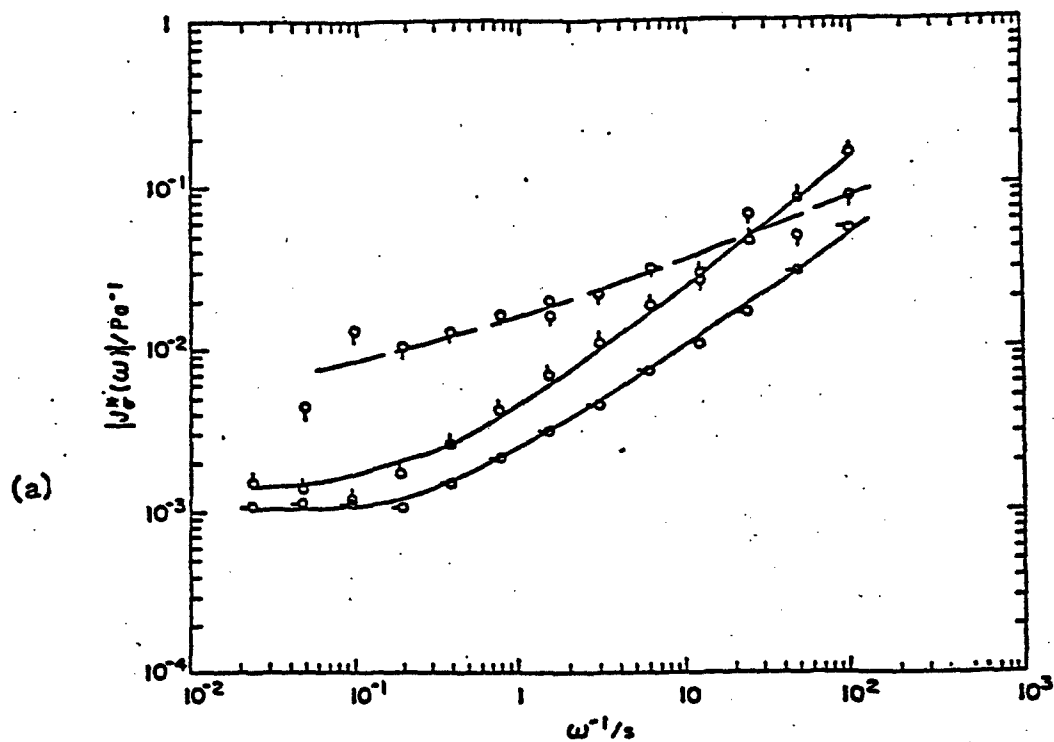


Figure 62:

Dynamic compliance $|J_{\sigma}^*(\omega)|$, a, and storage compliance $J'_{\sigma}(\omega)$, b, for rodlike polymer PBT-53 in MSA (0.0343 g/g), for several temperatures: \circ , 5°C; \circ , 40°C; \odot , 80°C.

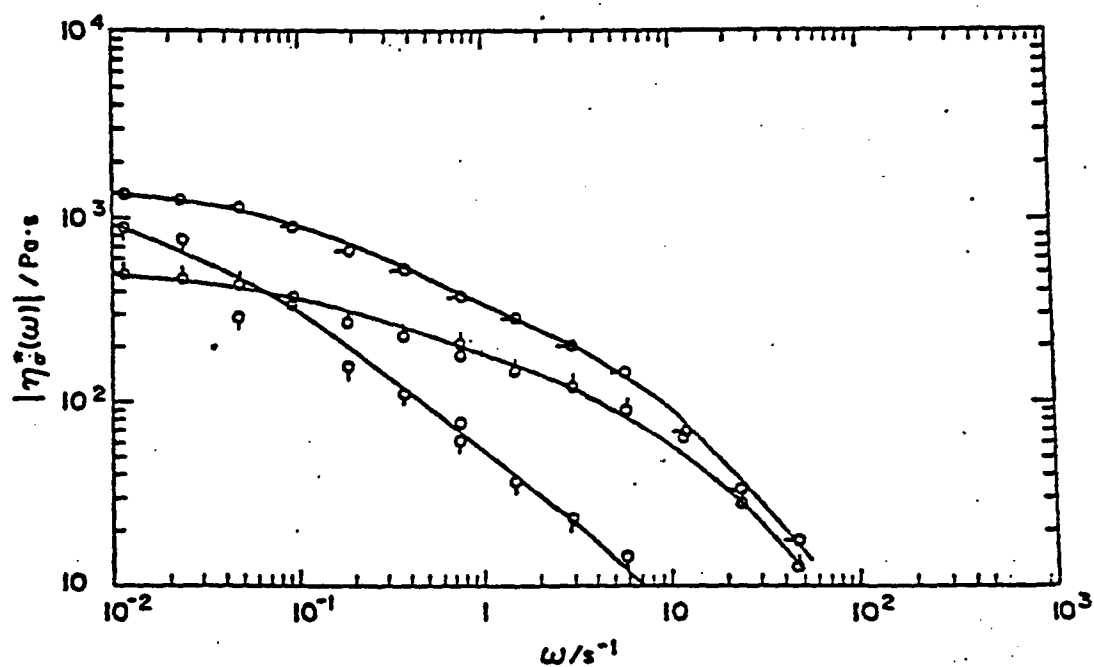


Figure 63:

Dynamic viscosity $|\eta^*(\omega)|$, for rodlike polymer PBT-53 in MSA (0.0343 g/g) for several temperatures: \circ , 5°C; $-O-$, 40°C; ϕ , 80°C

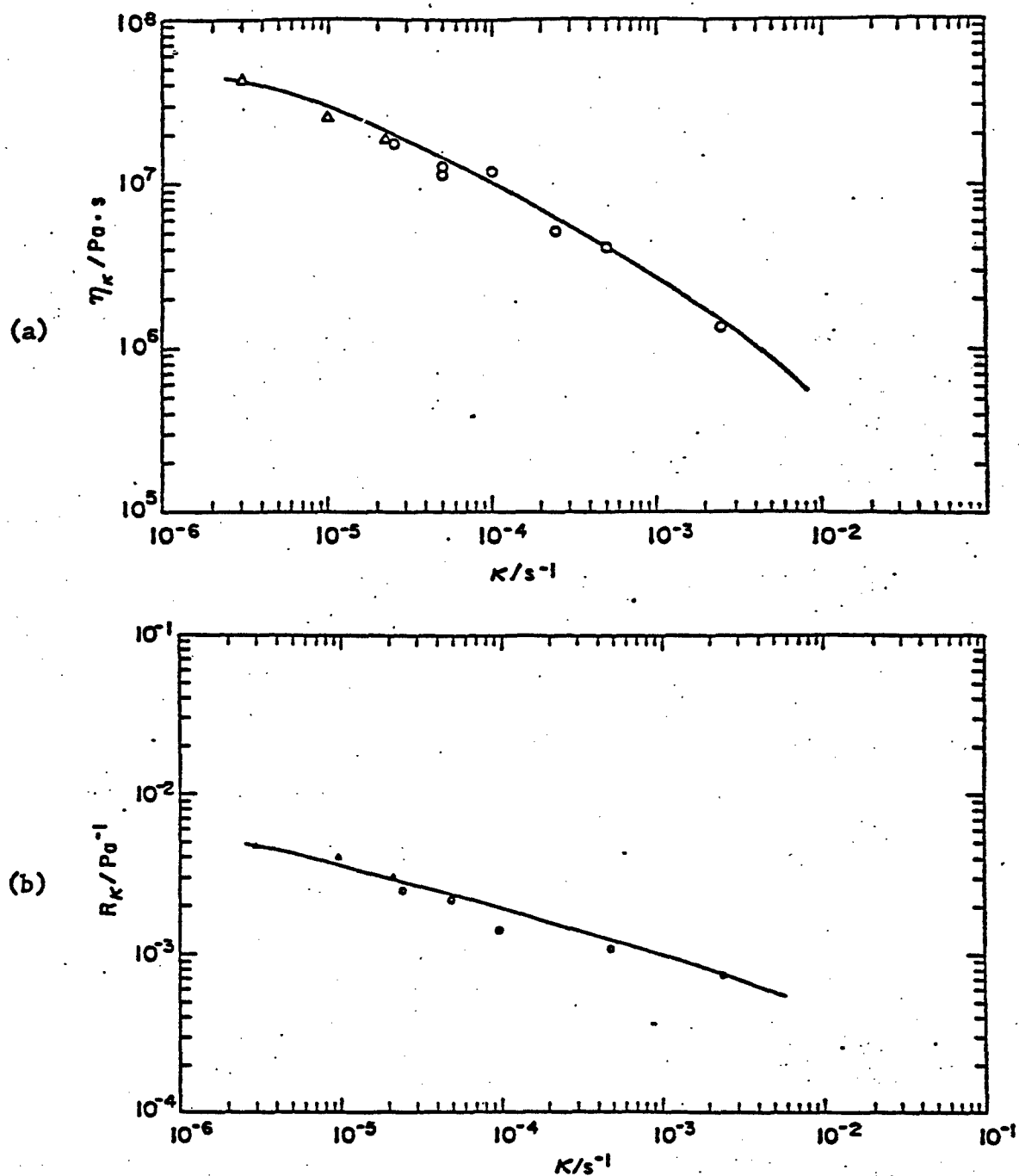


Figure 64:

Steady state viscosity η_K and recoverable compliance R_K for a rodlike PBO-PBT copolymer (0.75 mole fraction PBT), 0.057 g/g in PPA, at 26.6°C. Data from creep experiment Δ .

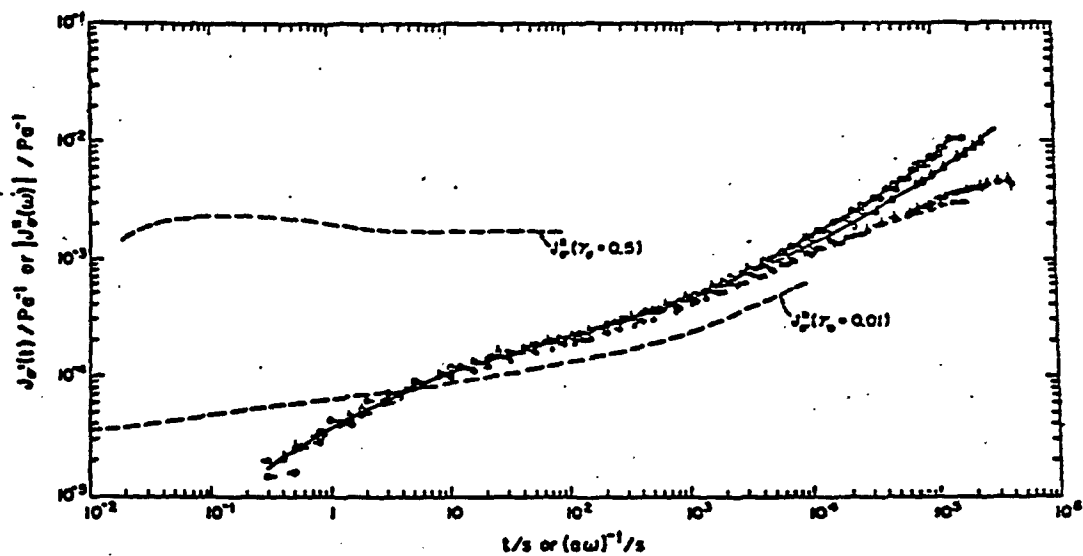


Figure 65:

Creep compliance $J_\sigma(t)$ and recoverable compliance function $R_\sigma(S, t)$ for the solution described in the caption to Fig. 64; the creep duration S may be obtained by inspection of the creep data. Stresses used were 130 Pa, \circ ; 248 Pa, $-o$; and 405 Pa, \circ . The dashed line is $|J_\sigma^*(\omega)|$ versus $(a\omega)^{-1}$ for a deformation with peak-to-peak amplitude 0.01; a_1 is 0.88 at 10°C ; -0.80 at 40°C ; -1.77 at 80°C ; and -1.96 at 100°C .

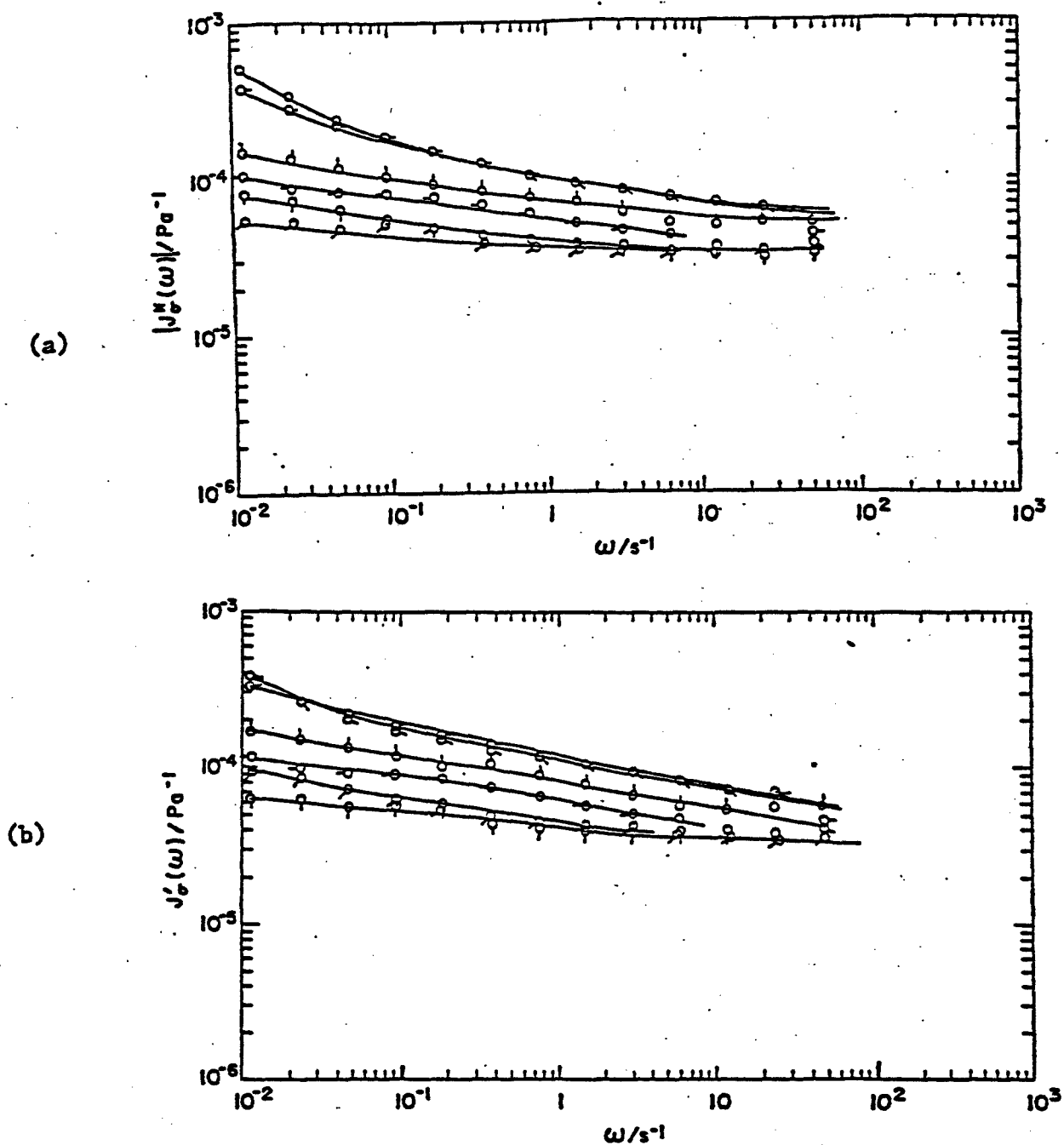


Figure 66:

Dynamic compliance $|J^*(\omega)|$, a, and storage compliance $J''(\omega)$, b, for the rodlike copolymer solution described in the caption to Fig. 64. Data are at -8°C , \circ ; 10°C , \square ; 27°C , \triangle ; 40°C , \diamond ; 80°C , \times ; and 100°C , \circ . In Figure b, -8°C , \circ , 10°C , \square .

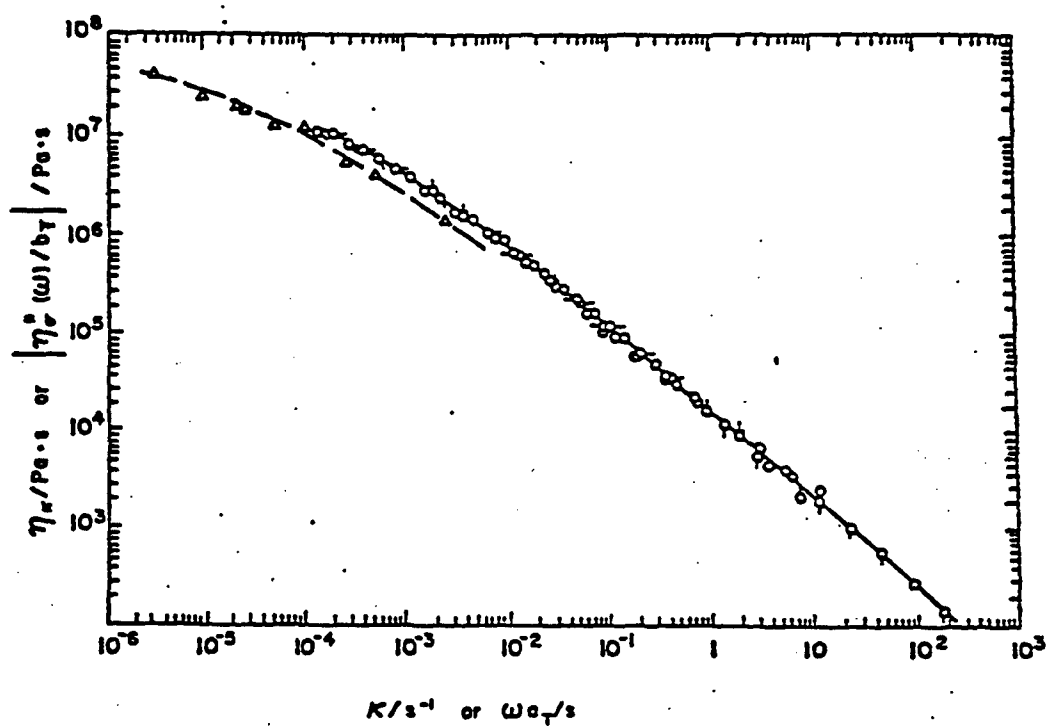


Figure 67:

Steady state viscosity η_K versus (Δ) or dynamic viscosity $|\eta_o^*(\omega)| b_T^{-1}$ versus $a_T \omega$ (O) for solutions of the rodlike copolymer described in Fig. 64. Data on η_K at 27°C ; data on $|\eta_o^*(\omega)| b_T^{-1}$ at 10°C ($a_i = 7.60$), O ; 27°C ($a_i = 1.0$), $-O$; 40°C ($a_i = 0.16$), \dot{O} ; 80°C ($a_i = 0.02$), O ; and 100°C ($a_i = 0.011$), Q .

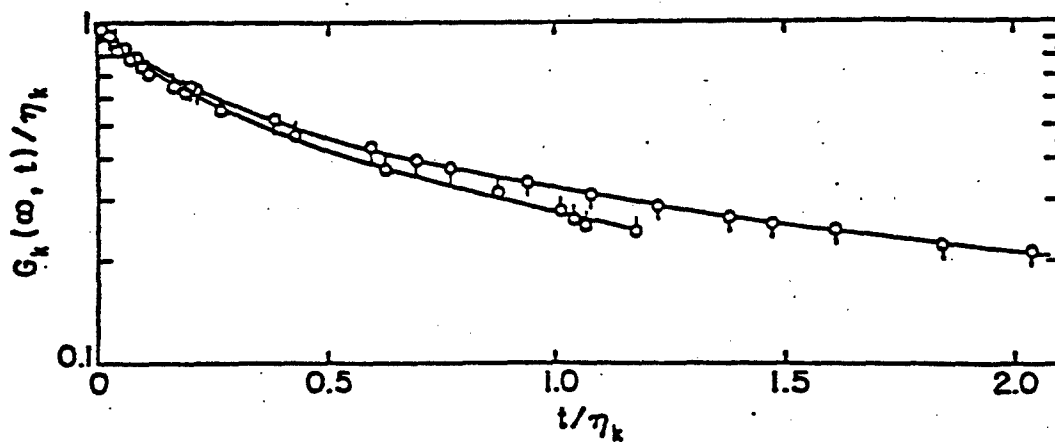


Figure 68:

The relaxation function $G_K(\omega, t)/\eta_K$ versus t/τ_K at 27°C for solutions of the rodlike copolymer described in Fig. 64, for K equal to $5.02 \times 10^{-5}\text{s}^{-1}$, \dot{O} ($\tau_K = 2.74 \times 10^4\text{s}$) $25.1 \times 10^{-5}\text{s}^{-1}$, \dot{Q} ($\tau_K = 0.76 \times 10^4\text{s}$).

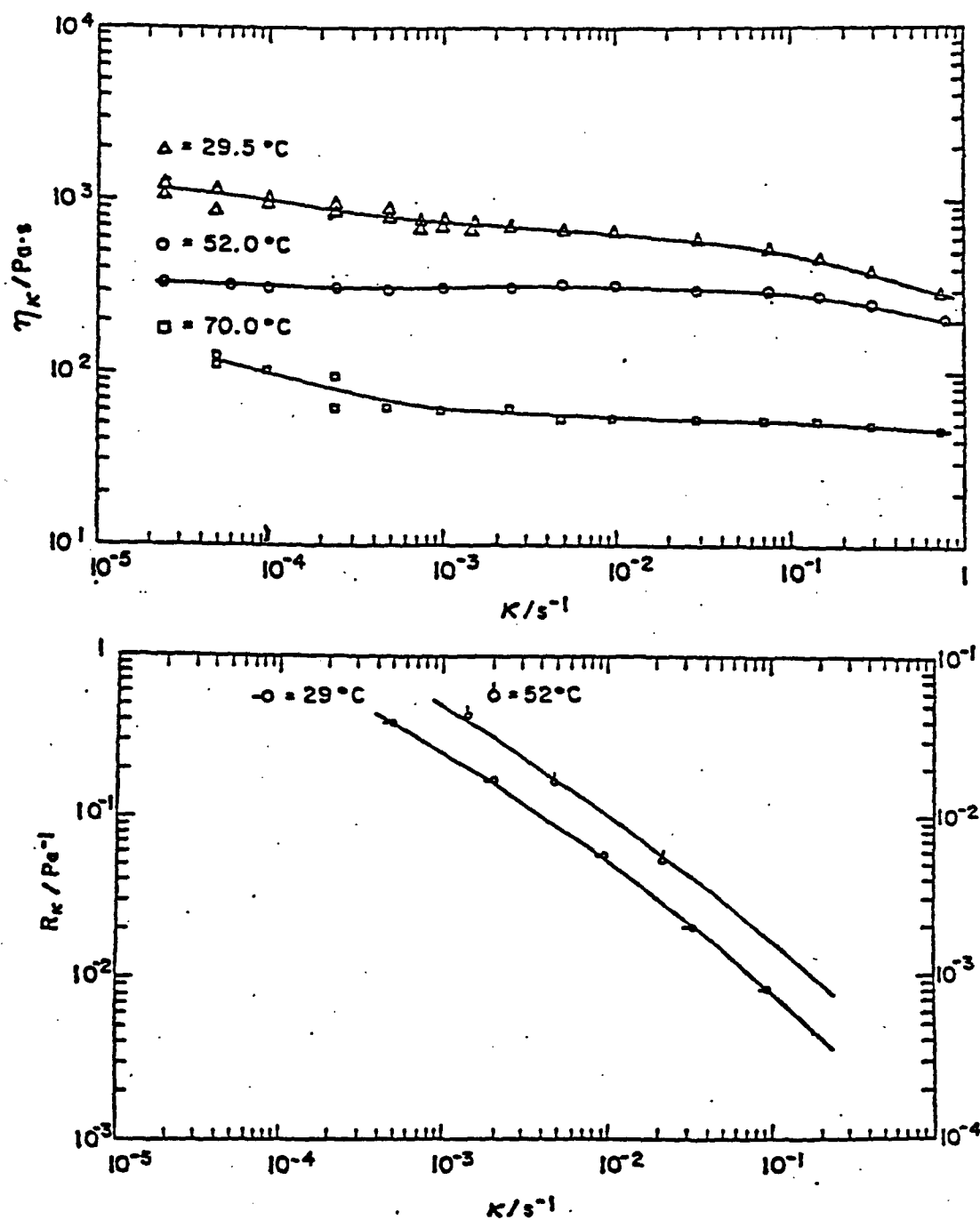


Figure 69:

Steady state viscosity $\eta_{\dot{\gamma}}$ and recoverable compliance $R_{\dot{\gamma}}$ for a mixture of rodlike PBT-53 (0.0105 g/g) and the articulated copolymer 352-34 (0.0395 g/g) in MSA at several temperatures: 29.5 and 52°C, nematic, and 70°C, biphasic.

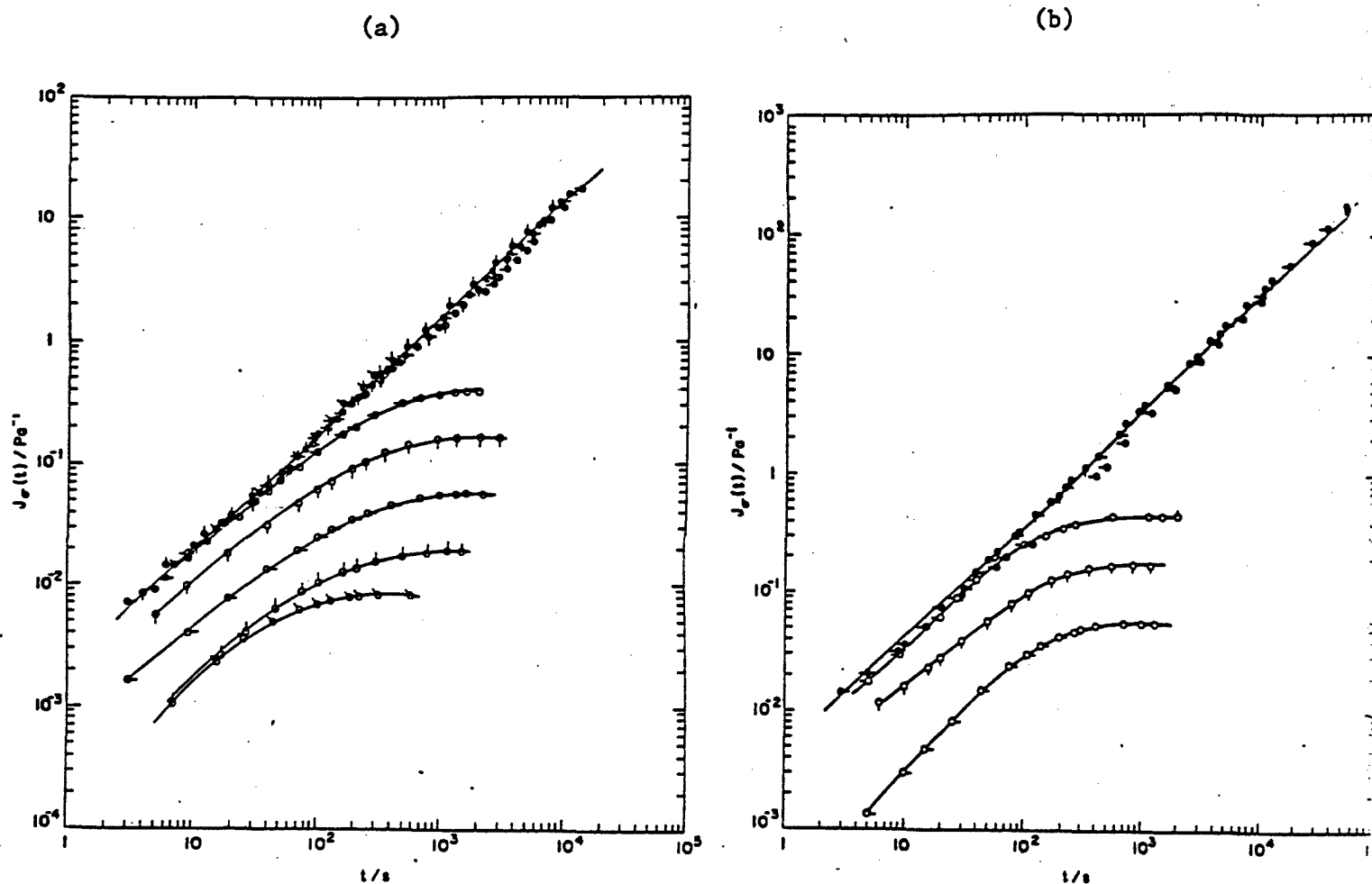


Figure 70:

Creep compliance $J_\sigma(t)$ and recoverable compliance $R_\sigma(S, t)$ for the mixture described in the caption to Fig. 69. The creep duration S may be obtained by inspection of the figure. Stresses used were part a, at (29°C) 0.38 Pa, \circ ; 1.37 Pa, \square ; 6.33 Pa, \triangle ; 19.6 Pa, \diamond ; 48.2 Pa, \times ; part b, (at 52°) 0.42 Pa, \circ ; 1.46 Pa, \square ; 6.57 Pa, \triangle .

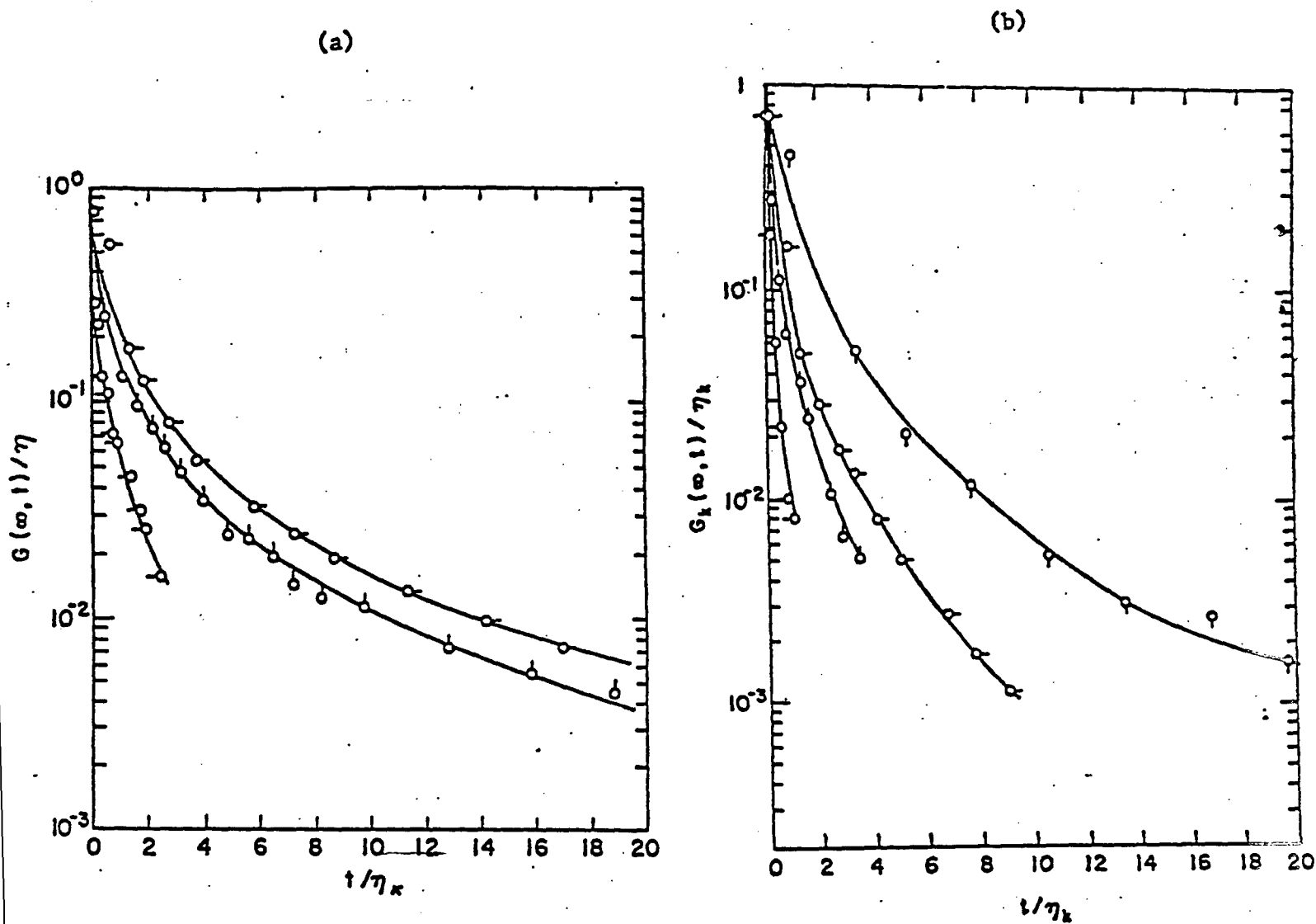


Figure 71:

The relaxation function $G_K(\infty, t)/\eta_K$ versus t/K for the mixture described in the caption to Fig. 69 at 29°C, a, and 52°C, b. In part a, K is 0.00502 s⁻¹ ($\tau_K = 56$ s), -O; 0.0305 s⁻¹ ($\tau_K = 13.25$ s), O; and 0.0752 s⁻¹ ($\tau_K = 6.25$ s), O-. In part b, K is 0.0075 s⁻¹ ($\tau_K = 38.4$ s), -O; 0.030 s⁻¹ ($\tau_K = 13.65$ s), O; 0.0752 s⁻¹ ($\tau_K = 7.1$ s), O-; and 0.3 s⁻¹ ($\tau_K = 2.1$ s), O.

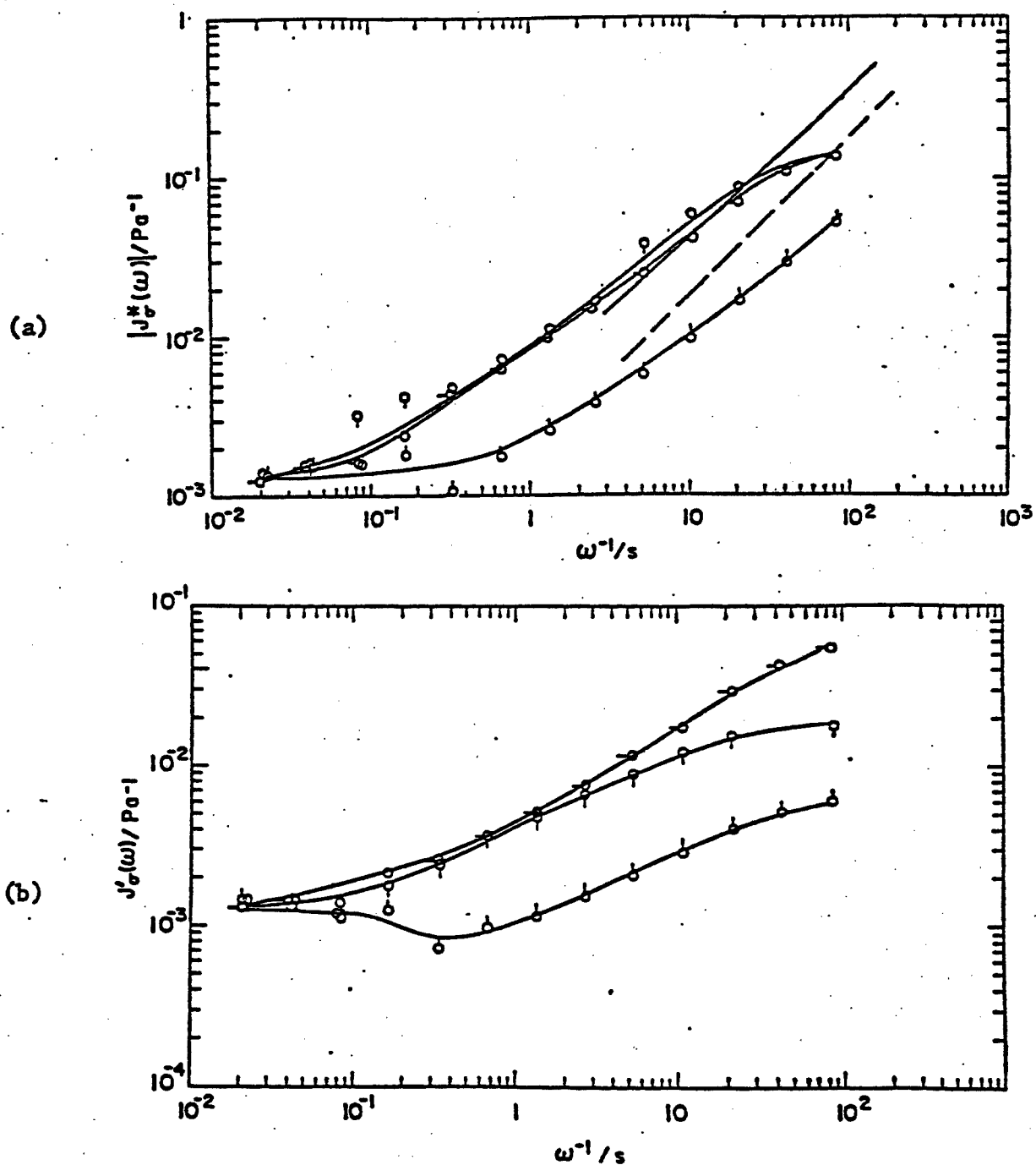


Figure 72:

Dynamic compliance $|J_{\sigma}^*(\omega)|$, a, and storage compliance $J'_{\sigma}(\omega)$, b, for the mixture described in the caption to Fig. 69. Data are at 5°C, \circ ; 40°C, \circ - \circ (both nematic); and 80°C, \circ (isotropic). The lines with no points give $J_{\sigma}(t)$ versus t^{-1} for the same mixture at 52°C, —, and 29°C, —.

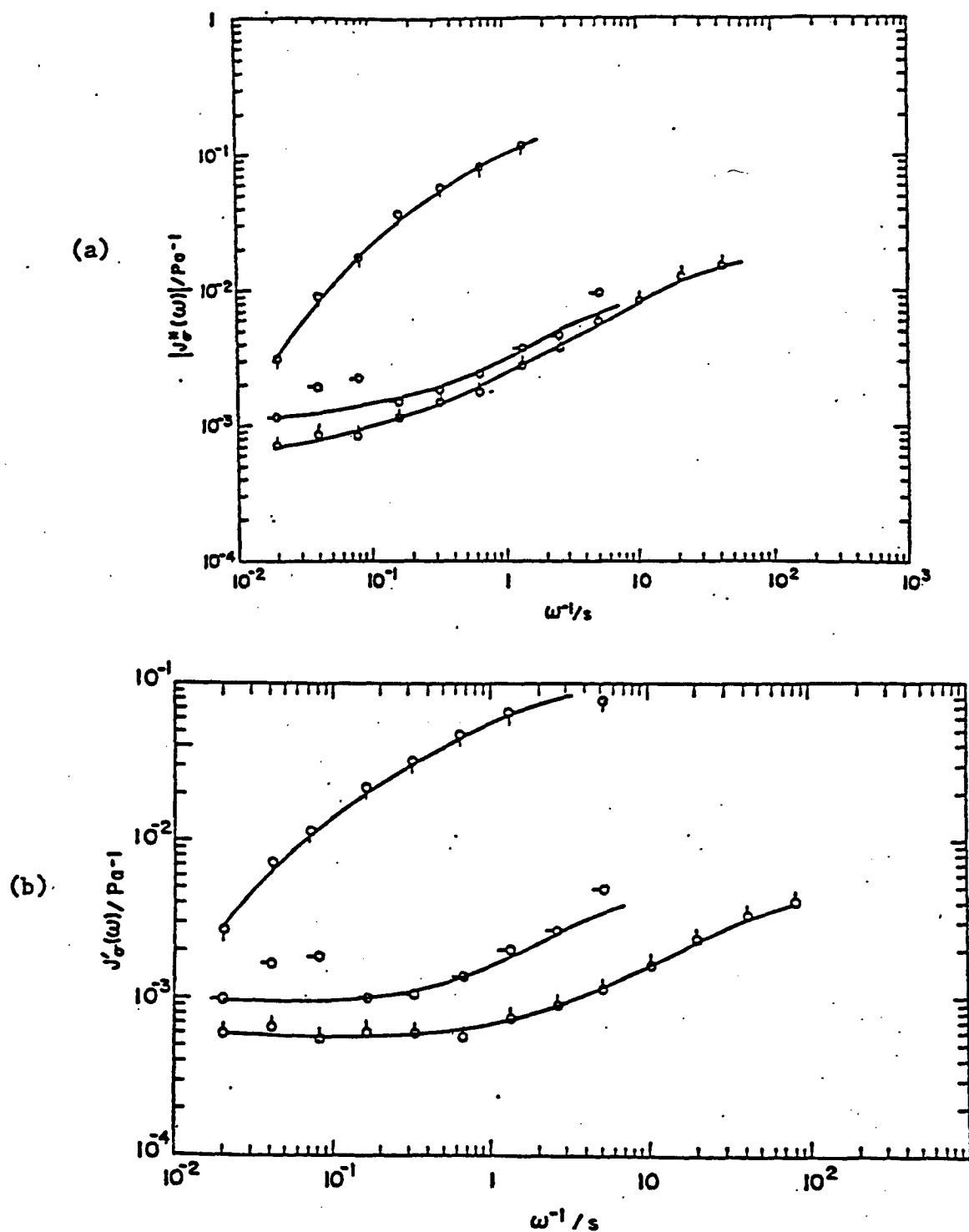


Figure 73:

Dynamic compliance $|J^*(\omega)|$, a, and storage compliance $J'_\sigma(\omega)$, b, for a mixture of the rodlike PBT-53, 0.0118 g/g, and the articulated copolymer 352-4, 0.0341 g/g, in MSA. Data are at 8.5°C, \circ ; 40°C, \circ (both nematic); and 80°C, \square (isotropic).

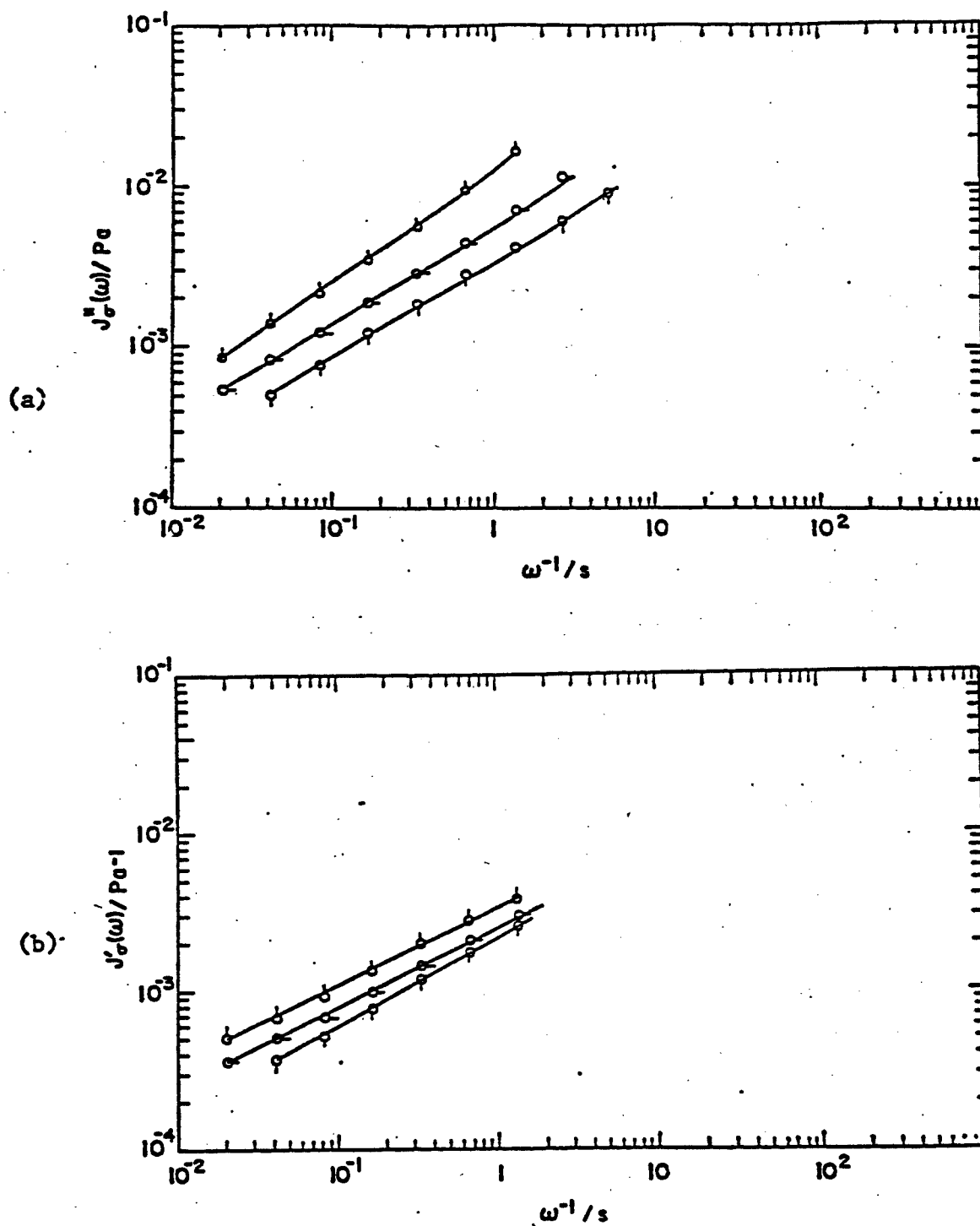


Figure 74:

Dynamic compliance $|J^*(\omega)|$, a, and storage compliance $J'(\omega)$, b, for a mixture of the rodlike PBT-53, 0.0397 g/g, and the articulated copolymer 352-4, 0.0132 g/g, in MSA. Data are at 40°C, Q (nematic); 63°C, O- (biphasic); and 80°C, O (isotropic).

IV PROCESSING OF ARTICULATED POLYMERS

14. INTRODUCTION

The ribbon fabrication apparatus designed, constructed and modified in this laboratory has earlier been used to fabricate ribbons of rodlike polymers from solutions in different solvents. During this report period the work has been concentrated on the preparation of polymer solutions in appropriate solvents, and then processing these to fabricate ribbons using the modified fabrication apparatus. The polymers used in the present study are as follows:

1. SPBT 388/88
2. PBT/PBO (75:25) copolymer solution in PPA (5.7%)
3. PBT/PBO (90:10) copolymer solution in PPA (7.75%)

The SPBT articulated polymer was received as a solid, whereas the copolymers PBT/PBO were received as solutions in PPA, directly from the respective polymerization batches.

15. RIBBON FORMATION APPARATUS

A schematic drawing of the apparatus used for fabrication is given in a previous report³⁰ and the details are described in earlier reports. The principle of the ribbon formation apparatus involves molecular orientation of a solution in a shear flow, followed by coagulation in a time short in comparison with the disorientation relaxation time. The solution is forced into the space between a stationary plate and a moving mylar tape. In the present study the polymer solution in the syringe was heated by wrapping with heating coil. The shear plate I was also heated by circulating hot oil (110°C) through small heat exchanger placed in the shearing compartment, touching the back of the plate I. The speed of the syringe plunger was adjusted to such a rate that no overflowing of the polymer solution takes place at the exit point in shearing plate as seen through the glass window.

15.1 Ribbon Fabrication

15.2 SPBT Articulated Polymer

A homogeneous solution of dried SPBT polymer in methane sulfonic acid (0.075 weight fraction polymer) was prepared by stirring the mixture at 110°-120° for one week. The polymer solution was transferred to a syringe under nitrogen atmosphere. After initial trial experiments, the polymer solution was processed to obtain a ribbon which coagulated easily in water. The ribbon came off nicely from the carrier mylar tape and had a deep orange color. The sample showed birefringence when examined under a microscope. However, the ribbon in the dry state was extremely brittle and easily fractured; consequently, it was not possible to study tensile creep properties at this point. Samples of the ribbon have been sent to the University of Massachusetts for X-ray characterizations.

15.3 Fabrication of PBT/PBO Copolymers

a) PBT/PBO (75:25) 5.7% Polymer by Weight in PPA

Attempts to process this solution are summarized in Table 12. The copolymer PBT/PBO received from SRI was still dissolved in the polymerization solvent PPA, and had a very high viscosity (section 12.2.3). The polymer solution does not show any sign of flowing, even at temperatures up to 150°C. As such, it was not possible to process this solution for ribbon making. Attempted dilution of the copolymer with more PPA failed to result in a

homogeneous solution. In fact, it was not possible to break up the lumps by stirring at elevated temperature (150°) for long periods of time. Further efforts were directed to make solution in methane sulfonic acid. Dilution of the copolymer (3% polymer weight) did not yield a homogeneous solution. Further addition of MSA to 1.8% and 1.4% level resulted in homogeneous solutions. The ribbons were fabricated from these solutions. The shearing compartment was held at 110° for this experiment. Ribbons were quenched in water. Ribbons show birefringence but were mechanically weak.

b) PBT/PBO (90:10) Copolymer 7.75% in PPA

This copolymer was also received from SRI research laboratory, dissolved in the polymerization solvent PPA. A number of trials were made to prepare homogeneous solutions of this polymer in methane sulfonic acid (Table 12). At 3% by weight dilution in MSA no significant homogeneity was achieved. Lowering the polymer content to ~ 2% in MSA resulted in non-homogeneous solutions in two cases. The greenish-yellow solution looked like a suspension and would not undergo dissolution after stirring at 130-140° for two weeks. Finally, a homogeneous solution of the copolymer (2% by weight) was prepared and processed. The ribbon was quenched in water and comes off easily from the mylar tape. Surprisingly the color of the film was yellowish-orange rather than deep orange as obtained in the case of SPBT and PBT/PBO (75:25) polymers. Sampled showed very weak birefringence.

Since it is not possible to achieve a homogeneous solution of the copolymers at concentration higher than 2%, further efforts should include examination of variations in ribbon making parameters. Efforts are underway to increase the gap between mylar tape and stationary plate I, by making the groove in stainless steel plate I deeper. This way we should be able to load more fluid on to the moving mylar tape, resulting in thicker and stronger ribbons after coagulation. Rheological study of the solutions made and characterization of the ribbons to evaluate the modulus as processed are in progress.

Table 12: SUMMARY OF PROCESSING EXPERIMENTS

Polymer	Solvent ^(a)	Concentration by weight	Solution	Processing
388-38	MSA	7.5	Homogeneous	Orange color ribbon
	MSA	7.5	"	"
PBT/PBO	PPA	3.0	Non-homogeneous	Not suitable
75:75	MSA	3.0	"	"
5.7% in PPA	MSA	1.89	Homogeneous	Orange color ribbon very thin in thickness
	MSA	1.41	"	"
PBT/PBO	MSA	3%	Non-homogeneous	X
90/10	MSA	2.0	"	X
7.75% in	MSA	2.0	Dull greenish	Coagulation not good dull greenish film
PPA	MSA	2.10	Homogeneous	Yellowish-orange ribbon

(a) MSA = methane sulfonic acid
PPA = polyphosphoric acid

16. SUMMARY

A special ribbon forming apparatus has been used to process solutions of rodlike polymers, rodlike copolymers, and articulated rodlike copolymers into oriented ribbons. Orientational relaxation was too rapid with the articulated polymers to permit successful processing with the apparatus in hand, and the rodlike copolymers did not appear to give homogeneous solutions, with consequential degradation of the orientation achieved in flow.

V APPENDIX

17. THE THIRD FACTORIAL MOMENT TO THE PHOTON COUNT DISTRIBUTION

The third factorial moment $n^{(3)}(\Delta\tau)-1$ is calculated from Eqs. (9) and (12) as:

$$\begin{aligned}
 n^{(3)}(\Delta\tau)-1 = & 4f(A) \left\{ \sum_{i,j,k} r_i r_j r_k \left[\frac{(\gamma_i + \gamma_j)(\gamma_j + \gamma_k)(\gamma_k + \gamma_i)}{2(\gamma_i + \gamma_j + \gamma_k)} \right. \right. \\
 & - \frac{(\gamma_i + \gamma_j)^2(2\gamma_k + \gamma_i + \gamma_j) + (\gamma_j + \gamma_k)^2(2\gamma_i + \gamma_j + \gamma_k) + (\gamma_k + \gamma_i)^2(2\gamma_j + \gamma_k + \gamma_i)}{(\gamma_i + \gamma_j)^2(\gamma_j + \gamma_k)^2(\gamma_k + \gamma_i)^2} \\
 & + \frac{(2\gamma_k - \gamma_i - \gamma_j)e^{-\gamma_i + \gamma_j}}{(\gamma_i + \gamma_j)^2(\gamma_k - \gamma_i)(\gamma_k - \gamma_j)} + \frac{(2\gamma_i - \gamma_j - \gamma_k)e^{-\gamma_j + \gamma_k}}{(\gamma_j + \gamma_k)^2(\gamma_i - \gamma_j)(\gamma_i - \gamma_k)} + \left. \frac{(2\gamma_j - \gamma_k - \gamma_i)e^{-\gamma_k + \gamma_i}}{(\gamma_k + \gamma_i)^2(\gamma_j - \gamma_k)(\gamma_j - \gamma_i)} \right] \\
 & + 3(1-r) \sum_{i,j} r_i r_j \left[\frac{2}{\gamma_i \gamma_j} - \frac{2(\gamma_i + \gamma_j)}{\gamma_i^2 \gamma_j^2} + \frac{1}{\gamma_i \gamma_j (\gamma_i + \gamma_j)} \right. \\
 & + \frac{(2\gamma_i - \gamma_j)e^{-\gamma_i}}{\gamma_i^2 \gamma_j (\gamma_j - \gamma_i)} + \frac{(2\gamma_j - \gamma_i)e^{-\gamma_j}}{\gamma_i \gamma_j^2 (\gamma_i - \gamma_j)} - \left. \frac{e^{-\gamma_i + \gamma_j}}{\gamma_i \gamma_j (\gamma_i + \gamma_j)} \right] \Big\} \\
 & + 6f(A) \left\{ \sum_{i,j} r_i r_j \left[\frac{1}{(\gamma_i + \gamma_j)} - \frac{1}{(\gamma_i + \gamma_j)^2} + \frac{e^{-\gamma_i + \gamma_j}}{(\gamma_i + \gamma_j)^2} \right] \right. \\
 & + 2(1-r) \sum_i r_i \left(\frac{1}{\gamma_i} - \frac{1}{\gamma_i^2} + \frac{e^{-\gamma_i}}{\gamma_i^2} \right) \Big\}
 \end{aligned}$$

Here $f(A)$ is a coherence factor determined by the detector optics.

18. COMPILATION OF RHEOLOGICAL TERMS, SYMBOLS AND RELATIONS

18.1 Basic Experiments and Material Properties

The viscoelastic properties of a material are most readily defined in terms of a few basic experiments:

1) Creep experiment. A shear stress σ is applied at a time $t=0$ and maintained constant thereafter. The strain $\gamma_\sigma(t)$ for times, $t > 0$, defines the *shear creep compliance* $J_\sigma(t)$:

$$\gamma_\sigma(t) = \sigma J_\sigma(t) \quad (A1)$$

For some materials, called *viscoelastic fluids*, in a creep experiment, a steady state is reached. The rate of shear $d\gamma_\sigma(t)/dt$ approaches a constant value κ as t increases indefinitely. The *viscosity function* η_κ is defined as

$$\eta_\kappa = \sigma / \kappa \quad (A2)$$

2) Recovery experiment. After a creep experiment has proceeded until $t = S$, the shear stress is then removed. From the shear strain at a time θ after the stress is removed, the *recoverable strain* $\gamma^R(S, \theta)$ is defined as

$$\gamma^R(S, \theta) = \gamma_\sigma(S) - \gamma_\sigma(S + \theta) \quad (A3a)$$

and the *recovery function* $R_\sigma(S, \theta)$ is defined:

$$R_\sigma(S, \theta) = \gamma^R(S, \theta) / \sigma \quad (A3b)$$

If the creep of a viscoelastic fluid is permitted to continue until the steady state with the shear rate κ is reached ($S \rightarrow \infty$) and then a recovery experiment is allowed to continue indefinitely ($\theta \rightarrow \infty$), then $R_\sigma(S, \theta)$ approaches a limit called the *steady state recoverable shear compliance* R_κ :

$$R_\sigma(\infty, \infty) = R_\kappa \quad (\text{A4})$$

3) Stress relaxation experiment. A shear strain γ is applied at $t = 0$ and maintained constant thereafter. The shear stress $\sigma_\gamma(t)$ for times $t > 0$ define the *shear relaxation modulus* $G_\gamma(t)$:

$$\sigma_\gamma(t) = \gamma G_\gamma(t) \quad (\text{A5})$$

4) Ramp experiment. At a time t after a constant shear rate κ is applied, the stress $\sigma(t)$ defines the *shearing viscosity function* $\eta_\kappa(t)$:

$$\eta_\kappa(t) = \sigma(t) / \kappa \quad (\text{A6})$$

If the deformation is allowed to proceed until $t = S$ and then stopped, the stress $\sigma(S, \theta)$ at a time θ after the strain stopped defines the *relaxation function* $G_\kappa(S, \theta)$:

$$G_\kappa(S, \theta) = \sigma(\theta) / \kappa \quad (\text{A7})$$

5) Sinusoidal experiment. If a sinusoidal shear stress $\sigma^*(t) = \sigma_0 e^{i\omega t}$ is imposed, the shear strain in the steady state has a Fourier component of the same frequency which can be represented as $\gamma_1^* = \gamma_0 e^{i(\omega t - \delta)}$. The *complex dynamic shear compliance* $J_\sigma^*(\omega)$ is defined by:

$$J_{\sigma}^*(\omega) = \gamma_1^*(t)/\sigma^*(t) = J'_{\sigma}(\omega) - iJ''_{\sigma}(\omega) \quad (\text{A8})$$

where $J'_{\sigma}(\omega)$, the real part of $J_{\sigma}^*(\omega)$, is called the *storage shear compliance* and $J''_{\sigma}(\omega)$, the imaginary part, is called the *loss shear compliance*.

The *complex dynamic viscosity* $\eta_{\sigma}^*(\omega)$ is defined as

$$\eta_{\sigma}^*(\omega) = \sigma^*(t)/\dot{\gamma}_1^*(t) = \eta'_{\sigma}(\omega) - i\eta''_{\sigma}(\omega) \quad (\text{A9})$$

where $\dot{\gamma}_1^*(t)$ is the rate of strain $d\gamma_1^*(t)/dt$, and where $\eta'_{\sigma}(\omega)$ is called the *dynamic viscosity*. It can be readily shown from these definitions that:

$$\eta'_{\sigma}(\omega) = J''_{\sigma}(\omega)/\omega |J_{\sigma}^*(\omega)|^2 \quad (\text{A10})$$

$$\eta''_{\sigma}(\omega) = J'_{\sigma}(\omega)/\omega |J_{\sigma}^*(\omega)|^2 \quad (\text{A11})$$

where $|J_{\sigma}^*(\omega)|$, the *absolute value* of $J_{\sigma}^*(\omega)$, is

$$|J_{\sigma}^*(\omega)|^2 = [J'_{\sigma}(\omega)]^2 + [J''_{\sigma}(\omega)]^2 \quad (\text{A12})$$

18.2 Linear Viscoelasticity

If the stresses in the above experiments become small, various of the above-defined material function approach limiting values and are interrelated by expressions which can be derived from the theory of linear viscoelasticity.

1) Creep experiment. For sufficiently small stress σ , $J_{\sigma}(t)$ becomes a stress independent function, $J(t)$ and η_{σ} becomes a constant η_0 , often called the *zero shear viscosity*. For a linear viscoelastic fluid, one can write $J(t)$ as:

$$J(t) = R_0(t) + t/\eta_0 \quad (A13)$$

where $R_0(t)$ is the limiting value of the recovery function $R_\sigma(\infty, t)$ as σ approaches zero. [The subscript zero is not used in $J(t)$ and other linear viscoelastic properties in order to conform to the standard notation].

2) Recovery experiment. For sufficiently small stress σ , $R_\sigma(S, \theta)$ becomes independent of σ and approaches $R_0(S, \theta)$:

$$R_0(S, \theta) = J(S) - J(S + \theta) + J(\theta) \quad (A14)$$

and the steady state recoverable compliance R_∞ approaches a limiting value

$$R_0(\infty, \infty) = R_0(\infty) = R_0 \quad (A15)$$

3) Stress relaxation experiment. For sufficiently small strain γ , the shear relaxation modulus $G_\gamma(t)$ becomes $G(t)$ independent of γ . From the theory of linear viscoelasticity it is shown that $J(t)$ and $G(t)$ are interrelated:

$$\int_0^t J(s)G(t-s)ds = t \quad (A16)$$

and that

$$\eta_0 = \int_0^\infty G(t)dt \quad (A17)$$

$$\tau_c = R_0\eta_0 = \int_0^\infty tG(t)dt / \int_0^\infty G(t)dt \quad (A18)$$

where τ_c is a useful time constant characterizing viscoelastic behavior.

4) Ramp experiment. When κ is sufficiently small, $\eta_\kappa(t)$ approaches $\eta_0(t)$, a function independent of κ :

$$\eta_0(t) = \int_0^t G(s) ds \quad (A19)$$

5) Sinusoidal experiment. For sufficiently small σ_0 , the shear strain in the steady state is $\gamma^*(t) = \gamma_0 e^{i(\omega t - \delta)}$ and the various associated viscoelastic properties become independent of the σ . This is signified by omitting the σ in the subscript, e.g. $J_\sigma^*(\omega)$ goes to $J^*(\omega)$, $J_\sigma'(\omega)$ to $J'(\omega)$, $\eta_\sigma'(\omega)$ to $\eta'(\omega)$, etc.

From the theory of linear viscoelasticity, it is known that

$$J'(\omega) = R_0 - \omega \int_0^\infty [R_0 - R_0(t)] \sin \omega t \, dt \quad (A20)$$

$$J''(\omega) = (\omega \eta_0)^{-1} + \omega \int_0^\infty [R_0 - R_0(t)] \cos \omega t \, dt \quad (A21)$$

A useful approximation is

$$J(t) \simeq |J^*(\omega = t^{-1})| \quad (A22)$$

where we use the notation $F(x=z)$ to mean the value of $F(x)$ for $x=z$.

6) Retardation spectrum. Another useful method of representing linear viscoelastic behavior is through the use of the *retardation spectrum* $L(\tau_d)$ of *retardation times* τ_d which may be defined by the equation:

$$R_0(t) = J_g + \int_{-\infty}^{\infty} L(\tau_d) [1 - \exp\{-t/\tau_d\}] d \ln \tau_d \quad (A23)$$

where the *glassy compliance* J_g is $R_0(0)$.

18.3 Time-Temperature Equivalence

For many materials (e.g. random coil polymers and their concentrated solutions) the logarithmic plot of $J(t)$ for the temperature T can be superimposed on that for the temperature T_0 (called the reference temperature) by a translation by $\log a_T$ along the $\log t$ axis and by a much smaller translation, $\log b_T$, along the $\log J$ axis. In such a case, using the notation $J(t, T)$ to indicate the function $J(t)$ at the temperature T , we can then write

$$b_T J(t, T) = J(t/a_T, T_0) \quad (A24)$$

and plots of $b_T J(t, T)$ for various values of T will fall on one *reduced* graph if plotted against a reduced time t/a_T . The material is said to be *thermorheologically simple* and *time-temperature superposition* is said to be applicable. It can be shown that similar reduced plots can be made for the other viscoelastic function: e.g., $b_T J'(\omega, T)$, $b_T J''(\omega, T)/b_T a_T$ and $\eta'(\omega)/b_T a_T$ versus $a_T \omega$. It can then be shown that, for a viscoelastic fluid, that

$$a_T = \tau_c(T)/\tau_c(T_0) \quad (A25)$$

$$b_T = R_0(T_0)/R_0(T) \quad (A26)$$

where τ_c , a useful time constant for the material is given by

$$\tau_c = \eta_0 R_0 \quad (A27)$$

Using time-temperature equivalence, Eqn. (A8) can be recast to a form which will give a universal curve for various temperatures:

$$J(t/\tau_c) \simeq R_0 [\psi(t/\tau_c) + t/\tau_c] \quad (A28)$$

where

$$\psi(t) = [R_0(t) - J_g]/[R_0 - J_g] \quad (A29)$$

The concept of thermorheological simplicity is found to be valid for nonlinear viscoelastic properties as well. Data on η_κ at various temperatures (and to a certain extent at various molecular weights and concentrations c for polymer solutions) fall on a single plot when plotted in the form of η_κ/η_0 versus $\tau_c\kappa$. This is expressed by the equation:

$$\eta_\kappa = \eta_0 Q(\tau_c\kappa) \quad (A30)$$

where $Q(\tau_c\kappa)$ is independent of T (and of c). Typically $Q(\tau_c\kappa)$ exhibits a crossover from $Q(\tau_c\kappa) = 1$ to $Q(\tau_c\kappa) = q(\tau_c\kappa)^{-m}$ behavior at $\tau_c\kappa \simeq 1$. It is also observed that R_κ for various temperatures can be similarly represented by:

$$R_\kappa = R_0 P(\tau_c\kappa) \quad (A31)$$

where $P(\tau_c\kappa)$ is independent of temperature.

REFERENCES

1. H. Z. Cummins and E. R. Pike, *Photon Correlation and Light Beating Spectroscopy*, Plenum Press, New York, NY, 1974.
2. B. Chu, *Laser Light Scattering*, Academic Press, New York, NY, 1974.
3. B. J. Berne and R. Pecora, *Dynamic Light Scattering*, Wiley, New York, NY, 1976.
4. J. M. Schurr, *CRC Critical Rev. in Biochem.*, 371 (1977).
5. B. Chu, *Phys. Sci.* 19, 458 (1979).
6. E. Jakeman and E. R. Pike, *J. Phys. A.* 2, 115 (1969).
7. A. K. Jaiswal and C. L. Mehta, *Phys. Rev.* 2, 168 (1970).
8. E. R. Pike and E. Jakeman, *Adv. Quantum Electronics* 2, 1 (1974).
9. D. E. Koppel, *J. Appl. Phys.* 42, 3216 (1971).
10. P. N. Pusey, D. E. Koppel, D. W. Schaefer, R. D. Camerini-Otero, and S. H. Koenig, *Biochemistry* 13, 952 (1974).
11. E. Jakeman and E. R. Pike, *J. Phys. A.* 1, 128 (1968).
12. G. Bedard, J. C. Chang, and L. Mandel, *Phys. Rev.* 160, 1496 (1967).
13. E. Jakeman, Photon Correlation in *Photon Correlation and Light Beating Spectroscopy*, (H. Z. Cummins and E. R. Pike, Eds.), Plenum Press, New York, NY, 1974.
14. G. C. Berry, *Discuss. Farad. Soc.* 49, 121 (1970).
15. J. Castell-Evans, *Physico-Chemical Tables*, (C. Griffin, Ed.), London, 1911; and R. C. Weast, *Handbook of Chemistry and Physics*, 55th ed., CRC Press, Cleveland, OH, 1975.
16. A. V. Tobolsky, *Properties and Structure of Polymers*, Wiley, New York, NY, 1960.
17. G. C. Berry, *J. Poly. Sci., Poly. Symp.* 15, 143 (1978).
18. G. C. Berry, E. F. Casassa, P. Metzger, and S. Venkatraman, *Technical Report AFML-TR-79*, 1979.
19. G. C. Berry, E. F. Casassa, P. Metzger, and S. Venkatraman, *AFML-TR-78-164, Part II*, January, 1980.
20. K. E. Van Holde, *Physical Biochemistry*, Prentice-Hall, Englewood Cliffs, NJ, 1971.

21. E. Gulari, Y. Tsunashima, and B. Chu, *Polymer* 20, 347 (1979).
22. C. C. Lee, S.-G. Chu, and G. C. Berry, *J. Polym. Sci., Phys. Ed.*, in press.
23. P. J. Flory, *Macromolecules* 11, 1141 (1978).
24. R. R. Matheson, Jr. and P. J. Flory, *Macromolecules* 14, 954 (1981).
25. P. J. Flory and R. S. Frost, *Macromolecules* 11, 1126 (1978); and references cited therein.
26. G. C. Berry and C.-P. Wong, *J. Polym. Sci., Phys. Ed.* 13, 1761 (1975).
27. G. C. Berry, B. L. Hager, and C.-P. Wong, *Macromolecules* 10, 361 (1977).
28. W. W. Graessley, *Adv. Polym. Sci.* 16, 1 (1974).
29. A. V. Tobolsky and W. J. MacKnight, *Polymeric Sulfur and Related Polymers*, Interscience Publ., New York, NY, 1965.
30. G. C. Berry, *Physical Chemical Studies of Polymers with Rodlike Backbone Elements*, Technical Report AFWAL-TR-80-4099, August, 1980, p. 50.